

SYNTHESIS OF TiO₂-BASED NANOSTRUCTURED MATERIALS
USING A SOL-GEL PROCESS IN SUPERCRITICAL CO₂

(Spine Title: TiO₂-based Nanomaterials in scCO₂)

(Thesis format: Monograph)

by

Rahima A. Lucky

Graduate Program in Engineering Science, Department of Chemical and
Biochemical Engineering

A thesis submitted in partial fulfilment of the requirements for the degree of
Doctor of Philosophy

School of Graduate and Postdoctoral Studies

The University of Western Ontario
London, Ontario, Canada

THE UNIVERSITY OF WESTERN ONTARIO
SCHOOL OF GRADUATE AND POSTDOCTORAL STUDIES

CERTIFICATE OF EXAMINATIONS

Supervisor

Prof. Paul A Charpentier

Supervisory Committee

Prof. Hugo deLasa

Prof. Amin Rizkalla

Examiners

The thesis by
Rahima A. Lucky

Entitled:
**Synthesis of TiO₂-based nanostructured materials using a sol-gel
process in supercritical CO₂**

is accepted in partial fulfillment of the
requirements for the degree of
Doctor of Philosophy

Date _____

Chair of Thesis Examination Board

ABSTRACT

One-dimensional nanostructures (e.g. nanotubes, nanowires, nanobelts) of titania (TiO_2) are receiving considerable attention due to their unique physical properties, high activity, strong oxidation capability, chemical stability and numerous potential applications in solar energy systems. These nanostructured materials bear tremendous promise in the effective utilization of solar energy based on photovoltaic and water-splitting devices. However, the available preparation techniques have limitations. In this respect, a sol-gel process using supercritical carbon dioxide (scCO_2) as solvent offers a viable alternative to obtain these nanostructured materials, due to the unique enabling properties of scCO_2 .

This research has focused on the synthesis and modification of TiO_2 nanomaterials via an acid modified sol-gel process in scCO_2 . In this regard, the doping agents used were Fe, Zr, and N. Because of its zero surface tension, scCO_2 helps to form and maintain nanostructures and high surface areas of the synthesized nanomaterials. The low dielectric constant results in lower solubility with LA-LB interactions helping to stabilize the hydrolysis products, resulting in new and desirable morphologies. The synthesis was carried out in a batch reactor, i.e. in a view cell equipped with sapphire windows, for observation of the phase changes. The synthesis process was also studied using in situ FTIR spectrometry with the resulting nanomaterials being characterized using electron microscopy, N_2 physisorption, FTIR, XRD, XPS, thermal analysis, TPD and UV-Vis analysis. A kinetic model for the phase changes involved during heat treatment of the synthesized nanomaterials was developed, and the performance of the

synthesized nanomaterials was evaluated as a photocatalyst to degrade methylene blue in aqueous solution under UV light.

The results showed that the type of dopant significantly altered the morphology as well as the surface properties of the hybrid nanomaterials. For instance, while being synthesized under similar experimental conditions in scCO₂ pure TiO₂ formed nanofibers of 20-50 nm dia, Zr doped TiO₂ samples formed sheets with 100-300 nm width and nanotubes with a diameter of 50–140 nm, depending on the initial concentration of precursor(s). However, Fe doped samples showed a flake type flat structure while zirconia modified N doped TiO₂ samples showed a sheet type structure. Crystalline structures were obtained when the prepared materials were calcined at 500 °C. Anatase TiO₂ nanocrystallites with a size range *ca.* 6-14 nm were obtained depending on the amount and type of doping. The resulting materials exhibited a mesoporous structure and a higher surface area compared to pure TiO₂ nanomaterials.

This work revealed that the direct sol-gel process in scCO₂ is a promising technique for synthesizing and modifying TiO₂ nanomaterials. The formed modified TiO₂ nanostructured materials had a higher surface area, smaller crystallite size, and greater thermal stability, which are all desirable features for catalysts, support materials, semiconductors, and electrodes in dye-sensitized solar cells (DSSC). The simple synthesis procedure, which is scalable, used mild reaction conditions with a green solvent, providing a high yield and high quality nanomaterials, making this route potentially attractive for commercial employment.

Key Words: nanomaterials, TiO₂, ZrO₂ doped TiO₂, N doped TiO₂, Fe doped TiO₂, aerogel, modified sol-gel process, green solvent, scCO₂, photocatalyst, solar energy. solid state reaction kinetics, activation energy

To my parents-----
And my daughter-----

ACKNOWLEDGEMENT

I would like to express my sincere thanks to my supervisor Professor Paul A. Charpentier, for giving me the opportunity to work on such a fascinating project with all necessary supports and continuous guidance throughout my study at Western.

Many thanks to Professor Hugo de Lasa and Professor Amin Rizkalla, members of the Advisory committee, for their important guidance and suggestions.

I would like to express my gratitude to the following people for their help in material characterization: Fred Pearson of the Brockhouse Institute for Materials Research, McMaster University, Ron Smith of the Biology Department, Dr. Todd Simpson and Nancy Bell of the Western Nanotech Laboratory, Alexgander aubin, Mary Jane, Mark beisinger of UWO. Special thanks as well to Joanna and Kathy, the administrative staff of the Department of Chemical and Biochemical Engineering for their continuous help.

I would like to gratefully acknowledge the financial support of the Natural Science and Engineering Research Council of Canada (NSERC), the Materials and Manufacturing Ontario Emerging Materials program (MMO-EMK), and the Canadian Foundation for Innovation (CFI).

I am also very grateful to fellow colleagues and friends for their continuous support, and advices.

Finally, I like to thanks my parents for their endless love and unconditional moral support. I also like to thank my little princess, Sarah for her sacrifices and love.

TABLE OF CONTENTS

	Page
ABSTRACT	iii
ACKNOWLEDGEMENT	vi
LIST OF FIGURES	xii
LIST OF TABLES	xx
NOMENCLATURE	xxii
CHAPTER 1	1
1. Background	1
1.1. Energy and the Environment	1
1.2. Solar Energy.....	2
1.2.1. Heating.....	3
1.2.2. Electricity.....	4
1.2.3. Chemical Processes.....	4
1.3. TiO ₂ and Solar Energy	5
CHAPTER 2	8
2. Introduction.....	8
2.1. TiO ₂ Nanostructured Materials	9
2.1.1. Photocatalytic Applications	10
2.1.2. Photovoltaic Applications.....	13
2.1.3. Other Potential Applications.....	15
2.2. Modifications of TiO ₂ Nanomaterials.....	15
2.2.1. Bulk Modification of TiO ₂ Nanomaterials	17
2.2.2. Electronic Properties and Optical Response of TiO ₂	19
2.3. Synthesis Methods	24
2.3.1. Conventional Sol-gel Method.....	24
2.3.2. Sol Method.....	28
2.3.3. Hydrothermal Method.....	28
2.3.4. Solvothermal Method.....	30
2.3.5. Chemical Vapor Deposition (CVD).....	30
2.3.6. Thermal Decomposition and Pulsed Laser Ablation	31
2.3.7. Templating	31

2.3.8.	N Doped TiO ₂ Nanomaterials	32
2.4.	Supercritical Fluids (SCFs) and supercritical CO ₂ (scCO ₂)	33
2.5.	Properties of supercritical CO ₂	37
2.6.	TiO ₂ Based Nanostructured Materials in scCO ₂	42
2.7.	Scope of the Research	49
CHAPTER 3		51
3.	Introduction	51
3.1.	Synthesis of TiO ₂ Based Nanomaterials	52
3.1.1.	Materials	52
3.1.2.	Experimental Set-Up	53
3.1.3.	Experimental Procedure	54
3.2.	Characterization Methods	56
3.2.1.	Electron Microscopy	56
3.2.2.	Thermal Analysis	59
3.2.3.	X-ray Photon Spectroscopy (XPS)	61
3.2.4.	Powder X-Ray Diffraction (XRD)	63
3.2.5.	Raman Spectroscopy	65
3.2.6.	N ₂ Physisorption	66
3.2.7.	UV-Vis Spectroscopy	71
3.2.8.	In-situ ATR-FTIR Analysis	73
3.2.9.	Temperature Programmed Desorption (TPD)	74
3.2.10.	Evaluation Procedure	75
CHAPTER 4		77
4.	Introduction	77
4.1.	Experimental	79
4.2.	Effects of Pressure	80
4.3.	Effects of Temperature	83
4.4.	Effects of Concentration	90
4.5.	Effects of Acid to Metal Alkoxide Ratio	94
4.6.	Effects of Zr compositions	98
4.6.1.	Morphology	99

4.6.2.	Composition.....	102
4.6.3.	Thermal Decomposition Behavior.....	106
4.6.4.	Phase Structure and Crystallite Size.....	108
4.6.5.	Surface Area and Pore Volume.....	110
4.7.	Mechanism of Binary Nanotube Formation.....	113
4.8.	Reaction Scheme in scCO ₂	115
4.9.	Conclusions.....	118
CHAPTER 5.....		120
5.	Introduction.....	120
5.1.	Experimental.....	122
5.2.	Morphology.....	122
5.3.	Composition.....	125
5.4.	Crystallinity and Phase Structure.....	128
5.5.	Surface area and Pore Volume.....	130
5.6.	Gelation Time.....	134
5.7.	Discussion.....	136
5.8.	Conclusions.....	140
CHAPTER 6.....		141
6.	Introduction.....	141
6.1.	Solid-State Reaction Kinetics.....	142
6.1.1.	Decomposition.....	142
6.1.2.	Phase Transformation.....	145
6.2.	Experimental.....	146
6.2.1.	SEM/TEM.....	146
6.2.2.	Decomposition Behavior (TGA/FTIR).....	148
6.2.3.	XRD and HRTEM.....	151
6.2.4.	Raman.....	156
6.2.5.	BET Analysis.....	157
6.3.	Solid State Reaction Kinetics.....	160
6.4.	Conclusions.....	165
CHAPTER 7.....		166

7.	Introduction.....	166
7.1.	Experimental.....	168
7.2.	Morphology.....	169
7.3.	Thermal Analysis.....	174
7.4.	Phase Structure.....	177
7.5.	Surface Area and Pore Volume.....	181
7.6.	Surface Acidity.....	183
7.7.	Photo Response.....	184
7.8.	Photocatalytic Performance.....	185
7.9.	Conclusions.....	187
	CHAPTER 8.....	188
8.	Introduction.....	188
8.1.	Experimental.....	189
8.2.	SEM.....	191
8.3.	Thermal Analysis.....	193
8.4.	XRD Analysis.....	195
8.5.	Raman.....	196
8.6.	HRTEM Analysis.....	197
8.7.	XPS Analysis.....	199
8.8.	BET Analysis.....	202
8.9.	Photocatalytic Performance.....	204
8.10.	Conclusions.....	206
	CHAPTER 9.....	207
9.	Introduction.....	207
9.1.	Direct Sol-Gel Process in scCO ₂	207
9.2.	The Synthesis Parameters of the Direct Sol-Gel Process in CO ₂	208
9.3.	Mechanism of Nanostructure Formation.....	209
9.4.	Chemistry of the Direct Sol-gel Process in CO ₂	209
9.5.	Performance of TiO ₂ -based Nanostructured Materials.....	210
9.6.	Recommendations.....	210
	References.....	212

Appendices.....	228
Appendix 1. Copyright Permissions of Advanced Materials.....	228
Appendix 2. Copyright Permissions of Acta Crystallographica Journals.....	228
Appendix 3. Physical Properties of the Raw Materials Used in this dissertation.....	229
Appendix 4. Powder XRD Analysis Conditions.....	229
Appendix 5. Typical EDX spectrum for binary Zr-Ti nanomaterials.....	230
Appendix 6. Typical DSC curves for binary Zr-Ti nanomaterials at different heating rate.....	230
Appendix 7. Typical XPS deconvoluted spectra for N doped TiO ₂ nanomaterials.....	232
Appendix 8. Evaluation of the modified nanomaterials as a photocatalyst.....	232
Appendix 9. ZrO ₂ /TiO ₂ Binary Nanotubes as Fillers	237
CURRICULAM VITA	240

LIST OF FIGURES

Figure 1.1: Mechanism of semiconductor photocatalysis. ¹⁵	5
Figure 2.1: The principle of TiO ₂ photocatalysis. ³⁷	11
Figure 2.2: Principle of operation and energy level scheme of the dye-sensitized nanocrystalline TiO ₂ solar cell. ⁴⁰	14
Figure 2.3: The bonding diagram of a perfect TiO ₂ crystal. ⁸⁷	21
Figure 2.4: Hydrolysis and condensation steps for sol-gel mechanism.....	25
Figure 2.5: Aerogel synthesis scheme by the conventional sol-gel route.....	27
Figure 2.6: Schematic of the phase diagram of a typical material. ¹²³	34
Figure 2.7: Reduced pressure (P _r) vs. reduced density (ρ _r) diagrams at various reduced temperatures (T _r). ¹³⁵	38
Figure 2.8: Solubility parameters of CO ₂ . ¹³⁶	39
Figure 2.9: Diffusivity of CO ₂ vs temperature at various pressures. ¹³⁷	40
Figure 2.10: Surface tension of saturation liquid CO ₂ as a function of pressure. ¹²³	41
Figure 2.11: Binding modes of acetic acid with metal: (a) chelating bidentate and (b) bridging bidentate and (c) monodentate.	47
Figure 2.12: Schematic diagram of the direct sol-gel process in scCO ₂ for the synthesis of nanostructured materials.....	48
Figure 3.1: Schematic diagram of experimental set-up; A-CO ₂ tank, B- Syringe pump, C- View cell, D- Temperature controller, E- Pressure indicator.....	53
Figure 3.2: Preparation scheme for TiO ₂ based nanomaterials by sol-gel process.....	55
Figure 3.3: Schematic interactions of a specimen with incident electrons.....	57
Figure 3.4: A schematic DSC curve demonstrating the appearance of phase transition. ¹⁵⁷	61
Figure 3.5: A typical high resolution XPS spectrum with corresponding information.....	63
Figure 3.6: Schematic of X-ray reflection on the crystal planes. ¹⁵⁸	64
Figure 3.7: BET plot of N ₂ adsorption on silica gel at 91 K. ¹²³	67

Figure 3.8: Curves of x/x_m vs. p/p_0 calculated from the BET equation for different values of c . I, $c=1$; II, $c=11$; III, $c=100$; IV, $c=10000$. ¹⁶⁰	68
Figure 3.9: Classification of hysteresis loops as recommended by the IUPAC.	70
Figure 3.10: Interaction of light with solid sample.	72
Figure 3.11: Schematic of the reactor with the ATR-FTIR (A) computer; (B) FTIR; (C) temperature and RPM controller with pressure display; (D) 100 ml autoclave equipped with diamond IR probe; (E) needle valves; (F) check valves; (G) syringe pump; (H) container for carboxylic acid; (I) CO ₂ cylinder. ¹²³	74
Figure 4.1: SEM images for materials synthesized at (a) 3000 (b) 5000 and (c) 6000 psig pressures. (<i>Bar represents 200 nm</i>).	81
Figure 4.2: N ₂ adsorption/desorption isotherms of as-prepared ZrO ₂ -TiO ₂ nanomaterials synthesized at different pressures.	82
Figure 4.3: BJH pore size distribution of as-prepared ZrO ₂ -TiO ₂ nanomaterials synthesized at different pressures.	83
Figure 4.4: SEM images for materials synthesized at: (a) 40 °C and (b) 80 °C temperature. (<i>Arrows indicate sheet type structure in materials synthesized at 40 °C</i>).	84
Figure 4.5: Effects of temperature on the morphology of ZrO ₂ -TiO ₂ nanomaterials, TEM images of calcined materials (a) & (c) synthesized at 40 °C, and (b) & (d) synthesized at 80 °C temperature. (<i>Bar represents 100 nm</i>).	85
Figure 4.6: N ₂ adsorption/desorption isotherms of the ZrO ₂ -TiO ₂ as-prepared nanomaterials synthesized at different temperatures.	86
Figure 4.7: BJH pore size distribution of the ZrO ₂ -TiO ₂ as-prepared nanomaterials synthesized at different temperatures.	87
Figure 4.8: The gelation time as a function of reciprocal of absolute process temperature.	89
Figure 4.9: Effects of concentration on the morphology of ZrO ₂ -TiO ₂ nanomaterials synthesized using (a) C-0.35 mol/L, (b) C-0.7 mol/L and (c) C-1.4 mol/L. (<i>Bar represents 1 μm</i>).	91

Figure 4.10: N ₂ adsorption/desorption isotherms of the ZrO ₂ -TiO ₂ as-prepared nanomaterials synthesized using different alkoxide concentrations.	92
Figure 4.11: BJH pore size distribution of as-prepared ZrO ₂ -TiO ₂ nanomaterials synthesized using different precursor concentrations.....	93
Figure 4.12: Effects of acid to metal alkoxide ratio on the morphology of ZrO ₂ -TiO ₂ nanomaterials synthesized using (a) R-3, (b) R-4 and (c) R-6. (<i>Bar represent 500 nm</i>).	94
Figure 4.13: N ₂ adsorption/desorption isotherms of as-prepared ZrO ₂ -TiO ₂ nanomaterials synthesized using different acid to metal alkoxide ratios.....	96
Figure 4.14: BJH pore size distribution of as-prepared ZrO ₂ -TiO ₂ nanomaterials synthesized using different acid to metal alkoxide ratios.....	96
Figure 4.15: Zr-Ti binary calcined nanomaterials with different zirconium compositions (a) undoped TiO ₂ , (b) 4%, (c) 8%, and (d) 10%. (<i>Bar represents 200 nm. All the samples were examined after platinum coating. Arrows indicate tubes</i>).	100
Figure 4.16. TEM image of 4% Zr-Ti binary TiO ₂ nanomaterials. (<i>Bar represents 100 nm</i>)......	101
Figure 4.17: TEM: Zr-Ti binary nanomaterials with different zirconium composition (a) undoped TiO ₂ , (b) 4% Zr doped TiO ₂ . (<i>Bar represents 100 nm</i>)......	101
Figure 4.18: Powder ATR-FTIR spectra of as-prepared ZrO ₂ -TiO ₂ binary nanomaterials (a) pure TiO ₂ , (b) 10% ZrO ₂ , and (c) Zr-Ti binary single crystal.	103
Figure 4.19: A typical Ti, Zr EDX mapping for as-prepared Zr-TiO ₂ sample. (<i>Bar represents 20 μm</i>).	104
Figure 4.20: XPS spectrum for typical ZrO ₂ modified TiO ₂ nanotubes.	105
Figure 4.21: Weight loss of Zr-Ti binary metal oxide nanomaterials as a function of temperature.	107

Figure 4.22: XRD patterns for Zr-Ti binary metal oxide nanomaterials with various % ZrO ₂ compositions.	109
Figure 4.23: N ₂ adsorption/desorption isotherms of the Zr-Ti binary metal oxide nanomaterials with different % ZrO ₂ compositions.....	111
Figure 4.24: BJH pore size distribution of Zr-Ti binary metal oxide nanomaterials at different % ZrO ₂ compositions.....	111
Figure 4.25: Pore volume of as prepared and calcined binary nanomaterials with various % ZrO ₂ compositions.	112
Figure 4.26: Surface area of as-prepared and calcined Zr-Ti binary metal oxide nanomaterials as a function of zirconium compositions.....	113
Figure 4.27: Acid modified Zr-Ti alkoxide single crystal (a) one unit,(b) cell along [100] plane, and (c) ZrO ₂ -TiO ₂ nanotube formed via roll up of sheet. (Color code for a,b: Pink-Titanium, Green-Zirconium, Red-oxygen, Gray- Carbon).....	115
Figure 4.28: In situ FTIR spectra for 1:1 mol ratio TIP and ZPO with acetic acid at R 5 (acid to metal alkoxide ratio) in scCO ₂ from 0-1200 minutes.....	116
Figure 5.1: SEM: ZrO ₂ -TiO ₂ nanomaterials in different solvents: (a) scCO ₂ , (b) Hexane, (c) Xylenes, (d) Iso-propanol, and (e) Ethanol. (<i>Bar represents 200 nm. All the samples were examined after platinum coating</i>).	123
Figure 5.2: TEM: ZrO ₂ -TiO ₂ nanomaterials in different solvents (a) scCO ₂ , (b) Hexane, (c) Xylenes, (d) Iso-propanol, and (e) Ethanol. (<i>Bar represents 300 nm. All samples were calcined at 500°C</i>).	124
Figure 5.3: Powder ATR-FTIR spectra of as-prepared ZrO ₂ -TiO ₂ nanomaterials in different solvents: (a) Hexane, (b) scCO ₂ (c) Xylenes, and (d) Iso-propanol.....	126
Figure 5.4: A typical TG/DTG curve for ZrO ₂ -TiO ₂ nanomaterials synthesized in hexane.	127

Figure 5.5. Powder XRD spectra of the ZrO ₂ -TiO ₂ nanomaterials calcined at 500 °C synthesized in different solvents (a) scCO ₂ , (b) Hexane, (c) Xylenes, (d) Iso-propanol, and (e) Ethanol.....	129
Figure 5.6: N ₂ adsorption/desorption isotherms of as-prepared ZrO ₂ -TiO ₂ nanomaterials synthesized in different solvents.	131
Figure 5.7: BJH pore size distribution of calcined ZrO ₂ -TiO ₂ nanomaterials, synthesized in different solvents.....	131
Figure 5.8: Surface area of as-prepared and calcined nanomaterials synthesized in different solvents as a function of solvent's dielectric constant (ε).....	133
Figure 5.9: Gelation time of nanomaterials synthesized in different solvents as a function of solvent's dielectric constant (ε).....	135
Figure 6.1: SEM: Zr-TiO ₂ nanotubes calcined at (a) as-prepared, (b) 600, (c) 800 and (d) 1000 °C. (<i>Bar represent 200 nm. All the samples were examined after platinum coating.</i>)	147
Figure 6.2: TEM: ZrO ₂ -TiO ₂ nanotubes calcined at (a) as-prepared,(b) 500, (c) 900 and (d) 1000 °C.....	148
Figure 6.3: Weight loss of nanotubes as a function of temperature.....	149
Figure 6.4: Powder ATR-FTIR spectra of ZrO ₂ -TiO ₂ nanotubes calcined at different temperatures.	151
Figure 6.5: Powder XRD spectra of ZrO ₂ -TiO ₂ nanotubes calcined at different temperatures. (<i>A-anatase, R-rutile</i>).....	152
Figure 6.6: HRTEM: ZrO ₂ -TiO ₂ nanotubes calcined at (a) as-prepared,(b) 500, and (c) 1000 °C. (<i>Bar represent 10 nm.</i>)	156
Figure 6.7: Raman spectra of ZrO ₂ -TiO ₂ nanotubes calcined at: (a) 500, (b) 600, (c) 700, (d) 800, (e) 900, and (f) 1000 °C. (<i>A-anatase, R-rutile</i>).....	157
Figure 6.8: N ₂ adsorption/desorption isotherms of ZrO ₂ -TiO ₂ nanotubes calcined at different temperatures.....	158
Figure 6.9: BJH pore size distribution of the ZrO ₂ -TiO ₂ nanotubes calcined at different temperatures.	159

Figure 6.10: Surface area and pore volume of ZrO ₂ -TiO ₂ nanotubes as a function of calcination temperature.	160
Figure 6.11. Conversion-temperature profiles for different steps of thermal decomposition during heat treatment. [\blacksquare -Experimental data for step I, \blacktriangle - Experimental data for step II, solid line for model predicated value].	162
Figure 6.12. Plot of $\ln(\beta/T_p^2)$ vs $1/T_p$ for anatase and rutile phases.....	163
Figure 6.13: Ln of anatase and rutile crystallite size in nm as a function of reciprocal of absolute temperature.(\blacksquare -Anatase, \bullet/\circ rutile).	164
Figure 7.1: SEM: Fe doped TiO ₂ nanomaterials: (a) S1-0% (b) S2-0.2%, (c) S3-0.36%, and (d) S4-0.49%. (Fe in at. %. All the samples were examined after platinum coating).	169
Figure 7.2: TEM: Fe doped TiO ₂ nanomaterials: (a) S1-0%, & (b) S4-0.49%, (c) S1, and (d) S4. (As-prepared (a) & (b), calcined (c)&(d), Bar represent 100 nm.)	171
Figure 7.3: O, Ti and Fe mapping for Fe doped TiO ₂ (S4) nanomaterials.	174
Figure 7.4: Powder ATR-FTIR spectra of as-prepared (a) TiO ₂ & (b) Fe doped TiO ₂ (S4) nanomaterials.	175
Figure 7.5: (a) TG and (b) DTG curves for Fe doped nanomaterials as a function of temperature.....	176
Figure 7.6: Powder XRD spectra of Fe doped TiO ₂ nanomaterials: (a) S1-TiO ₂ , (b) S2, (c) S3, (a-c) calcined at 500°C (d-f) S4 calcined at 400- 600 °C, respectively.....	178
Figure 7.7: Ln size of anatase crystallite in nm as a function of reciprocal of absolute temperature.	180
Figure 7.8: HRTEM: (a) S1- TiO ₂ , and (b) S4-Fe doped TiO ₂ nanomaterials (calcined at 500°C (a) & (b). (Bar represent 10 nm. Arrows indicate defects and pore).	181
Figure 7.9: (a) N ₂ adsorption/desorption isotherms, and (b) BJH pore size distribution of Fe doped TiO ₂ nanomaterial calcined at 500 °C.	182

Figure 7.10: BET surface area of Fe doped TiO ₂ nanomaterials calcined at different temperatures.	183
Figure 7.11: The diffuse reflectance spectra of the Fe doped TiO ₂ nanomaterials calcined at 500 °C: S1-TiO ₂ , S2-0.2%, S3-0.36%, and S4-0.49% at. Fe. (a) Kubelka-Munk unit and (b) modified Kubelka-Munk function, respectively.	184
Figure 7.12: The calculated degradation rate of various Fe doped TiO ₂ by eq. 3.13.....	186
Figure 8.1. Effect of 1:1 Triethyleamine/ TIP with Acetic acid at R5, (A)TIP+HOAc formed yellow colour solution , (B) TIP+HOAc+ TEA formed brown solution, (C) TIP+HOAc+TEA+H ₂ O formed gel.....	190
Figure 8.2: SEM: (a) TiO ₂ , (b) TiO ₂ -N1, (c) Zr-TiO ₂ -N1, and (d) Zr-TiO ₂ -N2. (<i>Bar represents 500 nm. All the samples were examined after platinum coating</i>).	192
Figure 8.3: TEM: (a) TiO ₂ , (b) TiO ₂ -N1, (c) Zr-TiO ₂ -N1, and (d) TiO ₂ -N2. (<i>Bar represents 30 nm</i>).	193
Figure 8.4: TG/DTG curves for N-doped nanomaterials synthesized by sol-gel process as a function of temperature.....	194
Figure 8.5: Powder XRD spectra of the Zr modified N doped TiO ₂ nanomaterials calcined at 500°C: (a) TiO ₂ , (b) TiO ₂ -N1, (c) TiO ₂ -N2, (d) Zr-TiO ₂ , (e) Zr-TiO ₂ -N1, and (f) Zr-TiO ₂ -N2.....	196
Figure 8.6: Raman spectra around 142 cm ⁻¹ for Zr modified N doped TiO ₂ nanomaterials calcined at 500 °C.....	197
Figure 8.7: HRTEM for N-doped TiO ₂ nanomaterials: (a) TiO ₂ , (b) TiO ₂ -N1, (c) Zr-TiO ₂ -N1, and (d) TiO ₂ -N2. (<i>Bar represent 5 nm. Arrows indicate defects</i>).	198
Figure 8.8: Typical XPS spectrum for Zr modified N doped TiO ₂ as-prepared nanomaterials.	201
Figure 8.9: N ₂ adsorption/desorption isotherm of the Zr modified N doped TiO ₂ calcined nanomaterials. Inset shows the pore size distribution.	203

Figure 8.10: A typical partially hydrolyzed metal oxo-polymer.	204
Figure 8.11. The variation of the calculated degradation rate for Zr modified N doped TiO ₂ nanomaterials.....	206

LIST OF TABLES

Table 2.1: Critical properties for selected supercritical fluids. ¹²⁶	36
Table 2.2: Comparison of the properties of Gas, SCF and Liquid. ¹³⁵	40
Table 2.3. Carboxyl stretching frequencies and structures of carboxylate complexes.	48
Table 4.1: Solubility parameters of scCO ₂ under selected temperatures and pressures.....	80
Table 4.2. Synthesis conditions of Zr-TiO ₂ nanostructures in scCO ₂ and characterization results.....	81
Table 4.3: Surface area, pore volume and average pore diameter of as-prepared nanomaterials synthesized at various concentrations.	91
Table 4.4: Surface area, pore volume and average pore diameter of as-prepared nanomaterials synthesized with different acid to metal alkoxide ratios.....	95
Table 4.5: Results of Zr-Ti binary metal oxide nanostructures in scCO ₂	99
Table 4.6; Results of XPS analysis for selective Zr-Ti binary metal oxide nanostructures in scCO ₂	106
Table 5.1: Physical properties and dielectric constant of the solvents used in this study.	121
Table 5.2: Composition and weight loss at different stages of thermal analysis.....	127
Table 5.3: Crystallinity, crystal structure and size of the nanomaterials calcined at 500°C.	130
Table 5.4: Surface area, pore volume and average pore diameter of as-prepared and calcined nanomaterials synthesized in various solvents.	132
Table 5.5: Partial charge, δ , mol complexity and coordination number, n of titanium and zirconium alkoxides. ²⁰⁵	137
Table 6.1: Avrami-Erofeev models ²¹³	144
Table 6.2: The important rate equations used in kinetic analysis of solid-state reactions	145

Table 6.3: Crystal size and crystal structure at different calcination temperatures.....	153
Table 6.4: The calculated kinetic parameters for the decomposition of binary nanotubes during heat treatment.	162
Table 6.5: The calculated activation energy for the phase change of binary nanotubes during heat treatment.	164
Table 7.1: Crystallites size and surface area of undoped and doped nanomaterials calcined at different temperatures.	173
Table 8.1: Surface area, pore volume, pore diameter, and crystallites size for calcined undoped and doped nanomaterials.	195
Table 8.2: Surface N composition of as-prepared and calcined nanomaterials with N peak positions.....	202
Table 8.3: Charge distribution according to the partial charge model.....	204

NOMENCLATURE

Abbreviations:

Abs	absorbance
ATR-FTIR	attenuated total reflection fourier transform infrared spectroscopy
BET	brunauer-emmett-teller
CB	conduction band
DSC	differential scanning calorimetry
DSSC	dye sensitized solar cell
1D	one dimensional
FTIR	fourier transform infrared spectroscopy
HOAc	acetic acid
SCF	supercritical fluid
scCO ₂	supercritical CO ₂
SEM	scanning electron microscopy
PV	photovoltaic
TCD	thermal conductivity detector
TiO ₂	titania
TEM	transmission electron microscopy
TGA	thermogravimetric analysis
TIP	titanium(IV) <i>iso</i> -propoxide
TPD	temperature programmed desorption
UV	ultraviolet

VB	valence band
VOCs	volatile organic compounds
XPS	x-ray photon spectroscopy
XRD	x-ray diffraction
ZPO	zirconium(IV) propoxide

Symbols:

I_R	integrated intensity of rutile
I_A	integrated intensity of anatase
C	concentration
D_{pore}	adsorption average pore diameter
D_{crys}	crystallite size
E_a	activation energy
k	reaction rate constant
l	path length
P_c	critical pressure
P_{re}	reaction pressure
R	universal gas constant
R	acid to metal alkoxide ratio
T_c	critical temperature
T_{re}	reaction temperature
V	molar volume
V_{pore}	pore volume per gram

X_{Rutile}	weight fraction of rutile
α	absorbitivity
β	half-width at half-height of the diffraction peak
Δ	symmetric and asymmetric stretching vibration frequency difference
δ_{sc}	solubility parameter of supercritical fluid
ΔH_v	enthalpy change during vaporization
θ	half the angle of diffraction
λ	x-ray wavelength
ρ_{Rsc}	reduced density of supercritical fluid
ρ_{RL}	reduced density of liquid at its normal boiling point

CHAPTER 1

INTRODUCTION

1. Background

1.1. Energy and the Environment

The quality of human life, economic prosperity, and global stability largely depends on a ready and reliable supply of energy. The global current rate of energy consumption is approximately 4.1×10^{20} J/yr, which is equivalent to 13 trillion watts. The World Bank predicts that the demand for energy will double (to 30 trillion watts) by 2050 with an increase of the world's population to 9 billion people accompanied by a rapid technological development and economic growth.¹ According to the U.S. Department of Energy's International Energy Outlook 2006 report, fossil fuels currently supply about 80% of the worldwide energy demand.² The reserves of fossil fuels will run out during this century and renewable energy sources will need to be harnessed to satisfy this enormous energy demand. Moreover, environmental pollution is rising and threatens climate change due to the rising levels of greenhouse gases and pollutants produced by the combustion of fossil fuels, which has also increased public concern. Therefore, finding and utilizing carbon neutral renewable energy sources to satisfy the world's growing energy demand and solve the pollution problem are society's foremost challenges for the coming years.^{3, 4} In this regard, solar energy is considered to be the most promising and long lasting source in order to meet this growing energy demand with minimal associated environmental pollution. The annual total energy coming to the earth from the sun is approximately 3×10^{24} joules, which is about 10^4 times more than the

worlds current energy demand. Therefore, by utilizing solar energy, it is possible to satisfy the enormous energy demand as well as to solve the environmental pollution problem.

1.2. Solar Energy

The energy from the sun arrives on earth as radiation distributed across the electromagnetic spectrum from infrared to ultraviolet wavelengths. The amount of solar energy available at the Earth's surface in the direction of the sun is typically 1000 W/m^2 . In the 21st century, solar energy is certainly expected to make increasing contributions to the world's energy supply because it has the following advantages compared to conventional energy:⁵

1. Solar energy is virtually free after the initial cost has been recovered. Therefore, payback times can be very short when compared to the cost of current carbon based energy sources.
2. Solar and other renewable energy systems can be stand-alone; thereby not requiring connection to a power or natural gas grid.
3. The utilization of solar energy reduces environmental pollution.

There are many ways that solar energy can be used effectively. However, the applications of solar energy can be grouped into three primary categories: (i) heating or solar thermal, (ii) electricity production and (iii) chemical processes.

1.2.1. Heating

The most widely used applications of solar energy are for water and space heating. Solar energy can be used to heat homes and commercial buildings and can also be applied to industrial use in many different ways such as crop drying, outdoor and indoor pools, preheating boiler feed water etc. In active solar-heating systems, solar collectors are the key component which gather the sun's energy, transform it into heat, and then transfer the heat to water, solar fluid, or air. There are several types of solar collectors such as flat-plate collectors, evacuated-tube collectors and integral collector-storage systems. Usually, copper pipes are used in the solar collector system. However, there is a tremendous energy loss due to thermal radiation which can be reduced by using an optically selective absorber surface. The ideal behavior of an optical selective absorber surface is a high absorption in the solar spectral region and a low emittance in the thermal radiation region. Presently, no perfectly optically selective material has yet been found. Two approaches can be followed to achieve optical selectivity: (i) opposite to a black absorber a heat mirror is placed, reflecting the thermal infrared radiation, and transmitting the solar radiation, and (ii) a special coating, which absorbs the solar radiation, but transmits the infrared radiation.⁶ TiN_xO_y has been found a good optical selective coating on copper substrates.⁷

A solar heating system saves energy, reduces utility costs, and produces clean energy. The efficiency and reliability of solar heating systems have increased dramatically, making them attractive options in either home or business use.

1.2.2 Electricity

Photovoltaic (PV) devices typically consist of a series of thin semiconductor layers that are designed to convert sunlight to direct-current electricity. As long as the device is exposed to sunlight, a PV cell produces an electric current proportional to the amount of light it receives. PV cells can help to reduce the widespread dependence on dwindling oil reserves and mitigate adverse effects on the environment. Currently, crystalline silica-based solar cells are the most popular form of PV device, given their high solar conversion efficiencies, ease of manufacture, resistance to degradation, and the abundance of siliceous starting materials.⁸ However, for PV to be a competitive energy alternative, their cost needs to be reduced to at least 20% of their current market value.⁹ Hence, there is a need to investigate new highly efficient PV materials. According to the recent literature reports, TiO₂ nanostructured materials offer tremendous opportunities to enhance the efficiency of capturing solar energy, thereby reducing the overall cost.^{10 11, 12}

1.2.3 Chemical Processes

In chemical processes, solar energy can be used in two ways: i) solar detoxification technologies for cleaning water and air, and ii) producing fuel such as H₂ and CH₃OH by photoelectrolysis of water and reducing CO₂¹³, respectively, in the presence of a suitable catalyst such as TiO₂ or TiO₂ supported Pt, Cu. Figure 1.1 depicts the basic principle by which solar energy removes organics from polluted water or produces fuel. When TiO₂ (a semiconductor) absorbs ultraviolet radiation from sunlight, it produces pairs of electrons and holes. The excess energy of this excited electron promotes the electron to the conduction band thereby creating electron (e⁻) and hole (h⁺)

pairs. The positive-hole of TiO_2 breaks apart the water molecule to form hydrogen gas and a hydroxyl radical, which rapidly destroys the chemical bonds of the contaminant. The negative-electron reacts with an oxygen molecule to form a super oxide anion. This cycle continues as long as light is available.¹⁴

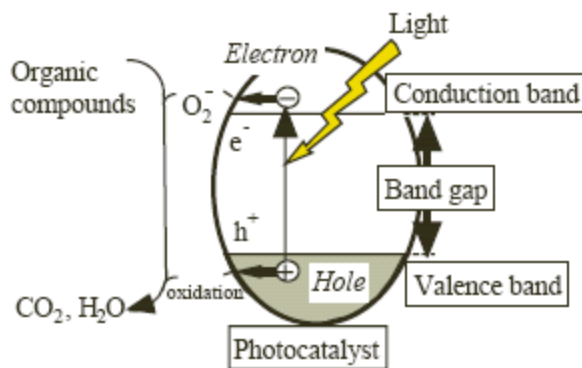


Figure 1.1: Mechanism of semiconductor photocatalysis.¹⁵

1.3. TiO_2 and Solar Energy

TiO_2 nanomaterials are one of the potential candidates for solar energy application due to TiO_2 's unique optoelectronic and photochemical properties.^{16, 17} Especially, as a photocatalyst to clean air/water and in electrolysis of water to produce hydrogen, TiO_2 nanomaterials have been receiving a great deal of attention.^{14, 16} However, its ability to generate oxidizing agents using sunlight as the primary energy source is very limited, because it only absorbs 3% of the solar energy. Consequently, a substantial portion of the available solar energy is not utilized.^{3, 18} Moreover, the low surface area and high electron-hole recombination rate of TiO_2 nanomaterials are also considered as negative

factors to wide-scale application. Bulk modification by cation and anion doping has been found very effective to improve the properties of TiO₂.^{4, 19-25}

Hence, significant progress in the research and development of nano TiO₂ is required to assure that solar technology can achieve its full potential. Solar electricity from photovoltaics is currently very costly with a limited production capacity. Solar thermal systems provide the lowest-cost solar energy but require large areas in the Sun Belt. Hence, the practical utilization of solar energy is strongly limited due to the available low efficiency and high cost materials with ≤ 2 % of the available solar energy currently being used. Therefore, it is highly desirable to enhance the performance of solar energy systems by designing new materials as well as increasingly understanding the electronic and molecular basis of capture, conversion, and storage of this clean, abundant, and economic energy. One of the most important research areas towards this means is to synthesize new efficient nanostructured materials for solar energy applications with low cost using a green technology.

This study aimed at developing superior quality TiO₂ based nanomaterials utilizing the green solvent scCO₂ for solar energy applications, with the major contributions of this study being the following:

- i. Synthesis of Fe, Zr and N-modified TiO₂ nanomaterials using an acid modified sol-gel technique in scCO₂,
- ii. Investigation of the effects of doping materials and synthesis technique on the characteristics of the TiO₂ nanomaterials,

- iii. Optimizing the synthesis conditions towards synthesizing superior quality of low cost material by a green solvent process for potential widespread solar energy application.

CHAPTER 2

LITERATURE REVIEW

(TiO₂ Based Nanostructured Materials in scCO₂)

2. Introduction

Recently, considerable effort has been devoted to synthesizing inorganic one-dimensional (1D) nanostructures (e.g. nanotubes, nanowires, nanobelts) given their unique physical properties compared to their bulk counterparts.^{26, 27} The favorable properties of the 1D nanomaterials make them very attractive in various applications including catalysis, high efficiency solar cells, coatings, and sensors.^{10, 28, 29} Amongst the 1D nanostructures reported in the literature, TiO₂ nanomaterials have received a great deal of attention due to their high activity, strong oxidation capability, and chemical stability.^{30, 31} TiO₂ nanomaterials offer tremendous opportunities to improve the efficiency of the solar energy derived systems that is expected to help reduce our dependency on conventional fossil-fuel based energies. Perhaps even more importantly, TiO₂ nanomaterials are very promising as a source of hydrogen energy through effective utilization of solar energy based on photovoltaic and water-splitting devices. Therefore, TiO₂ nanomaterials can play a crucial role not only in establishing a wide source of energy supply, but also solving the environmental pollution challenges by minimizing the dependencies on fossil fuel based energy sources.¹⁶

Currently, several different processing techniques have been investigated for the preparation of TiO₂-based nanostructures, such as anodization, template techniques, hydrothermal processes, and soft chemical processes. However, each of these methods

has limitations. For instance, the templating technique requires high calcination temperatures to remove the template, resulting in a collapse of the tubular structure in the product.³² Anodizing processes produce nanotubes with relatively large diameters.³³ The multi step hydrothermal process requires a large amount of inorganic solvents, which may lead to environmental pollution. In this regard, the sol-gel techniques using a green solvent such as supercritical carbon dioxide (scCO₂) is considered as an attractive alternative to synthesize TiO₂-based nanostructured materials with desired characteristics. In this chapter, the advanced applications, and various modifications and synthesis procedures for preparing of TiO₂ nanostructured materials are reviewed.

2.1. TiO₂ Nanostructured Materials

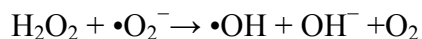
Titanium (Ti) is a transition metal with atomic number 22. It is a light, strong, lustrous, and corrosion-resistant metal. Titanium dioxide (TiO₂) is the most commonly used compound of titanium. Since its commercial production in the early twentieth century, TiO₂ has been widely used as a pigment in sunscreens, paints, ointments, and toothpaste. It is also used in cements, gemstones, as an optical opacifier in paper, and a strengthening agent in graphite composite fishing rods and golf clubs. TiO₂ powder is chemically inert, stable under sunlight, and is very opaque.³⁴ This allows it to impart a pure and brilliant white color to the brown or gray chemicals that form the majority of household plastics. However, in 1972, Fujishima and Honda discovered the phenomenon of photocatalytic splitting of water on a TiO₂ electrode under ultraviolet (UV) light.¹¹ Since then, enormous efforts have been devoted to the research of TiO₂, which has led to

many promising applications such as photocatalysis, photovoltaics, photoelectrochromics and sensors. Some potential applications of TiO₂ are mentioned below.

2.1.1. Photocatalytic Applications

TiO₂ is considered as the most efficient photocatalyst for the degradation of various organic and inorganic pollutants in water. The commonly studied principle of the photocatalysis reaction mechanisms is given in Figure 2.1. Upon absorption of photons with energies larger than the band gap of TiO₂, electrons are excited from the valence band to the conduction band, creating electron-hole pairs.³⁵ These photogenerated charge carriers undergo recombination, become trapped in metastable states, or migrate to the surface of the TiO₂, where they can react with adsorbed molecules. In an air-saturated aqueous environment, the photogenerated electrons and holes participate in reacting with dissolved molecular oxygen, surface hydroxyl groups, and adsorbed water molecules to form hydroxyl and superoxide radicals. Although the detailed mechanism of TiO₂ photocatalysis reactions differs from one pollutant to another, it has been widely recognized that superoxide and, specifically, •OH hydroxyl radicals act as active reagents in the degradation of organic compounds. These radicals are formed by scavenging of the electron-hole pair by molecular oxygen and water, through the following sequences:³⁶





2.5

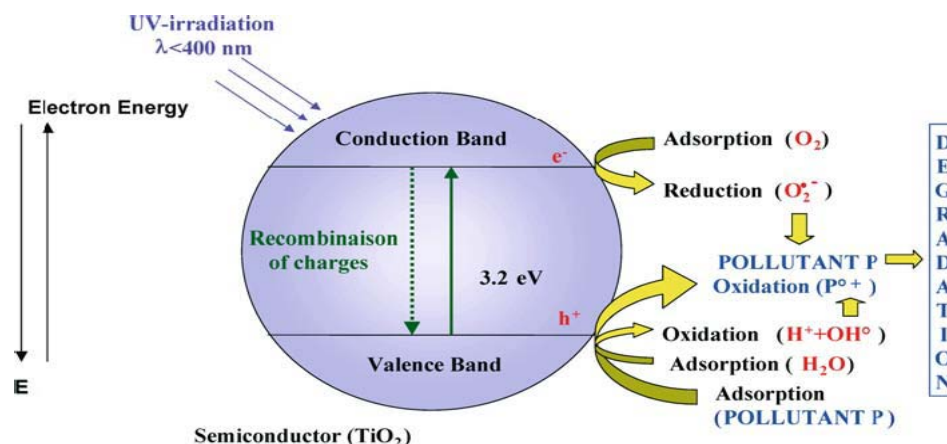


Figure 2.1: The principle of TiO₂ photocatalysis.³⁷

Following a similar mechanism, the TiO₂ photocatalyst can reduce CO₂ to CH₃OH or produce H₂ in a controlled environment (inert or oxygen free). However, the photocatalytic activity of a semiconductor widely depends on its: (i) light absorption properties, (ii) surface reduction and oxidation rates by the electron and hole, and (iii) electron-hole recombination rates. On the other hand, the following three factors pertaining to the band structure of semiconductors have the greatest effect on the photocatalytic reactions: (i) band gap energy, (ii) position of the lowest point in the conduction band, and (iii) position of the highest point in the valence band. In photocatalytic reactions, the band gap energy principally determines which light wavelength is the most effective, and the position of the highest point in the valence band is the main determinant of the oxidative decomposition power of the photocatalyst.

Naturally occurring TiO_2 has three polymorphs, i.e. anatase, brookite, and rutile. Although all three types of polymorphs are expressed using the same chemical formula (TiO_2), their crystal structures are different. Rutile is thermodynamically the most stable phase, although the anatase phase forms at lower temperatures. Both of these phases show photocatalytic activity whereas the brookite phase does not. Despite the fact that the band gap values are 3.0 eV for the rutile and 3.2 eV for the anatase phases, both absorb only UV rays. Such characteristics of the rutile phase seem more suitable for use as a photocatalyst because the rutile phase can absorb light of a wider range. However, the anatase phase exhibits higher photocatalytic activity.³⁷ The most prominent reasons are attributed to the difference in the energy structure between the two phase types and the surface area. In both phases, the position of the valence band is deep, and the resulting positive holes show sufficient oxidative power. However, the conduction band in the anatase phase is closer to the negative position than in the rutile phase. Therefore, the reducing power of the anatase phase is stronger than that of the rutile phase. Usually, the anatase crystal phase forms at lower temperatures, showing higher surface areas compared to the rutile phase. A larger surface area with a constant surface density of adsorbents leads to faster surface photocatalytic reaction rates. In this sense, the higher the specific surface area, the higher the photocatalytic activity that one can expect. Therefore, the anatase phase exhibits higher overall photocatalytic activity compared to the rutile phase. However, Li et al. hypothesized that the anatase and rutile mixed phases showed better photocatalytic activity because any kind of solid–solid interface is a key structural feature that facilitates the charge separation to hinder recombination. The interface also acts as an active site to initiate the catalytic activity and enhance

photocatalytic efficiency.^{30, 38} In addition, TiO₂ nanomaterials with high crystallinity show superior photocatalytic activity. High temperature treatment usually improves the crystallinity of TiO₂ nanomaterials, which can induce the aggregation of small nanoparticles and decrease the surface area.^{36, 39} Therefore, it is very difficult to predict a priori the photocatalytic activities from the physical properties of TiO₂ nanomaterials. Optimal conditions are sought by taking into account all these considerations, which may vary from case to case (a detailed discussion is provided in photocatalytic performance section of this dissertation).

2.1.2. Photovoltaic Applications

Nanocrystalline TiO₂ electrodes in photovoltaic's are another important application of TiO₂. A schematic presentation of the structure and operating principles of a dye sensitized solar cell (DSSC) is presented in Figure 2.2.⁴⁰ The nanocrystalline TiO₂ film, with a monolayer of charge transfer dye adsorbed to its surface, is considered the main part of the cell. The film is placed in contact with a redox electrolyte or an organic hole conductor. Upon photoexcitation, the dye provides an electron which is injected into the conduction band of TiO₂. The electron can then be conducted to the outer circuit to make electric power, while the original state of the dye is restored by electron donation from the electrolyte. The electrolyte is usually an organic solvent containing a redox system, such as the iodide/triiodide couple. The regeneration of the sensitizer prevents the conduction band electron from being captured by the oxidized dye. The iodide is regenerated in turn by the reduction of triiodide at the counter electrode. Under illumination, the voltage generated corresponds to the difference between the Fermi level

of TiO_2 and the redox potential of the electrolyte. Overall, the DSSC generates electric power from light without suffering any permanent chemical transformations. The mesoporosity and nanocrystallinity of the TiO_2 semiconductor is important because a large amount of dye can be adsorbed on the high surface area. In addition, (i) small particles become almost totally depleted upon immersion in the electrolyte and (ii) the proximity of the electrolyte to all particles makes electron injection and their transport relatively easy.¹⁶

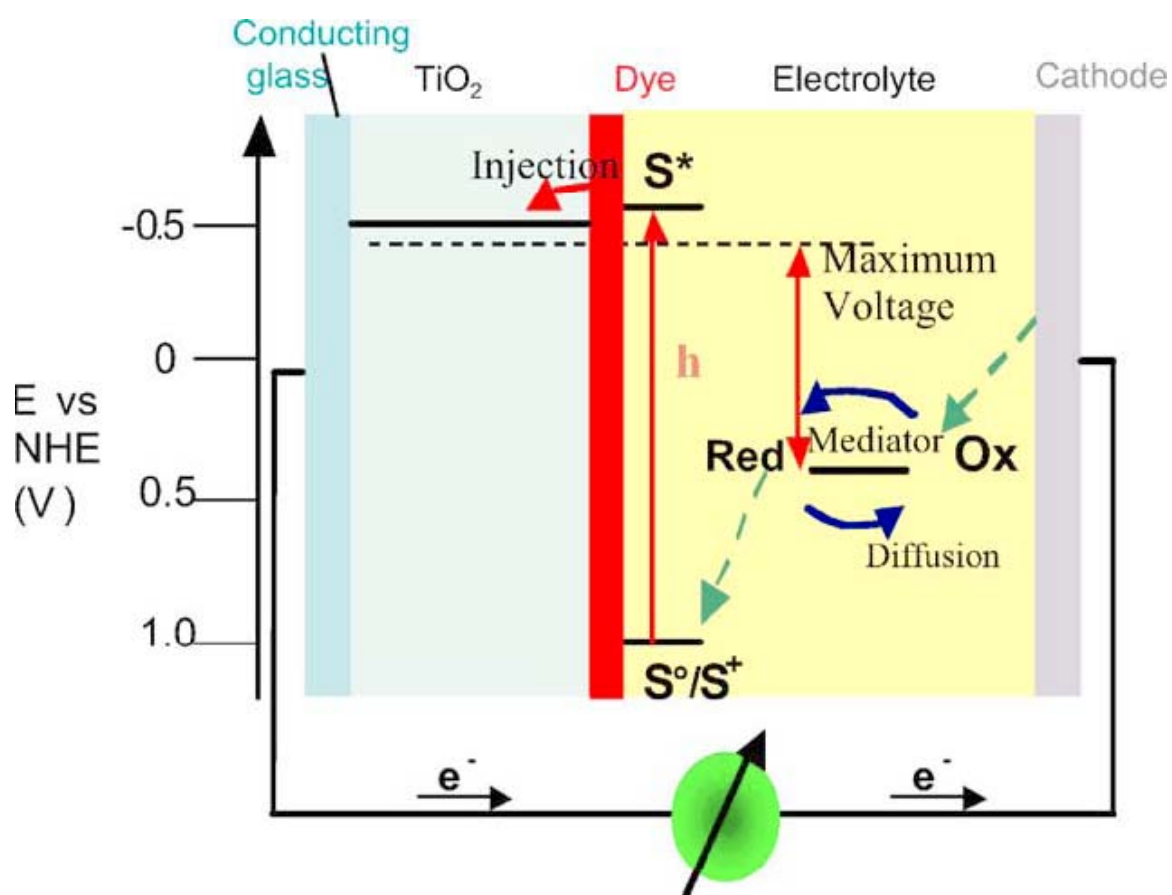


Figure 2.2: Principle of operation and energy level scheme of the dye-sensitized nanocrystalline TiO_2 solar cell.⁴⁰

2.1.3. Other Potential Applications

In addition to the above discussed photocatalysis and photovoltaic applications, TiO₂ nanomaterials can also be used in biomedical applications,⁴¹ functionalized hybrid materials,⁴² and in sensors and nanocomposites.^{43, 44} The one dimensional TiO₂ nanotubes are promising for reinforcement due to their unique physical properties, i.e. large surface to volume ratio, low cost and better biocompatibility compared with carbon nanotubes.⁴⁵ These materials can be used as fillers for many applications such as a radiopacifier in bone cement, a solid plasticizer of poly (ethylene oxide) for lithium batteries, a dye in a conjugated polymer for photoelectrochemical photoconductive agents, and as a photocatalyst in a photodegradable TiO₂-polystyrene nanocomposite film.⁴⁵⁻⁴⁸ Moreover, TiO₂ nanocrystalline films have been widely studied as sensors for various gases. For instance, Varghese et al. observed that TiO₂ nanotubes were excellent room-temperature hydrogen sensors not only with a high sensitivity but also with an ability for self cleaning after environmental contamination.⁴⁹ TiO₂ nanomaterials also have been widely explored as electrochromic devices, such as electrochromic windows and displays. Electrochromism can be defined as the ability of a material to undergo color change upon oxidation or reduction. Electrochromic devices are able to vary their throughput of visible light and solar radiation upon electrical charging and discharging using a low voltage.¹⁶

2.2. Modifications of TiO₂ Nanomaterials

The performance of titania nanomaterials in the above mentioned applications strongly relies on their physicochemical characteristics such as crystallinity, crystallite size, crystal structure, specific surface area, thermal stability and quantum efficiency.^{17,}

⁵⁰ For example, in solar applications a narrower band gap energy is favorable to obtain a higher photon capture efficiency. Undoped TiO₂ offers a wide band gap, which allows utilizing only a small fraction of the available solar energy (<5%). Therefore, it is highly desirable to improve the TiO₂ nanomaterials in order to increase their optical activity by shifting the onset of the response from the UV to the visible region. Indeed, a great deal of research is focusing on modifying the properties of TiO₂ in order to achieve these desirable properties. Generally, the modification of TiO₂ nanomaterials can be divided into two main groups, (i) bulk modification and (ii) surface modification.

Bulk modification

Foreign-element-doping is one of the well-known methods to enhance the performance of titania nanomaterials.¹⁶ Usually, two different approaches: 1) Zr, Al, or Si are added to increase the thermal stability, and surface area,^{24, 51-53} or 2) Fe, Cr, V, Mn, Co, C, N, S, are added to shift the absorption edge over a broader range.⁵⁴⁻⁶¹ In some cases, simultaneous cation and anion doping of TiO₂ also helps in improving the desirable bulk properties of TiO₂. Wang et. al investigated the role of a potential promoter, ZrO₂, in enhancing the activity of TiO_{2-x}N_x for the oxidation of gaseous organic compounds.⁶² The nitrogen-doped photocatalysts were synthesized by reacting amorphous metal oxide xerogels via a sol-gel process with an ammonia solution, followed by calcining the products. They reported that ZrO₂ helped to preserve the surface area and prevent grain growth resulting in higher activity.

Surface modification

Sensitizing TiO₂ with colored inorganic or organic compounds can improve its optical absorption in the visible light region.^{10, 63} In addition, modification of the TiO₂

nanomaterials surface with other semiconductors can alter the charge-transfer properties between TiO₂ and the surrounding environment.⁶⁴⁻⁶⁷

In this project, TiO₂ nanomaterials were modified following the bulk modification approach. Hence, the various bulk modification approaches along with associated properties and the synthesis processes are reviewed.

2.2.1. Bulk Modification of TiO₂ Nanomaterials

In the recent technical literature, numerous studies have focused on shifting the bandgap of TiO₂ to the visible spectral region which would potentially allow more efficient utilization of solar energy and, hence, greatly expand its applications.^{23, 68} The transition metal ions such as Fe, Cr, V, Mn and Co can be added as dopants.^{4, 16, 23, 54, 69-71} This type of doping also increases the photoinduced electron/hole charge recombination lifetimes by acting as an electron-hole trap site. Among the various metal ions, doping with Fe (III) has been widely used due to Fe's unique electronic structure and size that closely matches that of titanium (IV).⁷²

A separate approach to shift the absorption edge over a broader range⁵⁵⁻⁶¹ is by modifying TiO₂ with anions such as C, N, S, and F. Asahi et al. showed that the substitutional doping of N was the most effective among all anions for band gap narrowing, because N's p states mixed with O 2p states.¹⁹

In addition, the technical literature has shown that the performance of TiO₂ nanomaterials also strongly relies on their crystallinity, specific surface area, and thermal stability with these properties significantly varying with the synthesis method, type and amount of dopant loading, and the subsequent heat treatment.⁷²⁻⁷⁵ Altering the textural

properties of TiO_2 is another way to enhance the catalytic performance of nanomaterials.⁷⁶ It has been suggested that a well ordered mesoporous TiO_2 material can enhance catalytic performance due to the large accessible surface area and uniform pore structure. Research on mesoporous silica has shown that the structure of silica can be stabilized by incorporation of metal elements such as Fe (III), La (III) and Al (III) into its framework. By adapting this approach, Wang et al. synthesized mesoporous Fe doped titania using surfactant by a hydrothermal process, and found that the synthesized materials had better ordered mesoporous structure.⁷⁷ However, Al, Si, or Zr are usually used to increase thermal stability and surface area but the effect of the dopant strongly relies on the synthesis process, composition and selected application.^{51, 78-81} Considering solar energy applications, Zr has been reported as one of the most suitable dopants to enhance the thermal stability and activity of TiO_2 nanomaterials.^{24, 53, 82, 83} Research has demonstrated that $\text{TiO}_2\text{-ZrO}_2$ binary metal oxides exhibit higher activity than either of the pure counterparts.⁸⁴ The increase in surface area compared to pure TiO_2 , the rise in surface acidity, or the creation of active sites on the surface have been considered as possible causes of this improvement.^{82, 85}

Surface Properties of Metal doped TiO_2 Nanomaterials

As discussed above, a suitable metal dopant can lead to improvement of the textural properties of TiO_2 , an increase in the acidity of its surface, acceleration of phase transfer, and an increase in the degree of separation of any photogenerated charges. These factors are controlled by changes in the preparation method, loading of a catalyst, and type of dopant element. Gnatuyak et al. synthesized mesoporous zirconium-containing

TiO₂ films by a sol–gel process and studied their structural and sorption characteristics, surface acid functionality, and photocatalytic activity for the gas-phase oxidation of aliphatic alcohols. They observed that the zirconium content changes the acidity and specific surface area of the films.⁸⁶ The increase in photocatalytic activity of TiO₂/ZrO₂ compared to pure TiO₂ is connected with the increase in thermal stability of the porous structure, the increase in the acidity of the surface, and with the generation of structural defects due to the incorporation of impurity ions into the TiO₂ lattice. In all cases, the incorporation of Zr into TiO₂ leads to a notable increase in surface area, while stabilizing the anatase phase.

Most of the research has mainly focused on the surface area, crystalline structure and anatase to rutile phase transformation. In addition to crystal structure, the hybrid materials structural properties/morphology is also important. This can affect the transport of reactants and products to or from the catalytic active sites, the light absorbance for the photo-excitation of the catalyst, and the generation of electron–hole pairs. In the literature, only a limited number of articles have focused on the possible influence of structural differences originated by the synthesis procedure and process variables for preparing TiO₂–ZrO₂ binary metal oxides. Given the limited studies, the relationship between the structure and the performance of these photocatalysts synthesized via different processes has yet to be established.

2.2.2. Electronic Properties and Optical Response of TiO₂

The optical response of any material is largely dependent on its underlying electronic structure. The electronic structure of a nanomaterial is closely related to its

chemical composition, arrangement, and physical dimensions. The electronic states of TiO₂ are generally considered to consist of three parts: (1) valence band, (2) lower conduction band, and (3) upper conduction band (Figure. 2.3).⁸⁷

- (1) Valence band: The VB consists of three parts: σ bonding of the O $p\sigma$ and Ti e_g states in the lower energy region; the π bonding of the O $p\pi$ and Ti e_g states in the middle energy region; and the O $p\pi$ states in the higher energy region.
- (2) Lower conduction band: The bottom of the lower conduction band (CB) consists of the Ti d_{xy} orbital, which contributes to the metal metal interactions due to the σ bonding of the Ti t_{2g} -Ti t_{2g} states. At the top of the lower CB, the remaining Ti_{2g} states are antibonding with the O $p\pi$ states.
- (3) Upper conduction band: The upper CB consists of the σ antibonding orbitals between the O $p\sigma$ and Ti e_g states.

As discussed above in section 2.2.1, the chemical composition of TiO₂ applicable for solar applications can be altered by incorporating a dopant. Specifically, the metal (Ti) or the nonmetal (O) component can be replaced by the dopant material in order to alter the optical properties. The following section shows the effects of metal and non-metal doping on both the electronic properties and the optical response of TiO₂ nanomaterials.

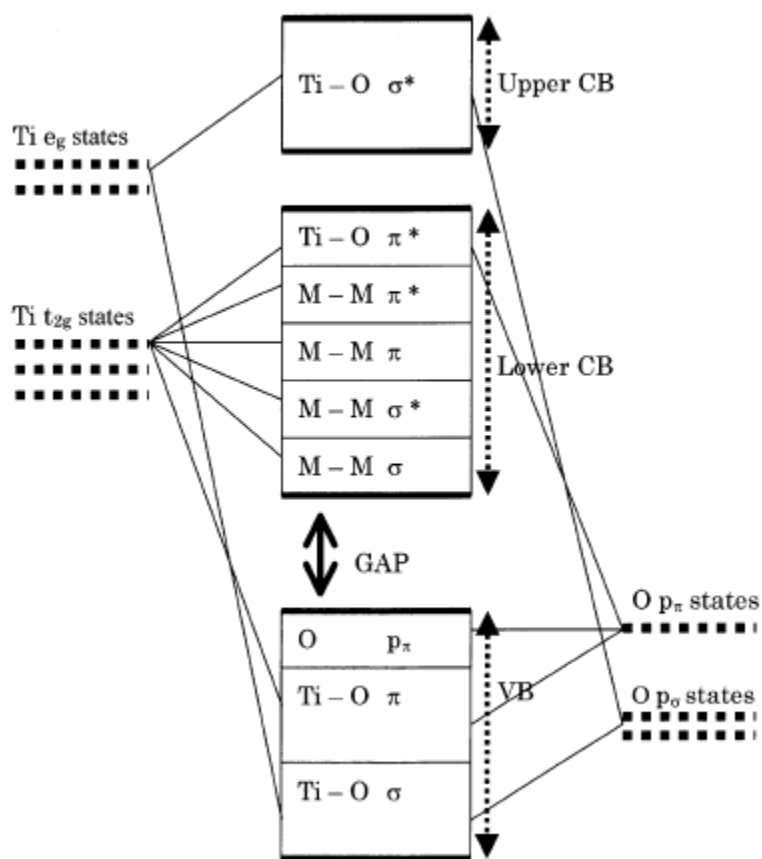


Figure 2.3: The bonding diagram of a perfect TiO₂ crystal.⁸⁷

Metal-Doped TiO₂ Nanomaterials

When a doping agent such as V, Cr, Mn, Fe, or Co is introduced into TiO₂, an electron occupied level forms and the electrons are localized around each dopant. With a dopant with a higher atomic number, the localized level shifts to a lower energy. The energy of the localized level due to Co doping is low enough that it lies at the top of the valence band, while the other metals produce midgap states.⁸⁷ The states due to the 3d dopants shift to a lower energy level as the atomic number of the dopant increases. The electron densities around the dopant are large in the VB and small in the CB compared to the case of pure TiO₂. The metal-O interaction strengthens, and the metal metal

interactions become weak, as a result of the 3d metal doping.¹⁶ The optical response or the absorption spectra are also shifted to a lower energy region due to narrowing of the band gap. This “red shift” is attributed to the charge-transfer transition between the d electrons of the dopant and of the TiO₂. However, this shift strongly depends on the preparation method, type and amount of dopant.⁸⁸

Nonmetal-Doped TiO₂ Nanomaterials

Recent theoretical and experimental studies have shown that the desired band gap narrowing of TiO₂ can also be achieved by using a nonmetal, although there is controversy regarding the origin of the resulting band gap narrowing. Asahi and co-workers calculated the electronic band structures of anatase TiO₂ with different substitutional dopants, including C, N, F, P, or S and found that the substitutional doping of N was the most effective for band gap narrowing. This is because the p states of N mix with the 2p states of O, while the molecularly existing species, e.g., NO and N₂ dopants, give rise to the bonding states below the O 2p valence bands, while the antibonding states deep within the band gap hardly interact with the band states of TiO₂.¹⁹ Di Valentin et al. reported that the N 2p orbital formed a localized state just above the top of the O 2p valence band, both for the anatase and rutile phases. However, these two crystal systems showed the opposite photoresponse. In anatase, these dopant states caused a red shift of the absorption band edge toward the visible region, while in rutile, an overall “blue shift” was observed. This experimental evidence confirmed that N-doped TiO₂ formed N-induced midgap levels slightly above the oxygen 2p valence band.⁸⁹ Lee et al. also found that the bands originating from the N 2p states appeared in the band gap of TiO₂;

however, the mixing of N with O 2p states was too weak to produce a significant band gap narrowing.⁹⁰ Nakano et al. reported that in N-doped TiO₂, deep levels located at approximately 1.18 and 2.48 eV below the conduction band were attributed to the O vacancy state and a band gap narrowing was achieved by mixing with the O 2p valence band, respectively.⁹¹ Okato et al. found that with high doping levels, that N was difficult to substitute for O to contribute to band gap narrowing, instead, giving rise to undesirable deep-level defects.⁹² N-doped TiO₂ normally has a color from white to yellow or even light gray, and the onset of the absorption spectra red shifts to longer wavelengths. In N-doped TiO₂ nanomaterials, the band gap absorption onset shifted 600 nm from 380 nm for the undoped TiO₂, extending the absorption up to 600 nm. The optical absorption of N-doped TiO₂ in the visible light region was primarily located between 400 and 500 nm, while that for oxygen deficient TiO₂ was mainly above 500 nm. N-F-co-doped TiO₂ prepared by spray pyrolysis was shown to absorb light up to 550 nm in the visible spectrum.⁹³ Livraghi et al. recently found that N-doped TiO₂ contained single atom nitrogen impurity centers, localized in the band gap of the oxide, which were responsible for the visible light absorption with promotion of electrons from the band gap localized states to the conduction band.⁹⁴ Nick Serpone proposed that generally in all doped TiO₂ nanomaterials, that the red shift of the absorption edge is in fact due to the formation of color centers that absorb the visible light radiation.⁹⁵

2.3. Synthesis Methods

Metal-Doped TiO₂ Nanomaterials

There are many synthetic processes currently being used to produce different metal doped TiO₂ nanomaterials, including sol-gel, hydrothermal, solvothermal, chemical vapor deposition (CVD), thermal decomposition, pulsed laser ablation and templating. These methods are briefly outlined below.

2.3.1. Conventional Sol-gel Method

The sol-gel method is a versatile process used for synthesizing various oxide materials.⁹⁶ This synthetic method generally allows control of the texture, the chemical, and the morphological properties of the solid. This method also has several advantages over other methods, such as allowing impregnation or coprecipitation, which can be used to introduce dopants. The major advantages of the sol-gel technique includes molecular scale mixing, high purity of the precursors, and homogeneity of the sol-gel products with a high purity of physical, morphological, and chemical properties.⁹⁷ In a typical sol-gel process, a colloidal suspension, or a sol, is formed from the hydrolysis and polymerization reactions of the precursors, which are usually inorganic metal salts or metal organic compounds such as metal alkoxides.⁹⁸ When a metal precursor alkoxide/salt reacts with water, nucleophilic substitution occurs as shown in Figure 2.4. For the coordinatively saturated metals such as the metal alkoxides, hydrolysis and condensation both occur by nucleophilic substitution (S_N) mechanisms, in which coordination and proton transfer are involved and followed by removal of either alcohol or water.

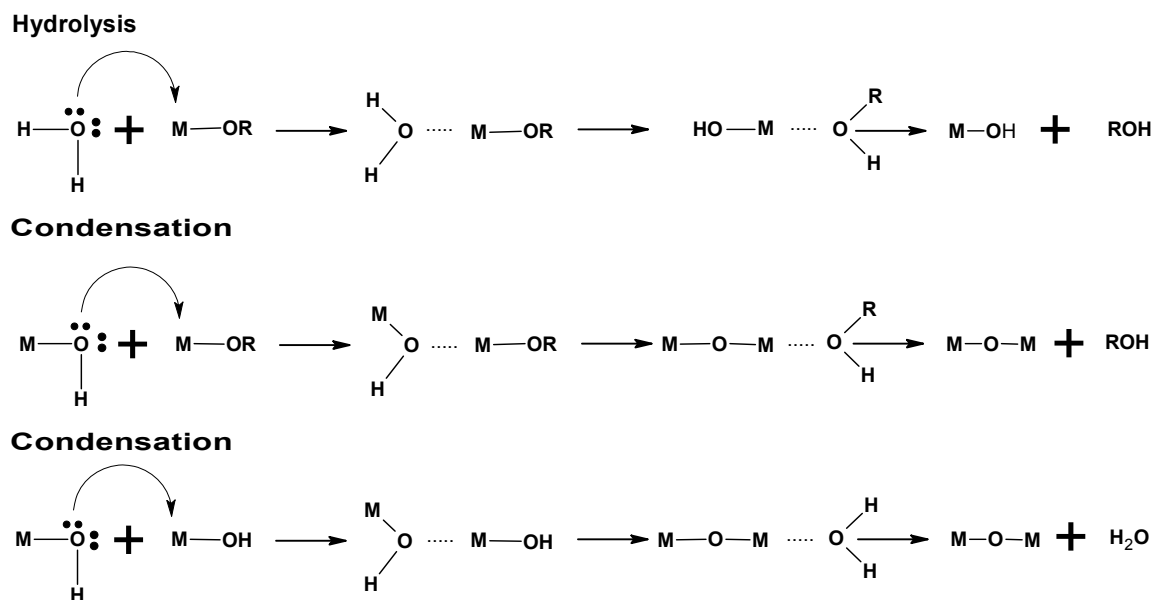


Figure 2.4: Hydrolysis and condensation steps for sol-gel mechanism.

Complete polymerization and loss of solvent leads to the liquid sol transforming into a solid gel phase. Thin films can be produced on a piece of substrate by spin-coating or dip-coating. A wet gel will form when the sol is cast into a mold, and the wet gel is converted into a dense ceramic upon further drying and heat treatment. A highly porous and extremely low-density material, called an aerogel, is obtained if the solvent in a wet gel is removed under supercritical conditions. Figure 2.5 shows the conventional scheme to produce aerogels. This method involves hydrolysis of the metal alkoxide with water and a catalyst, i.e. an acid or a base, condensation into macromolecules, forming a colloidal sol and subsequently three-dimensional network, solvent exchange to remove water by alcohol, then drying the wet gel using a supercritical fluid to produce the aerogel.⁹⁹ Aerogels can be used for advanced applications including electrochemical devices, thin coatings, composite biomaterials, catalysts, ceramics, and heat and electric insulation devices due to the aerogels having unique morphological and chemical

properties.¹⁰⁰ Ceramic fibers can be drawn from the sol when the viscosity is adjusted into the proper range. Since the precursors react with water quickly and tend to precipitate, many methods have been used to control the reaction rate in order to obtain desired nanostructures. For instance, TiO₂ nanoparticles with a diameter of *ca.* 14 nm were prepared using a sol-gel process of isopropoxide with the aid of ultrasonication.¹⁰¹ However, in binary metal systems, the main difficulty is to control the hydrolysis rate of the precursors.⁹⁸ Modifying the precursors with a suitable complexing agent is one way to alter the hydrolysis rate,¹⁰² while generating *in-situ* water (instead of externally added water) is another possible way to control the hydrolysis rate.⁸¹ In practice, acetic acid is often used to modify the reactivity of metal alkoxides by replacing the alkoxy groups bonded to the metal by acetate groups, forming M-OAc complexes and alcohols. Moreover, acetic acid (HO-Ac) can react with the alcoholic solvent and intermediates, (produced by modification reaction) to form water via an esterification reaction.¹⁰²

However, the properties of the sol-gel products depend on the precursors, processing temperature, catalyst, solvents, and solvent removal process.⁹⁹ Choi et al. performed a systematic study of TiO₂ nanoparticles doped with 21 metal ions by the sol-gel method and found that the presence of the metal ion significantly influenced the photoreactivity, charge carrier recombination rates, and interfacial electron transfer rates.¹⁶ Li et al. developed a La₃⁺-doped TiO₂ by a sol-gel process and found that lanthanum doping could inhibit the phase transformation of TiO₂, enhancing the thermal stability of the TiO₂, reducing the crystallite size, and increasing the Ti₃⁺ content on the surface.¹⁰³

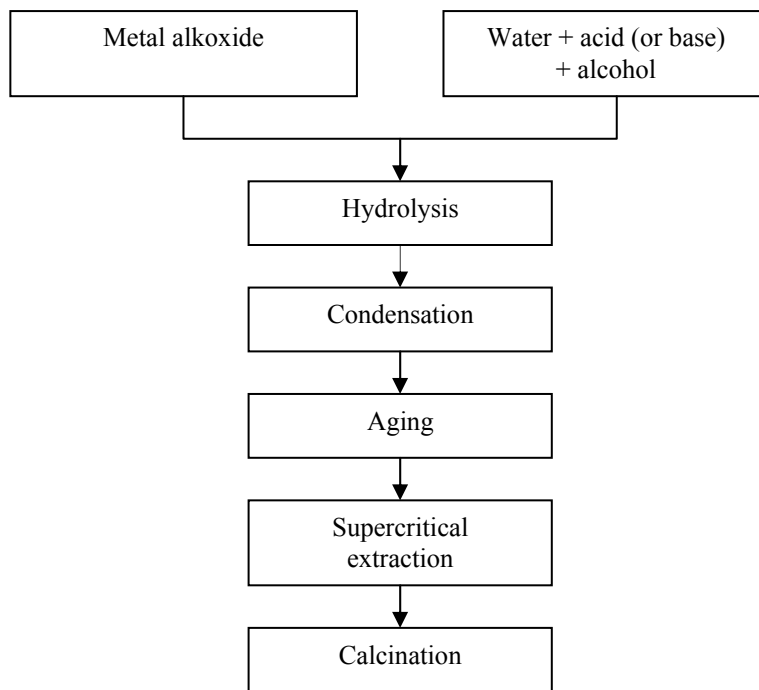


Figure 2.5: Aerogel synthesis scheme by the conventional sol-gel route.

Kelonko et al. synthesized mesoporous nanosized TiO_2 and $\text{Zn}_x\text{Ti}_{1-x}\text{O}_{2-x}$ solid solutions having a Zn content below 10 mol % with a particle size between 13 and 17 nm by a template-free sol-gel method in absolute ethanol followed by high-temperature supercritical drying in 2-propanol. It was shown that the proposed synthesis technique leads to the formation of a $\text{Zn}_x\text{Ti}_{1-x}\text{O}_{2-x}$ solid solution based on the anatase crystal structure rather than a two-phase sample. High-resolution electron microscopy and electron diffraction indicated that the distribution of zinc atoms throughout the anatase structure did not lead to a considerable deformation of the crystal structure.⁹⁷ In addition, Weissman et al. synthesized $\text{TiO}_2/\text{ZrO}_2$ mixed oxides by a sol-gel process following supercritical fluid (SCF) drying. The synthesized materials exhibited two to five times greater surface areas than their conventionally prepared equivalents.¹⁰⁴

2.3.2. Sol Method

The sol process refers to the nonhydrolytic sol-gel process which usually involves the reaction of titanium halide with a variety of different oxygen donor molecules, such as:



The condensation between Ti-X and Ti-OR leads to the formation of Ti-O-Ti bridges. In this process, a metal alkoxide was rapidly injected into the hot solution of titanium halide mixed with trioctylphosphine oxide (TOPO) under dry inert gas protection, with the reactions being completed within 5 min. Following a similar procedure, Chang et al prepared Zr-doped anatase TiO₂ nanorods through the cross-condensation of Zr/TiCl₄ with Zr/ Ti(OPr)₄ in anhydrous TOPO at either 320 or 400 °C. The kinetics of the alkyl halide elimination involving the Ti and Zr species was found to play a crucial role in determining the morphologies, chemical compositions, and crystalline phases of the Zr-doped TiO₂ nanorods.¹⁰⁵

2.3.3. Hydrothermal Method

The hydrothermal method is widely used for the production of small particles in the ceramics industry. Usually, this process is conducted in steel pressure vessels called autoclaves under controlled temperature and/or pressure with the reactions occurring in aqueous solution. The temperature can be elevated above the boiling point of water, reaching the pressure of vapor saturation. The temperature and the amount of solution added to the autoclave largely determine the internal pressure produced. The

hydrothermal method has been widely used to prepare TiO₂ nanotubes after the pioneering work by Kasuga et al. in 1998.¹⁰⁶ Generally, several grams of TiO₂ powders are added to concentrated NaOH solution and held at 20-110 °C for 20 h in an autoclave. TiO₂ nanotubes were obtained after the products were washed with a dilute HCl aqueous solution and distilled water. When the raw TiO₂ material was treated with NaOH aqueous solution, some of the Ti-O-Ti bonds were broken and new Ti-O-Na and Ti-OH bonds were formed. New Ti-O-Ti bonds were formed after the Ti-O-Na and Ti-OH bonds reacted with acid and water. The bond distance from one Ti atom to the next Ti atom on the surface was found to decrease. This resulted in the folding of the sheets and connection between the ends of the sheets, resulting in the formation of a tube structure. In this mechanism, the TiO₂ nanotubes were formed in the stage of the acid treatment following the alkali treatment. However, Du and co-workers found that the nanotubes were formed during the treatment of TiO₂ in NaOH aqueous solution.¹⁰⁷ A 3D→2D →1D formation mechanism of the TiO₂ nanotubes was proposed by Wang and co-workers. They stated that the raw TiO₂ was first transformed into lamellar structures which then bent and rolled to form the nanotubes.¹⁰⁸ In all the proposed mechanisms, the two-dimensional lamellar TiO₂ was essential for the formation of the nanotubes. The hydrothermal method is also currently being used to produce many new hybrid materials with new morphologies and improved crystallinity. Wang et al. prepared Fe(III)-doped TiO₂ nanoparticles with a hydrothermal method and found that anatase, brookite, and a trace of hematite coexisted at lower pH (1.8 and 3.6) when the Fe(III) content was as low as 0.5% and the distribution of iron ions was nonuniform between particles. At a higher pH (6.0), a uniform solid solution of iron-titanium oxide was formed.^{75, 109}

2.3.4. Solvothermal Method

The solvothermal method is identical to the hydrothermal method except that a variety of solvents other than water can be used for this process. This method has been found to be a versatile route for the synthesis of a wide variety of nanoparticles with narrow size distributions, particularly when organic solvents with high boiling points are chosen. The solvothermal method normally has better control of the size and shape distributions and the crystallinity than the hydrothermal method, and has been employed to synthesize TiO₂ nanoparticles and nanorods with/without the aid of surfactants.

2.3.5. Chemical Vapor Deposition (CVD)

This process is often used in the semiconductor industry to produce high-purity, high-performance thin films. In a typical CVD process, the substrate is exposed to volatile precursors, which react and/or decompose on the substrate surface to produce the desired film. Frequently, volatile byproducts that are produced are removed by gas flow through the reaction chamber. The quality of the deposited materials strongly depends on the reaction temperature, the reaction rate, and the concentration of the precursors.^{110, 111} Cao et al. prepared Sn₄⁺-doped TiO₂ nanoparticle films by the CVD method and found that more surface defects were present on the surface due to doping with Sn.¹¹² Gracia et al. synthesized M (Cr, V, Fe, Co)-doped TiO₂ by CVD and found that TiO₂ crystallized into the anatase or rutile structures depending on the type and amount of cations present in the synthesis process. Moreover, upon annealing, partial segregation of the cations in the form of M₂O_n was observed.⁷⁰ The advantages of this method include the uniform

coating of the nanoparticles or nanofilm. However, this process has limitations including the higher temperatures required, and it is difficult to scale up.¹¹³

2.3.6. Thermal Decomposition and Pulsed Laser Ablation

Pure and doped metal nanomaterials can be synthesized via decomposing metal alkoxides and salts by applying high energy using heat or electricity. However, the properties of the produced nanomaterials strongly depend on the precursor concentrations, the flow rate of the precursors and the environment. Kim et al. synthesized TiO₂ nanoparticles with a diameter less than 30 nm via the thermal decomposition of titanium alkoxide or TiCl₄ at 1200 °C.¹¹¹ Liang et al. produced TiO₂ nanoparticles with a diameter ranging from 3 to 8 nm by pulsed laser ablation of a titanium target immersed in an aqueous solution of surfactant or deionized water.¹¹⁴ Nagaveni et al. prepared W, V, Ce, Zr, Fe, and Cu ion-doped anatase TiO₂ nanoparticles by a solution combustion method and found that the solid solution formation was limited to a narrow range of concentrations of the dopant ions.¹¹⁵ However, the drawbacks of these methods are high cost and low yield, and difficulty in controlling the morphology of the synthesized nanomaterials.⁹⁶

2.3.7. Templating

The synthesis of nanostructured materials using the template method has become extremely popular during the last decade.¹⁰⁶ In order to construct materials with a similar morphology of known characterized materials (templates), this method utilizes the morphological properties with reactive deposition or dissolution. Therefore, it is possible

to prepare numerous new materials with a regular and controlled morphology on the nano- and microscale by simply adjusting the morphology of the template material. A variety of templates have been studied for synthesizing titania nanomaterials.^{116 117} This method has some disadvantages including the complicated synthetic procedures and, in most cases, templates need to be removed, normally by calcination, leading to an increase in the cost of the materials¹⁰⁶ and the possibility of contamination.

2.3.8. N Doped TiO₂ Nanomaterials

Through extensive theoretical and experimental investigations conducted by Ashai and coworkers, along with other groups, on the effects of different non metal doping in TiO₂, N-doping has been shown to be the most effective technique for band gap narrowing, resulting in visible light absorption.^{19, 22} Therefore, only N-doping methods are reviewed here. The synthesis of N doped TiO₂ can be classified into three groups: (i) sputtering and implantation techniques, i.e. directly treating the target TiO₂ film with high energy N-containing gas flow, (ii) high temperature sintering of TiO₂ under a N-containing atmosphere and (iii) sol–gel method involving the hydrolysis of Ti precursors in alcohol and water in the presence of N-precursors such as ammonia and organic amines.^{18, 118} Amongst these methods, the sol–gel method is the most successful to synthesize N-doped TiO₂ nanomaterials because of its simplicity that provides controlling the nitrogen doping level and particle size by simple variations in experimental conditions.¹⁸

There is no well known direct correlation between the properties of TiO₂ based nanomaterials and photocatalytic activity, although the synthesis process is considered

one of the most important factors controlling the reactivity of the doped TiO₂.^{73, 119} However, most of the methods currently being used suffer scale-up problems, and are not environmentally friendly. For example, the conventional sol-gel process and template methods utilize volatile organic compounds (VOCs), and high temperature treatment is required to remove the template which reduces the surface area of the synthesized materials;³² hydrothermal or solvothermal methods involve high temperatures in an autoclave that generates corrosion and safety problems,¹²⁰ while CVD processes are difficult to scale-up. Considering all these limitations, alternative processes using a green solvent such as supercritical carbon dioxide (scCO₂) is attractive to synthesize TiO₂-based nanostructured materials.

2.4. Supercritical Fluids (SCFs) and supercritical CO₂ (scCO₂)

Since the early 1960's, environmental statutes and regulations have proliferated at an exponential rate. Due to these regulations and increased environmental concerns, the use of volatile organic compounds (VOCs) are becoming increasingly restricted.¹²¹ Consequently, during recent years considerable efforts have been devoted to finding environmental friendly solvents and processes for industrial application. In this way, researchers in industry and academia find supercritical fluids (SCFs) as useful alternative solvents.¹²² The SCFs exhibit a range of unusual properties that can be exploited for new reactions and new routes to process materials that have significant benefits for the specialty chemical and pharmaceutical industries.

A SCF can be defined either as a compressed gas or as an extended liquid. Thermodynamically, a fluid is in the supercritical domain when both the temperature and

pressure are above the critical values, T_c and P_c , respectively. In practice, this definition is restricted to a fluid close to its critical point. SCFs have liquid-like density and gas-like viscosity and diffusivity. So SCFs have considerably better solvent strength than what gases can offer, and better transport properties than what liquids have. Figure 2.6 shows a typical phase diagram indicating the supercritical region. In the P-T phase diagram of a pure substance, below the critical point the phase boundary lines divide the diagram into solid, liquid and gas regions. However, there is no boundary line in the supercritical region.

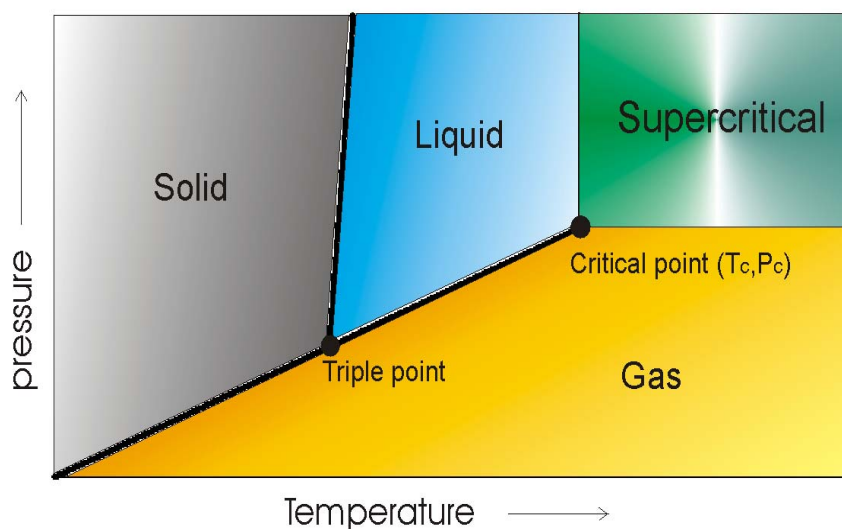


Figure 2.6: Schematic of the phase diagram of a typical material.¹²³

Critical properties are very important for fluids with every fluid having its own critical properties. Table 2.1 shows the T_c , P_c and ρ_c (the density at the critical point) of some selected substances that have been used as SCFs for material processing and chemical reactions.¹⁰⁸ For practical purposes, only a few fluids can be used under

supercritical conditions because some fluids are corrosive, toxic or have a relatively high critical temperature (T_c) and pressure (P_c). Generally speaking, low T_c and P_c of a substance are desirable due to their economic favorability. Moreover, the safety and environmental issues as well as the solvent power of the substance have to be considered when one selects a SCF. For instance, ethane is a flammable organic compound, so it requires special safety precautions. On the other hand, methanol has a high solvent strength, but it is not commonly used as a SCF due to its high critical temperature. Ammonia has the ability to dissolve polar compounds; i.e. it can dissolve pump seals, and it is difficult to pump. In addition to its high polarity, it is highly reactive making it a poor SCF candidate. The following factors should be considered when selecting a SCF for a given process.¹²⁴

- i) toxicity and reactivity,
- ii) critical temperature and pressure,
- iii) flammability,
- iv) cost,
- v) availability,
- vi) environmentally compatible

Considering all these factors, among the candidates for useful SCFs, CO_2 is considered to be the most desirable given its relative low T_c and P_c , low cost, abundance, and that it is environmentally benign. Usage of scCO_2 instead of water or organic solvents can reduce the water pollution and emission of VOCs. Moreover, it is available through various industrial sources including the flue gas from power stations, or as a by-product of existing processes such as ethanol, ammonia and hydrogen production.¹²³ The

main problem with supercritical carbon dioxide is its relatively low solvent strength at typical pressures. This problem can be addressed by using modifiers (co-solvent) or surfactants.¹²⁵

Table 2.1: Critical properties for selected supercritical fluids.¹²⁶

Solvents	T_c (°C)	P_c (psi)	ρ_c (g/cm³)
Ethylene	9.3	731	0.22
Xenon	16.6	847	1.11
Fluoroform	26.2	705	0.53
Carbon dioxide	31.1	1070	0.47
Ethane	32.2	708	0.20
Nitrous oxide	36.5	1050	0.45
Sulfur hexafluoride	45.6	545	0.73
Difluoromethane	78.4	846	0.43
Propylene	91.8	667	0.23
Propane	96.7	616	0.22
Dimethyl ether	126.9	760	0.26
Ammonia	132.4	1646	0.23
n-Pentane	196.6	489	0.24
Acetone	235.0	680	0.28
Isopropanol	235.1	690	0.27
Methanol	239.5	1173	0.27
Ethanol	240.7	891	0.28
Water	374.2	3208	0.32

Note: T_c, P_c and ρ_c are critical temperature, critical pressure and critical density, respectively.

In the following section, different aspects of supercritical carbon dioxide are reviewed.

2.5. Properties of supercritical CO₂

Recently, significant interest has developed to utilize supercritical carbon dioxide (scCO₂) as an attractive replacement for organic solvents in a wide range of chemical processes.¹²⁷⁻¹³⁰ This is due to scCO₂ being nontoxic, nonflammable, inexpensive, naturally abundant, and chemically inert.¹²² With a critical temperature of 31.1 °C and a critical pressure of 1070 psig, the critical conditions of scCO₂ are easily achievable so that a lower capital cost is required for the autoclave materials, and a lower operation cost is required due to lower energy consumption. Low viscosity, “zero” surface tension and high diffusivity of scCO₂ are considered highly favorable properties for synthesizing superior ultrafine and uniform nanomaterials. These properties also help to increase the reaction rates.^{131, 132} In addition, its physical properties such as density and solubility can be “tuned” by adjusting the operating temperature and pressure providing an easily tunable reaction medium.^{133, 134} Moreover, when reactions are carried out in scCO₂, reaction products can be easily recovered by simply venting the solvent, hence, no drying process is required and the porous nanostructure can be maintained without collapsing. Particularly, supercritical drying extinguishes the liquid surface tension, which causes collapse of small pores during drying, resulting in shrinkage of the solid; hence the microstructure and high surface area of the aerogel can be maintained by a supercritical drying process. As a result, scCO₂ has been widely employed for synthesizing aerogels. Furthermore, scCO₂ can be easily recycled after the pressure is diminished for potential scale-up applications. The following section focuses on the variation of the various properties of CO₂ as a function of temperature and pressure.

The Density of CO₂

The density of CO₂ is very sensitive to operating temperature and pressure, especially near the critical region. It is very important to understand how the density changes with pressure and temperature for utilizing scCO₂ for an intended application. Figure 2.7 shows the variation of reduced density as a function of reduced pressure at various reduced temperatures.¹³⁵ Here, the reduced density is $\rho/\rho_c = \rho_r$, the reduced pressure is $P/P_c = P_r$ and the reduced temperature is $T/T_c = T_r$. The critical point is the reduced pressure P_r that equals the reduced temperature, $T_r = 1$. At high values of T_r , the fluid density is reduced where the solvents properties are no longer favorable. It can be concluded from Figure 2.7 that a smaller change in pressure at $T_r = 1.0 - 1.2$ results in a substantial change in density. However, when T_r is increased to 1.5, the same change in pressure hardly changes the fluid density.

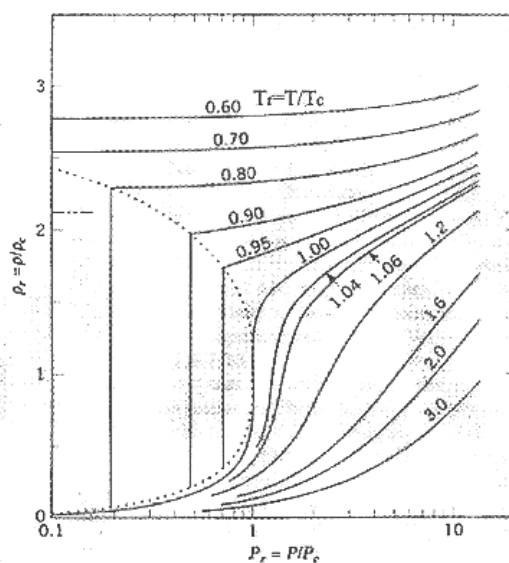


Figure 2.7: Reduced pressure (P_r) vs. reduced density (ρ_r) diagrams at various reduced temperatures (T_r).¹³⁵

It is generally accepted that the solvating power of a given solvent is directly related to its density. Increasing the density of scCO₂ results in a higher solubility. Although the relationship between solubility and density is simple, the relationships between solubility and temperature and pressure is more complex. When CO₂ is near T_c, small changes in the pressure can create large changes in density resulting in substantial changes in the solvating strength of CO₂. The variation of the solvating strength of CO₂ with pressure is shown in Figure 2.8.¹³⁶ The solubility parameter δ is the square root of the cohesive energy density and the value for gaseous CO₂ is essentially zero. However, this value becomes comparable with that of a hydrocarbon for liquid CO₂. It can be observed from Figure 2.8 that the solubility of CO₂ can be tuned continuously over a wide range with a small pressure change.¹³⁶ Near the critical pressure, CO₂ exhibits a decrease in solubility with an increase in temperature. However, at higher pressures the solubility increases with increasing temperature because the solute vapor pressure becomes significant.

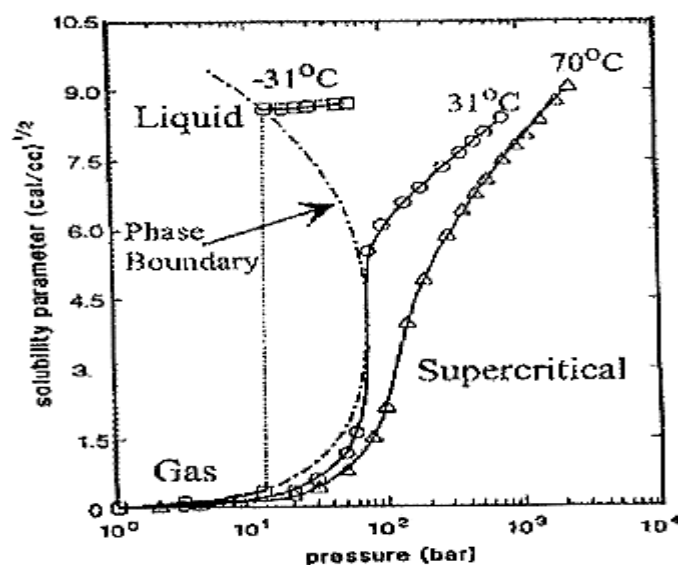


Figure 2.8: Solubility parameters of CO₂.¹³⁶

The Physical Properties of CO₂

The physicochemical properties of SCFs are another attractive and useful feature, which are intermediate between those of liquids and gases. Table 2.2 compares the properties of gases, liquids and SCFs. A SCF has a density comparable with a liquid, which enables it to function as a solvent, and a viscosity similar to a gas, which provides superior mass and heat transfer compared with a conventional solvent.

Table 2.2: Comparison of the properties of Gas, SCF and Liquid.¹³⁵

Properties	Gas	SCF	Liquid
Density, g/cm ³	0.001	0.2-1	0.6-1.6
Diffusivity, cm ² /s	0.1	0.001	0.00001
Viscosity, g/(cm·s)	0.0001	0.001	0.01

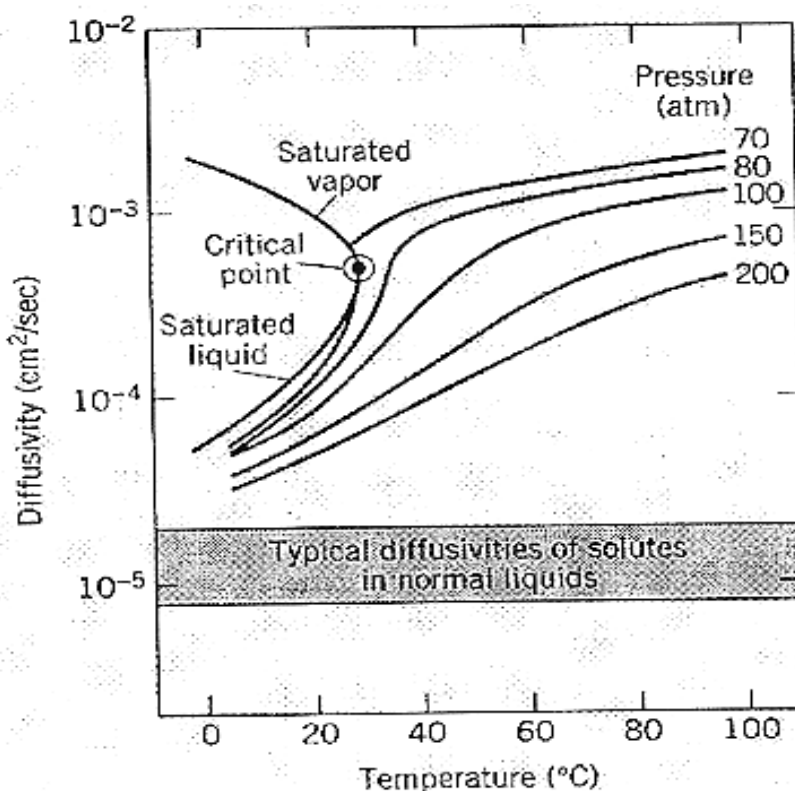


Figure 2.9: Diffusivity of CO₂ vs temperature at various pressures.¹³⁷

The diffusivity of scCO₂ varies between 10^{-4} and 10^{-3} cm²/s. These values are as much as 100 times higher than those typically observed in conventional liquids.¹³⁵ The diffusivity of CO₂ also depends on the temperature and pressure with a typical variation of diffusivity with temperature and pressure being shown in Figure 2.9.¹³⁷ When the pressure is increased, the diffusivity of scCO₂ approaches that of liquid. The diffusivity will increase with an increasing of the temperature.

The physical and chemical behavior of a fluid cannot be understood without considering surface tension. Surface tension is caused by the molecules of the liquid at the surface that are subject to an inward force of molecular attraction by various intermolecular forces. The surface tension of the saturated liquid CO₂ as a function of pressure/temperature is plotted in Figure 2.10. In the saturated liquid region, the surface tension decreases as the pressure/temperature increases. In the supercritical region, however, there is no surface tension due to the disappearance of the interface between the liquid and vapor phases.

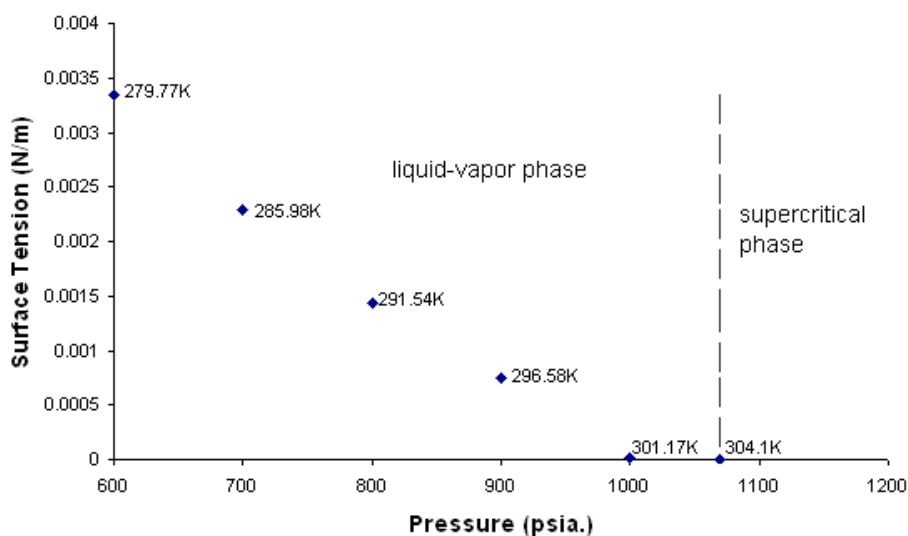


Figure 2.10: Surface tension of saturation liquid CO₂ as a function of pressure.¹²³

2.6. TiO₂ Based Nanostructured Materials in scCO₂

In the past decade, a direct approach for synthesizing oxide nanomaterials with a variety of morphologies, such as aerogel nanospheres, monoliths, films, and pillared structure, have been developed in SCFs. In addition, the technical literature shows that the direct sol-gel process in scCO₂ is a promising technique for synthesizing metal oxide nanomaterials. However, due to the low solubility of precursors in CO₂ and for the sake of desired nanostructure formation, various surfactants are often used in the sol-gel process in CO₂. The morphology strongly varies with the type of surfactant and the water/surfactant ratio. For example, Tadros *et al.* synthesized TiO₂ nanoparticles in scCO₂ by hydrolysis and condensation of titanium alkoxides using the anionic fluorinated surfactant, [F(CF₂CF₂)_zCH₂CH₂O]_xP(O)(ONH₄)_y (where x = 1 or 2, y = 2 or 1, z = 1 – 7). The surfactant was able to stabilize the tiny water droplets in scCO₂ at 45 °C and 1400 psig, and spherical particles of TiO₂ with low anatase crystallinity were formed.¹³⁸

Using the same anionic fluorinated surfactant, Stallings and Lamb conducted a more systematic study on the direct sol-gel process of titanium isopropoxide (TIP) in scCO₂. They injected pure TIP into water in scCO₂ dispersions using a batch reactor. Spherical titania particles with a broad particle size distribution (20-800 nm) were obtained. The surface area of the as-prepared material, 100 ~ 500 m²/g, was attributed to the internal porosity of the spherical titania particles.¹³⁹ Hong et al. and Keith Johnson and his group prepared TiO₂ nanospherical particles by the direct sol-gel process of titanium isopropoxide (TIP) in water-in-CO₂ microemulsions using ammonium carboxylate perfluoropolyether (PFPE-NH₄) as the surfactant, with water in CO₂ at 25°C and 4000 psig. The particle size was found to be a function of the molar ratio of water to

surfactant, the precursor concentration, and the TIP injection rate. As the surfactant remained attached to the particles, coalescence of the particles was prevented. The crystallinity and crystallite size of the nanoparticles was increased with an increase of the molar ratio of water to surfactant (W_0).¹⁴⁰

Although the synthesis of TiO_2 powders in scCO_2 by hydrolysis of titanium (IV) isopropoxide (TIP) has been reported, this pathway is problematic because CO_2 is highly hydrophobic and water is only slightly soluble in scCO_2 (≈ 0.1 wt%). Using fluorinated anionic surfactants can help form stable water-in- CO_2 dispersions to produce TiO_2 particles via TIP in $\text{H}_2\text{O}/\text{CO}_2$ microemulsions. The synthesis conditions must be strictly controlled otherwise; amorphous TiO_2 particles with a wide size distribution were formed.¹⁴¹

Only a small amount of work has been published for TiO_2 nanomaterials synthesized without surfactant directly in scCO_2 . Reverchon *et al.* prepared amorphous titanium hydroxide nanoparticles on the pilot scale in scCO_2 without the assistance of surfactant. Two solutions of TIP and water in scCO_2 were prepared by flowing scCO_2 in two contactors, containing TIP and water, respectively. Following this, the two supercritical solutions were injected into the reactor and $\text{Ti}(\text{OH})_4$ was produced by hydrolysis. $\text{Ti}(\text{OH})_4$ spherical nanoparticles with mean diameters ranging between 70 and 110 nm were produced, with surface areas larger than $300 \text{ m}^2/\text{g}$. The formed particles were separated with the liquid in a downstream separator. The synthesized $\text{Ti}(\text{OH})_4$ particles were amorphous and had a narrow particle size distribution.^{142, 143}

There are some other results from the literature using different substances instead of surfactants to synthesize various forms of TiO_2 materials in scCO_2 . For instance, Yoda

et al. synthesized TiO₂-pillared clay montmorillonite (MNT) in scCO₂ following a two step scheme. In the first step, the interlayer cations were exchanged with hydrophobic cations; in the second step, the intercalation of a metal alkoxide dissolved in scCO₂ was undertaken, followed by hydrolysis with adsorbed water present in the interlayer space. Nano-sized anatase crystal structures were observed in the calcined samples. Sun *et al.* also grafted mono and bi layers of TiO₂ on mesoporous SiO₂ molecular sieve SBA-15 via a surface sol-gel process in scCO₂. The process involved grafting of TIP onto the surface of the molecular sieve, extraction of extra TIP, followed by hydrolysis of the impregnated TIP with an excess amount of water and calcination. The XPS results confirmed the formation of Ti-O-Si and Ti-O-Ti bonds.¹⁴⁴

Tatsuda *et al.* prepared TiO₂-coated activated carbon by the penetration of TIP dissolved in supercritical CO₂ into the nano-spaces of activated carbon. The conversion of TIP to TiO₂ through thermal decomposition was confirmed by evolved gas analysis during heat treatment under N₂ flow. Acetone was detected in the evolved gas, which suggested that some isopropoxide groups in TIP reacted with the carbonyl groups on the activated carbon surface. This chemical reaction with carbon was expected to be advantageous for favourable attachment to the carbon surface. The crystallite size of anatase in the TiO₂/carbon composites was 4.1 nm, as estimated from the X-ray diffraction pattern, which almost corresponded to the graphene crystallite size. These results confirmed that the anatase crystals were present in the carbon pores and the crystal growth of TiO₂ was influenced by the carbon nano-spaces.¹⁴⁵

Sun *et al.* prepared titania-silica binary oxides using the inorganic precursors, tetraethyl orthosilicate (TEOS) and titanium isopropoxide (TIP), simultaneously or

sequentially impregnated into a polypropylene (PP) matrix using supercritical carbon dioxide as a swelling agent and carrier. Hydrolysis and condensation reactions of the precursors were confined to the polymer network, and then the PP matrix was decomposed at higher temperatures resulting in titania-silica binary oxides. It was demonstrated that the structure of the oxides depended strongly on the procedure to impregnate the precursors.¹⁴⁶

Jensen *et al.* followed a very different method called seed enhanced crystallization (SSEC) to prepared anatase TiO₂ at a temperature as low as 100 °C in scCO₂. To prevent the premixing of the reactants before addition of CO₂, TIP and water were injected in the upper third and lower third, respectively, of an autoclave. A seeding material was located in the middle of the autoclave. After addition of CO₂, the reactants were able to mix and the sol-gel reaction was initiated. A crystallinity as high as *ca.* 60% was obtained without downstream calcination. The authors claimed a mechanism that water dispersed into CO₂ and reacted with TIP sitting on the surface of the seeding material, and the seeding material acted as heterogeneous seeds for the nuclei formation and facilitated the formation of crystalline nuclei.^{123, 147} Moreover, recently, Jensen *et al.* studied the formation of TiO₂ particles with reaction time by this method using in situ small-angle X ray scattering (SAXS) and wide-angle scattering (WAXS), and it was found that the sol-gel process in scCO₂ was faster than in the organic solvent.¹⁴⁷

A modified non-aqueous sol-gel route was first reported by Loy *et al.* in 1997, in which the direct synthesis of SiO₂ aerogel monolith in CO₂ was studied by using formic acid as the polycondensation agent.¹⁴⁸ Because organic acid/anhydrate and titanium alkoxides are soluble in scCO₂, this route is likely to be suitable to prepare TiO₂ powders

in scCO₂, as the reaction can be carried out in a homogeneous phase. Moreover, the observed reaction rate was lower than that of a hydrolytic route, allowing for more uniform particle sizes that were attained by using this surface-assisted hydrolysis technique. Keeping this in mind, Guo et al. prepared TiO₂ powders via non-hydrolytic acylation/deacylation in scCO₂ from TIP and acetic anhydride or trifluoroacetic anhydride. The as-prepared TiO₂ nanopowders were amorphous, but readily converted to anatase by heat treatment at 500 °C for 5 h. The photocatalytic activity of the prepared TiO₂ in scCO₂ was higher than that of TiO₂ prepared from titanium(IV) isopropoxide and acetic anhydride, or of commercial T805 TiO₂.¹⁴¹ However, the properties of the synthesized materials strongly depend on the synthesis parameters such as the precursor, polycondensing agent, temperature and pressure.

Recently, Sui et al. synthesized TiO₂ nanofibers having diameters that ranged from 9 to 100 nm with nanocrystallites via a sol-gel route in scCO₂. The nanofibers were formed by the esterification and condensation of titanium alkoxides using acetic acid as the polymerization agent in scCO₂ from 40 to 70 °C and 2500 to 8000 psia. The nanofibers exhibited relatively high surface areas up to 400 m²/g and anatase and/or rutile nanocrystallites were formed after calcination.¹⁴⁹ The same group (Charpentier lab) synthesized porous ZrO₂ aerogels using a similar procedure. The synthesis involved the coordination and polycondensation of a zirconium alkoxide using acetic acid in CO₂, followed by scCO₂ drying and calcination. Both mesoporous monoliths and nanoparticles were produced. The as-prepared materials exhibited a high surface area (up to 399 m²/g). Moreover, they intensively performed an in situ infrared spectroscopy analysis for the TiO₂ and ZrO₂ system and found that different M-acetate coordinate complexes were

formed at the initial stages of the polycondensation reactions, followed by further condensation of the complexes into macromolecules.¹⁴⁹⁻¹⁵¹

Extensive IR studies on the formation of metal complexes with carboxylic acid have shown that carboxylate ion may coordinate to a metal in one of the following modes provided in Figure 2.11:

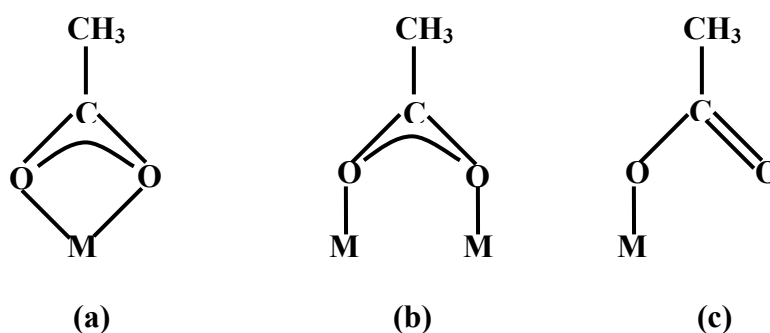


Figure 2.11: Binding modes of acetic acid with metal: (a) chelating bidentate and (b) bridging bidentate and (c) monodentate.

In the first structure, carboxylate is bound to one M center in a chelating bidentate mode (a), the carboxyl group could bind with each of its oxygen atoms to two M atoms yielding the bridging bidentate mode (b), and the carboxylate could also be bound to one M in a monodentate (esterlike linkage) mode (c). Deacon and Phillips made the following conclusions from their IR spectra of known acetates crystal structures:

- I) Chelating complexes (structure a) exhibit Δ values [$\nu_a(\text{COO}^-) - \nu_s(\text{COO}^-)$] which are significantly smaller than the ionic complexes.
- II) The bridging complexes (structure b) exhibit Δ values which are greater than chelating complexes and close to the ionic values.

III) The Δ values for monodentate complexes (structure c) are much greater than the values of the ionic complexes.

In the following Table 2.3, the stretching frequencies and the structures of some carboxylate complexes are provided.¹⁵²

Table 2.3. Carboxyl stretching frequencies and structures of carboxylate complexes.

Compound	$\nu_a(\text{COO}^-)$	$\nu_s(\text{COO}^-)$	Δ	Structure
HCOO^-	1567	1366	201	Ionic
CH_3COO^-	1578	1414	164	Ionic
$\text{CrO}_2(\text{OAc})_2$	1710	1240	470	Monodentate
$\text{RuCl}(\text{OAc})(\text{CO})(\text{PPh}_3)_2$	1507	1465	42	Chelating
$\text{RuH}(\text{OAc})(\text{PPh}_3)_2$	1526	1449	77	Chelating
$\text{Rh}_2\text{Cl}(\text{OAc})_2(\text{CO})_3(\text{PPh}_3)$	1580	1440	140	Bridging
$[\text{Cr}_3\text{O}(\text{OAc})_6(\text{H}_2\text{O}_3)]^+$	1621	1432	189	Bridging
$\text{Rh}(\text{OAc})(\text{CO})(\text{PPh}_3)_2$	1604	1376	228	Monodentate

Based on the previous discussion and FTIR analysis, it can be easily predicted on how carboxylic acid coordinates with metal ions in the direct sol-gel process.

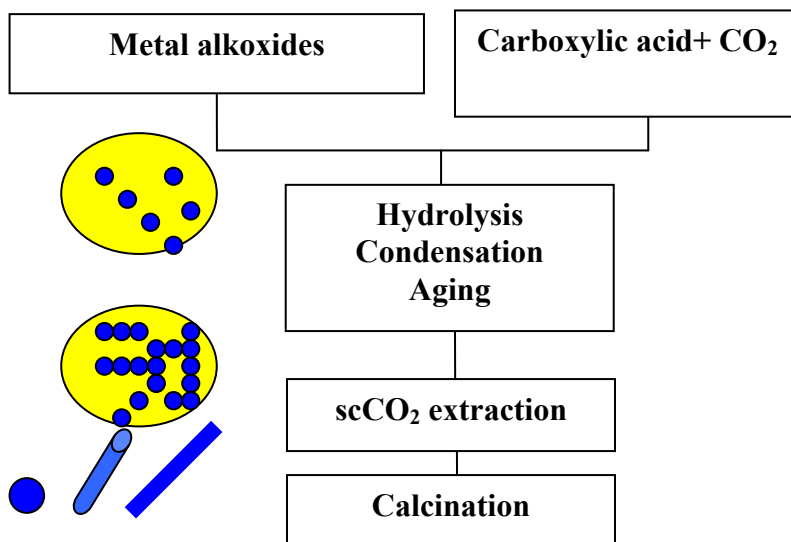


Figure 2.12: Schematic diagram of the direct sol-gel process in scCO_2 for the synthesis of nanostructured materials.

The schematic diagram of the direct sol-gel process in scCO_2 is given in Figure 2.12. This process has significant advantages such as combining the reaction process and the drying process into one step, maintaining higher surface areas, and being a low temperature process. However, no one has synthesized anion or cation doped TiO_2 based nanostructures following this simple route.

2.7. Scope of the Research

TiO_2 nanomaterials are one of the potential candidates for solar applications due to their unique optoelectronic and photochemical properties, such as high refractive index, high dielectric constant, and excellent optical transmittance in the visible and near-IR region, high activity, strong oxidation capability, and chemical stability. In addition, being a low cost material, TiO_2 is favorable for potential large scale commercial applications. However, the performance of TiO_2 nanomaterials strongly relies on their crystallinity, crystallite size, crystal structure, specific surface area, thermal stability and quantum efficiency. Bulk modifications such as cation or anion doping have been found very effective to improve the properties of TiO_2 to enhance their performance. Several different processing techniques have been used for the preparation of TiO_2 -based nanostructures, such as template techniques, hydrothermal processes, and soft chemical processes. However, each of these methods has limitations. Due to these limitations, alternative processes using a green solvent such as supercritical carbon dioxide (scCO_2) is attractive to synthesize TiO_2 -based nanomaterials. The main objective of this project was to develop a synthesis route to produce superior quality TiO_2 based nanomaterials by introducing Zr, Fe and N as doping materials. Another important aspect of this study was

the investigation of the use of scCO_2 which is a green solvent, as an alternative to the conventional toxic organic solvents in nanomaterial synthesis.

The following have been identified as the specific objectives of this project:

- I. Synthesis of the following three different types of nanomaterials using an acid modified sol-gel technique in scCO_2 :
 - a. Binary $\text{ZrO}_2\text{-TiO}_2$
 - b. Zr modified and N doped TiO_2
 - c. Fe doped TiO_2
- II. Characterization of the synthesized nanomaterials using different physical and chemical techniques in order to,
 - a. Study the surface characteristics, morphology, composition and electronic properties.
 - b. Investigate the effects of different operating variables and doping agents (ions) on the properties.
- III. Development of a kinetics model for the solid-state reactions involved during heat treatment of the synthesized nanomaterials and estimation of the kinetic parameters.
- IV. Evaluation of the performance of selective nanomaterials as photocatalysts for the degradation of methylene blue (a model compound).

CHAPTER 3

EXPERIMENTAL METHODS

3. Introduction

In this chapter, the experimental procedures followed in this investigation are described sequentially, and divided into two main sections; (i) synthesis of TiO₂ based nanomaterials, and (ii) characterization techniques and evaluation procedures used to analyze the synthesized nanomaterials. The materials used, and the general procedures followed to synthesize the nanomaterials are described in section 3.1. The nanomaterials were synthesized in a high-pressure view cell reactor. The high-pressure reactor was connected with CO₂ along with having temperature and pressure controllers. Detailed information about the experimental set-up used to synthesize the nanomaterials is also reported in this section. Characterization methods of the synthesized materials include: Scanning Electron Microscopy (SEM), Transmission Electron Microscopy (TEM), High Resolution TEM (HRTEM), ThermoGravimetric Analysis (TGA), Differential Thermal Analysis (DTA), powder ATR-FTIR, Energy Dispersive X-ray (EDX) and X-ray Photon Spectroscopy (XPS), powder X-ray Diffraction (XRD), Temperature Programmed Desorption (TPD) and UV-Vis analysis, Differential Scanning Calorimeter (DSC), and N₂ physisorption. In situ attenuate total reflection Fourier transmission infrared spectroscopy (ATR-FTIR) was also used to study the reaction mechanism. The detailed information on these characterization methods are described in section 3.2.

3.1. Synthesis of TiO₂ Based Nanomaterials

In this investigation, Zr modified TiO₂ nanotubes, Fe doped TiO₂, and Zr modified N doped TiO₂ were synthesized by an acid modified sol-gel process in scCO₂ for potential solar related applications. The materials and procedure used for this study are given in the following sections.

3.1.1. Materials

Zr modified TiO₂ was synthesized using a reagent grade 97% titanium(IV) isopropoxide (TIP), and 70% zirconium(IV) propoxide (ZPO) as TiO₂, and ZrO₂ precursors, respectively.

In the synthesis of Fe doped TiO₂, reagent grade 97% titanium(IV) isopropoxide (TIP) was used as the TiO₂ precursor. Given that Fe(NO₃)₃·9H₂O is a solid material, 1 wt % solution of Fe(NO₃)₃·9H₂O was prepared by dissolving 1g of Fe(NO₃)₃·9H₂O in 99g of isopropanol, which was used as the stock solution.

In the case of N doped TiO₂ synthesis, 99% triethylamine (TEA) was used as the nitrogen source. Generally, acetic acid was used as the polycondensation agent and scCO₂ as solvent throughout the study. However, 98.5% hexane, 99% xylenes, 99.5% isopropanol, and anhydrous ethanol were also used as solvents in the solvent effect study. All chemicals were purchased from Aldrich Chemical Co and used without further purification.

3.1.2. Experimental Set-Up

The synthesis experiments were carried out in a 10 or 25 mL view cell made of stainless steel with two sapphire windows. The view cell is ideal for observation of any phase changes. Moreover, the view cell is considered an ideal reactor for synthesizing small-scale materials in SCFs, especially for scCO₂ in the laboratory.¹⁵³⁻¹⁵⁶ The schematic diagram of the experimental set-up is shown in Figure 3.1.

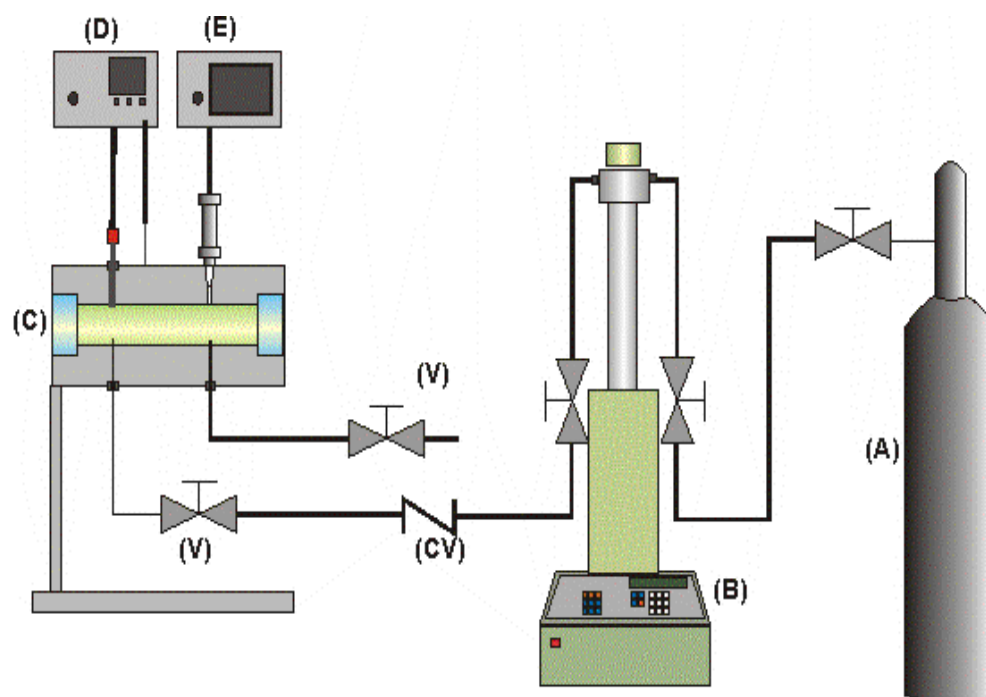


Figure 3.1: Schematic diagram of experimental set-up; A-CO₂ tank, B- Syringe pump, C- View cell, D- Temperature controller, E- Pressure indicator.

As can be seen in Figure 3.1, a 10 or 25 mL stainless steel view cell was connected with a syringe pump (ISCO 100 DM) in order to pump CO₂ from a dip tube. The check valve next to the pump was used to prevent possible back flow from the view

cell. The temperature in the view cell was measured and maintained by means of a T-type thermocouple, a heating tape (Omega SRT051-040, 0.5×4 FT) and a temperature controller (Fuji PXZ-4).¹²³

3.1.3. Experimental Procedure

In a typical experiment, the appropriate amount of precursors and acetic acid were quickly placed in the view cell followed by addition of CO₂ at the desired temperature and pressure under stirring conditions. Initially, a transparent homogeneous phase was observed. After the reaction mixture was stirred about 30 minutes to several hours, the fluids in the view cell became semitransparent then turned white, indicating a phase change. This turning point was considered as the gelation point and the time to reach this point was recorded. After 5 days of aging, a few droplets were vented and placed in a test tube, followed by addition of water and nitric acid. If there was no white precipitate formed, this indicated complete polymerization. In order to remove the unreacted acetic acid and condensation byproducts, i.e. alcohol, ester and water from the gel formed in the view cell, a CO₂ wash step was conducted. To prevent collapse of the gel network, both CO₂ washing and venting were conducted carefully in a controlled manner. The resulting as-prepared materials were amorphous. To form crystalline phase, the synthesized materials were calcined in air at different temperatures using a heating rate of 10 °C/min, the holding time was 2 h, and the cooling rate to room temperature was 0.5 °C/min. The nanomaterials were synthesized according to the scheme as given in Figure 3.2.

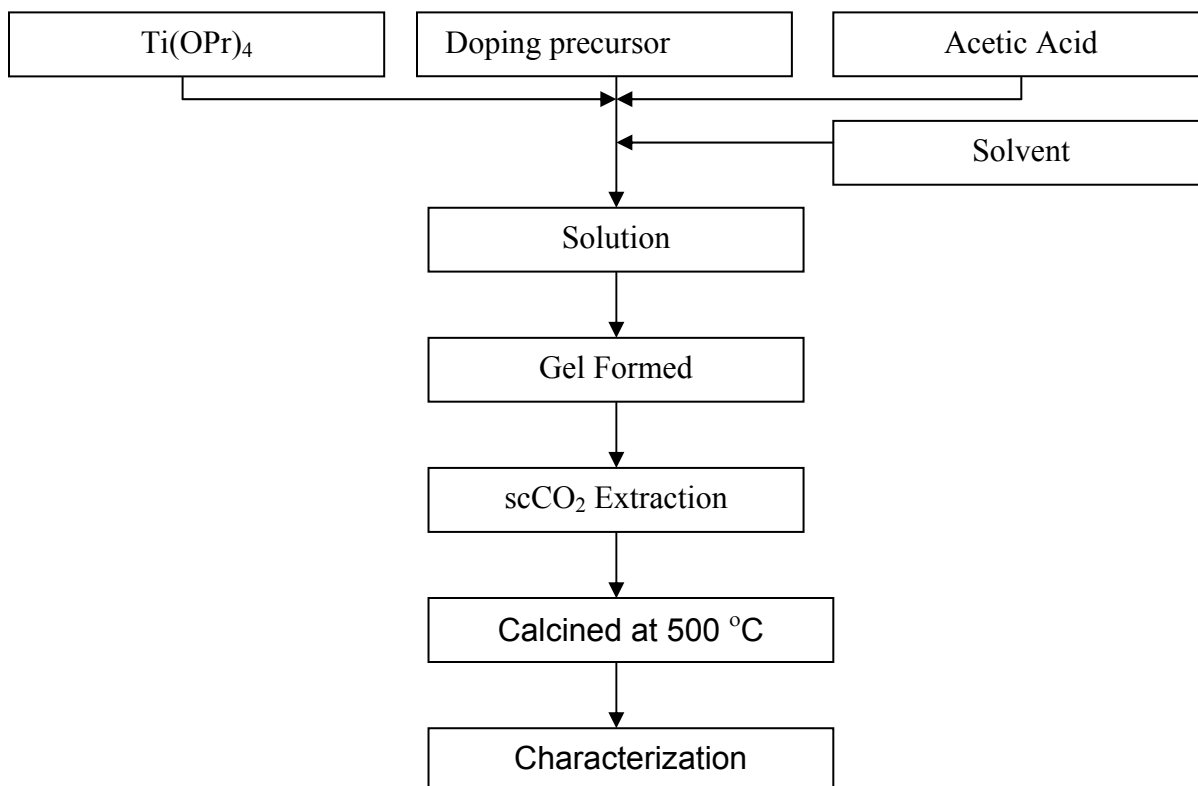


Figure 3.2: Preparation scheme for TiO₂ based nanomaterials by sol-gel process.

Zirconia Modified Titania

Four different studies were conducted in this part of the project. For this reason, different experimental conditions as well as characterization methods were used. Detailed information about the experimental conditions and methods are given in the related chapters.

Synthesis of Fe Doped TiO₂

The appropriate amount of stock solution and TIP was used to synthesize Fe doped TiO₂ at 60 °C and 5000 psig following the standard procedure previously discussed. Four samples using 0, 1, 1.5, and 2 mL Fe stock solution were synthesized and

named S1, S2, S3 and S4, respectively. The synthesized materials were calcined at 400, 500, and 600 °C to investigate the heat effects.

Nitrogen Doped Titania

The synthesis procedure for preparing N-doped TiO₂ was the same as the Zr modified TiO₂ procedure previously discussed with the appropriate amount of TEA added as the N precursor to the system. In this study, six samples were prepared and named as TiO₂, TiO₂-N1 and TiO₂-N2 respectively, based on the amount of triethylamine used in the preparation step. The amount of TEA was 0.4 and 0.6 molar ratio to metal precursor for N1 and N2 named samples respectively.

3.2. Characterization Methods

3.2.1. Electron Microscopy

An electron microscope, such as a transmission electron microscope (TEM), or a scanning electron microscope (SEM), is a microscope that uses a beam of electrons to illuminate a specimen and create an enlarged image, which provides the surface and internal information on a nanometer scale. Electron microscopes have much greater resolving power than light microscopes, and can obtain much higher magnifications. The electron microscope is extensively used for inspection, quality assurance and failure analysis applications in industry, in particular, for microelectronic device fabrication. TEM and SEM have made crucial contributions to science and engineering, and made them indispensable tools in nanotechnology for analyzing nanostructures.

Transmission Electron Microscopy (TEM): In 1931, Knoll and Ruska built the first electron microscope prototype. In 1938, Eli Franklin Burton built the first practical

electron microscope and in 1939, Siemens produced the first commercial TEM. However, the TEM was not used for material studies until 40 years ago, when the thin-foil preparation technique was developed. More improvements of the TEM technique in the 1990s provided 0.1 nm of resolution, which made TEM an indispensable analysis technique for studying materials in the micron or nano size region.¹²³

Usually the incident electrons interact with a specimen and X-ray, cathode luminescence and six type of electrons: (1) transmission, (2) back-scattered, (3) reflected, (4) secondary, (5) Auger and (6) trapped electrons are generated (Figure 3.3). The transmission and scattered electrons are collected for TEM imaging.¹²³

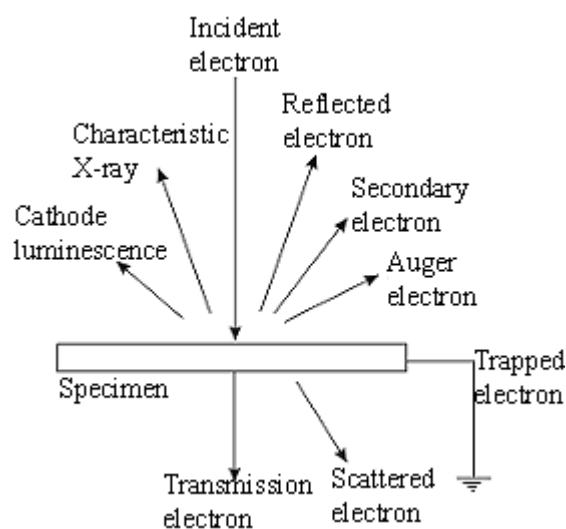


Figure 3.3: Schematic interactions of a specimen with incident electrons

TEM is the only technique allowing a 3D observation and quantitative characterization of most kinds of lattice defects. Its high spatial resolution for orientation

determination and the high resolution of TEM images can be advantageous over SEM for nanomaterial analysis.

A TEM such as the Philips CM10 has a resolution of 0.5 nm, while a high resolution transmission electron microscopy (HRTEM), e.g., JOEL 2010, is capable of a spatial resolution of 0.194 nm and can provide images with 1024×1024 pixel resolution by using a multiscan digital camera. The diffraction patterns of HRTEM images are also very useful for studying the nanocrystalline phases of metals and nanoceramics.

Scanning electron microscopy (SEM)

Manfred von Ardenne pioneered the scanning electron microscope (SEM) and built his universal electron microscope in the 1930s. In the SEM, a very fine beam of electrons with energies up to several tens keV is focused on the surface of a specimen, and is scanned across it in a parallel pattern. The intensity of emission of secondary and backscattered electrons is very sensitive to the angle at which the electron beam strikes the surface of the sample. The emitted electron current is collected and amplified. The magnification produced by the SEM is the ratio between the dimension of the final image display and the field scanning on the specimen. Usually, the magnification range of the SEM is between 10 to 222,000 times, and the resolution is between 4-10 nm. Generally, the TEM resolution is about an order of magnitude greater than the SEM resolution, however, because the SEM image relies on surface processes rather than transmission, it is able to image bulk samples and has a much greater depth of view, and so can produce images that are a good representation of the overall 3D structure of the sample.

SEM usually images conductive or semi-conductive materials. A common preparation technique is to coat the sample with a several-nanometer layer of conductive material, such as gold, or platinum, from a sputtering machine. However, this process can damage delicate samples. It should also be mentioned that the specimen might be damaged by the electron-beam focusing for a long time on a small spot. SEM measurements were conducted to determine the size and morphology of synthesized nanomaterials using a LEO 1530 Scanning Electron Microscope. Both TEM and SEM were widely used in this thesis for studying the morphology of the synthesized pure and doped TiO₂ nanomaterials. Bulk compositions were determined using energy dispersive X-ray spectroscopy attached to the LEO 1530 Scanning Electron Microscope.

3.2.2. Thermal Analysis

Thermal analysis is an important technique for the characterization of solid materials, as it provides information on the physical and chemical changes involving endothermic and exothermic processes, temperatures for phase transitions, melting points and crystallization, and the weight loss when the temperature is increased.

Differential Scanning Calorimetry (DSC): DSC is a thermal analysis technique that is used to measure the heat flows associated with transitions in materials as a function of time or temperature. This technique provides both qualitative and quantitative information about the physical and chemical changes that are involved in endothermic processes such as melting, and exothermic processes such as crystallization, or changes in heat capacity such as at the glass transition temperature (T_g) (Figure 3.4). DSC can

determine the T_g of polymers and the phase transition temperatures of solids. This makes DSC an indispensable technique for the characterization of polymer and oxide materials.

An alternative technique which shares much in common with DSC is differential thermal analysis (DTA). In this method, the heat flow to the sample and the reference remains constant, with the instrument measuring the temperature difference. When the sample and reference are heated, identical phase changes and other thermal processes cause a difference in temperature between the sample and reference. Both DSC and DTA provide similar information; however, DSC is the more widely used technique amongst these two techniques. As the temperature increases, an amorphous solid becomes less viscous. At some point the molecules may obtain enough freedom of motion to spontaneously arrange themselves into a crystalline form. This is known as the crystallization temperature (T_c). This transition from amorphous solid to crystalline solid is an exothermic process, and results in a peak in the DSC/DTA signal. As the temperature increases, the sample eventually reaches its melting point (T_m). The melting process results in an endothermic peak in the DSC/DTA curve. The ability to determine the transition temperatures and enthalpies makes DSC/DTA an invaluable tool in producing phase diagrams for various chemical systems measuring any changes of the sample weight with increasing temperature.

Thermogravimetric Analysis (TGA): TGA, another important thermal technique, is widely used for the characterization of solid materials including polymer, organic, inorganic and composite materials. Especially, TGA can be used to determine the percentage of inorganic fillers in inorganic/polymer composites.

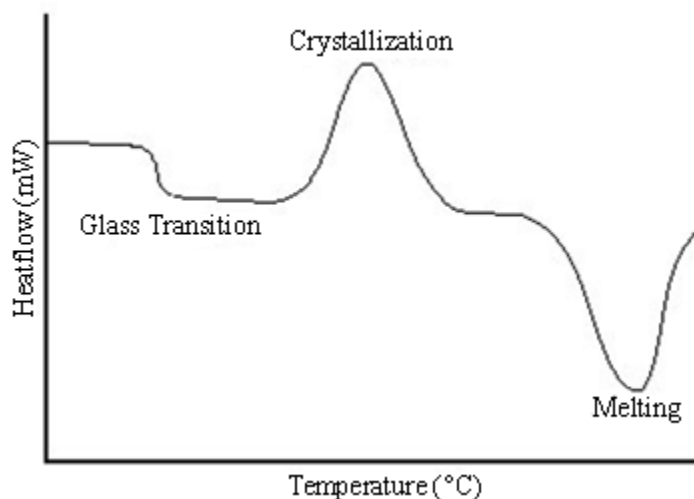


Figure 3.4: A schematic DSC curve demonstrating the appearance of phase transition.¹⁵⁷

TGA can determine: (1) moisture/liquid content and the presence of volatile species, (2) decomposition temperatures, and (3) the rate of degradation. TGA, in this work was performed under nitrogen/air atmosphere on a TA Instruments TA-Q500 or SDT-Q600 at a heating rate of 10 °C/min from room temperature to 1000°C.

3.2.3. X-ray Photon Spectroscopy (XPS)

XPS is a quantitative spectroscopic technique that measures the elemental composition, empirical formula, and the chemical state and electronic states of the elements that exist within a material. XPS spectra are obtained by irradiating a material with a beam of aluminium or magnesium X-rays while simultaneously measuring the kinetic energy (KE) and number of electrons that escape from the top 1 to 10 nm of the material being analyzed. Because the energy of a particular X-ray wavelength equals a known quantity, we can determine the electron binding energy (BE) of each of the

emitted electrons by using an equation that is based on the work of Ernest Rutherford (1914):

$$E_{\text{binding}} = E_{\text{photon}} - E_{\text{kinetic}} - \Phi \quad 3.1$$

where E_{binding} is the energy of the electron emitted from one electron configuration within the atom, E_{photon} is the energy of the X-ray photons being used, E_{kinetic} is the kinetic energy of the emitted electron as measured by the instrument, and Φ is the work function of the spectrometer. It is important to note that XPS detects only those electrons that have actually escaped into the vacuum of the instrument. The photo-emitted electrons that have escaped into the vacuum of the instrument are those that originated from within the top 10 to 12 nm of the material. All of the deeper photo-emitted electrons, which were generated from the X-rays which penetrated 1–5 micrometers into the material, are either recaptured or trapped in various excited states within the material. For most applications, XPS is a non-destructive technique to measure the surface chemistry of any inorganic compounds, metal alloys, semiconductors, polymers, or catalysts. Figure 3.5 represents a typical XPS spectrum which gives valuable information on the surface composition. XPS is a very useful technique especially for multicomponent samples such as the binary metal oxides, Fe doped TiO₂, and N-doped TiO₂ synthesized in this study.

The surface composition was determined by XPS using a Kratos Axis Ultra spectrometer using a monochromatic Al K (alpha) source (15 mA, 14 kV). Survey and high-resolution spectra were obtained using an analysis area of ~300x700 microns and pass energies of 160 eV and 20 eV, respectively. Spectra were charge corrected to the main line of the carbon 1s spectrum (C-C, C-H) set to 285.0 eV.

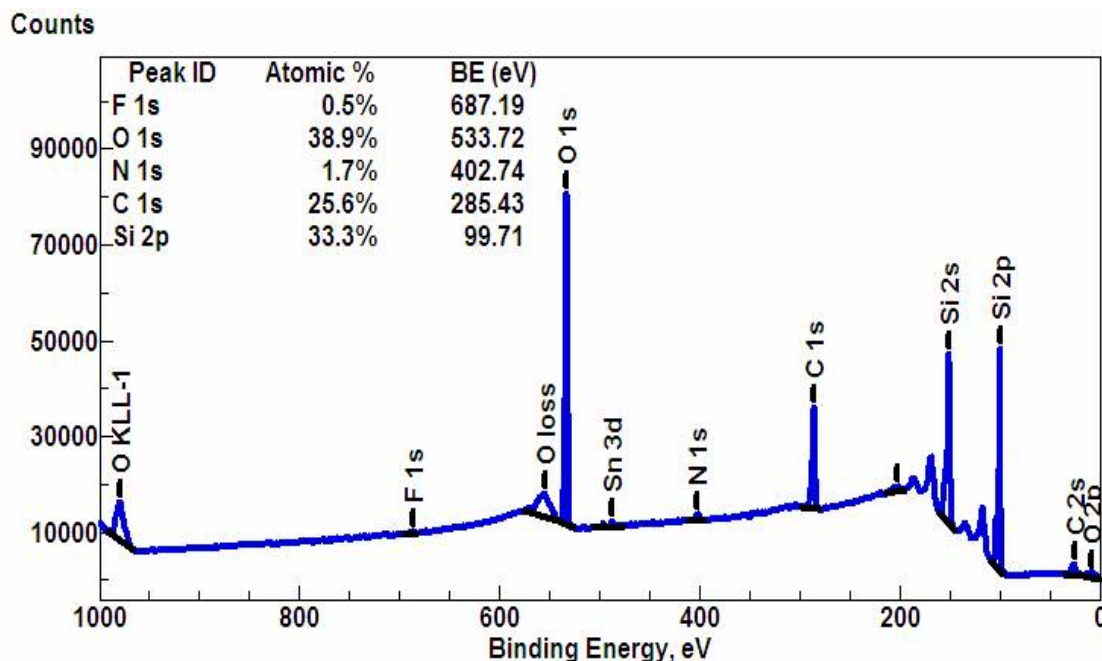


Figure 3.5: A typical high resolution XPS spectrum with corresponding information.

3.2.4. Powder X-Ray Diffraction (XRD)

Powder XRD is one of the primary techniques used to characterize solid-state materials. It can provide valuable information about the crystalline phase and average crystallite size. The crystal size measured by this technique is smaller than the measurement limit of the optical or electronic microscope.¹⁵⁸ The structure of a crystal is analyzed by the X-ray diffraction patterns. The X-ray diffraction of a crystal can be formulated by means of Bragg's law (Figure 3.6):

$$2d\sin\theta = n\lambda \quad 3.2$$

where d is the d-spacing, perpendicular distance between pairs of adjacent planes in the crystal, θ is the incident angle, n is the layer of planes, and λ is the wavelength of the X-rays.

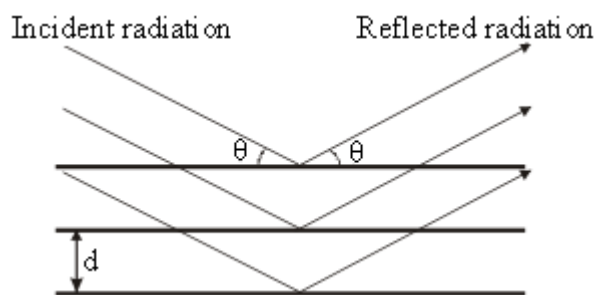


Figure 3.6: Schematic of X-ray reflection on the crystal planes.¹⁵⁸

The d spacing can be expressed through cell parameters and the Miller index by the following equation:

$$\frac{1}{d^2} = \frac{h^2}{a^2} + \frac{k^2}{b^2} + \frac{l^2}{c^2} \quad 3.3$$

where, d is the d-spacing; a, b, c are sides of the unit cell; and h, k, and l are the Miller indices, which are used to describe the lattice planes and directions in a crystal.

XRD was performed utilizing a Rigaku instrument employing $\text{CuK}\alpha_1 + \text{K}\alpha_2 = 1.542 \text{ \AA}$ radiation with a power of 40 kV-35mA for the crystalline analysis. The broad-scan analysis was typically conducted within the $2\text{-}\theta$ range of $10\text{-}80^\circ$. The strongest peak for the anatase (101) and the rutile (110) phases of TiO_2 was used to determine the average size of the metal oxide nanocrystallites using Scherrer's equation¹⁵⁸:

$$D_{\text{cryst}} = \frac{0.9\lambda}{\beta \cos \theta} \quad 3.4$$

where D_{cryst} - is the average nanocrystallite size (nm), λ - is the X-ray wavelength (1.542 Å), β - is the full-width at half-maximum (FWHM) intensity (in radians), and θ - is the half of the diffraction peak angle. The fraction of rutile phase in the crystal was

calculated using the integrated intensities of the anatase (101) (I_a) and rutile (110) (I_r) peaks by the following formula developed by Spur and Myers.¹⁵⁹

$$X_{rutile} = \frac{1}{1 + K(I_a/I_r)} \quad 3.5$$

3.2.5. Raman Spectroscopy

Raman spectroscopy is used in condensed matter physics and chemistry to study vibrational, rotational, and other low-frequency modes in a system. It relies on inelastic scattering, or Raman scattering of monochromatic light, usually from a laser. The laser light interacts with phonons or other excitations in the system, resulting in the energy of the laser photons being shifted up or down. The shift in energy gives information about the phonon modes in the system. Infrared spectroscopy yields similar, but complementary information.

For a molecule to exhibit a Raman Effect, a change in polarizability or the amount of deformation of the electron cloud with respect to the vibrational coordinate, is required. The amount of the polarizability change will determine the Raman scattering intensity, whereas the Raman shift is equal to the vibrational level that is involved. Raman spectroscopy is commonly used in chemistry, since vibrational information is very specific for the chemical bonds in molecules. In solid state physics, Raman spectroscopy is used to, amongst other things, characterize materials, measure temperature, and find the crystallographic orientation of a sample. In this study the samples were analyzed using a Renishaw Model 2000 Raman spectrometer equipped with a 633 nm laser. The power at the sample varied between 0.2 and 0.5 mW with the beam defocused to an area of approximately 5-10 microns in diameter.

3.2.6. N₂ Physisorption

The textural characterization, such as surface area, pore volume and the pore size distribution of the as-prepared aerogels and oxides were obtained by N₂ physisorption at 77 K using a Micromeritics ASAP 2010. Prior to N₂ physisorption, the samples were degassed at 200 °C under vacuum for 2 hours. From the N₂ adsorption isotherms, the specific surface area was calculated. The mesopore volume (V_{BJH}), the average pore diameters (D_{pore}), and the pore size distributions were estimated by the Barret–Joyner–Halenda (BJH) method applied to the desorption branch of the isotherm. Below is presented some theoretical information related to the surface area and pore volume calculations used in this thesis.

BET Surface Area

When a highly dispersed solid is exposed in a closed space to a gas or vapor at some definite pressure, the solid begins to adsorb the gas. Adsorption on porous materials proceeds via monolayer adsorption followed by multilayer adsorption and capillary condensation.¹⁶⁰ At a low relative pressure, a monolayer of adsorbent is adsorbed on the surface like non porous materials. The amount of adsorbent is used to calculate the surface area. Using the Brunauer, Emmett and Teller (BET) theory, one can calculate the specific surface area of a solid sample from the number of monolayer gas molecules required to cover the solid surface, and the cross-sectional area of the gas molecule being adsorbed.

The BET equation is written as:

$$\frac{1}{v[(P_0/P)-1]} = \frac{1}{v_m c} \left(\frac{P}{P_0} \right) + \frac{1}{v_m} \quad 3.6$$

where, P and P_0 are the equilibrium and the saturation pressures of adsorbates at the temperature of adsorption, v is the adsorbed gas quantity (for example, in volume units), and v_m is the monolayer adsorbed gas quantity, c is the BET constant and can be expressed as:

$$c = \exp\left(\frac{E_1 - E_L}{RT}\right) \quad 3.7$$

where E_1 is the heat of adsorption of the first layer, and E_L is the heat for liquefaction.

Equation 3.6 is an adsorption isotherm and can be plotted as a straight line, called a BET plot, with $P/v(P_0 - P)$ on the ordinate and P/P_0 on the abscissa according to experimental results. The value of the slope and the y-intercept of the line are used to calculate the monolayer adsorbed gas quantity, v_m , and the BET constant, c , respectively.¹⁶¹ An example of a BET plot of N_2 adsorption in silica gel at 91 K is shown in Figure 3.7, from which v_m and the BET constant c can be determined as 116.2 ml/g and 80.6, respectively.^{123, 161}

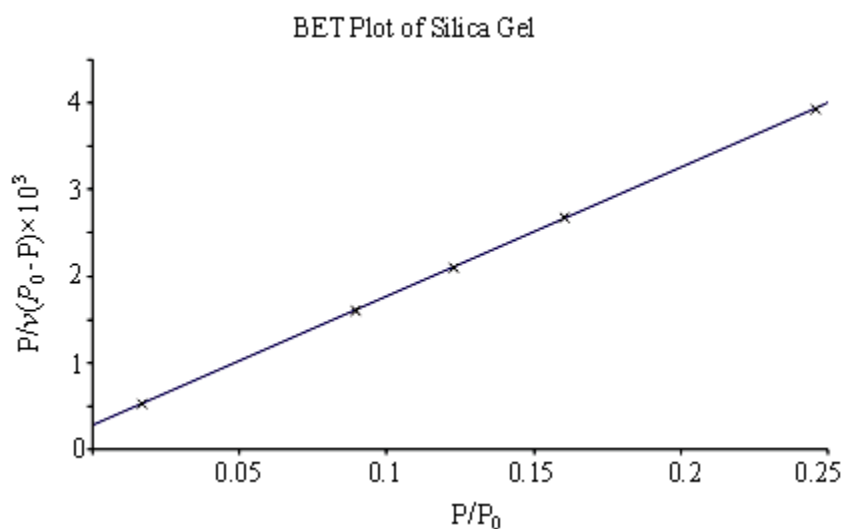


Figure 3.7: BET plot of N_2 adsorption on silica gel at 91 K.¹²³

The numerical value of the BET constant c controls the shape of the knee of the isotherm and depending on the knee shape; different isotherms as shown in Figure 3.8 can be obtained. For example, a typical type II isotherm can be obtained when the c value is greater than 2. The type III isotherm results when the value of c is positive but less than 2.

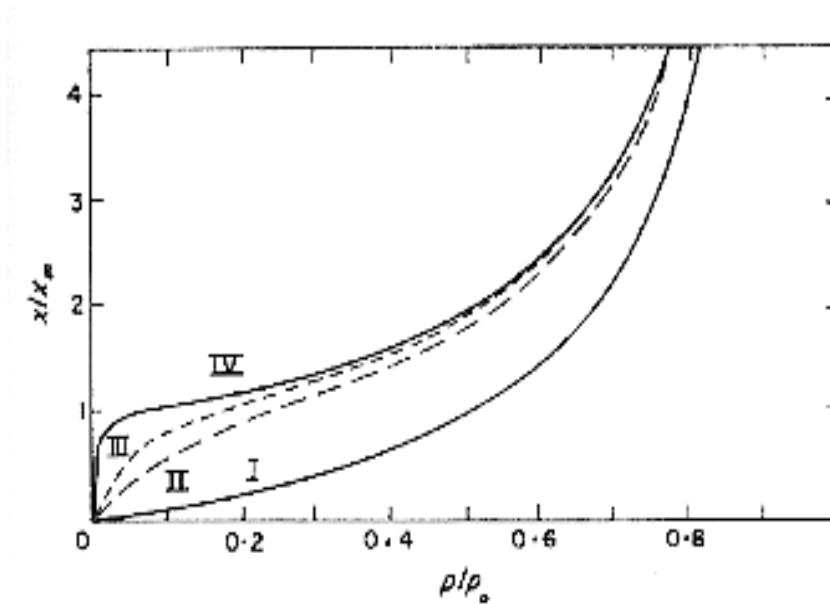


Figure 3.8: Curves of x/x_m vs. p/p_0 calculated from the BET equation for different values of c . I, $c=1$; II, $c=11$; III, $c=100$; IV, $c=10000$.¹⁶⁰

The total surface area (S_{total}) and a specific surface area (S) can be calculated as:

$$S_{total} = \frac{(v_m \cdot N \cdot s)}{M} \quad 3.8$$

$$S = \frac{S_{total}}{a} \quad 3.9$$

where, S_{total} = total surface area, N = Avogadro's number, s = adsorption cross section, M = molecule weight of adsorbate, S = specific surface area, and a = weight of solid sample.

BJH Pore-Size Distribution and Pore Volume

According to the IUPAC definitions, microporous, mesoporous and macroporous materials exhibit pore diameters of less than 2 nm, in the range of 2-50 nm and above 50 nm, respectively.¹⁶⁰

During a physisorption process, beyond a monolayer formation, the amount of adsorbed gas gradually increases as the relative pressure increases, and then at higher pressures, the amount of gas adsorbed increases steeply due to capillary condensation in the mesopores. Once these pores are filled, the adsorption isotherm is complete. The capillary condensation is believed to be proportional to the equilibrium gas pressure and the size of the pores inside the solid. The Barrett, Joyner and Halenda (BJH) computational method allows the determination of pore sizes from the equilibrium gas pressures. The BJH method for calculation of pore size distribution is based on a model of the adsorbent exhibiting cylindrical pores.¹⁶² During desorption, a pore loses its condensed liquid adsorbates, known as the core of the pore, at a particular relative pressure related to the core radius by the Kelvin equation (Equation 3.10).

$$\log\left(\frac{P}{P_0}\right) = \frac{-2\sigma V}{8.316 \times 10^7 \times 2.303 \times T \times r_k} = \frac{-4.14}{r_k} \quad 3.10$$

where, σ is the surface tension of liquid nitrogen, V is the liquid molar volume of nitrogen, r_k is the radius of capillary in cm, T is the absolute temperature in K, and 8.316×10^7 is the gas constant in ergs per degree.

After the core is evaporated, a layer of adsorbate remains on the wall of the pore. The thickness of this layer can be calculated for a particular relative pressure from a

thickness equation. Using this approach, the pore size distribution and pore volume of solid with various pore sizes can be determined.¹⁶²

Hysteresis Loops

After an adsorption isotherm, the desorption isotherm can be generated by withdrawing the adsorbed gas by reducing the pressure. However, capillary condensation and capillary evaporations do not take place at the same pressure, resulting in hysteresis loops. The resulting hysteresis loops can be mechanistically related to particular pore shapes. Figure 3.9 shows the classification of hysteresis loops denoted as H1, H2, H3 and H4 by IUPAC. Type H1 and H2 loops were obtained from agglomerated spherical particles and corpuscular systems, respectively, while type H3 and H4 were obtained from slit-shaped pores or plate-like particles.¹⁶⁰

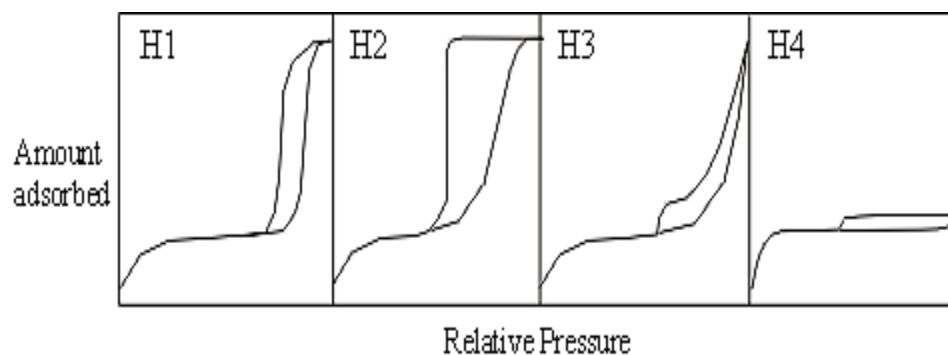


Figure 3.9: Classification of hysteresis loops as recommended by the IUPAC.

The relationship between the morphology of the pores and the hysteresis profile has been previously studied using computational simulations. Although gas adsorption techniques and the data analysis methods appear to be well established, it is still difficult

to evaluate the pore structures accurately, due to the surface heterogeneity and structural heterogeneity of the solid materials.¹⁶³

3.2.7. UV-Vis Spectroscopy

Many molecules absorb ultraviolet (UV) or visible light. The absorption of UV or visible radiation is caused by the excitation of outer electrons, from their ground state to an excited state. The Bouguer-Lambert-Beer law forms the mathematical physical basis for the light absorption measurements on gas and in solution. According to this law, absorbance is directly proportional to the path length, l , and the concentration of the absorbing substance, c , and can be expressed as $A = \alpha lc$, where α is a constant of proportionality, called the absorptivity.¹⁶⁴ In addition, absorption strongly depends on the types of samples, and the environment of the sample. For instance, molecules absorb radiation of various wavelengths depending on the structural groups present within the molecules, and show a number of absorption bands in the absorption spectrum. The solvent in which the absorbing species is dissolved also has an effect on the spectrum of the species. Moreover, the size of the particle is also important. If the size of the particle $d \gg \lambda$, light interacts with the samples instead of absorption, with parts of the light scattered and reflected.

When dealing with solid samples (Figure 3.10), light penetrates into the sample; undergoes numerous reflections, refractions and diffraction and emerges finally diffusely at the surface. The Bouguer-Lambert-Beer law cannot handle solid samples, which is based on the assumption that the light intensity is not lost by scattering and reflection processes.¹⁶⁴

Diffuse reflectance measurements are usually analyzed on the basis of the Kubelka-Munk equation:

$$F(R_{\infty}) = \frac{k}{s} = \frac{(1-R)^2}{2R} \quad 3.11$$

where k and s are absorption and scattering coefficients respectively, and R is the reflectance at the front face. $F(R_{\infty})$ is termed the Kubelka-Munk function and is proportional to the concentration of the adsorbate molecules. From the onset of the plot of Kubelka-Munk function vs wavelength or photoenergy, the band gap energy of a semiconductor can be easily calculated. However, to measure a diffuse reflectance spectrum, the diffusely reflected light must be collected with an integrated sphere, avoiding secularly reflected light, and using a reference standard (BaSO_4 or white standard).

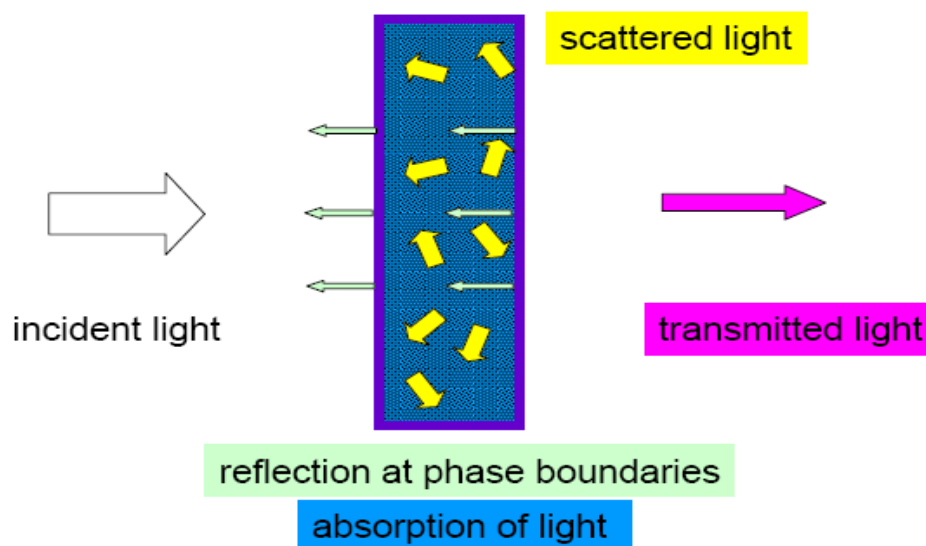


Figure 3.10: Interaction of light with solid sample.

3.2.8. In-situ ATR-FTIR Analysis

ATR-FTIR spectroscopy is a powerful tool for in situ measurement of concentration, solubility, and supersaturation in crystallization processes for the chemical and pharmaceutical industries.^{165, 166} The IR spectrometry is a type of absorption spectrometry that uses the infrared region of the electromagnetic spectrum to determine the molecular structure by analyzing the absorption frequency, at which chemical bonds vibrate in either a stretching or bending mode. FTIR is an improved technique to make the IR measurements easier and faster, in which the IR beam is guided through an interferometer. A FTIR spectrum is obtained from performing a mathematical Fourier Transform on the interferegram. ATR spectroscopy uses the phenomenon of total internal reflection. In this technique, the radiation beam is directed onto an angled crystal and reflected within the crystal until it emerges from the other “end”, where it is collected. Figure 3.11 shows a schematic of the in-situ ATR-FTIR set-up used in this dissertation. In this measurement, carbon dioxide and precursor were pumped using syringe pumps (ISCO 260D). All feed lines have check-valves to prevent backflow and rupture disks (HIP) for safety in case of over pressurization. The reactor is a 100-mL stainless steel stirred autoclave (Parr Instruments) with a turbine impeller to provide mixing of ingredients. The reactor is heated by a heating mantle, and has an installed pressure transducer (Ashcroft K25F) and a thermo well containing a thermocouple (Parr-A472E2). The reactor temperature was controlled using a digital controller (Parr 4842). In the ReactIR-4000 main box, there are instrument computer boards, a laser power supply, an IR source, and a detector. A mirrored optical conduit with 25 mm interior diameter is

used to transmit the light between the IR source/detector and the diamond probe, which is located at the bottom of the reactor.

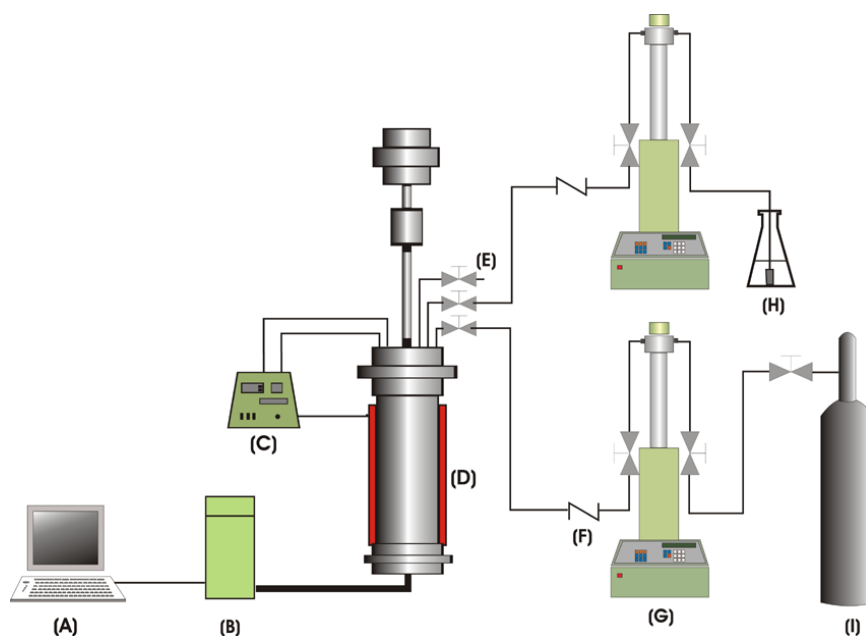


Figure 3.11: Schematic of the reactor with the ATR-FTIR (A) computer; (B) FTIR; (C) temperature and RPM controller with pressure display; (D) 100 ml autoclave equipped with diamond IR probe; (E) needle valves; (F) check valves; (G) syringe pump; (H) container for carboxylic acid; (I) CO₂ cylinder.¹²³

3.2.9. Temperature Programmed Desorption (TPD)

TPD characterizations are most commonly used to determine the number, type and strength of active sites available on the surface of a solid material from measurements of the amount of gas desorbed at various temperatures. In this study, this technique was used to determine surface acidity from desorption of NH₃. The sample was degassed under argon flow. During TPD, the sample was saturated with NH₃ at 40 °C constant temperature by flowing NH₃ gas. Physically adsorbed NH₃ was removed by flowing argon gas at a rate of 50 mL/min for one hour. The temperature of the sample

was increased from ambient to 750°C at a linear heating rate of 10°C/min under an argon gas flow. A TCD detector analyzed the gas leaving the sample and chromatograms were collected for pre-specified heating rates for each sample. After each experiment, the sample was purged with argon flow at 300 °C for 1 h.

3.2.10. Evaluation Procedure

Dyes are widely used in industry; therefore the elimination of these compounds is becoming an increasingly important environmental problem. Methylene blue (MB, 0.05 wt % water solution, Sigma-Aldrich), was chosen as the model organic compound to evaluate the photoactivity of the prepared TiO₂ based nanomaterials. The catalytic performance was evaluated under UV light irradiation using a 100 W high-pressure mercury lamp (UVP, USA). The wavelength range and peak wavelength of the UV lamp were 320–400 nm and 365 nm, respectively. Typically, a mixture of methylene blue solution (15 µmol/L 100 mL) and 25 mg of catalyst was vigorously stirred for 30 min to establish an adsorption/ desorption equilibrium. Then the reaction solution was stirred under light irradiation. The temperature of the photocatalytic reaction was measured by thermometer and found not to change significantly from room temperature. At given time intervals, 3 mL aliquots were sampled and centrifuged to remove the particles. The filtrates were analyzed by measuring the absorption band maximum (665 nm) using a Cary 50 UV-vis spectrophotometer. The methylene blue concentration was calculated by using a calibration curve (Appendix 8) according to the absorbance intensity at 665 nm in the photocatalytic process. The blank reaction was carried out following the same procedure without adding catalyst. Repeat tests were run to ensure data reliability.

The Langmuir-Hinshelwood kinetic model is widely used to describe the kinetics of photodegradation of many organic compounds, and is described as:

$$r = -\frac{dc}{dt} = \frac{kKc}{1 + Kc} \quad 3.11$$

where r is the rate of reaction (mol/L.min), c is the equilibrium concentration of reagent (mol/ L), t is the time (min), k is the rate constant (1/min), and K is the Langmuir constant (L/mol). This equation is simplified to a pseudo-first-order expression, when the concentration of reagent being reacted is low, as

$$r = -\frac{dc}{dt} = kc \quad 3.12$$

Equation (3.12) can be integrated, resulting in

$$\ln \frac{c_0}{c} = kt \quad 3.13$$

where c is the dye concentration at instant t (mol/L), c_0 is the dye concentration at $t = 0$ (mol/L), k is the pseudo-first-order rate constant (1/min), and t is the irradiation time (min).

CHAPTER 4

EFFECTS OF Zr DOPING IN TiO₂ NANOMATERIALS

4. Introduction

Recently, considerable effort has been devoted to synthesizing materials with one dimensional (1D) nanostructures due to their unique properties and potential applications in a diversity of areas including catalysis, high efficiency solar cells, coatings, and sensors.¹⁶⁷ Particularly, TiO₂ nanotubes are receiving considerable attention due to titania's high activity, strong oxidation capability, and chemical stability. As was previously discussed in chapter 2, various methods have been used to prepare TiO₂ nanotubes including anodization,¹⁶⁸ template techniques,^{169, 170} hydrothermal processes,^{171, 172} and soft chemical processes.³² Moreover, as was discussed in the literature review section (chapter 2), the performance of the titania nanostructures strongly relies on their crystallinity, crystallite size, crystal structure, specific surface area, thermal stability and quantum efficiency.^{17, 50} Small amounts of metal doping, particularly Zr, has been found very effective to enhance the thermal stability and activity of TiO₂ nanomaterials^{24, 53, 82, 83} and TiO₂-ZrO₂ binary metal oxides have received considerable attention as catalysts. However, the performance of these materials significantly varies with the synthesis process, and the subsequent heat treatment.

Conventionally, the sol-gel process or impregnation or coprecipitation methods have been widely used for synthesizing various oxide materials. However, with several advantages over other methods, the sol-gel process has become a standard technique for synthesizing multioxide materials.⁹⁶ The major advantages of the sol-gel technique

include molecular scale mixing, high purity of the precursors, and homogeneity of the sol-gel products with a high purity of physical, morphological, and chemical properties.⁹⁷ However, the properties of the multicomponent sol-gel products depend on the composition, precursors, and operating variables.⁹⁹ The conventional sol-gel process requires an organic solvent. Due to environmental regulations and increased environmental concerns, the use of volatile organic compounds (VOCs) is becoming increasingly restricted. Hence, alternative processes using a green solvent such as supercritical carbon dioxide (scCO₂) is attractive to synthesize TiO₂ nanostructures. Moreover, it is well documented that the operating temperature and pressure controls the physical properties of CO₂ such as density and solubility as well as all the chemical reaction steps.^{98, 149} Furthermore, the alkoxide concentration and the acid to metal alkoxide ratio are very important parameters controlling both the nucleation and growth steps.⁹⁸ Therefore, it is highly desirable to investigate the effects of the operating variables in scCO₂ on the porous structure of the modified nanomaterials to gain a fundamental understanding on how the morphologies and porosity of the nanomaterials are affected, and to find the optimum operating conditions for preparing the desired nanostructure.

Therefore, in this chapter, both TiO₂ and Zr doped TiO₂ metal oxides were synthesized by a direct sol-gel process in scCO₂, and the effects of different operating variables on the binary nanostructure were investigated.

4.1. Experimental

ZrO₂ modified TiO₂ nanostructures were synthesized by a direct sol-gel method in scCO₂ using temperature (40-80°C), pressure (3000-6000psig), concentration (0.35-1.4 mol/L), acid/metal alkoxide ratio (3-7) and Zr composition (0-20%) following the same procedure described in Chapter 3. In a typical experiment, the appropriate amount of precursors and acetic acid were quickly placed in the view cell followed by addition of CO₂ under stirring conditions and heating. After 5 days aging, the nanomaterials were washed with CO₂ at a controlled flow rate. The resulting as-prepared materials were amorphous. To form crystalline phase, the synthesized materials were calcined in air at 500 °C using a heating rate of 10 °C/min, holding time 2 h, and a cooling rate to room temperature 0.5 °C/min. The synthesized as-prepared and calcined materials were characterized using several physiochemical techniques, which were described in chapter 3.

Moreover, the initial gelation kinetics were studied in terms of the gelation time, with the gel point used according to the definition by Loy et al., (i.e. when the entire view cell was filled with gel and the stir bar was not observed).¹⁴⁸ The gel point for every experiment was determined at least twice. In addition, the solubility parameters of CO₂ were calculated for selected temperature and pressure conditions using the density according to Giddings *et al.* with the provided values given in Table 4.1,¹⁷³

$$\delta_{SC} = 1.25\sqrt{P_c} \frac{\rho_{Rsc}}{\rho_{RL}} = 0.384\rho \quad 4.1$$

where, P_c is the critical pressure in atmospheres, $\rho_{R_{sc}}$ is the reduced density of CO₂, $\rho_{RL} = 2.66$ is the reduced density of liquid CO₂ at its normal boiling point, and ρ is the density of CO₂ in mol/L.

Table 4.1: Solubility parameters of scCO₂ under selected temperatures and pressures.

Temperature (°C)	40	60	60	60	80
Pressure (psia)	5000	3000	5000	6000	5000
Density (mol/L)	21.19	18.42	19.54	20.38	17.84
Solubility parameter (cal/cm ³) ^{1/2}	8.13	7.07	7.5	7.82	6.85

4.2. Effects of Pressure

To investigate the effects of pressure, the nanomaterials were synthesized using scCO₂ pressures from 3000-6000 psig, keeping the other parameters constant, with the morphology and size of the as-prepared materials characterized by SEM analysis. From the SEM images given in Fig 4.1, it can be seen that for all pressures, nanotubes with diameter 50-150 nm were formed. The morphology of the nanotubes did not change significantly, although at a low pressure (3000 psig) more agglomerated nanotubes were formed. These results can be explained using the calculated solubility parameter of CO₂ provided in Table 4.1, at 3000 psig was 7.07 (cal/cm³)^{1/2} becoming 7.8 (cal/cm³)^{1/2} at 6000 psig. Comparing the solubility parameter, it is clear that while keeping the temperature constant, changing the pressure did not change the density as well as the solvating power of CO₂ significantly.

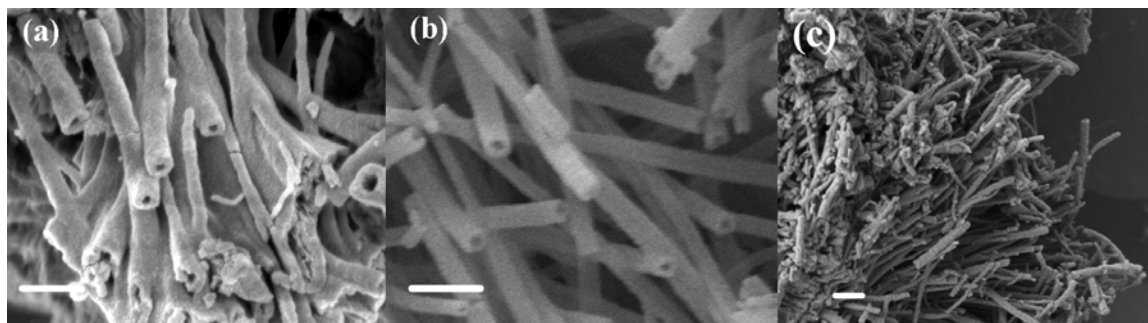


Figure 4.1: SEM images for materials synthesized at (a) 3000 (b) 5000 and (c) 6000 psig pressures. (Bar represents 200 nm).

Table 4.2. Synthesis conditions of Zr-TiO₂ nanostructures in scCO₂ and characterization results.

Pres. (psig)	Temp. (°C)	BET (m ² /g)	Pore Vol. (cm ³ /g)	Pore Dia (nm)	Morphology
3000	60	376	0.28	3.0	Rod/Nanotubes
5000	60	394±10	0.39±0.02	3.9	Nanotubes
6000	60	430	0.34	3.2	Nanotubes
5000	40	350	0.34	3.9	Nanotubes
5000	80	300	0.32	4.3	Rod/Nanotubes

N₂ physisorption analyses were performed to determine the surface area and pore volume and are given in Table 4.2. The BET surface area calculated from the N₂ adsorption reveals that the specific surface area of the synthesized materials increased with increasing pressures. For instance, the BET surface areas increased from 376 to 430 m²/g for increasing pressures from 3000 to 6000 psig. The isotherms provided in Figure 4.2 show that the ZrO₂-TiO₂ nanomaterials exhibit a type IV isotherm with a hysteresis loop. The calculated pore volumes and surface areas given in Table 4.2 show that the pore volume varied with pressure and were *ca.* 0.28, 0.39 and 0.35 cm³/g for the materials synthesized at 3000, 5000 and 6000 psig pressures, respectively. The BJH pore size

distributions of the as-prepared nanomaterials synthesized at 3000-6000 psig provided in Figure 4.3 show quite different pore size distributions. The materials synthesized at 3000 psig shows a multimodal distribution, though most of the pores were smaller than 7 nm. The pore size distribution for the materials synthesized at 5000 and 6000 psig are bimodal. The first peak was at *ca.* 4 nm and the second peak at *ca.* 37 nm. The area of the larger peak increases significantly with pressure indicating more larger pores are present in the higher pressure samples. The calculated average pore diameter ranged from 3.9-3.2 nm for 3000-6000 psig pressures samples, respectively, not varying significantly with pressure.

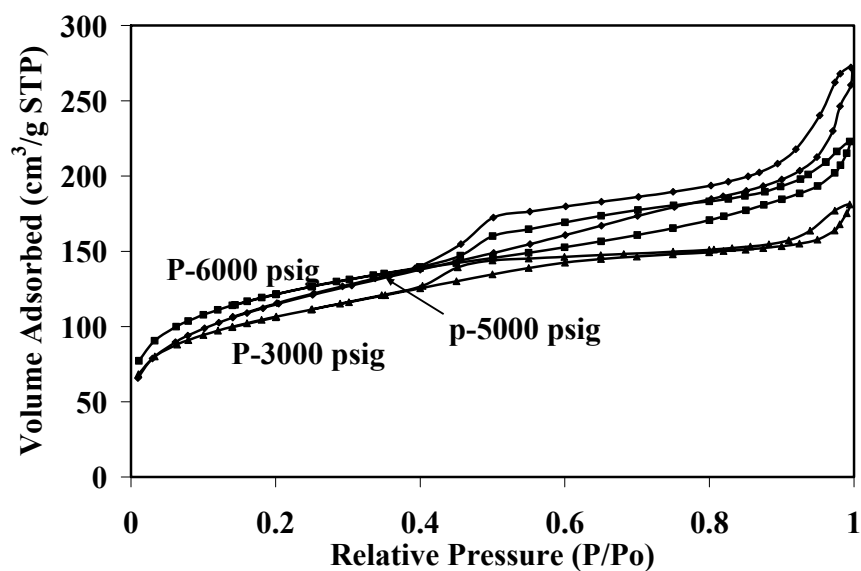


Figure 4.2: N₂ adsorption/desorption isotherms of as-prepared ZrO₂-TiO₂ nanomaterials synthesized at different pressures.

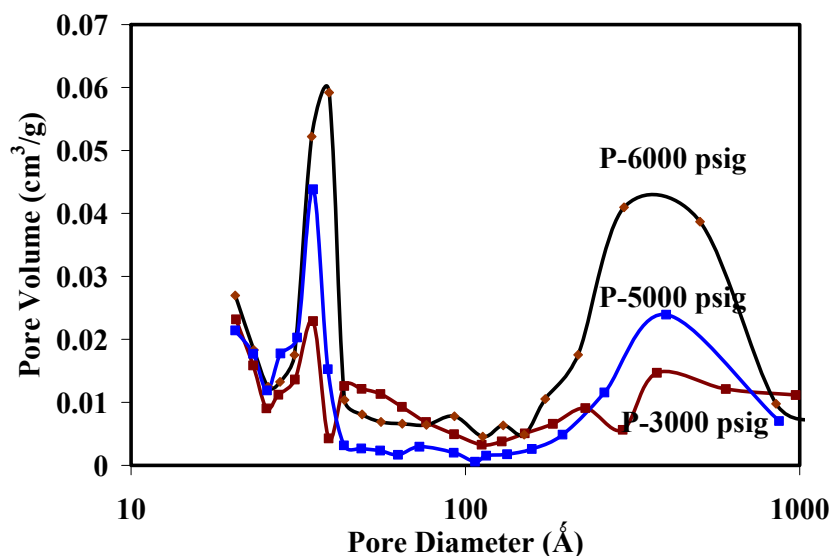


Figure 4.3: BJH pore size distribution of as-prepared $\text{ZrO}_2\text{-TiO}_2$ nanomaterials synthesized at different pressures.

4.3. Effects of Temperature

To investigate the effects of temperature, the materials were synthesized in a temperature range of 40-80 °C at 5000 psig keeping the other parameters constant, with the morphology and size of the as-prepared materials characterized by SEM and TEM analysis. The SEM micrographs (Figures 4.4a and 4.4b) show that the as-prepared aerogel powders were composed of 1D nanostructure. At a close look, these figures also reveal that the 1D nanostructure differs significantly from the nanotubes' morphology and dimension described in the previous section. Figure 4.4(a) clearly demonstrates that the materials synthesized at low temperature were smaller in diameter (10-100 nm), compared to those synthesized at 80 °C, Figure 4.4(b). Moreover, the SEM images also reveal that a significant amount of nanosheet type structure is present in the sample, as shown by the arrow in Figure 4.4(a). It should be mentioned that the examined materials

were taken directly from the reaction after CO₂ washing without any further purification steps.

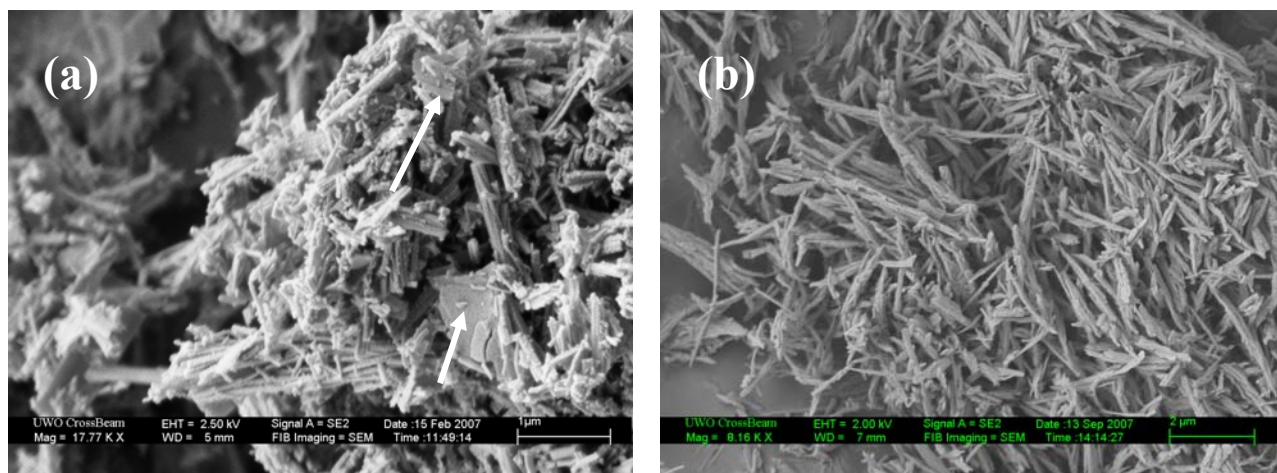


Figure 4.4: SEM images for materials synthesized at: (a) 40 °C and (b) 80 °C temperature. (Arrows indicate sheet type structure in materials synthesized at 40 °C).

It is very difficult to determine from the SEM images whether these nanostructures were nanotubes or nanorods. Therefore, TEM analysis was performed on the calcined nanomaterials, as shown in Figure 4.5a and 4.5b. At 40 °C the materials are tubes whereas at 80 °C nanorod/nanotubes were formed. The TEM images also confirmed that at 40 °C, all sheets cannot convert into nanotubes: hence a large amount of sheet structure (Figure 4.5c) is formed. The nanomaterials synthesized at higher temperature 80 °C are all nanorod/tubes (Figure 4.5d) with similar results being observed at 60 °C.

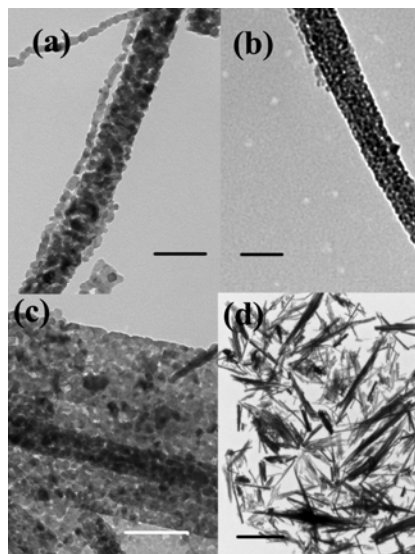


Figure 4.5: Effects of temperature on the morphology of $\text{ZrO}_2\text{-TiO}_2$ nanomaterials, TEM images of calcined materials (a) & (c) synthesized at 40°C , and (b) & (d) synthesized at 80°C temperature. (Bar represents 100 nm).

To measure the surface area and pore volume, N_2 physisorption analysis was performed, with the isotherms provided in Figure 4.6. The results show that all the $\text{ZrO}_2\text{-TiO}_2$ nanomaterials exhibited a type IV isotherm with a hysteresis loop, indicating the presence of mesopores.¹⁶⁰ Typically, slit-shaped pores or plate-like particles have provided this type of shape, as previously described in section 3.2.6.¹⁶⁰ Although gas adsorption techniques and the data analysis methods appear to be well established, it is still difficult to evaluate the pore structures accurately, due to the surface and structural heterogeneity of the solid materials.¹⁶³ At 60°C , the hysteresis loop is positioned at the top, giving a higher surface area whereas low (40°C) and high (80°C) temperatures have lower values.

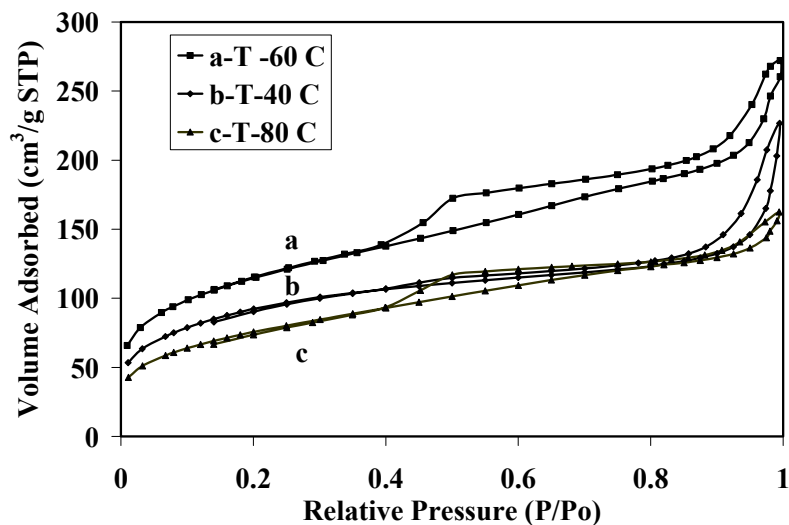


Figure 4.6: N₂ adsorption/desorption isotherms of the ZrO₂-TiO₂ as-prepared nanomaterials synthesized at different temperatures.

The calculated pore volume and surface area are given in Table 4.2 which shows that for materials synthesized at 40 °C, the pore volume was 0.34 cm³/g and a maximum pore volume 0.39 cm³/g was reached for 60 °C and became 0.32 cm³/g for materials synthesized at 80°C. The BJH pore size distributions of the as-prepared nanomaterials synthesized at different temperatures are shown in Figure 4.7. The pore size distributions are rather different for the shown samples, although all are bimodal. The average pore diameter for the first peak in the pore size distribution was *ca.* 4 nm for all systems. However, the second peak at *ca.* 37 nm, which according to the IUPAC definition, still is in the mesoporous range. The mesopore volume was highest (0.33 cm³/g) for the materials synthesized at 40°C, whereas the other two samples possessed the same value of 0.31cm³/g. However, the materials synthesized at 60°C showed a good balance between small pores (4 nm) and larger pores (37 nm). The BET surface area calculated

from the N_2 adsorption reveals that the specific surface area of the synthesized materials varied significantly with the synthesis temperature, such as $350 \text{ m}^2/\text{g}$ at 40°C which drops to $300 \text{ m}^2/\text{g}$ for the 80°C samples. Previously, it was observed that 10 % ZrO_2 modified TiO_2 nanotubes possess *ca* $400 \text{ m}^2/\text{g}$ surface area at 60°C . The significant reduction in surface area is attributed to the morphological change.

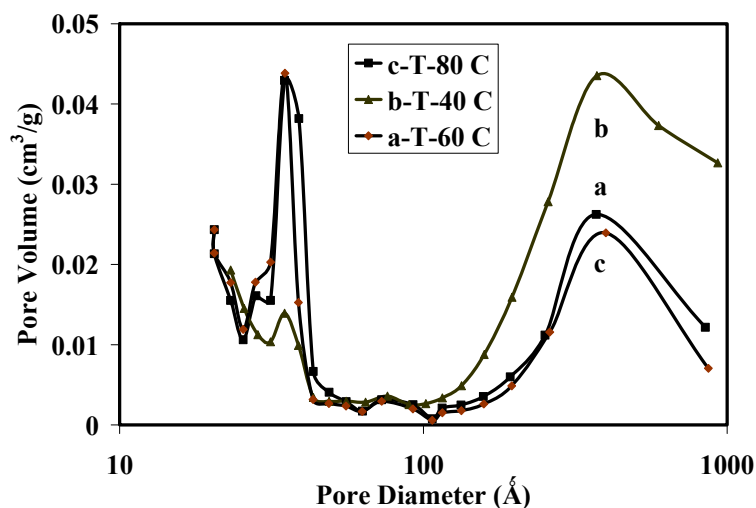


Figure 4.7: BJH pore size distribution of the ZrO_2 - TiO_2 as-prepared nanomaterials synthesized at different temperatures.

In order to investigate the temperature effects on the initial gelation rate, the gelation time was recorded for 40 - 80°C keeping the other variables constant. Since the hydrolysis and condensation reactions of the sol-gel process in $scCO_2$ are thermally accelerated as the temperature increases, the gelation time was studied as seen in Figure 4.8.⁹⁹ The gelation time for 40°C was more than 3 hours, with this value decreasing upon increasing temperature. When the process temperature increased to 50°C , the gelation time was reduced significantly to 70 min. However, a further increase in temperature

reduced the gelation time very slowly, becoming *ca.* 30 min for 80 °C. The temperature dependence of gelation can be represented by an Arrhenius equation:

$$\ln(t_{gel}) = \frac{E}{RT} + A \quad 4.2$$

where A is a constant, R is the universal gas constant, and T is temperature. The activation energy, E, depends on the reaction environment, catalyst and alkoxy group.¹⁷⁴ For the gels obtained in this work, E was calculated to be 44 kJ/mole. It is not possible to associate this activation energy with any specific reaction step, because this process includes hydrolysis, condensation, nucleation and growth steps as the products form gel. In comparison, Birnie et al. calculated an activation energy for titanium isopropoxide modified with acetic acid in propanol and the value was 67.6 kJ/mole.¹⁷⁵ It is well known that zirconium is more active compared to titanium.¹⁷⁶ Hence, upon introducing 10 % zirconium propoxide into the reaction system, the activation energy for zirconium–titanium binary system is reduced, likely due to the higher activity of Zr and faster reaction rates in CO₂.

The direct sol-gel technique consists of esterification, hydrolysis and condensation of titanium and zirconium alkoxides in the presence of acetic acid in scCO₂. The effects of operational variables such as temperature not only change the reaction rate, but also change the solubility parameter of the system. The solubility is known to have significant effects on the morphology of the gel products.⁹⁹ The nucleation and growth processes are two important parameters controlling the nanomaterials evolution, which strongly depends on the solubility of the solvent which controls the saturation.¹⁵⁸ For example, large hexagonal prismatic crystals of Ca(OH)₂ were formed at high saturation in

low temperatures, whereas fine plate like crystals were obtained with low saturation at high temperatures.¹⁵⁸

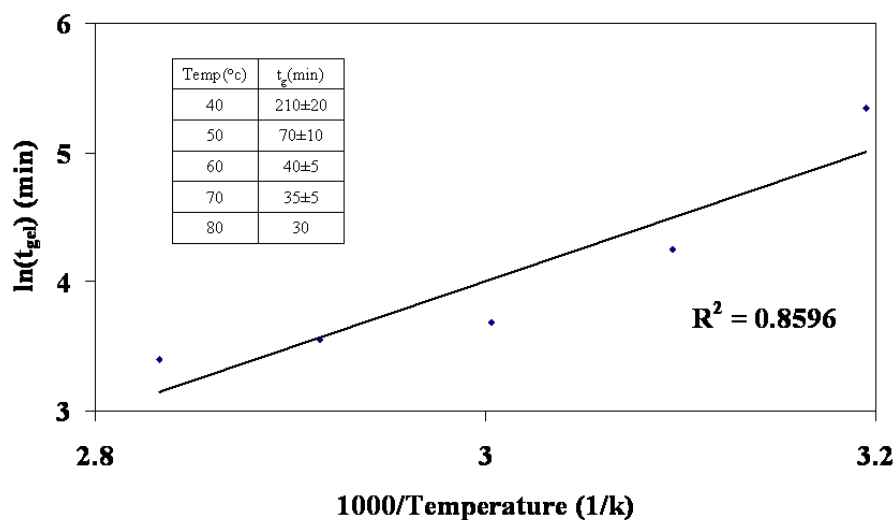


Figure 4.8: The gelation time as a function of reciprocal of absolute process temperature.

According to Table 4.1, the solubility parameter of CO₂ is 8.12 (cal/cm³)^{1/2} at 40 °C with this value changing significantly with operating temperature, becoming 7.5 (cal/cm³)^{1/2} and 6.84 at 60 °C and 80 °C, respectively. Temperature shows two opposing effects: on the one hand it increases the reaction rate, while on the other hand it reduces the solubility parameter. Both effects have a very significant influence on the final sol-gel product, likely influencing the morphological change of nanotubes synthesized in scCO₂ at different temperatures. Hence, for desired nanostructure evolution, there will be an optimum temperature which maintains the reaction rate with the required solubility of the system.

4.4. Effects of Concentration

To investigate the effects of alkoxide concentration, the materials were synthesized using a concentration range 0.35-1.4 mol/L, while keeping the other variables unchanged. The morphology and size of the as-prepared materials were characterized by SEM and TEM analysis. The initial gel time and other characteristics are reported in Table 4.3. The SEM micrographs are given in Figure 4.9 and show that concentration had a significant influence on the morphology of the synthesized nanomaterials. The SEM images suggest that the as-prepared aerogel powders are composed of mixed structure for very low (0.35 mol/L) and very high (1.4 mol/L) concentration. Nanosheets and nanotubes were only formed in the middle concentration region. For low concentrations, sheet, rod and cubic structured material with different dimensions were observed. Nanosheet type structures with 150-375 nm width were observed for 0.7 mol/L concentration of alkoxides, whereas 50-135 nm dia nanotubes were formed at 1.14 mol/L concentrated solutions. With a further increase in concentration to 1.4 mol/L, the morphology changed to a mixed sheet and rod- type structure being formed. This result can be explained by the effects of concentration on supersaturation. According to Yasue et al., smaller crystals are formed at a higher initial degree of supersaturation, while larger crystals are obtained with lower supersaturation.¹⁷⁷ Kim et al. also proposed that the initial concentration was a very important factor to obtain monodispersed titania.¹⁷⁸ The growth and nucleation rate is a function of the solute concentration.⁹⁸ The hydrolysis and condensation products of the precursors are considered as solute, and this concentration will increase with the initial precursor's concentration. It is known that for solutions having a higher initial concentration, gelation is faster.¹⁷⁹ The increase in initial

concentration of the metal alkoxide decreased the gelation time, as observed in this study (Table 4.3), also supporting this theory. In this case, simply the solution is more concentrated, so more monomers can participate in the condensation reaction.¹³¹

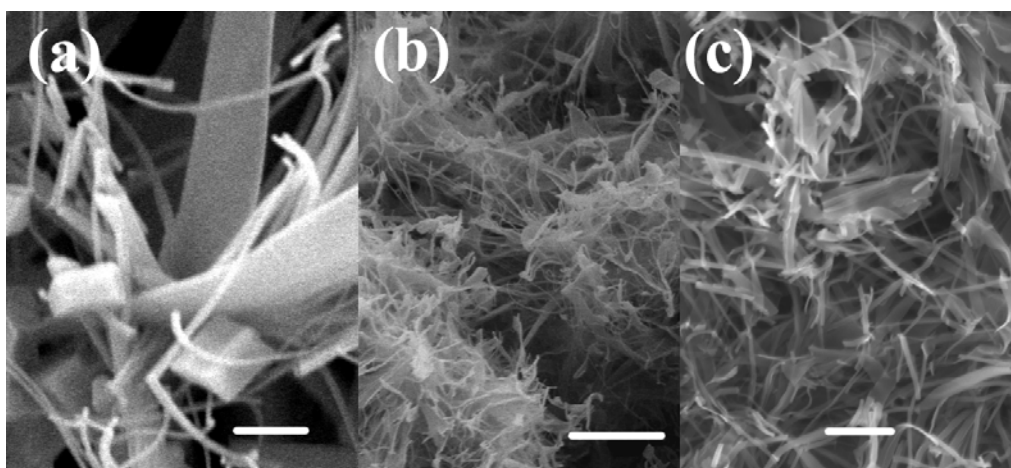


Figure 4.9: Effects of concentration on the morphology of ZrO_2-TiO_2 nanomaterials synthesized using (a) C-0.35 mol/L, (b) C-0.7 mol/L and (c) C-1.4 mol/L. (Bar represents $1\mu m$).

Table 4.3: Surface area, pore volume and average pore diameter of as-prepared nanomaterials synthesized at various concentrations.

Sam ples	Con (mol/L)	Gel time(t_g) Min	Surfac e Area (m^2/g)	Meso Pore Volume (cm^3/g)	Micro Pore Vol (cm^3/g)	Pore Diameter (nm)	Nanostructure
C-1	0.35	180	237	0.57	0.028	10.2	Mixed structure
C-2	0.7	110	377	0.29	0.059	3.7	Sheets
C-3	1.17	40	394	0.34	0.056	3.9	Tubes
C-4	1.4	50	355	0.29	0.046	3.9	Sheet/Rod

N_2 adsorption/desorption isotherms are shown in Figure 4.10. The results show that all the ZrO_2-TiO_2 nanomaterials exhibit isotherms with H3 hysteresis loops,

indicating the presence of mesopores.¹⁶⁰ However, the shape of the isotherms are different from the nanotubes isotherms, as the adsorption branches are very flat compared to the type IV isotherms. The type III isotherms exhibit a plateau in the volume adsorbed at intermediate pressures whereas the type IV isotherm shows a monotonic increase in

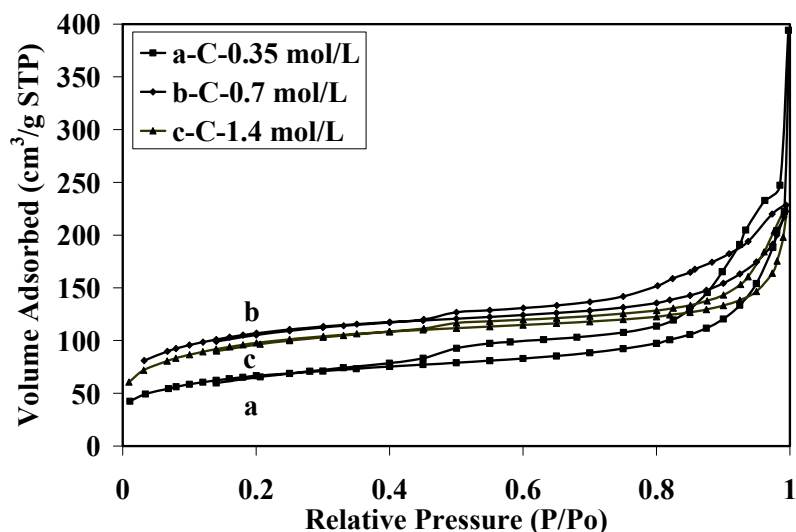


Figure 4.10: N₂ adsorption/desorption isotherms of the ZrO₂-TiO₂ as-prepared nanomaterials synthesized using different alkoxide concentrations.

adsorption with increasing relative pressure. The materials with type III isotherms having hysteresis loops represent mesoporous structure. The micropore volume was calculated from the t-plot (Table 4.3) showing that all nanomaterials, regardless of concentration, have micropores. The micropore volume is 0.028 cm³/g for 0.35 mol/L whereas *ca.* 0.056 cm³/g for materials synthesized using the intermediate concentration. This micropore volume reduced with a further increasing in concentration. Considering the mesopores, the low concentration samples possessed the highest i.e. 0.57 cm³/g among all samples. The mesopore volume reduced with increasing concentration, becoming *ca.* 0.3 cm³/g for the rest of the samples.

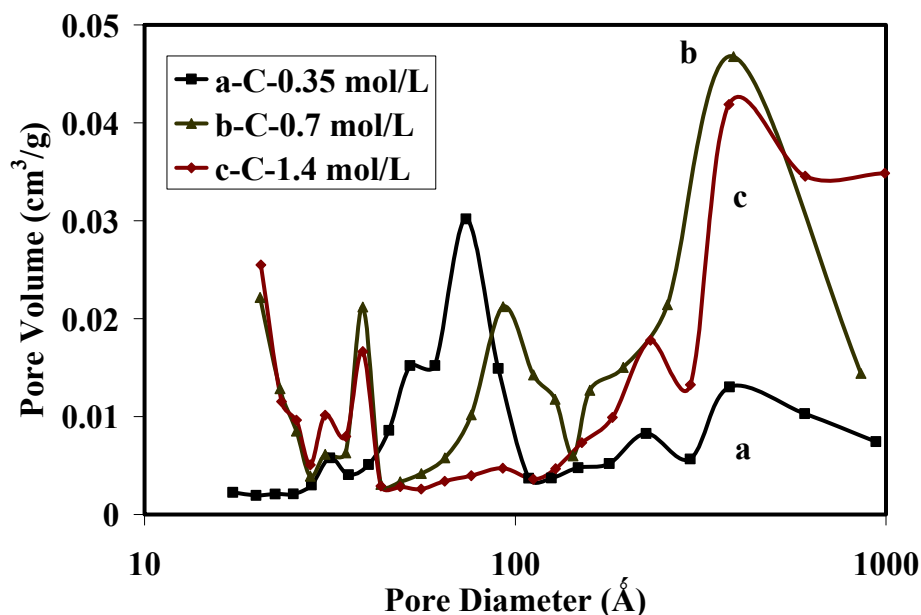


Figure 4.11: BJH pore size distribution of as-prepared $\text{ZrO}_2\text{-TiO}_2$ nanomaterials synthesized using different precursor concentrations.

The BJH pore size distributions of the as-prepared nanomaterials synthesized using different concentrations are shown in Figure 4.11. The pore size distribution significantly varies with concentration, and they are multimodal instead of bimodal which was previously observed with the $\text{TiO}_2/\text{ZrO}_2$ nanotubes. The calculated average pore diameter was *ca.* 4 nm for all systems except C-1, whose pore diameter is 10 nm since this sample had a higher pore volume and a lower surface area. The BET surface area calculated from the N_2 adsorption revealed that the specific surface area of the synthesized materials increased with concentration up to 1.17 mol/L. Further increasing in concentration slightly reduced the surface area. It is important to note that the gelation time also increased for this sample, although it is difficult to explain the origin of this result. Further detailed kinetic studies are required.

4.5. Effects of Acid to Metal Alkoxide Ratio

In order to investigate the effects of the acid to metal alkoxide ratio (R) on the morphology, surface area and pore volume, the 10 % ZrO₂ modified TiO₂ nanotubes using R values ranging from 3-7 were synthesized in scCO₂. The initial gel time and other characteristics are presented in Table 4.4. SEM images of the nanomaterials with R (3, 4 and 6) are shown in Figure 4.12. At R =3, a pillar type structure with 2 μm widths and several μm length were formed, and no nanostructure was observed. This might be attributed to the lack of gel formation. When the R value was increased to 4; gel was

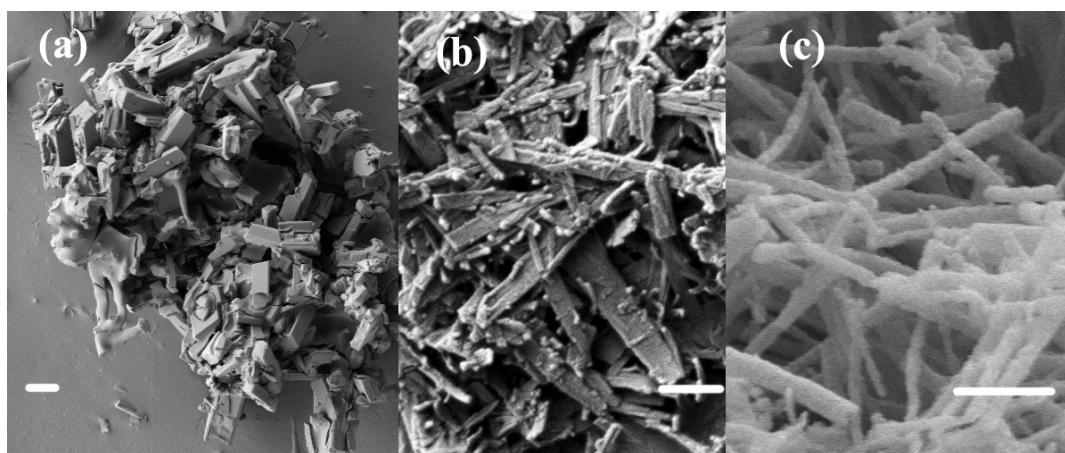


Figure 4.12: Effects of acid to metal alkoxide ratio on the morphology of ZrO₂-TiO₂ nanomaterials synthesized using (a) R-3, (b) R-4 and (c) R-6. (Bar represent 500 nm).

formed and a thick sheet type structure with ca 200 nm widths and 1-2 μm lengths were observed (Figure 4.12b). As previously observed at R= 5 and 6, nanotubes with 50-135 nm dia and 40- 100 nm dia were formed, respectively. Further increasing of R to 7 led to precipitation, showing that the nanotubes were only formed at R 5-6. Investigations of silicon alkoxide showed that variations of the hydrolysis ratio (H₂O/metal alkoxide)

caused a modification in the structure and in the properties of the polysilicated products, which strongly supports our observations.⁹⁹

To examine the surface area and pore volume, N₂ physisorption analysis was performed (Figure 4.13). The isotherm for R4 is type III, whereas type IV was obtained for R6. The calculated total pore volume (Table 4.4) increased with increasing R value. However, the micropore calculated from the t-plot indicates that there is no specific trend. The micropore volume was very low for R4 (0.004 cm³/g) and 0.025 cm³/g for R6.

Table 4.4: Surface area, pore volume and average pore diameter of as-prepared nanomaterials synthesized with different acid to metal alkoxide ratios.

Acid/ Metal alkoxide Ratio	Gelation time(tg) Min	Surface Area (m ² /g)	Meso. Pore Volume (cm ³ /g)	Mic. Pore Volume (cm ³ /g)	Pore Diameter (nm)	Nanostructure
R-3	No gel	n.d	n.d.	n.d	n.d.	No structure
R-4	80±10	335	0.31	0.014	4.2	Sheet
R-5	40±5	394	0.34	0.056	3.8	Tubes
R-6	35±5	410	0.37	0.025	3.9	Tubes
R-7	precipitate	-----	-----		-----	-----

The BJH pore size distributions of the as-prepared nanomaterials using R4 and R6 are shown in Figure 4.14. The pore size distributions are similar and both are bimodal; the first peak at *ca.* 4 nm and the second peak at *ca.* 37 nm. The average pore diameter was *ca.* 4 nm for all systems. The BET surface area calculated from N₂ adsorption showed that the specific surface area of the synthesized materials varied significantly with metal alkoxide ratio at R4, while the surface areas were similar for R5 and R6. This observation also supports the morphological effects on surface area.

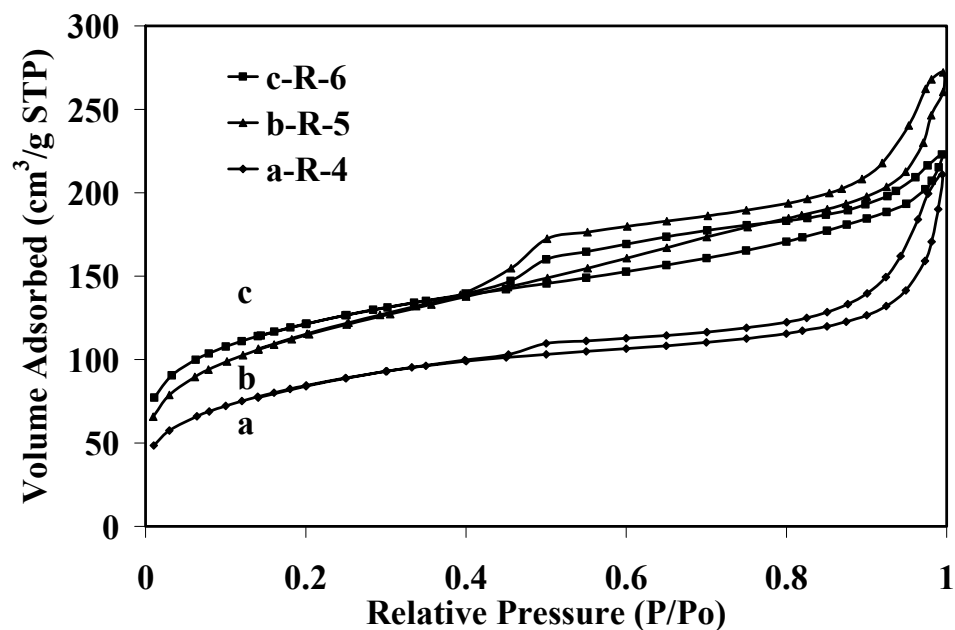


Figure 4.13: N_2 adsorption/desorption isotherms of as-prepared ZrO_2 - TiO_2 nanomaterials synthesized using different acid to metal alkoxide ratios.

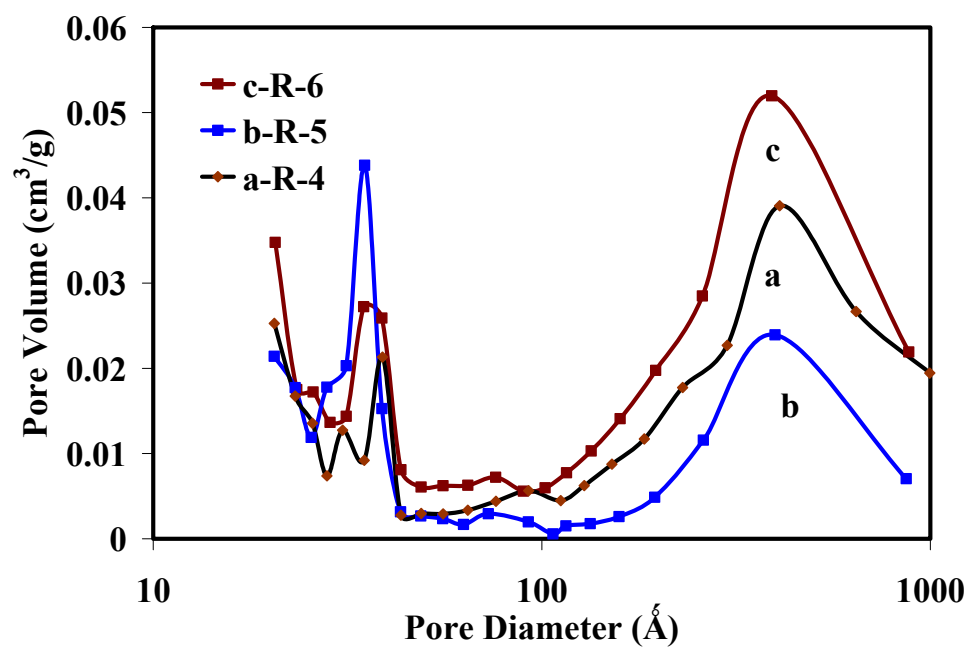
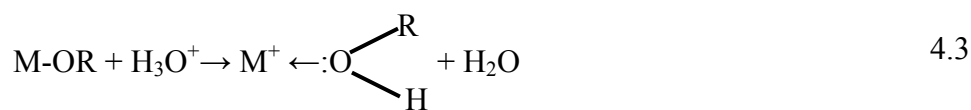


Figure 4.14: BJH pore size distribution of as-prepared ZrO_2 - TiO_2 nanomaterials synthesized using different acid to metal alkoxide ratios.

The acid to metal alkoxide ratio had a large effect on the morphology as well as on the surface properties. The origin of this effect is difficult to explain by only analyzing the morphology, because the nanostructure evolution is a very complex phenomenon, especially for a process using acetic acid. According to Doeuff et al., carboxylic acid not only acts as an acid catalyst, but also as a ligand and changes the alkoxide precursor at a molecular level by forming bridging or chelating complexes, therefore modifying the whole hydrolysis condensation process of titanium alkoxide in the presence of acetic acid.¹⁷⁹ In addition, as a catalyst and chelating agent, the acetic acid participated as a reactant in the binary system of the present study, which makes it more complicated to analyze its effect. There is a general agreement that 2 alkoxy groups bonded to metal can be replaced by acetate groups in solution relatively easily.¹⁸⁰ Hydrolysis of this new molecular precursor removes first the (OR) groups and then the bridging acetates. All bridging acetate groups will not hydrolyze even with excess water, and can only be removed by heat treatment.¹⁷⁹ The second important step is the esterification reaction, which results in the formation of water. Free acetic acid participates in the esterification reaction, with replaced alcohol since scCO_2 was used as the working solvent. Therefore, by changing R, the hydrolysis ratio is changed. According to Bradley et al., the hydrolysis ratio alters the structure forming different complexes, and the observed morphological change with R may be attributed to forming different complexes.¹⁸¹ Moreover, the acid catalyst influences both the hydrolysis and condensation rates, and the structure of the condensed product. The acid serves to protonate the negatively charged alkoxide group, enhancing the reaction kinetics by producing easily removable leaving groups,⁹⁹ which can be described by the following:



The relative rate of the hydrolysis and condensation steps alter the morphology and the other properties of the sol-gel products.¹⁸²

Therefore, here we explain the overall effects of acid to metal alkoxide ratio on the nanostructure evolution. When R was 3, the system started gelation by changing color at about 180 min. However, after five days it did not form any gel; hence no nanostructure was observed, which may be attributed to a lack of reactant(s). When the ratio was increased to 4, the gelation time was reduced to 80 min. With the acetic acid ratio increased beyond 4, the reaction proceeded much faster i.e. the gelation time for R5 and R6 was *ca.* 35 min. A further increase of R was found to result in quick precipitation. Birnie also observed similar effects for their titanium-acetic acid system.¹⁷⁵ Moreover, the technical literature showed that a large hydrolysis ratio produced Ti, Zr and Ta particles which also supports this observation.⁹⁹

4.6. Effects of Zr compositions

In order to investigate the effects of % Zr composition on the binary nanostructure, 0-20 % ZrO₂ modified TiO₂ nanomaterials were synthesized in scCO₂ at 5000 psig and 60 °C. As well, a 10 % Zr modified binary single crystal was also prepared following a similar procedure using 6.6 mmol TIP, 0.73 mmol ZPO and 9.8 mmol acetic acid (R-1.33) with characterization results presented in this section.

Table 4.5: Results of Zr-Ti binary metal oxide nanostructures in scCO₂

Sample Number	Nominal Zr mole %	Product mole % ^a	Zr Crys. (nm)	Latt. para (Å)		Cell V (Å) ³	Morphology
				a	c		
Zr-TiO ₂ -0	0	0	14.0	3.787	9.514	136.51	Fibers
Zr-TiO ₂ -4%	0.0425	0.04	13.7	3.787	9.531	136.74	Tubes /sheets
Zr-TiO ₂ -6%	0.063	0.0625	12.6	3.787	9.541	136.98	Tubes/sheets
Zr-TiO ₂ -8%	0.087	0.084±0.02	12.5	3.788	9.571	137.35	Tubes /sheets
Zr-TiO ₂ -10%	0.11	0.1066±0.1	12.2	3.798	9.6	138.47	Tubes/sheet
Zr-TiO ₂ -20%	0.25	0.19±0.1	-----	----	---	----	Tubes

Note-Experimental condition- Pressure-5000 psig, Temperature-60°C, Concentration-0.7 and 1.17 mol/L, Acid to metal Alkoxide Ratio-5. a-Product composition was measured by EDX

4.6.1. Morphology

The effects of Zr composition on the microstructures and morphology of the ZrO₂-TiO₂ nanomaterials were characterized by SEM and TEM analysis. Examining the SEM micrographs in Figure 4.15, it can be seen that the as-prepared aerogel powders were composed of one dimensional nanostructure, though the morphology of the individual nanostructure varies with the amount of Zr present in the samples. From Figure 4.15(a), it can be seen that pure TiO₂ formed nanofibrous structures having diameters 20-50 nm with lengths of up to several microns. These results are consistent with Sui et al.¹⁴⁹ who reported that 10-40 nm TiO₂ nanofibers were produced using TIP in scCO₂ following a similar procedure. It is seen from the SEM images that nanotubes with 40-150 nm in dia. were formed from the ZrO₂-TiO₂ binary samples. The dimensions of the nanotubes changed significantly with %Zr composition, which might be attributed to the formation of different Zr-Ti hexamer building blocks. The binary metal hexamer structure strongly depends on the ratio of the metal alkoxide used for the synthesis process.¹⁸³ The SEM images (Figure 4.15c and 4.15d), show that nanotubes with 8% Zr

composition were narrower (40-100 nm) compared to the 10% Zr containing tubes, with the diameter of the nanotubes becoming larger with increasing %Zr composition. The 10% Zr formed nanotubes with a diameter of 50–140 nm and a length of 1-4 μm .

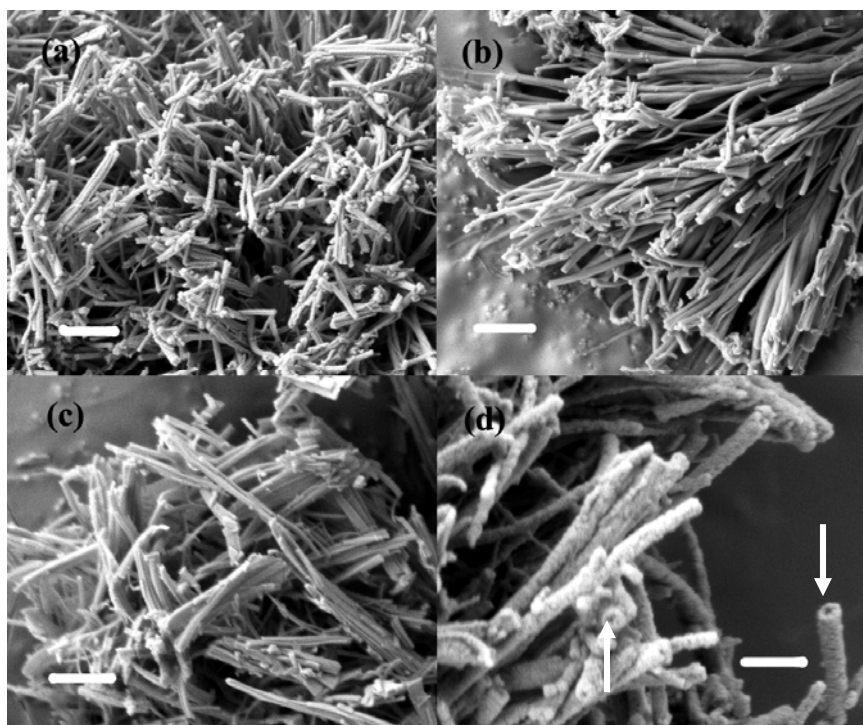


Figure 4.15: Zr-Ti binary calcined nanomaterials with different zirconium compositions (a) undoped TiO_2 , (b) 4%, (c) 8%, and (d) 10%. (Bar represents 200 nm. All the samples were examined after platinum coating. Arrows indicate tubes).

In order to obtain more detailed structural information, TEM analysis was performed for the low 4 % Zr samples and given in Figure 4.16. The TEM image shows *ca.* 100 nm in diameter nanostructures. However, it is difficult to determine whether these nanostructures are tubes or fibers at low %Zr composition. Therefore, a different approach was taken to confirm that even at very low Zr composition (4%), that binary nanostructures were being formed. It was previously discussed that $\text{ZrO}_2\text{-TiO}_2$ nanotubes

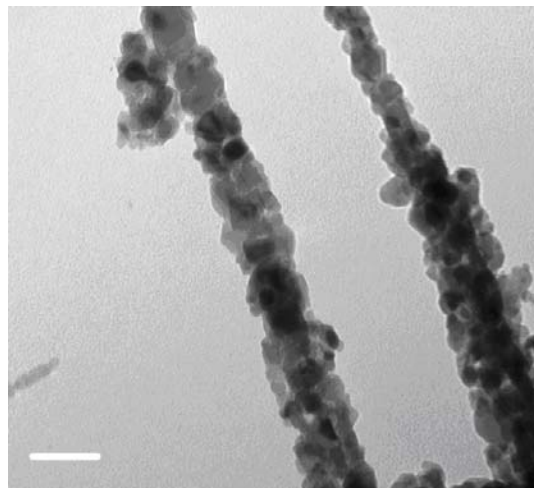


Figure 4.16. TEM image of 4% Zr-Ti binary TiO_2 nanomaterials. (Bar represents 100 nm).

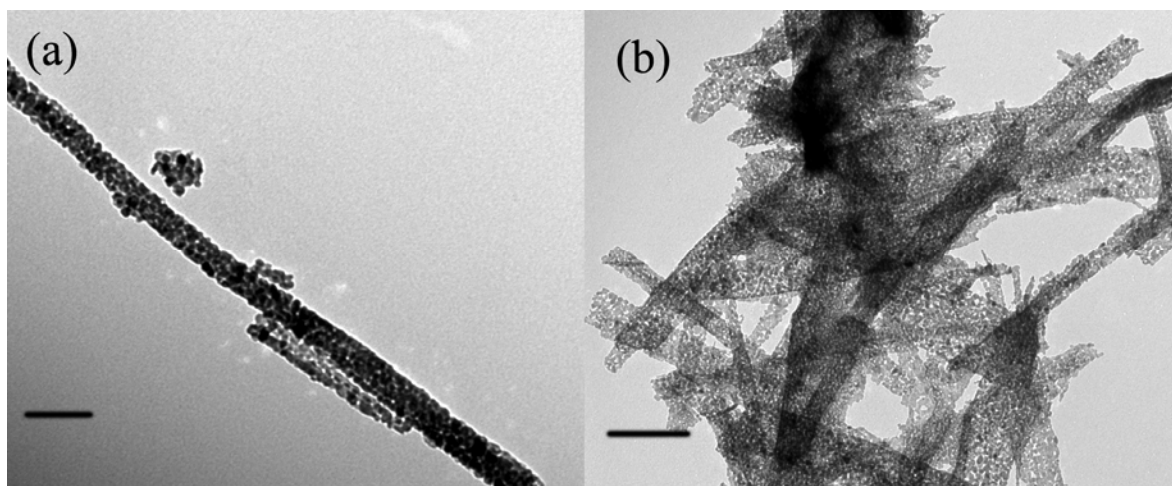


Figure 4.17: TEM: Zr-Ti binary nanomaterials with different zirconium composition (a) undoped TiO_2 , (b) 4% Zr doped TiO_2 . (Bar represents 100 nm).

were formed at higher alkoxide concentration (1.17 mol/L) whereas at low concentration (0.7 mol/L) ribbon or sheet type structures were formed. Keeping this in mind, binary nanostructure at low Zr % compositions (0-8%) were synthesized using a low precursor concentration (0.7 mol/L) with the materials analyzed by TEM. The TEM images, as

displayed in Figure 4.17, show that TiO_2 formed nanofibers (Figure 4.17a) while sheet type nanostructures with 50-100 nm width were formed at 4% Zr containing binary metal oxide (Figure 4.17b). This analysis indicates that even at very low composition (4 % Zr), the Zr alters the synthesized nanostructure morphology.

4.6.2. Composition

The powder ATR-FTIR spectra of the a) as-prepared TiO_2 b) typical ZrO_2 - TiO_2 binary metal oxide and c) crystal samples are given in Figure 4.18. The spectra for both (a & b) samples are rather similar, indicating the single and binary metal oxides are similar in IR observable functional groups. Considering the peak at 3400 cm^{-1} , which is assigned to the -OH group of absorbed water,¹⁸⁴ the binary sample peak is broad and intense compared to the pure TiO_2 sample. This indicates that more -OH groups are likely present in the binary sample. The peak at around 1550 and 1445 cm^{-1} for the pure and doped samples is due to symmetric and asymmetric stretching of the zirconium titanium acetate complex, respectively.¹⁵² The frequency difference (Δ) is *ca.* 100 cm^{-1} confirming that acetic acid formed bridging complexes with the metal ions. However, the peak position is not the same for both samples. For undoped TiO_2 , the peaks are at 1550 and 1446 cm^{-1} , which shifts slightly for the binary samples to 1546 and 1450 cm^{-1} . Therefore, the frequency difference (Δ) also changed from 106 cm^{-1} for the pure TiO_2 sample to 96 cm^{-1} for the binary sample. There is also a noticeable difference observed in the spectra for the two systems around 1410 cm^{-1} , where a sharp peak present at 1409 cm^{-1} in pure titania, while a shoulder at 1415 cm^{-1} is visible for the binary system. The - CH_3 group contributes to the small peak at 1343 cm^{-1} which is present for both samples. There

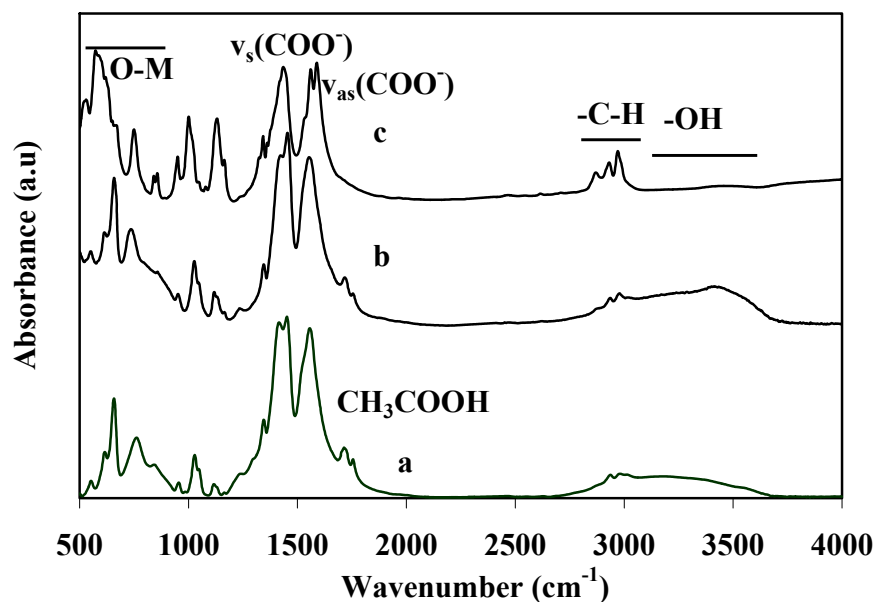


Figure 4.18: Powder ATR-FTIR spectra of as-prepared $\text{ZrO}_2\text{-TiO}_2$ binary nanomaterials (a) pure TiO_2 , (b) 10% ZrO_2 , and (c) Zr-Ti binary single crystal.

are also two small peaks at 1037, and 1024 cm^{-1} corresponding to the ending and bridging -OPr groups, respectively,¹⁵¹ indicating that unhydrolyzed -OPr groups were present in the as-prepared materials. The oxo bonds can be observed by the bands at 657 cm^{-1} .¹⁵² The single crystal spectrum is also presented in Figure 4.18c. This spectrum is very similar to the other two spectra except that there is no peak corresponding to the OH group. It is obvious that the Ti-Zr single crystal is saturated with lots of bridging and ending -OPr groups, and it also contains 10 acetate ligands.¹⁸⁵ It is very important to note that any peak corresponding to CO_2 was not detected indicating no CO_2 was present in the samples. The FTIR analysis confirmed that the as prepared materials contained a significant amount of organic residues as well.

In order to quantify the bulk composition, EDX analysis was performed with the results summarized in Table 4.5. EDX mapping (recorded on a LEO 1530 operated at 20 kV) of the $\text{ZrO}_2\text{-TiO}_2$ samples provided in Figure 4.19 revealed that the zirconium and titanium elements were homogeneously dispersed throughout the samples. The bulk compositions for all samples show good agreement between the targeted and actual values of the metals composition.

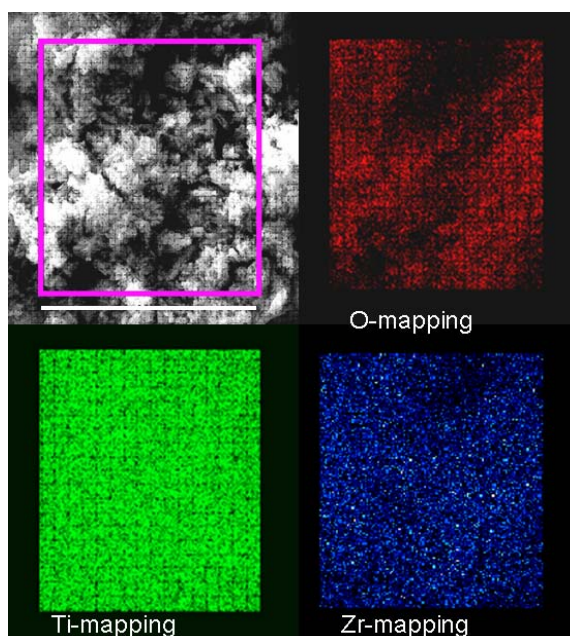


Figure 4.19: A typical Ti, Zr EDX mapping for as-prepared Zr-TiO_2 sample. (*Bar represents 20 μm*).

The XPS spectrum for a typical $\text{ZrO}_2\text{-TiO}_2$ binary nanotubes sample is given in Figure 4.20 indicating that the binary TiO_2 showed peaks at 529.9, 458.6, and 182.4 eV indicating a binding energy of O 1s, Ti $2p_{3/2}$, and Zr $3d_{5/2}$. However, the corresponding binding energies in the binary nanomaterials were highly sensitive to the composition of

the mixed oxide. The reported binding energies were 458.8 eV and 183 eV for pure Ti $2p_{3/2}$ and pure Zr $3d_{5/2}$, respectively.¹⁸⁶ The binding energy for pure TiO_2 in this study was

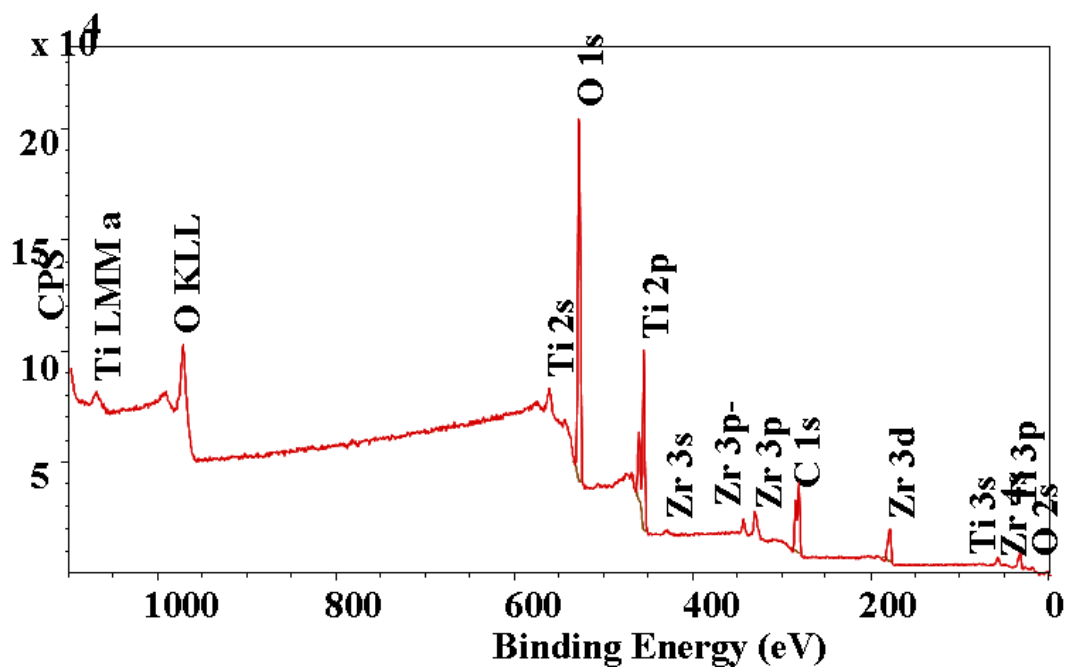


Figure 4.20: XPS spectrum for typical ZrO_2 modified TiO_2 nanotubes.

found to be 458.75 eV and showed good agreement with the previously reported values.¹⁸⁶ However, upon introducing Zr into the TiO_2 matrix, the binding energy for both Ti $2p_{3/2}$, and Zr $3d_{5/2}$ shifted towards lower energy, as shown in Table 4.6. For example, at 10% Zr composition the binding energy of Ti $2p_{3/2}$ and Zr $3d_{5/2}$ were 458.66 and 182.41 eV, respectively. These values became even lower after adding more Zr. This binding energy shift might be attributed to the presence of the second metal atom in the matrix and/or the change in the coordination number of the metal by the formation of a Zr–O–Ti bond. The presence of the second metal will change the electronic environment,

as well as the binding energy of the system. Similar results was observed by Reddy et al.¹⁸⁷ This analysis also indicates that the Zr atom was substituting for some Ti atoms in the TiO₂ lattice. The XPS analysis also revealed that the surface carbon content decreased with increasing amount of Zr % as shown in Table 4.6. Comparison of the EDX and XPS results reveal that the concentration of zirconia is higher on the surface compared to the bulk composition. This surface enrichment phenomenon is normally observed for this binary system, as reported by Galindo et al.¹⁸⁶ This result is attributed to the fact that XPS considers only a few nm from the top of the surface, and zirconium (IV) propoxide is more reactive than titanium (IV) isopropoxide.¹⁷⁶ The pure TiO₂ contained 43.2 at % whereas 38.5 and 35 at % carbon are present in the binary 10 and 20% Zr containing samples.

Table 4.6; Results of XPS analysis for selective Zr-Ti binary metal oxide nanostructures in scCO₂

Sample Number	% carbon	Surface Zr mole %	T _{2p} B.E. (eV)	Zr _{3d} B. E.(eV)	O _{1s} B.E.(eV) and area			
					(eV)	% area	(eV)	% area
Zr-TiO ₂ -0	43.2	0	458.75	-----	531.7	74.9	530.1	25.1
Zr-TiO ₂ -10%	38.6	0.173	458.66	182.41	531.9	65.1	52.9	34.9
Zr-TiO ₂ -20%	35.1	0.33	458.44	182.21	531.4	58.5	52.7	41.5

4.6.3. Thermal Decomposition Behavior

Thermogravimetric (TG) analysis was carried out to study the thermal decomposition behavior of the synthesized binary nanostructure and the TG curves for selective samples are given in Figure 4.21. The curves can be divided into three main regions 20–120°C, 120–500°C and above 500 °C. The first region is attributed to the removal of organic residues and physically adsorbed water present in the synthesized

materials. This part of the organic residue can be removed by drying at low temperature under vacuum. No peak around 1630 cm^{-1} was observed in the powder FTIR indicating no physically adsorbed water was present in the system. A very small *ca.* 3-8% wt was lost in this region, though the value is different for different samples. Only 3% wt was lost for pure TiO_2 while this value increased with increasing Zr composition. 5% wt loss was obtained for 10% and 8% wt loss for the 20 % Zr composition. The second region is attributed to the burnout of any bounded water and chemically bonded organic material. Significant differences were observed in this region among the samples with varying Zr

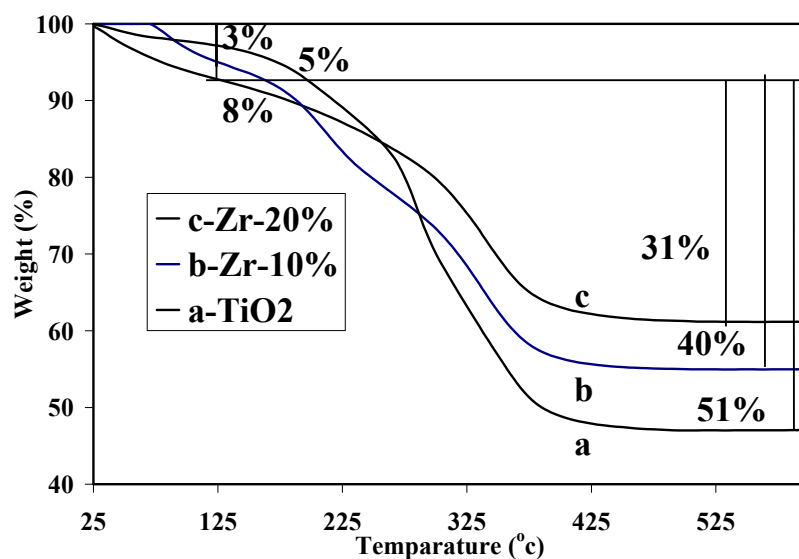


Figure 4.21: Weight loss of Zr-Ti binary metal oxide nanomaterials as a function of temperature.

composition. Around 51 % wt of pure TiO_2 was chemically bonded organic whereas 40 % and 31 % for the 10 % and 20 % Zr containing samples, respectively. This value was consistent with the XPS analysis, where the pure TiO_2 was found to have 43 % carbon

content. The at.% of carbon content decreased with Zr composition such as 38 % carbon present in the 10% samples, whereas only 35 % was present in the 20 % Zr composition. The weight loss over 500°C is extremely small and is attributed to the removal of bounded water. This TG analysis also demonstrated that higher Zr containing samples were more condensed compared to pure TiO₂, resulting in lower wt lost and a lower heat induced effect. In other words, it can be said that the higher %Zr containing samples had lower shrinkage and higher thermal stability.

4.6.4. Phase Structure and Crystallite Size

The effect of the Zr composition on the crystal size and phase structure was investigated by performing XRD analysis. The XRD patterns for all the samples calcined at 500 °C (except 20% Zr sample was amorphous) are given in Figure 4.22, indicating that the ZrO₂-TiO₂ binary nanomaterials consists of anatase crystal. There is no distinct zirconia peak, indicating no phase separation and that the Zr is well integrated into the anatase crystal structure for all investigated compositions. However, pure TiO₂ contains a very small rutile phase (4%) at this temperature. With increasing %Zr composition, the main (101) anatase peak shifts to lower 2-theta values, resulting in an increase in the d-spacing. The sizes of the crystallites, phase and lattice parameters were determined from the XRD peak boarding and are given in Table 4.5. The crystallite sizes decrease with increasing Zr composition, i.e. for pure TiO₂ crystallites were 14 nm whereas 10% Zr content crystallites were 12.2 nm. The Zr ion can either go into interstitial positions or substitute for Ti₄⁺ at lattice points.¹⁸⁸ Any substitution or insertion of a Zirconium ion for a titanium ion in the TiO₂ lattice would introduce a distortion, and change the cell

parameters. The TiO_2 anatase unit crystal is tetragonal, with lattice parameters ‘a’ and ‘c’. Therefore, the lattice parameters a’ and ‘c’ were calculated using the peak values of the anatase (101) and (200) reflections via Equations 3.2 and 3.3 and are provided in Table 4.5. According to the calculated data, the lattice parameter (‘a’ and ‘c’) increase with dopant addition (changed of the value of ‘a’ is insignificant), consequently the cell volume increases.⁸⁵ The cell volume of pure TiO_2 was 136.57 \AA^3 , whereas 10% Zr containing sample showed 138.47 \AA^3 . These results are consistent with previously reported cell volume for Ti-Zr binary solid solution prepared by Yu et al.¹⁸⁹ Moreover, this result is expected because the effective ionic radii of Ti_4^+ and Zr_4^+ are 0.68 and 0.79 \AA , respectively¹⁰⁵ and any substitution would increase the cell volume.

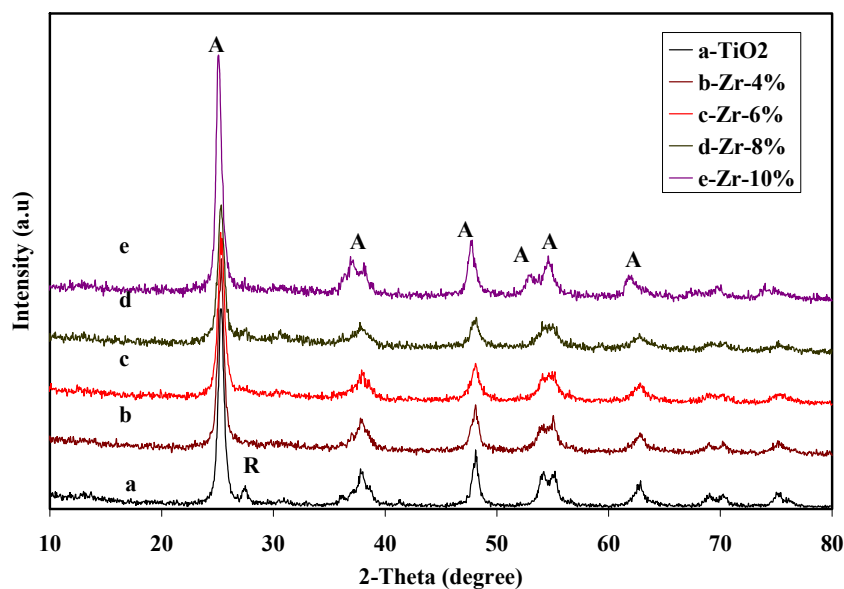


Figure 4.22: XRD patterns for Zr-Ti binary metal oxide nanomaterials with various % ZrO_2 compositions.

4.6.5. Surface Area and Pore Volume

The textural properties, i.e. the surface area, pore volume, and pore size distributions of all as-prepared and calcined (at 500 °C) samples were characterized by N₂ adsorption studies. Figure 4.23 shows the N₂ adsorption isotherms for the as-prepared materials, which exhibit type IV isotherms for all samples, except for low Zr composition, i.e. 4% and 8 % Zr containing samples which show type III isotherms having hysteresis loop typical for mesoporous materials.¹⁶⁰ The size distribution for all the as prepared samples is given in Figure 4.24, which indicates a bimodal pore size distribution. The pore volume for all the as-prepared and calcined materials is given in Figure 4.25, and clearly shows that the pore volume increases with increasing Zr % composition. The pore volume of the as prepared pure TiO₂ was 0.2 cm³/g whereas 20 % Zr showed 0.34 cm³/g. Due to the heat treatment, the small pores collapse and form larger pores resulting in a reduction of the pore volume. The average pore diameter for the single and binary nanomaterials was calculated using the 4V/S formula. For all the as prepared materials, the average pore diameter is *ca.* 3.5 nm, whereas the value for the corresponding calcined nanomaterials varies significantly. The average pore diameter was 14 nm for pure TiO₂, with this value decreasing with increasing %Zr composition. The value became *ca.* 10 nm for 10% Zr containing samples whereas for 20 % Zr composition, the average pore diameter was 4 nm.

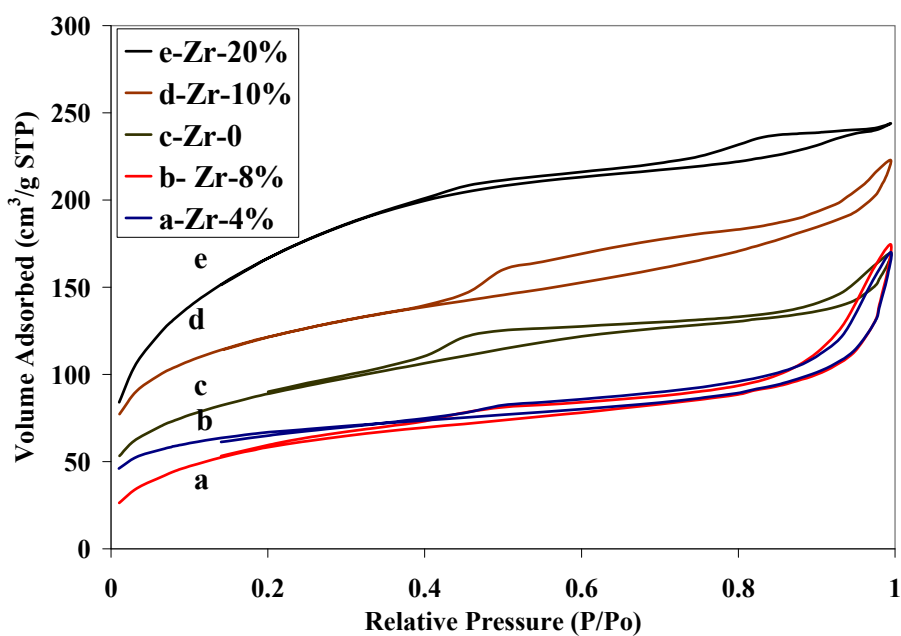


Figure 4.23: N_2 adsorption/desorption isotherms of the Zr-Ti binary metal oxide nanomaterials with different % ZrO_2 compositions.

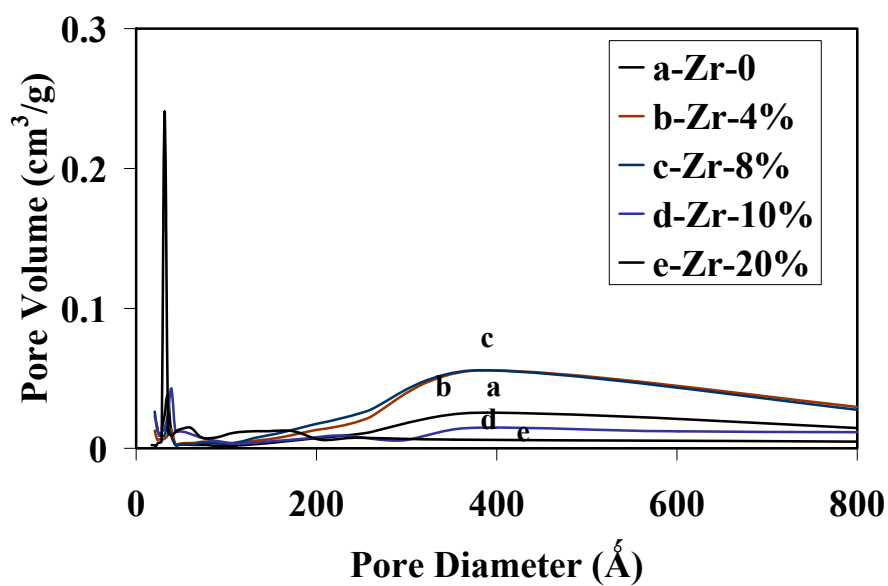


Figure 4.24: BJH pore size distribution of Zr-Ti binary metal oxide nanomaterials at different % ZrO_2 compositions.

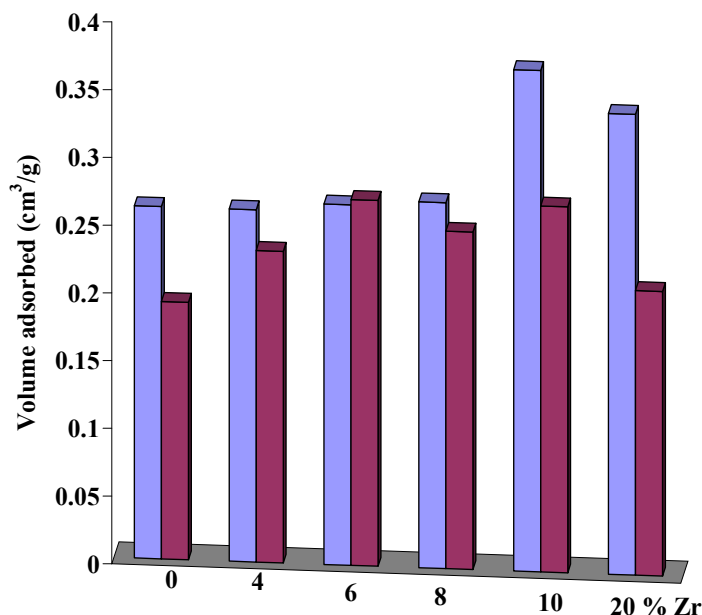


Figure 4.25: Pore volume of as prepared and calcined binary nanomaterials with various % ZrO₂ compositions.

The surface area of the as-prepared and calcined ZrO₂-TiO₂ nanomaterials is summarized in Figure 4.26. The surface area increased with increasing Zr composition though the as-prepared binary nanomaterials with low ≤ 10 % Zr composition possess lower surface area. This result is unexpected although Zou et al. observed similar results for a Ti-Zr binary system up to 10 % Zr composition, where the surface area did not increase, although they did not present results regarding materials synthesized using less than 10% Zr composition. However, from Figure 4.26 it can be seen that all calcined binary nanomaterials exhibited higher surface areas compared to pure TiO₂. These results along with the literature show the beneficiary effects of ZrO₂ present in the TiO₂ matrix, also showing higher thermal stability. This is due to the presence of Zr, which inhibits

phase transformations and reduces the sintering phenomena (described further in Chapter 6), hence showing higher surface areas.

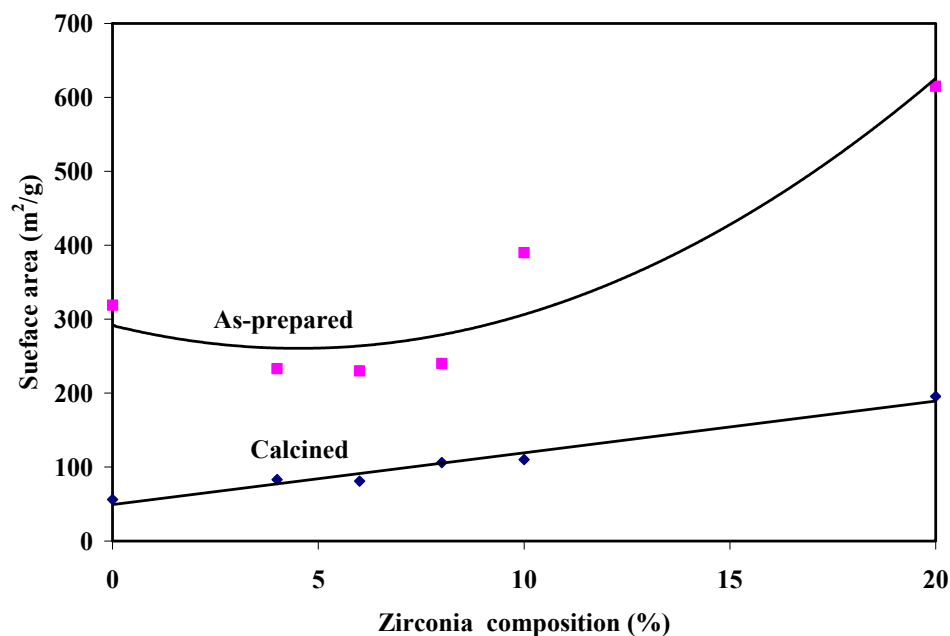


Figure 4.26: Surface area of as-prepared and calcined Zr-Ti binary metal oxide nanomaterials as a function of zirconium compositions.

4.7. Mechanism of Binary Nanotube Formation

The mechanism of the Ti-Zr nanotube formation in $scCO_2$ is complex due to involvement of both condensation and self-assembly processes. From others works on metal oxide nanotube formation, the formation mechanism is closest to the spontaneous growth, a process driven by the reduction of free energy of the system;¹⁷⁶ as any operating variables like temperature or pH did not change during the reaction process. Sui et al.,¹⁵¹ proposed a mechanism for the formation of titania nanofibers in $scCO_2$ using acetic acid where the titania formed a $Ti_6O_6(OPr^i)_6(OAc)_6$ hexamer, which was the

proposed building block for formation of the titania nanofibers. Similarly, single crystals of acid modified Zr-Ti alkoxide were also synthesized in $scCO_2$, as shown in Figure 4.27a.¹⁸⁵ The Zr modified $(Zr_2Ti_4(\mu_3-O)_4(OPr)_4(\mu-OPr)_2(\mu-OAc)_{10})$ hexamer is quite different from the previously observed titania hexamer. Figure 4.27b shows a typical unit cell containing four single units along the [100] plane in which the four end -OPr groups are situated on top, the other four groups on the bottom, and only two groups are present along the side. During the polycondensation process, the end -OPr groups will likely preferentially condense.⁹⁹ Furthermore, it is easier for cells to connect at the edge instead of the face.⁹⁹ Moreover, upon introducing Zr into the system, the Zr with different coordination number acts as an impurity in the structure, which is one of the required conditions for preferential condensation in one direction, usually known as anisotropic growth.¹⁷⁶ Hence, it is believed that a long sheet-type structure along the [100] plane was developed in the synthesis process. Moreover, the 150-375 nm width and several nanometer long dimensions of the sheet observed by SEM & TEM and given in section 4.4 were very close to that of the formed nanotubes, demonstrating these sheets play a key role in formation of the tubular structure. One can envision that as the sheet structure grows, at a certain stage in order to lower the energy of the system, it either rolls-up or folds along the [010] or [001] plane to form the tubular structure as shown in Figure 4.27(c). This “roll-up” mechanism has been used to explain the tubular structure of titanates and titania synthesized via the hydrothermal process,^{106, 188} and Cr doped alumina nanotubes via homogeneous precipitation upon heat treatment.

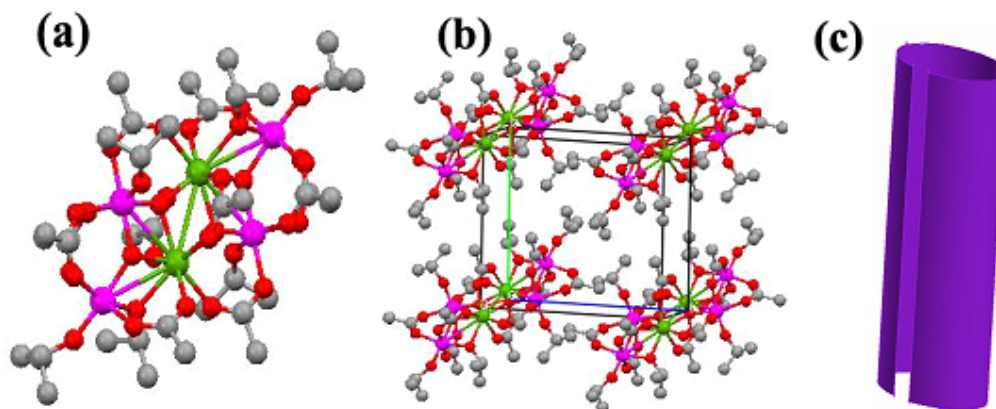


Figure 4.27: Acid modified Zr-Ti alkoxide single crystal (a) one unit, (b) cell along [100] plane, and (c) $\text{ZrO}_2\text{-TiO}_2$ nanotube formed via roll up of sheet. (Color code for a,b: Pink-Titanium, Green-Zirconium, Red-oxygen, Gray- Carbon).

4.8. Reaction Scheme in scCO_2

In situ ATR-FTIR was used to study the sol-gel process under actual reaction conditions in scCO_2 . Figure 4.28 shows in situ spectra for 1:1 mol TIP and ZPO reacting with acetic acid at R 5 (acid to metal alkoxide ratio) in scCO_2 from 0-1200 minutes. The first spectrum shows a strong peak at 1710 cm^{-1} indicating acetic acid, which drops with time showing consumption of acetic acid, as conveniently observed from the decreasing of this peak. The peaks from 1381 to 1458 cm^{-1} are due to the stretching and vibration of the aliphatic CH_2 and CH_3 groups, and the peaks from 1015 to 1160 cm^{-1} are due to the M-OPr groups. Therefore, the consumption of metal alkoxide precursors is difficult to observe due to the overlapping fingerprint region of acetic acid isopropanol and propyl acetate, hence being obscured. At the reaction time of 10 minutes, which is at the initial stage of the polycondensation reaction, the presence of peaks at 1557 and 1447 cm^{-1} provided evidence for the formation of the M-acetate complexes. At the initial stage of the reaction, one or two moles of OR groups can be replaced by acetate groups, with the

modification of the alkoxide monomer confirmed by this FTIR analysis.¹⁷⁵ The modification also alters the coordination number of the titanium and Zr atoms, which become 6 and 8 respectively. It also modifies the reactivity and the functionality of the new precursors toward hydrolysis. After 20 minutes reaction time, almost all acetic acid was consumed. However, peaks at 1557 and 1447 cm^{-1} changed further. At 30 minutes time, those peaks reached the saturation level, with no further intensity changes. However, shifting of the acetate bidentate peaks can be observed (1455-1600 cm^{-1}), indicating a change in the OCO bond angle and length during condensation. It is noted that water is required for the sol-gel process, which is generated through the esterification reaction at the initial stages. However, with the reactions proceeding, water can also be generated from the condensation reaction.

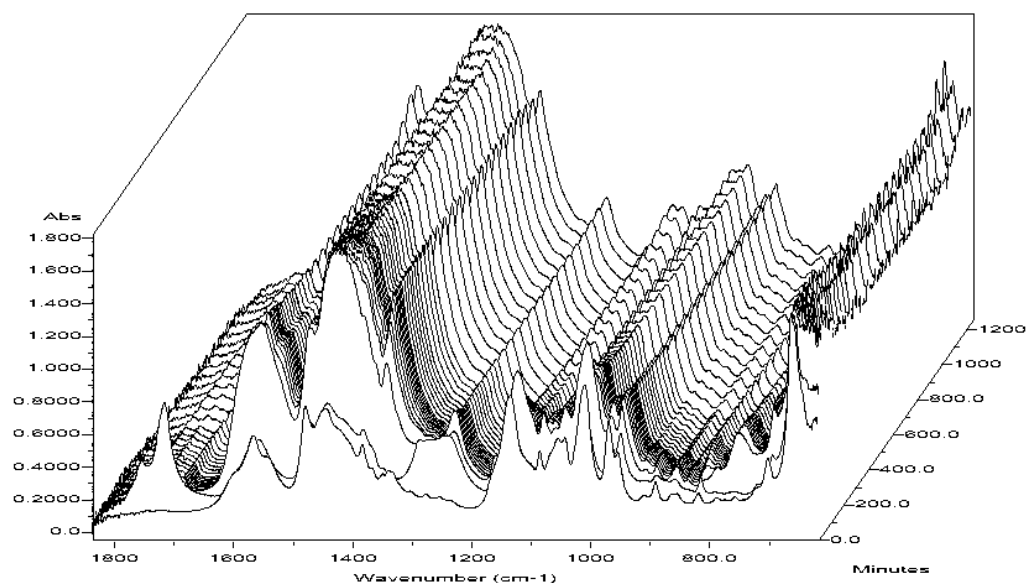
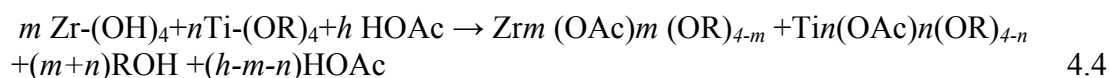


Figure 4.28: In situ FTIR spectra for 1:1 mol ratio TIP and ZPO with acetic acid at R 5 (acid to metal alkoxide ratio) in scCO_2 from 0-1200 minutes.

This in situ FTIR analysis indicates that acetic acid formed metal acetate complexes with metal alkoxide precursors, which were consumed very quickly (within 10 minutes) and are consistent with previously reported observations.^{149, 189} Moreover, the single crystal data reasonably matched with the powder FTIR data indicating that all content similar chemical functional groups.

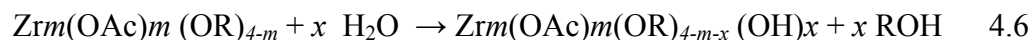
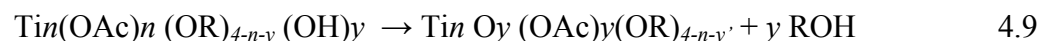
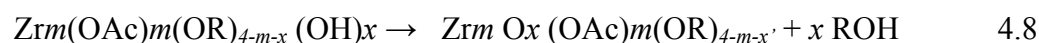
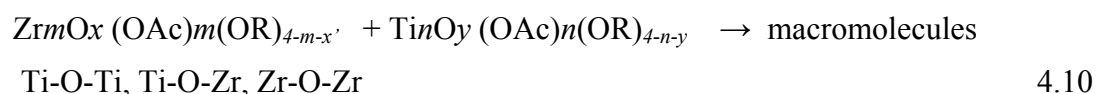
The chemistry of acid modified titanium and zirconium alkoxides in conventional solvents is reasonably well understood. According to Doeuff *et al.*, the formation of the Ti hexamer complex can be explained through modification, esterification, hydrolysis and condensation steps.¹⁹⁰ Zhong et al also followed the same scheme for explaining nanostructure formation through controlled hydrolysis of titanium alkoxide.¹⁹¹ Zirconium alkoxide reacting with carboxylic acid has also been studied in conventional solvents with the products characterized by single crystal XRD.¹⁹²⁻¹⁹⁴ According to Kickelbick,¹⁹⁵ the zirconium alkoxide also follows a similar reaction scheme. Sui et al. proposed similar reaction pathways for their TiO₂ and ZrO₂ nanomaterials formation in scCO₂ using alkoxides.^{149, 189} Following these works and the FTIR analysis results, it can be suggested that these above steps are quite general in the sol-gel chemistry. Hence, it is possible to propose a reaction scheme for the binary system based on the reaction scheme for titanium and zirconium alkoxides with acetic acid in simplified form.

Modification



Esterification



Hydrolysis*Oxolation**Condensation*

It should be mentioned that although the binary system likely follows the same reaction schemes, the relative rate of the reaction steps will be different, requiring careful further study.

4.9. Conclusions

The systematic investigation on the operating variables of ZrO₂-TiO₂ binary nanotubes revealed that the most important process variables were temperature, concentration acid/metal alkoxide ratio and composition. The morphology could be tailored by changing the operating variables. Moreover, nanotubes were only formed at concentration 1.17 mol/L using R 5-6 and 60 °C. The initial gelation kinetics for this system were studied and revealed that temperature, concentration of the starting materials, and the acid to metal (Zr and Ti) alkoxide ratio were the main factors which alter the gelation kinetics, as well as the basic properties of the synthesized nanomaterials. The activation energy for this 10% ZrO₂ modified system was 44 kJ/mol, calculated from an Arrhenius plot. Moreover, powder XRD analysis indicated that the

crystal size decreased with increasing zirconia content. BET analysis showed that higher than 10% Zr containing as-prepared and calcined binary metal oxide nanomaterials possessed higher surface areas compared to pure TiO₂. These results demonstrated that the presence of a small amount of ZrO₂ in TiO₂ matrix inhibited the grain growth, stabilized the anatase phase, and increased the thermal stability, resulting in larger surface area, pore volume and small crystallites materials. The in-situ FTIR study revealed that binary system also follows the similar reaction scheme as the single component TiO₂ or ZrO₂ systems.

CHAPTER 5

EFFECTS OF SOLVENT ON ZrO₂-TiO₂ BINARY NANOSTRUCTURE FORMATION

5. Introduction

The sol-gel process is becoming a standard synthesis route to produce low cost, high quality, homogeneous oxide materials with desired nanostructure.^{96, 196} However, the properties of the sol-gel products depend on the precursors, processing temperature, catalyst, solvents, and solvent removal process.⁹⁹ Among these experimental parameters, the precursors, catalyst and solvent have prominent influences on the reaction pathways of the synthesis process. Usually, the sol-gel process involves the hydrolysis of a metal precursor in an appropriate solvent with or without the use of a catalyst to form hydroxide, and subsequent polycondensation to provide the gel.¹⁹⁶ The hydrolysis reaction is catalyzed by acid, and the condensation reaction is catalyzed by base. At the end of the polycondensation reaction, the excess solvent can be removed by evaporation in an oven at atmospheric pressure or by employing supercritical drying.

The solvents used in the sol-gel process play an important role in the hydrolysis and condensation steps, as well as facilitating the porosity of the synthesized materials.^{197,}¹⁹⁸ The removal of working/residual solvent also has a prominent impact on the final materials.¹⁹⁹ The conventional heating/evaporation process may form xerogel resulting in low surface areas due to collapsing the pore structure of the material. On the other hand, recent studies suggest that mesoporous high surface areas of the final product can be obtained by supercritical (scCO₂) drying.¹⁵⁰ The scCO₂ drying technique also provides

desirable morphological characteristics of the synthesized materials.²⁰⁰ Therefore, the solvent elimination route might affect not only the surface features, but also the bulk and the morphological characteristics of the synthesized materials.²⁰⁰

Therefore, the purpose of this study was to investigate the influence of the solvents used for synthesis by studying common sol-gel solvents of varying dielectric constants, along with scCO₂, on the morphology, crystal structure, crystal size, surface area, pore volume and pore size distribution of Zr modified titania nanomaterials synthesized by a sol-gel process. The solvents, hexane, xylenes, isopropyl alcohol and ethanol (dielectric constant and physical properties given in Table 5.1) along with scCO₂ were used. In all cases, excess solvents and reaction by-products were removed by scCO₂ drying to separate the beneficiary effect of scCO₂ drying from the synthesis steps.

Table 5.1: Physical properties and dielectric constant of the solvents used in this study.

Solvent	Dielectric Constant (ϵ)	Surface Tension (mN./m) ²⁰	Viscosity (mPa.s) ²⁰¹	Solubility parameters, (cal/cm ³) ^{1/2} *
CO ₂	1.6	0.00	0.070	6.65
Hexane	1.6	17.9	0.532	7.26
Xylenes	2.4	29.5	0.121	8.81
Iso-propanol	18.3	21.2	0.310	11.54
Ethanol	24.3	21.9	0.035	12.73

*- The solubility parameters of CO₂ were obtained from Allada's method, while the other

solvents were calculated using: $\delta = \sqrt{\frac{\Delta H_v - RT}{V}}$

where, V is the molar volume of the liquid in cm³/mol, ΔH_v is the enthalpy change during vaporization in cal/mol, R is the gas law constant in cal/(mol·K), and T is the absolute temperature in K.

5.1. Experimental

In a typical experiment, 3 mL titanium (IV) isopropoxide, 0.48 mL zirconium (IV) propoxide, 3.16 mL acetic acid and CO₂/3mL solvent were quickly placed in a 10 mL view cell at 60°C under stirring. Initially a transparent homogeneous phase was observed. However, the entire view cell was filled with gel and the stir bar was not observed within 30 min to several hours depending on the solvent used. This time was considered as the gel point,¹⁴⁸ which for every experiment was determined twice.

5.2. Morphology

ZrO₂ modified TiO₂ nanomaterials were synthesized via an acid modified sol-gel process in various organic solvents and scCO₂. The morphology and particle size of the as-prepared and calcined ZrO₂-TiO₂ nanotubes were assessed by SEM and TEM analysis. Figure 5.1 and Figure 5.2 show the SEM and TEM micrographs of the samples prepared using the examined solvents for this study. When materials were synthesized in scCO₂, nanotubes having diameters of 55-140 nm and several μm in length were produced, as previously discussed and shown in Fig. 5.1(a). Samples with various morphologies were obtained when hexane, xylenes, or alcohol were used as the working solvent. As observed in these micrographs, the as-prepared powders were composed of one dimensional structure, although their size and morphologies were rather different depending upon the solvent used in their preparation step. Nanorods and/or tubes with diameter ranging from 40-250 nm were seen when the samples were prepared in xylenes, and ethanol. When hexane was used as the solvent, the rod/tube diameters were formed between 40-120 nm. However, in all cases the lengths of the nanorods/nanotubes were

approximately 1 to several microns. The surfaces of the tubes/rods were mainly smooth and were clearly separated from each other except for the samples prepared in xylenes, where agglomeration of the tubes/rods was noticed. Contrary to the above, a flake-type structure was obtained when isopropanol was used as the solvent during the synthesis step. The widths of those flakes were between ca. 200-350 nm, and length up to 4 microns.

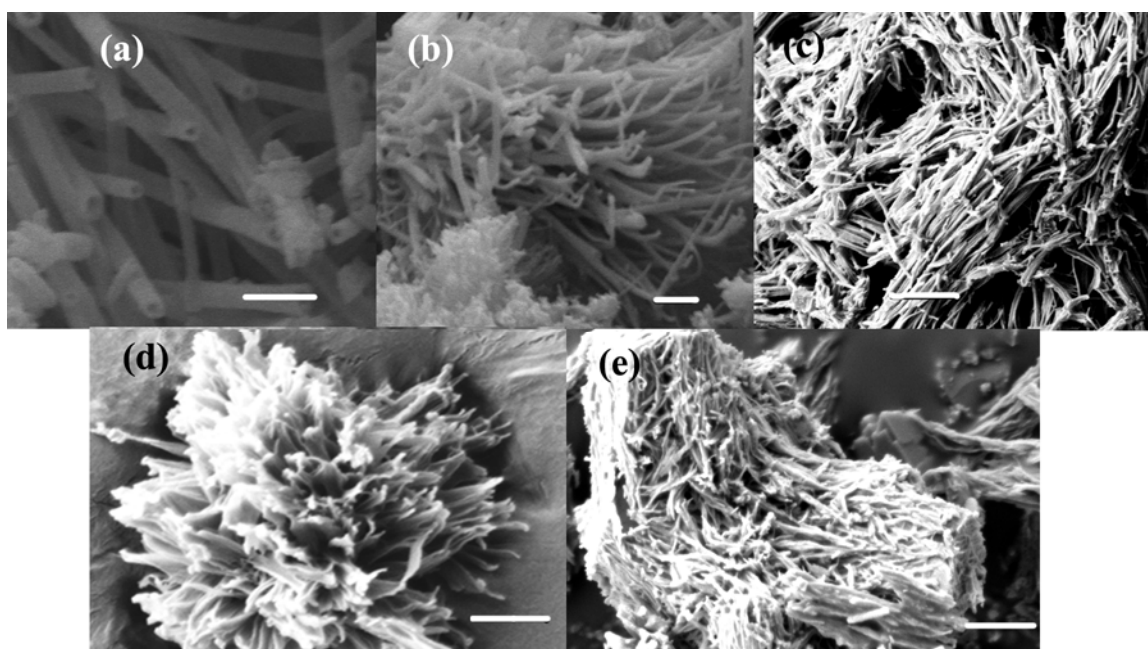


Figure 5.1: SEM: ZrO₂-TiO₂ nanomaterials in different solvents: (a) scCO₂, (b) Hexane, (c) Xylenes, (d) Iso-propanol, and (e) Ethanol. (Bar represents 200 nm. All the samples were examined after platinum coating).

One can notice from the SEM analysis that it is difficult to distinguish between the nanorods and nanotubes when nanomaterials synthesized with different solvents other than CO₂. The end closed nanotubes with 40 nm hole with 15nm wall thickness were observed for the samples prepared in CO₂. However, the TEM images of Figure 5.2 show

very narrow internal holes (ca. 10 nm) along the length, with thickness *ca.* 40 nm in the case of the larger diameter structures synthesized under hexane. However, the materials with small diameters were solid indicating a rod-type structure. The flakes type structure presented in the TEM images for calcined materials synthesized in iso-propanol support the SEM analysis. However, due to the thick wall of the materials synthesized using ethanol, it is very difficult to distinguish even by TEM whether the nanostructures are rods or tubes. Therefore, from this observation it appears that materials with larger diameters form thick wall tubes, while the smaller diameter materials are rods.

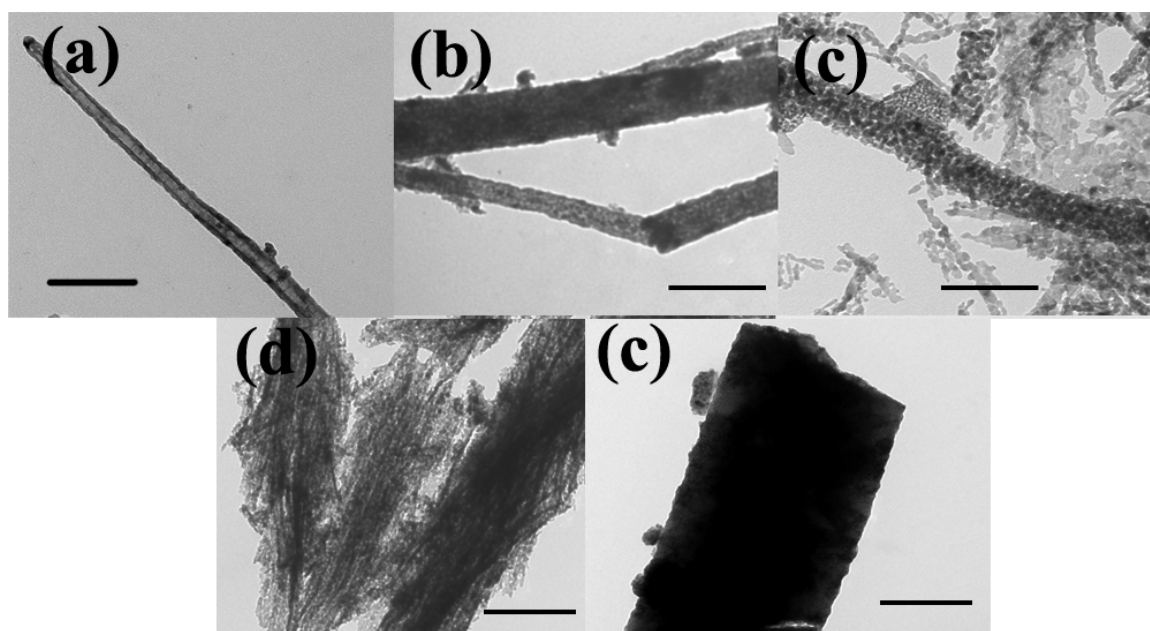


Figure 5.2: TEM: $\text{ZrO}_2\text{-TiO}_2$ nanomaterials in different solvents (a) scCO_2 , (b) Hexane, (c) Xylenes, (d) Iso-propanol, and (e) Ethanol. (Bar represents 300 nm. All samples were calcined at 500°C).

When the calcined samples were analyzed by TEM, the materials synthesized in scCO_2 , hexane, xylenes and isopropanol were composed of connected crystallites, while

the material synthesized in ethanol was mainly solid. This analysis illustrates that the solvent used for nanotubular synthesis has a significant effect on the morphology and the dimensions of the products.

5.3. Composition

In order to obtain more information about the presence and intensity of the different functional groups, the prepared $\text{ZrO}_2\text{-TiO}_2$ samples were further characterized using ATR-FTIR analysis. The powder IR spectra of the as-prepared materials synthesized in the various solvents are shown in Figure 5.3. As can be seen in this figure, all the samples had similar spectra although their peak heights were different depending on the solvent used for preparation. The broad peak at 3300 cm^{-1} was assigned to the -OH group of absorbed water¹⁵² while the peaks at 1548 and 1452 cm^{-1} are due to symmetric and asymmetric stretching of zirconium titanium acetate complexes, respectively. The delta value (ca. 100 cm^{-1}) between these symmetric and asymmetric stretching peaks confirmed that the acetic acid group formed bridging complexes with the metal atoms.¹⁵² The small peak at 1343 cm^{-1} indicates the presence of the $-\text{CH}_3$ group,¹⁵¹ while the two small peaks appearing at 1037 and 1024 cm^{-1} are attributed to the ending and bridging -OPr groups, respectively. The presence of unhydrolyzed -OPr groups in the as-prepared materials has also been reported in nanomaterials prepared under similar conditions.^{120,}¹⁹⁸ All spectra contain a small peak at 1710 cm^{-1} , due to residual acetic acid, and bands below 657 cm^{-1} , representing oxo bonds. It is important to emphasize that no solvent peaks were detected from the preparation of the various samples, indicating complete removal of the solvent through scCO_2 drying.

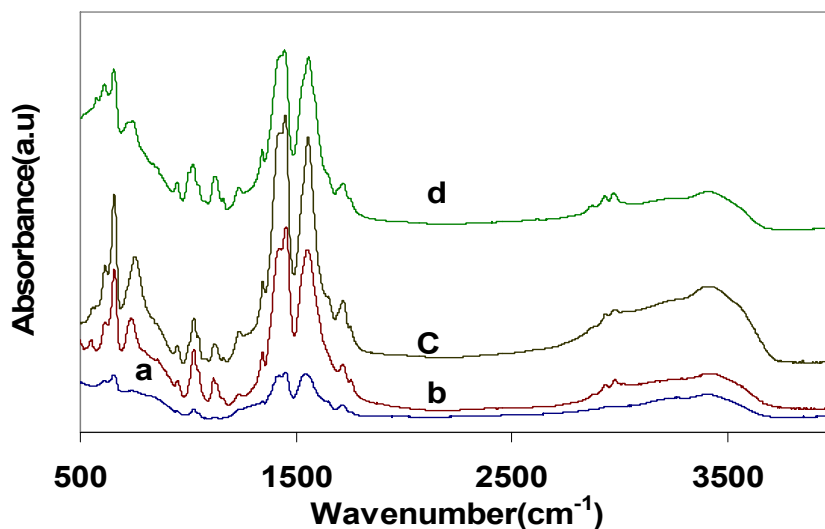


Figure 5.3: Powder ATR-FTIR spectra of as-prepared $\text{ZrO}_2\text{-TiO}_2$ nanomaterials in different solvents: (a) Hexane, (b) scCO_2 (c) Xylenes, and (d) Iso-propanol.

As mentioned above, although the peak positions were quite similar, the heights of the peaks were rather different for the various samples. For instance, if one considers the peaks at 1548 and 1452 cm^{-1} , their heights decreased according to: xylenes > isopropanol > scCO_2 > hexane. This suggests that the materials prepared using xylenes contain the highest amount of acetylated groups. This hypothesis was further examined by performing EDX elemental analysis, which is presented in Table 5.2. The residual carbon content in xylenes and isopropanol system was higher ca. 41-42% atomic ratio, respectively, whereas scCO_2 , hexane and ethanol system contains only 29-32 % carbon. This analysis corroborates the FTIR results and also reveals that xylenes and isopropanol stabilized the intermediates more than the ethanol and hexane systems. FTIR and EDX analysis showed that the as-prepared materials contain a significant amount of organic materials. Therefore, heat treatment was necessary to remove this organic residue, as well as to form crystalline materials.

The thermal decomposition behavior of the synthesized materials was carried out by employing TG–DTG analysis, with typical TG-DTG curves being given in Figure 5.4. It is interesting to note that all the samples showed four steps, although the peak positions varied depending on the solvent used in their preparation. In all cases, the sample decomposition contains the four following steps: (I) 25–120 °C, (II) 120–260 °C, (III) 260–500 °C and (IV) above 500 °C.

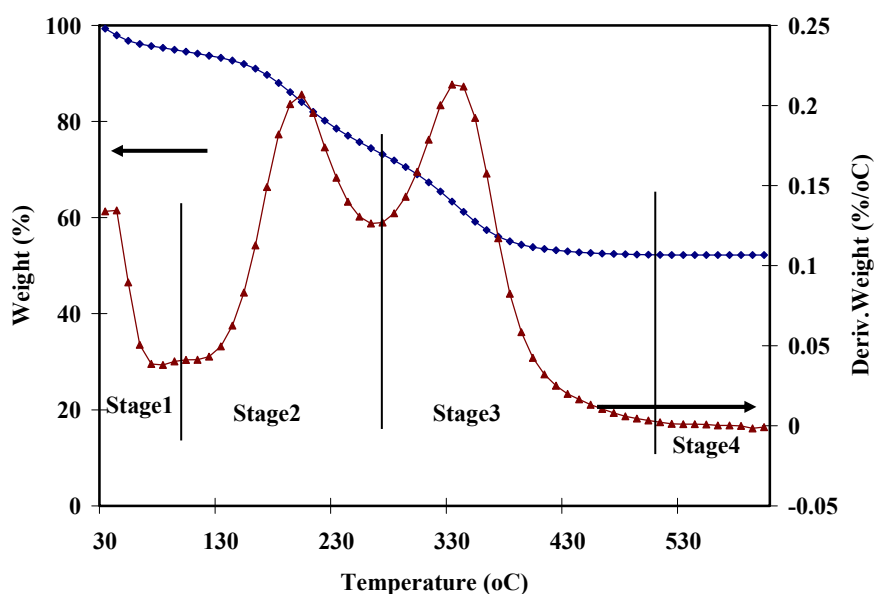


Figure 5.4: A typical TG/DTG curve for ZrO_2 - TiO_2 nanomaterials synthesized in hexane.

Table 5.2: Composition and weight loss at different stages of thermal analysis.

Solvent	Composition C: O: Ti:Zr ^a	Stage 1 25–120°C		Stage 2 120–260°C		Stage 3 260–500°C		Total wt loss
		T _{p1} (°C)	Wt.(%)	T _{p2} (°C)	Wt.(%)	T _{p3} (°C)	Wt.(%)	
CO ₂	31:55:13:2	40	6.02	200	20.68	343	18.97	45.72
Hexane	32:54:12:2	75	6.31	198	19.29	333	22.02	47.92
Xylenes	41:50:8:1	86	5.61	191	38.04	425	13.54	59.01
Iso-propanol	42:54:7:1	95	4.55	236	42.95	319	8.88	57.59
Ethanol	29:61:9:1	53	10.07	196	14.11	336	22.5	49.34

Note-a- composition of as prepared nanomaterials

Table 5.2 summarizes the composition, weight loss and peak temperature for the different stages of decomposition for the materials synthesized in the studied solvents. Generally, in stage I (25-120°C) physically adsorbed/absorbed water and organic residues were removed while the chemically bonded water and organics were removed in stages II and III. Regarding the weight loss during TGA, a small amount of material was lost in the first stage regardless of the solvents used in sample preparation. A major weight loss occurred in the second and third stages, while the weight loss in the fourth stage (over 500 °C) is extremely small. The total weight loss measured from the TG analysis was 59 % for xylenes, 57.6 % for isopropanol, 49.4 % for ethanol 47.9 % for hexanes, and 45.7 % for scCO₂. These results suggest that the highest amount of organic impurities were present in the synthesized materials when xylenes or isopropanol was used as solvent, which is consistent with the observations from the FTIR and EDX results.

5.4. Crystallinity and Phase Structure

Figure 5.5 depicts the crystal phases determined from the powder XRD patterns of the ZrO₂-TiO₂ samples calcined at 500°C. The XRD patterns of all the samples synthesized in different solvents showed the presence of anatase crystal structure of TiO₂, and no rutile phase being present. No distinct zirconia peak was observed for all the samples, indicating that the zirconium element was contained in the anatase crystal structure. Therefore, no significant phase separation took place during the calcination step at 500 °C.

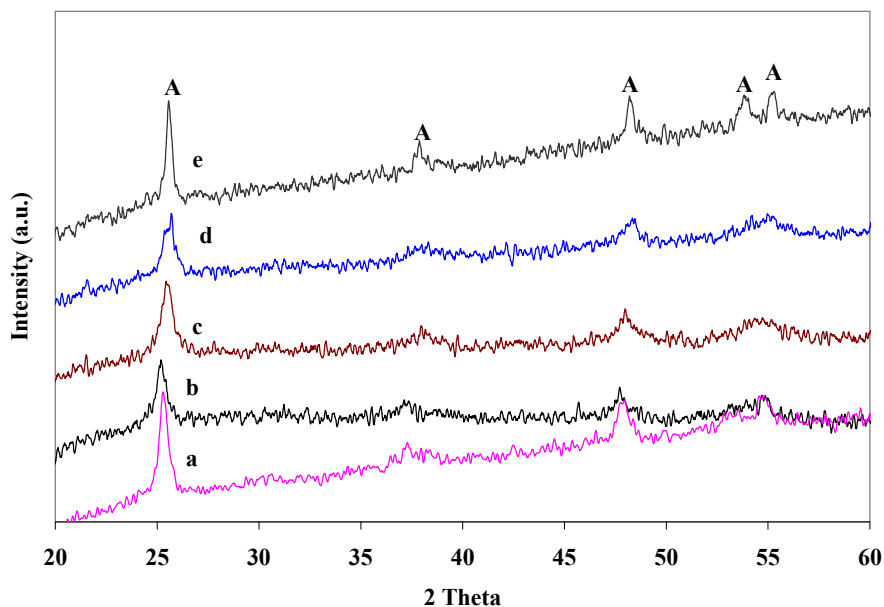


Figure 5.5. Powder XRD spectra of the $\text{ZrO}_2\text{-TiO}_2$ nanomaterials calcined at $500\text{ }^\circ\text{C}$ synthesized in different solvents (a) scCO_2 , (b) Hexane, (c) Xylenes, (d) Iso-propanol, and (e) Ethanol.

The crystallinity, crystal structure and the crystallite sizes obtained from the XRD data are reported in Table 5.3. Scherrer's equation (1) along with 2θ and full width at half maxima was used to calculate the crystallite size. As can be seen in the table, the smallest crystal size (12.47 nm) was found for the sample prepared in isopropanol, whilst the largest crystal (23.64 nm) was obtained from ethanol. During heat treatment, the amorphous materials reorganized to form a crystalline phase. It is already well established from the literature that any type of impurities such as cations, or anions present in the nanomaterials inhibits this type of organization, resulting in high temperature for amorphous to anatase to rutile transformation and smaller crystallite materials.⁸³ A similar phenomenon was observed in the current study. Smaller crystallite materials were formed in xylenes and iso-propanol with the EDX, FTIR, and TG results

suggesting that a larger amount of organic residues were present in the samples. However, when considering crystallinity, the materials synthesized in hexane and xylenes were poorly crystalline containing only ca. 37% whereas ca. 50% crystalline materials were obtained using isopropanol or ethanol. Therefore, the XRD results also reveal that the solvent type has a rather significant influence on crystallinity and crystal size.

Table 5.3: Crystallinity, crystal structure and size of the nanomaterials calcined at 500°C.

Solvent	Crystallinity(%) ^a	Crystal structure	Crystal size(nm) ^b
CO ₂	38.9	A	13.71±1
Hexane	36.4	A	13.95
Xylenes	37.3	A	12.79
Iso-propanol	48.9	A	12.47
Ethanol	50.2	A	23.64

a-based on anatase (101)peak area

b-using Scherrer's equation with the anatase (101) peak

5.5. Surface area and Pore Volume

The surface area and pore volume of the as-prepared and calcined materials were determined by nitrogen adsorption isotherm analysis. From the isotherms (Figure 5.6) it can be seen that the type IV isotherms exhibit H3 hysteresis loops typical for mesoporous materials.¹⁶⁰ The lower limit of the relative pressure for the hysteresis loop is a characteristic of a given adsorbate at a given temperature.¹⁹⁸ It can be seen from Figure 5.6 that the lower pressure limit of the hysteresis loop is at $P/P_0 = 0.4$, irrespective of the solvent used in the synthesis. However, for calcined materials this limit was shifted towards the right to a value of 0.5 for ethanol, and 0.6 for the other solvents, indicating that the pore sizes become larger after calcination (at 500 °C). Figure 5.7 shows the pore-size distribution of the calcined materials synthesized from the various solvents. For low dielectric solvents such as hexanes and xylenes, a narrow pore-size distribution is

observed, while gels prepared from solvents such as isopropanol and ethanol show a broad pore-size distribution.

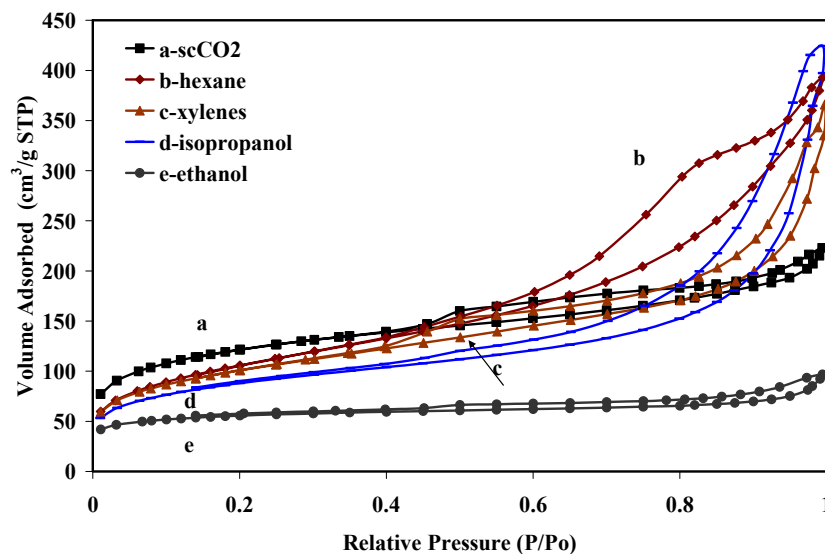


Figure 5.6: N₂ adsorption/desorption isotherms of as-prepared ZrO₂-TiO₂ nanomaterials synthesized in different solvents.

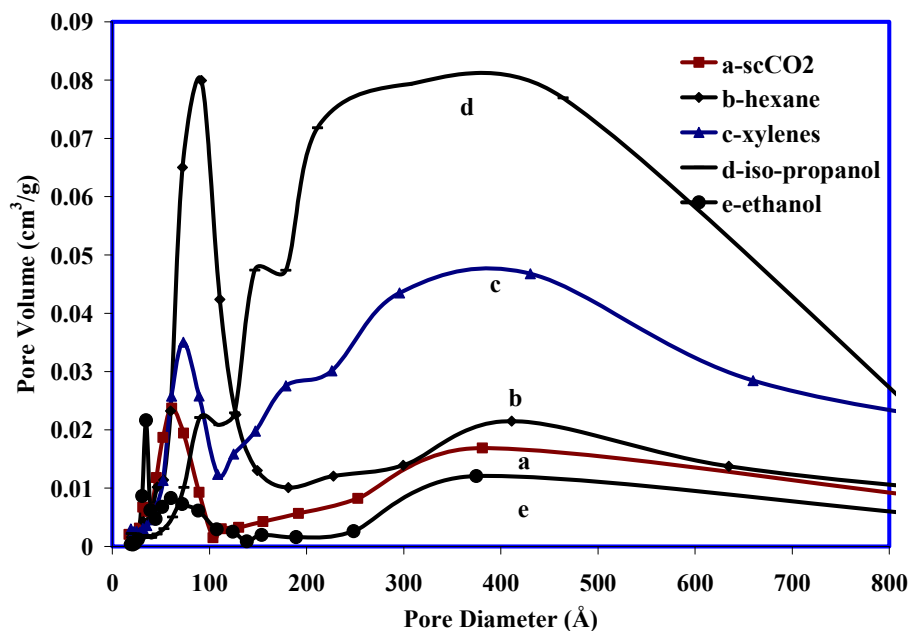


Figure 5.7: BJH pore size distribution of calcined ZrO₂-TiO₂ nanomaterials, synthesized in different solvents.

Table 5.4: Surface area, pore volume and average pore diameter of as-prepared and calcined nanomaterials synthesized in various solvents.

Solvent	As-prepared nanomaterials			Calcined nanomaterials		
	Surface area(m ² /g)	Pore V. (cm ³ /g)	Pore dia.(nm)	Surface area(m ² /g)	Pore V. (cm ³ /g)	Pore dia.(nm)
CO ₂	394	0.39	3.9	110	0.26	9.8
Hexane	376	0.61	6.4	132	0.36	7.8
Xylenes	363	0.56	6.0	107	0.37	11.0
Iso-propanol	360	0.65	7.2	92	0.42	17.8
Ethanol	191	0.15	3.0	50	0.10	7.8

The BET surface area, pore volume, and pore diameter of the as-prepared and calcined samples are reported in Table 5.4. Materials synthesized in low dielectric constant solvents such as scCO₂, hexanes and xylenes show higher BET surface areas for both the as-prepared and calcined materials, whereas low surface areas were obtained when using high dielectric constant solvents such as isopropanol and ethanol. Due to the sintering effect, the small pores collapse reducing the pore volume and lowering the surface area for the calcined materials. The values of the surface area were decreased by a factor of ca. 2–3.82. The decreasing factor was low (2.02) for hexane, and its value was increased with increasing dielectric constant of the solvents. This value was 3.82 for ethanol indicating that a higher reduction of surface area through calcination resulted in more dense materials. In addition to the sintering phenomenon, phase transformations were also responsible for reducing the surface area. Amorphous to anatase phase transformation were greater for the samples prepared in ethanol, resulting in more crystalline materials, which were also responsible for the larger reduction in surface area. Moreover, the pore volume was very low both for the as-prepared and calcined materials synthesized in ethanol. However, the average pore diameters for the as-prepared and

calcined materials were calculated from the BJH desorption isotherms, demonstrating that all the samples were mesoporous.

To investigate the effects of the solvent on the surface area and pore volume of the as-prepared and calcined materials, the measured results were plotted as a function of the dielectric constant of the solvent. The surface area of the as-prepared and calcined materials shows a linear relation with the dielectric constant of the solvent (Figure 5.8). Similar behavior is reported in the literature for magnesium oxide.¹⁹⁸ However, the pore volume did not show a similar linear trend. From Table 5.4, the pore volume for both the as-prepared and calcined materials show a similar trend and it is almost the same for hexane, xylenes and isopropanol but smaller for the ethanol system. All the previous discussed analysis results indicate that the ethanol system was more compacted (less porous). Therefore, the pore volume would be lower, and this is expected.

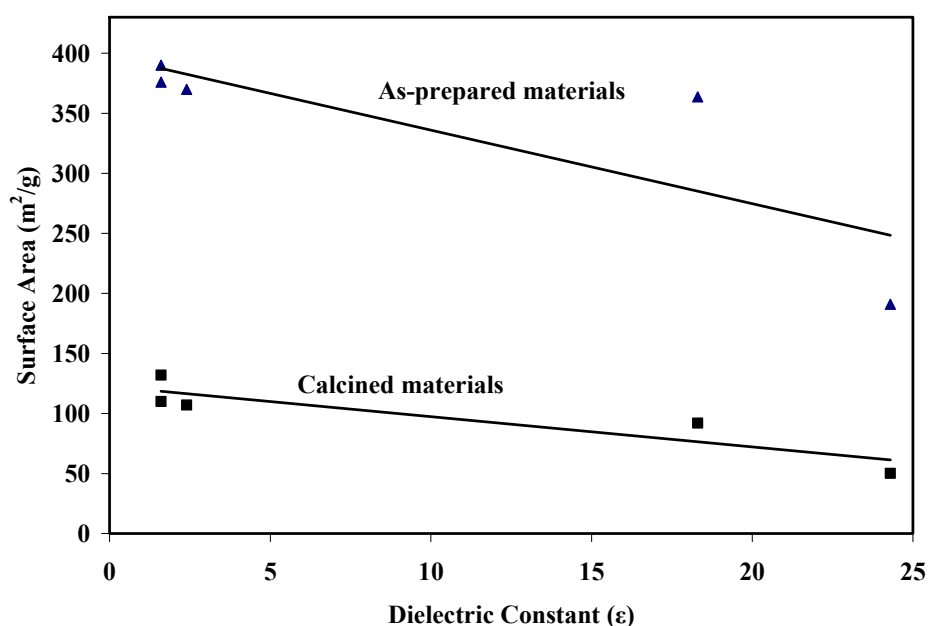


Figure 5.8: Surface area of as-prepared and calcined nanomaterials synthesized in different solvents as a function of solvent's dielectric constant (ϵ).

5.6. Gelation Time

In the sol-gel process, initially the precursors form a sol, a colloidal suspension of solid particles with several nm in a liquid. When sols attract one another, they form a network and reach macroscopic dimensions which extends throughout the solution, forming a gel. Hence, a gel is a substance that contains a continuous solid skeleton enclosing a continuous liquid phase.⁹⁹ The gelation time or gel point (t_g) is the time or the degree of reaction required to complete the gel network. However, the properties of a gel continue to change long after t_g because at the t_g , a substantial fraction of sols remains free to diffuse and react. This period is known as the aging time and may result in structural reorganization, including coarsening of the pores or stiffening of the network through formation of additional cross links. The working solvent has an important role in hydrolysis, and gel formation as well as the properties of the sol-gel product.⁹⁹ In this study, though gel was formed for all investigated working solvents, the gel times differed significantly depending on the used solvent. The gel time for nonpolar solvents e.g. $scCO_2$, hexane, and xylenes was shorter ca. 30-60 min whereas in polar solvents i.e. 2-propanol, ethanol, the gel time was longer ca. 120-250 min. In the published literature, the solvent had similar effects on gelation time for different precursors, solvent and catalyst systems. For example, Gash et al. synthesized chromia aerogel using chromim nitrate solution in different solvents. They observed that the gel time was 14h, 3.1h and 2.6 h for methanol, ethanol and isopropanol, respectively.²⁰² Recently, Gao et al. synthesized zinc oxide following a similar procedure, and observed the gel time for the synthesis in methanol was 8–10 h whereas that for 2-propanol was 2–3 h.²⁰³ They all explained the origin of this effect as the difference in solubility and stability of the metal

oxide sols in the various solvents. Moreover, Ranjit et al. investigated the solvent effects on the hydrolysis of magnesium methoxide. They observed that solvents having low dielectric constants accelerated the gelation process, while solvents having high dielectric constants did not have a significant effect on the gelation process. They also suggested that solvation of the alcohol-alkoxide mixture is an important parameter which influences the gelation time.¹⁹⁸

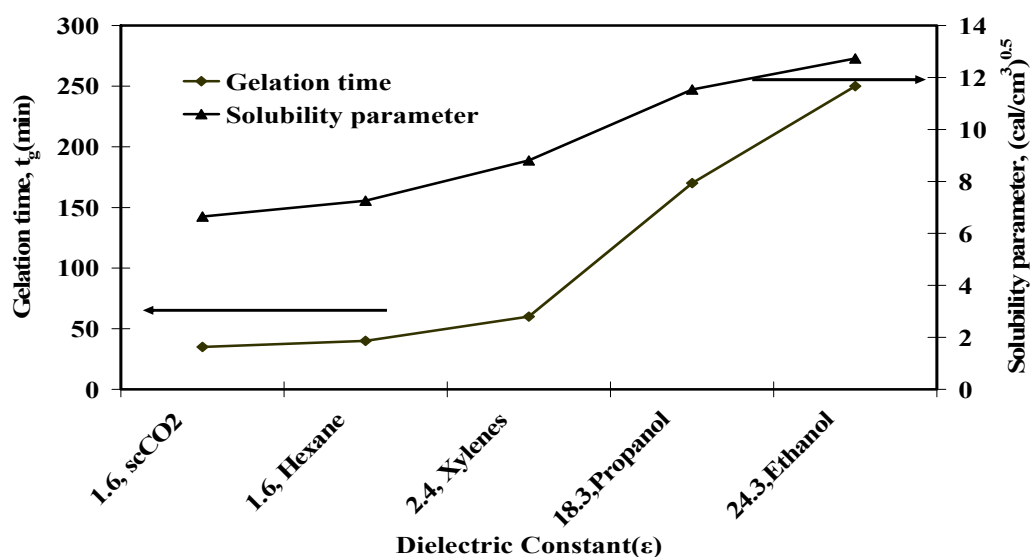


Figure 5.9: Gelation time of nanomaterials synthesized in different solvents as a function of solvent's dielectric constant (ϵ).

To understand the role of solvent in the hydrolysis reaction, the gelation time and measured solubility parameter were plotted as a function of the dielectric constants of the solvents used in this study (Figure 5.9). It can be seen that the gelation time and solubility parameter increased with an increase in the dielectric constant of the solvent. Previous work on Mg metal precursors in varying dielectric constant solvents showed a similar

trend.²⁰⁴ Therefore, it can be said that solvents with different dielectric constants have different solubilities of the alcohol-alkoxide mixture, which is the most important parameter controlling the gelation time, although the detailed mechanism is not well understood.

5.7. Discussion

The physical and chemical properties of a solvent have rather significant influences on the morphology, surface area and pore volume of the product. Typically, nanostructure evolution in the modified sol-gel process follows the following steps: (i) modification, (ii) hydrolysis, (iii) condensation, (iv) nucleation, and (v) growth. The rate of reaction of the different steps strongly depends on the reactivity of the metal atoms present in the precursor, the working solvent(s), and the pH of the system. Hence, the properties of the sol-gel product varies significantly with changing the above mentioned synthesis variables.

The metals reactivity largely depends on the extent of the charge transfer and the ability to increase the coordination number.¹⁷⁶ The charge transfer is influenced by the charge difference between the metal atom and the surrounding solvent, while the coordination expansion depends on the difference between the coordination number and the oxidation state of the metal. The unsaturated coordination number of a metal atom can be fulfilled by addition of an alkoxy ligand, or forming a complex with acetic acid or an alcoholic solvent. From the partial charge (δ) of a metal atom in the precursor, and the unsaturated coordination number, it is possible to estimate how a precursor is going to behave in a given synthesis process. The charge distribution of titanium and zirconium

alkoxides is given in Table 5.5. From this data, it is clear that irrespective of the ligand, the zirconium precursor is more reactive than the titanium precursor. Upon introducing 10% zirconium precursor in the synthesis process, the whole synthesis process was accelerated, as has been previously reported.¹⁸²

Table 5.5: Partial charge, δ , mol complexity and coordination number, n of titanium and zirconium alkoxides.²⁰⁵

Alkoxide	$\delta(M)$	Mol Complexity	n
Ti(OPr ⁱ) ₄	+0.61	1.4	6
Ti(OEt) ₄	+0.63	2.4	6
Zr (OPr ⁱ) ₄	+0.64	3.0	8
Zr(OEt) ₄	+0.65	3.6	8

The solvents studied in this work can be divided into two categories based on polarity, i.e. nonpolar solvents such as scCO₂, hexane and xylenes, and polar solvents such as isopropanol and ethanol. When a nonpolar aprotic solvent was used, acetic acid substitutes one or two (-OR) groups and liberates alcohol (ROH), which can react with acetic acid to produce the ester and water. The water formed during an esterification reaction will hydrolyze the metal alkoxide. Due to the low solubility of water in nonpolar solvents, these solvents could force the water molecules to form complexes with the metal ion more quickly to hydrolyze the metal alkoxide. The gelation time would thus be lowered, as was experimentally observed for the hexane, xylenes and scCO₂ solvents. However, due to steric hindrance, bulky aromatic and aliphatic groups could more easily stabilize organic groups toward hydrolysis, resulting in more impurities being formed for materials synthesized in xylenes and isopropanol. After introducing the hydroxide group into the coordination sphere of the metal atoms, condensation occurs followed by nucleation and growth. Considering the solubility parameters of the solvents used in this

study (see Table 5.1), high supersaturation values due to the low solubility of the hydrolyzed product in nonpolar solvents ($6.65\text{-}8.81 \text{ (cal/cm}^3)^{1/2}$) could promote nucleation. In addition, low solubility would inhibit dissolution, reprecipitation, repolymerization, and the formation of larger crystallites as well as densification of the gel network. The observed morphology, high surface area, porosity and smaller crystallites are consistent with this mechanism. Huang et al also observed similar effects for N-F-codoped TiO_2 synthesized by a sol-gel- solvothermal method.⁵⁵ When polar solvents such as ethanol and isopropanol ($11.54\text{-}12.73 \text{ (cal/cm}^3)^{1/2}$) were used in the synthesis process, the alkoxides were solvated to give $\text{M(OR)}_x\text{:ROH}$ and acetic acid was also found to react with solvent. Because of solvate formation, intermediates would be more stable toward hydrolysis, and hence the gelation times would be longer when polar solvents were used. Moreover, when ethanol instead of isopropanol was used, along with all the above mentioned reaction steps, alcohol interchange would be involved. The rate of hydrolysis and the properties of the product also depend on the OR group present in the precursor, as substitution can change the molecular complexity. Moreover, monomeric $\text{Ti(OPr}^i)$ formed oligomer upon replacing OPr groups by OEt groups. All these factors help to stabilize the hydrolysis product resulting in higher gelation times. Furthermore, the solubility of the hydrolysis products in polar solvents is higher, which would reduce supersaturation and promote dissolution, depolymerization, repolymerization, and help to form denser larger materials. However, the surface area and pore volume for the materials synthesized in isopropanol was higher than the linear values, which are consistent with the lower gelation time of the isopropanol system. These results can be attributed to the monomeric nature of the titania precursor.²⁰⁵

From the above results and discussion, it can be concluded that the polarity or dielectric constant of a solvent is one of the main properties that controls the surface area, and pore volume of the nanooxide materials. However, nanotubes were produced in scCO₂, whereas only very thick wall tubes or rods were obtained in hexane, although the two solvents are chemically similar with a polarity of 1.6. Therefore, along with polarity, a solvents' physical properties, and chemical structure are very important towards the desired end-product. Moreover, the synthesis conditions also have a prominent effect on the materials formation. For instance, some materials cannot be synthesized except under high pressure. According to Goodenough et al. high pressure helps by lowering the free energy resulting in easy formation of a new phase.²⁰⁶ The synthesis process involved pressure similar to hydrothermal and solvothermal techniques which are popular titanate nanotube synthesis processes, following the pioneering work of Kasuga et al.¹⁰⁶ Moreover, during synthesis, the formed metal-acetate group which has electron lone pairs can attract the partial positive carbon atom of CO₂ molecules. This is known as Lewis acid and Lewis base interaction and helps to stabilize the colloidal particles in scCO₂.²⁰⁷ Hence, the building blocks in scCO₂ most likely are different from those of conventional organic solvents, which help to form a sheet type structure, and at a suitable synthesis condition, the sheet rolls up and forms tubes¹⁸⁵ as described previously in section 4.7. Therefore, the nanotubes formation in scCO₂ can be attributed to its synthesis condition and different hexamer formation. It can be concluded that scCO₂ strongly influences the synthesis process resulting in superior quality materials.

5.8. Conclusions

The morphology and surface area of metal oxides synthesized by a sol-gel process is significantly altered by the solvent used. The polarity or dielectric constant of a solvent is one of the main properties to control the surface area, and pore volume. When low dielectric constant solvents such as scCO_2 , hexane, or xylenes are employed, the faster the hydrolysis reaction the lower the gelation time, and the higher the surface area of the nanomaterials. The presence of such solvents helps in the formation of porous structures and high surface area materials. However, when solvents having high dielectric constants such as alcohols are used, the gelation time is slower due to the possible formation of alkoxide-solvent complexes, which help stabilize hydrolysis. The partial charge model and solubility help to explain this observation. This study demonstrates that with the appropriate choice of solvents, high surface area porous inorganic oxides can be obtained.

CHAPTER 6

EFFECTS OF HEAT TREATMENT ON Zr MODIFIED TiO₂

NANOTUBES

6. Introduction

As discussed in Chapter 4, Zr modified TiO₂ (Zr-TiO₂) nanotubes were synthesized in scCO₂, and our preliminary results indicated that the as-prepared nanotubes gave a high surface area, up to 430 m²/g. According to several studies, a small amount of transition metal doping has been found very effective to improve the thermal stability and activity of TiO₂, particularly by using zirconia.^{24, 53, 82, 83} In addition to the synthesis conditions, the calcination conditions are very important to the crystal structures of the metal oxide nanomaterials obtained, and subsequently, their potential end use applications. Spijksma et al.²⁰⁸ synthesized titania-zirconia microporous composite membranes using a 1:1 molar ratio by using the sol-gel process. The crystallization temperature for these materials was 750°C; however after calcining at 800°C, an orthorhombic ZrTi₂O₆ structure was formed, commonly known as srilankite. Whereas, Zou et al.²⁰⁹ synthesized binary oxides by hydrolysis of titanium and zirconium nitrate solutions at various ratios. After calcining at 800°C, the binary oxides showed the presence of the ZrTiO₄ crystal phase, and very low surface areas. Kitiyanan et al.⁵³ synthesized 5 mol% zirconia modified TiO₂ using a sol-gel process. They showed that this small amount of Zr stabilized the anatase phase up to 800°C, but that the anatase phase completely transformed into the rutile phase at 1000°C. However, the materials calcined at these very high temperatures showed very low surface areas.

As the nanotubular structure of the bimetallic TiO₂/ZrO₂ nanotubes prepared by scCO₂ have many potential interesting applications, however, their structure and crystal morphology changes with calcination temperature have not been investigated. Hence, this study focused on the thermal behavior of the synthesized Zr-TiO₂ nanotubes prepared by an acetic acid modified sol-gel process in scCO₂. The synthesized materials were calcined at different temperatures and the effects of calcination temperature on the morphology, phase structure, mean crystallite size, specific surface area, and pore volume were investigated using a variety of physicochemical characterization techniques.

6.1. Solid-State Reaction Kinetics

Solid-state reaction and phase transformations through heat treatment are an important means for adjusting the microstructure, and thus tuning the properties of desired materials. To exploit this tool, a great deal of effort has been made on the modeling of solid state reaction kinetics. The required models should not be in particular of atomistic nature, but pertain to larger, mesoscopic and even macroscopic scales. This study can provide valuable information about the reaction mechanism/ kinetics parameters useful for modifying the course of the interested reaction. In the following, a model related to decomposition and phase transformation that is often invoked is briefly discussed.

6.1.1. Decomposition

In general, the decomposition reactions can be described by the following equation.



where, b, d, and e are the stoichiometric coefficients. The rate of the decomposition reaction can be expressed by the following:

$$\frac{d\alpha(t)}{dt} = k(T)f(\alpha) \quad 6.2$$

where, α is the progress of the reaction, which can be expressed in different ways based on the available measured variable(s). Usually, the extent of reaction is defined in terms of the change of mass of the sample or an equivalent basis in terms of gas consumed, gas evolved, heat consumed or heat evolved. In the present study, the degree of conversion was defined using TGA data. Thus, the solid conversion (α) during each solid-state reaction was calculated as:

$$\alpha(t) = \frac{w_i}{w_t} \quad 6.3$$

where, w_t is the total mass lost, and w_i is the cumulative mass lost, which varies with time through the reaction. The rate constant (k) is given by the Arrhenius equation:

$$k = k_0 \exp \left[\frac{-E_{app}}{R} \left(\frac{1}{T} - \frac{1}{T_m} \right) \right] \quad 6.4$$

where, E_{app} is the activation energy, k_0 is the pre-exponential factor and T_m the centering temperature that help minimizing cross-correlation between parameters.

Generally, the experimental α -t (conversion–time) profiles of a gas-solid reaction shows a sigmoid shape, and can be modeled by a nucleation and nuclei growth mechanism. This model is known as the Avrami-Erofeev (A-E) model²¹⁰⁻²¹² and was originally applied to describe the kinetics of phase transformations of steel. Later on, it found numerous applications in the kinetics of crystallization, precipitation,

decomposition of various solids, thin film growth and polymerization. According to the Avrami-Erofeev model:

$$f(\alpha) = n(1 - \alpha) [-\ln(1 - \alpha)]^{\frac{(n-1)}{n}} \quad 6.5$$

where, n is the Avrami exponent indicative of the reaction mechanism and crystal growth dimension. Different values of the n parameter lead to, as reported in Table 6.1, random nucleation, 2-dimensional nuclei growth and 3-dimensional nuclei growth.

After rearrangement, the following form of equation is obtained:

$$\frac{d\alpha(t)}{dt} = nk_0 \exp\left[\frac{-E_{app}}{R} \left(\frac{1}{T_0 + \beta t} - \frac{1}{T_m}\right)\right] (1 - \alpha) [-\ln(1 - \alpha)]^{\frac{(n-1)}{n}} \quad 6.6$$

with T_0 being the initial temperature and β the heating rate.

Table 6.1: Avrami-Erofeev models ²¹³

Value of n	Mechanism	Model formulation
n	Avrami-Erofeev model	$f(\alpha) = n(1 - \alpha) [-\ln(1 - \alpha)]^{(n-1)/n}$
1	Random nucleation	$f(\alpha) = 1 - \alpha$
2	2-dimensional nuclei growth (2D Avrami-Erofeev model)	$f(\alpha) = 2(1 - \alpha) [-\ln(1 - \alpha)]^{1/2}$
3	3-dimensional nuclei growth (3D Avrami-Erofeev model)	$f(\alpha) = 3(1 - \alpha) [-\ln(1 - \alpha)]^{2/3}$

However, the conversion-time (α - t) profile is not always sigmoidal. Brown reviewed alternate models to describe the gas-solid kinetics and its effects on the α - t profiles.²¹⁴ In the kinetic analysis of solid state reactions, the following rate equations, as provided in Table 6.2, are usually used to describe the different α - t curves in addition to the Avrami-Erofeev model.

Table 6.2: The important rate equations used in kinetic analysis of solid-state reactions

α -time curves	$f(\alpha)$
Acceleratory α -t curves	
Power law	$n(\alpha)^{(n-1)/n}$
Exponential	α
F nth order	$(1-\alpha)^n$

These models were evaluated in this chapter by using MATLAB (ODE 45 and LSQCURVEFIT) least square fitting of the kinetic parameters. The evaluation of reaction rate parameters was conducted using the TGA data points taken once every 10 °C interval and the samples were heated from room temperature to 500 °C at a 10 °C/min heating rate in flowing air using 20 mL/min flowrate.

6.1.2. Phase Transformation

Non-isothermal crystallization techniques are widely used for determining crystallization parameters, as they typically produce well-defined crystallization peaks that are usually easier to observe on the temperature–time or heat flow–temperature profiles. Therefore, the activation energy for crystallization of 10% ZrO₂-TiO₂ nanotubes was studied using the peak temperature at different heating rates from DSC curves by Kissinger's equations:²¹⁵

$$\ln(\beta / T_p^2) = -E / RT_p + const \quad 6.7$$

where, T_p is the peak temperature in Kelvin.

However, the activation energy (kJ/mol) of isothermal phase transformations can also be calculated from the slope of a plot of Ln rutile weight fraction versus the

reciprocal of annealing temperature from XRD spectra according to Burns et al.²¹⁶ This relationship is given as:

$$E_a = -\frac{\partial \ln(X_r)}{\partial (1/T)} \cdot R \quad 6.8$$

where T is the temperature in Kelvin, R is the universal gas constant (8.314 J/mol·K), and X_r is the weight fraction of the rutile phase as determined using Eq. (6.8).

6.2. Experimental

10% ZrO₂-TiO₂ nanotubes were synthesized following the procedure previously described in chapter 3, with the synthesized materials calcined at different temperatures. The effects of calcination temperature on the morphology, phase structure, mean crystallite size, specific surface area, and pore volume were investigated using a variety of physicochemical characterization techniques and given in the following section.

6.2.1. SEM/TEM

The effects of calcination temperature on the morphology of the ZrO₂-TiO₂ nanotubes size and shape was characterized by SEM and TEM analysis. In the SEM analysis for the as prepared materials, it can be seen in Figure 6.1(a) that the aerogel powders were composed of a one dimensional structure, with the nanotubes having a diameter of 50–140 nm and a length of several μm's. Throughout the course of heat treatment, phase changes (amorphous to anatase to rutile) and sintering phenomena of the nanotubes was revealed by the SEM and TEM investigation. The SEM image in Fig. 6.1(b) shows that the material calcined at 500°C has a similar structure, although very small holes are visible on the walls of the nanotubes. The morphology of the calcined

nanotubes at 800°C is still preserved, as shown in Fig. 6.1(c). As the temperature was further increased to 1000°C, the initial nanotubes disappeared and were replaced by nanometer sized aggregated particles in the 50-100 nm size range, as shown in Fig. 6.1(d).

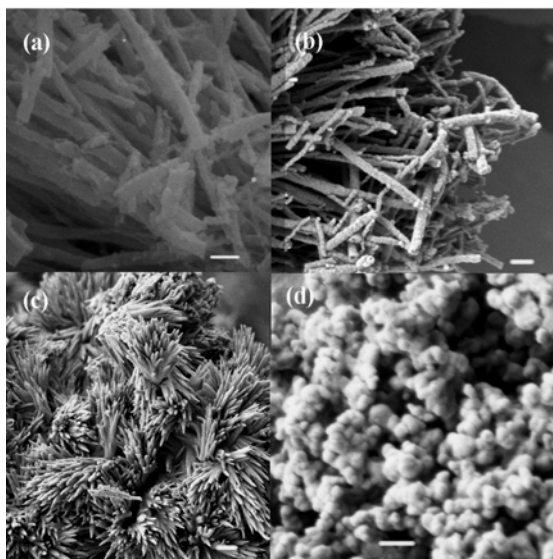


Figure 6.1: SEM: Zr-TiO₂ nanotubes calcined at (a) as-prepared, (b) 600, (c) 800 and (d) 1000 °C. (Bar represents 200 nm. All the samples were examined after platinum coating.)

Along with SEM, TEM images gave more detailed morphological information on the tubular structure. The TEM image in Fig. 6.2(a) indicates that the as-prepared nanotubes possessed uniform inner and outer diameters having thickness ca. 14-50 nm along their length. Upon heat treatment to 500 °C, the chemically bonded organic layer was removed from the synthesized nanotubes, resulting in small holes on the tube wall, which was confirmed by the TEM image in Fig. 6.2(b), although the internal structure was still maintained at this temperature. The SEM images showed that the outer morphology was preserved at 800 °C, although at 900 °C, the TEM images show that the

inner hole has almost vanished with this additional heat energy (Fig. 6.2(c)). The TEM images along with SEM images reveal that the nanotubes were deformed and the crystallites were fused together when the calcination temperature was increased to 1000°C (Fig. 6.2(d)).

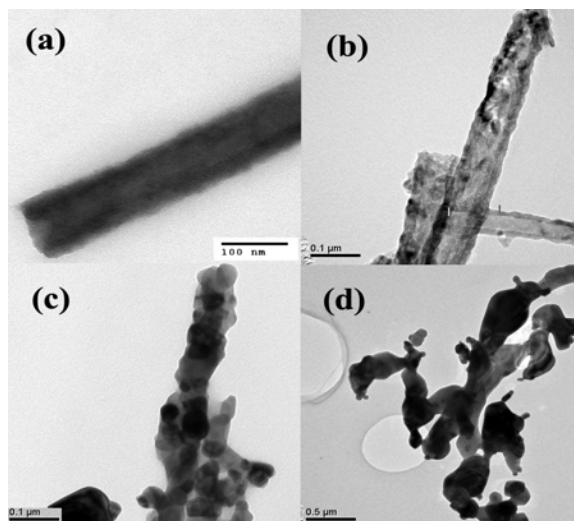


Figure 6.2: TEM: $\text{ZrO}_2\text{-TiO}_2$ nanotubes calcined at (a) as-prepared, (b) 500, (c) 900 and (d) 1000 °C.

6.2.2. Decomposition Behavior (TGA/FTIR)

TG–DTG analysis was carried out to study the thermal decomposition behavior of the synthesized $\text{ZrO}_2\text{-TiO}_2$ nanotubes. Figure 6.3 shows three main peaks in the TG-DTG analysis, which are in the ranges of 20–120°C, 120–250 °C and 250–500 °C. The first stage with peak maxima at 37 °C gave only 6% wt. loss, which we attribute to the removal of residual solvent present in the synthesized materials. The second peak with its maximum at 200 °C is attributed to the removal of bounded water and chemically bonded organic material, with ca.19 % wt. lost at this stage. The third peak, with its maximum at

341 °C, is broad and is attributed to the removal of any bonded/co-ordinated organic material and –OH groups, with ca. an additional 21% wt. loss at this temperature. The weight loss over 500°C was extremely small (0.14%) and attributed to removal of bounded -OH groups. The total weight loss measured from the TG curve was 46 wt%.

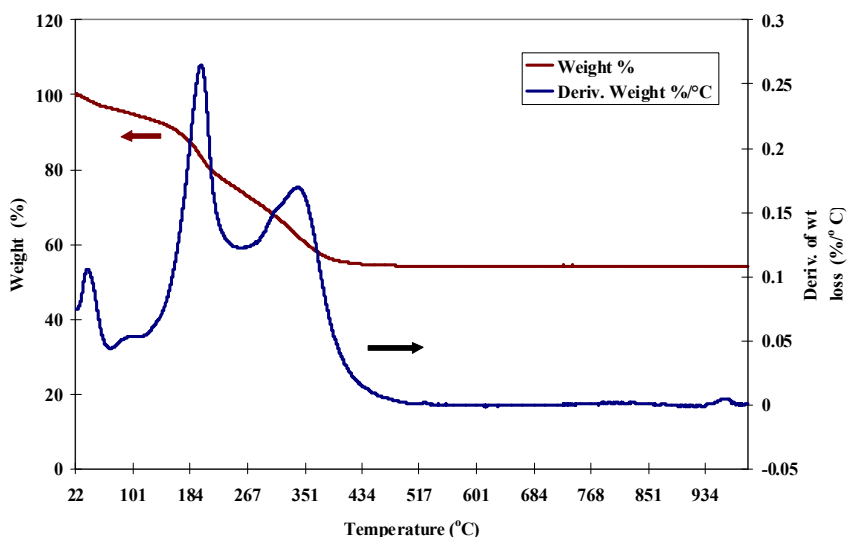


Figure 6.3: Weight loss of nanotubes as a function of temperature.

Elemental analysis (EDX) was also performed to investigate the change of composition with calcination temperature. It showed that the as-prepared nanotubes contained ca.30% carbon with this value decreasing upon increasing calcination temperature. At 300 °C, the carbon content was about 18%, while when the temperature was increased to 500 °C; all carbon containing organic material was removed, consistent with the TG-DTG results. Materials calcined at higher temperatures had only metal, oxygen, and a ratio of oxygen to metal atom change with temperature. Surfaces of metal oxides consist of unsaturated metal and oxide ions, and are usually terminated by -OH

groups. The -OH groups are formed by dissociative adsorption of H₂O molecules to reduce the coordinative unsaturation of the surface sites. It is very difficult to analyze the amount of oxygen bonded with metal atoms only by the EDX method, as the amount of H present in the materials cannot be determined by EDX due to the low atomic weight of H.

Infrared spectroscopy is an excellent method to study the behavior and properties of metal oxides.²⁰⁹ The powder ATR-FTIR spectra of the ZrO₂-TiO₂ nanotubes calcined at different temperatures in air are given in Figure 6.4. The spectra (Fig.6.4(a)) for the as-prepared nanotubes shows a broad peak at 3400 cm⁻¹, assigned to the -OH group of absorbed water.¹⁸⁴ The peaks at 1548 and 1452 cm⁻¹ are due to symmetric and asymmetric stretching of the zirconium titanium acetate complex, respectively.¹⁵² This metal acetate complex confirms that the acetic acid formed bridging complexes with the metal ions, helping to stabilize the structures during their synthesis and self-assembly into nanotubular structures in scCO₂. The -CH₃ group contributes the small peak at 1343 cm⁻¹, while the two small peaks at 1037 and 1024 cm⁻¹ correspond to the ending and bridging -OPr groups, respectively,¹⁵¹ indicating that unhydrolyzed -OPr groups were present in the as-prepared materials.⁹⁸ The oxo bonds can be observed by the bands present below 657cm⁻¹.¹⁵² Calcination at 400°C significantly diminishes the intensity of the C-H stretching at 2800-3000 cm⁻¹ and the zirconium titanium acetate complex band is observed at 1548 and 1452 cm⁻¹, as shown in Fig.6.4(b). This indicates that the calcination at 400°C removes any organic material present in the as-prepared nanotubes. No trace of IR bands from the organic groups was detected upon further heat treatment (Fig. 6.4(c)) and the broad peak at 3400 cm⁻¹ significantly decreased. The nanotubes

calcined at 1000 °C showed only a small band at 3400 cm^{-1} (Fig.6.4(d)) indicating only a small amount of -OH groups were still present at this high temperature. These results are consistent with the TG–DTG measurements, and the electron microscopy results.

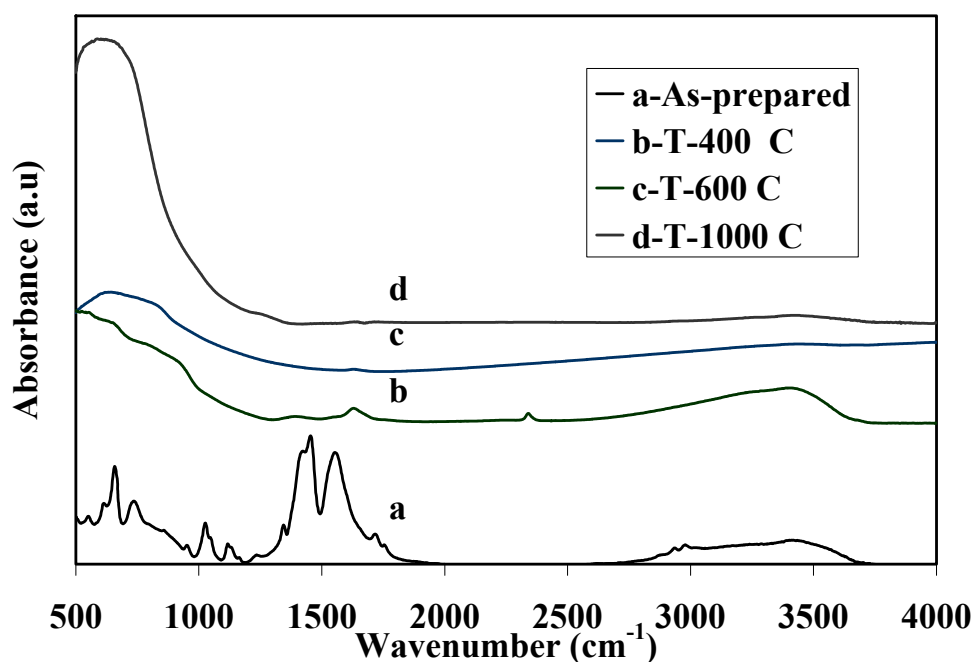


Figure 6.4: Powder ATR-FTIR spectra of $\text{ZrO}_2\text{-TiO}_2$ nanotubes calcined at different temperatures.

6.2.3. XRD and HRTEM

In order to examine the phase structure and crystallite size, XRD and HRTEM were used to investigate the effects of the calcination temperature on the crystal size and phase structure. During heat treatment, the as-prepared materials transferred from the amorphous to anatase to rutile phases. The XRD patterns (Figure 6.5) of all the calcined samples indicate that the $\text{ZrO}_2\text{-TiO}_2$ nanotubes consist of anatase crystal, with no rutile phase being present up to 700°C. The as-prepared materials were amorphous, while when

increasing the calcination temperature up to 400 °C, the material reorganized itself, and the anatase particles began to grow, resulting in crystalline material. There was no distinct Zr peak indicating no phase separation, and the Zr was integrated within the anatase crystal structure for this composition. Previous experiments showed that increasing concentrations of Zr alkoxide were incorporated homogeneously into the

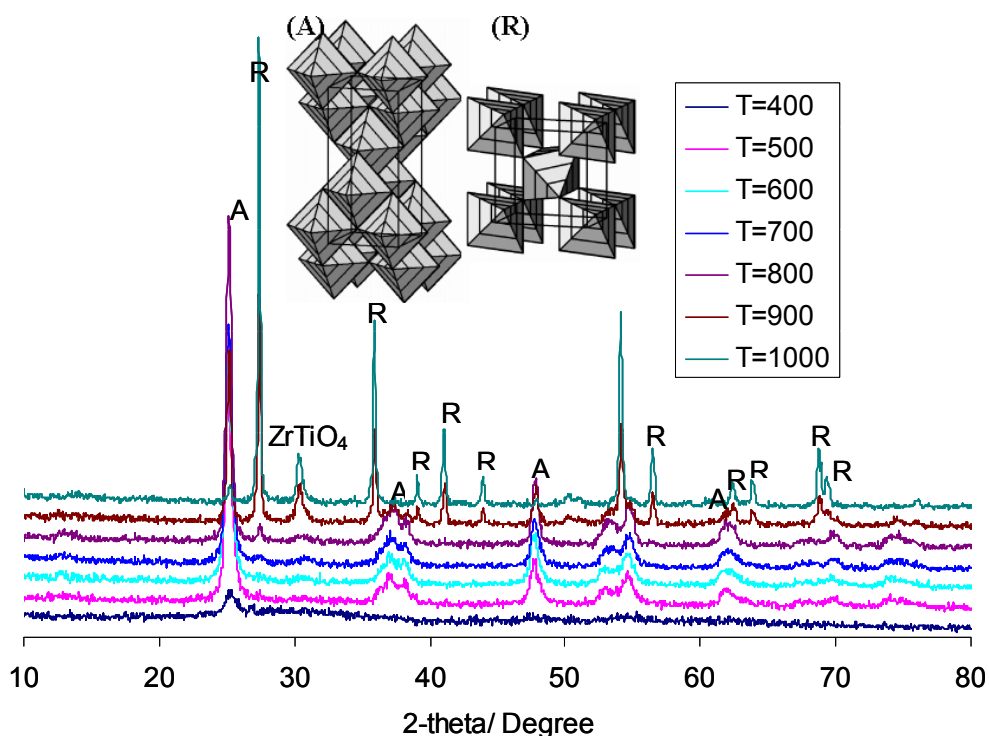


Figure 6.5: Powder XRD spectra of ZrO₂-TiO₂ nanotubes calcined at different temperatures. (*A*-anatase, *R*-rutile).

nanotubular structure.¹²⁰ As well, we previously prepared a crystal of Zr₂Ti₄(μ₃-O)₄(OPr)₄(μ-OPr)₂(μ-OAc)₁₀ using lower concentrations of acetic acid,¹⁸⁵ showing that the Zr is part of the crystal hexamer structure. By increasing the calcination temperature from 400 to 800 °C, the peak intensities increased as well as the width of the peaks

became narrower, indicating an improvement of the anatase phase, and simultaneously the growth of anatase crystallites. The XRD patterns for the observed nanotubes indicate that no rutile phase appeared up to calcination temperatures of 700°C. It also shows that heat treatment at 800°C forms a very small peak of the rutile phase, and further heat treatment increased the amount of rutile phase, and a new peak appeared at $2\theta = 30.4^\circ$, which is assigned to zirconium titanium oxide ($ZrTiO_4$).²⁰⁹

The crystallite sizes of the calcined samples are summarized in Table 6.3, and were estimated from these XRD patterns using Scherrer's equation:

Table 6.3: Crystal size and crystal structure at different calcination temperatures.

Sample (Cal.Temp°C)	Crystallite size (nm) ± 2.2	Crystal structure
As-prepared	-----	Amorphous
T-400	9.8	Anatase
T-500	12.5	Anatase
T-600	15.9	Anatase
T-700	19.5	Anatase
T-800	21.8	Anatase (88%)
	48.1	Rutile (12%)
T-900	27.8	Anatase (42%)
	69.5	Rutile (58%)
T-1000	28.3	Anatase (6%)
	90.8	Rutile (94%)

For the nanotubes calcined at 400°C, crystallite sizes of ca. 9.8nm were calculated, while further heat treatment increased the crystallite size moderately. Nanotubes calcined at 800°C gave crystallite sizes up to 21.8 nm, resulting in smaller crystallite materials, indicating that a small amount of zirconia inhibited grain growth during heat treatment.⁸³ The rutile crystallite size was calculated by Scherrer's equation

using rutile (110). The obtained crystallite size was >90 nm at 1000 °C calcination temperature, smaller than the value reported in the literature for rutile crystallites,¹⁸⁴ likely due to the constrained geometry of the nanotubular structure. The TEM images of the 1000°C calcined nanotubes previously showed that the crystallites were fused together forming larger crystallites. It is known that rutile and anatase share two and four polyhedra edges, respectively, although both are tetragonal.²¹⁷ Due to changes in the crystal structure, the nanotubes morphology deformed at higher calcination temperatures. The phase compositions of the calcined samples are also reported in Table 6.3, and were calculated using the integrated intensities of anatase (101) and rutile (110) peaks by the equation developed by Spurr and Myers:¹⁵⁹

$$X_{rutile} = \frac{1}{1 + K(I_a/I_r)} \quad 6.9$$

where I_a and I_r are the integrated peak intensities of the anatase and rutile phases, respectively, and the empirical constant K was taken as 0.79. From Table 6.3 it can be seen that the material calcined at 800°C contained only 12 % rutile. Further heat treatment caused a dramatic increase in both the composition and size of the rutile particles, where at 900°C, 58% of the material was converted into rutile, which increased to ca 94% at 1000°C.

Rutile is the most stable crystalline phase of TiO_2 , and the phase transformation (anatase to rutile) depends on both the size and dopant present in the system.⁸³ Sui et al. reported that anatase-type TiO_2 nanostructures transformed into rutile phase (56 %) after calcination at 600°C¹⁴⁹, whereas only 12 % of the nanomaterial was converted into rutile at 800°C in the present study. Hence, consistent with the literature for non nanotubular

structures,⁵³ the anatase phase of the bimetallic nanotubes can be stabilized by modifying titania with a small amount of ZrO₂. However, the mechanism by which the zirconia stabilizes the TiO₂ anatase phase at higher temperatures is unclear.

As shown in the XRD data, no distinct zirconium peak was observed, indicating that zirconia was well-integrated into the anatase structure. This suggests that particle agglomeration was not favored, and the particles grew by the Oswald ripening process during heat treatment.⁸³ Due to the presence of Zirconia, the Oswald ripening process was restricted, reducing the crystal growth rate and increasing the phase transformation temperature. Once individual crystallites reach a threshold size, a spontaneous phase change can occur. The rapid growth of rutile particles formed during heat treatment suggests that the growth mechanism consists of particle agglomeration or grain coalescence by grain boundary diffusion.²¹⁸ There may be a threshold size limit for this transformation, below which no transformation occurs, which was >27 nm for this study, similar to that reported for SiO₂ and ZrO₂ doping in a titania matrix.^{83, 218} For this reason, no rutile phase appeared up to 700°C. When calcined at 800°C, the crystallites size became > 27 nm, and the anatase phase started transforming rapidly into rutile phase.

In addition to the XRD data, detailed information on the structural transformations and crystal growth can be obtained using HRTEM. The HRTEM micrographs of the as-prepared nanotubes were amorphous (Fig.6.6 (a)) with no ordered structure. The lattice image of nanotubes calcined at 500 °C is given in Fig.6.6 (b), showing a grain size of ca.12 nm width with d-spacing 0.35 nm, very close to the lattice spacing of the (101) planes of the anatase phase. However, all grains were not the same in terms of size and shape. Some were long with significant lattice mismatch and grain

boundaries. All these defects prevent rapid grain growth. The HRTEM image for the material calcined at 1000 °C is given in Fig.6.6(c), where little amorphous phase is observed. The crystallites were very large having a d-spacing of 0.245nm, whose value is very close to the rutile (110) plane of TiO₂. These observations also support the XRD and TEM analysis.

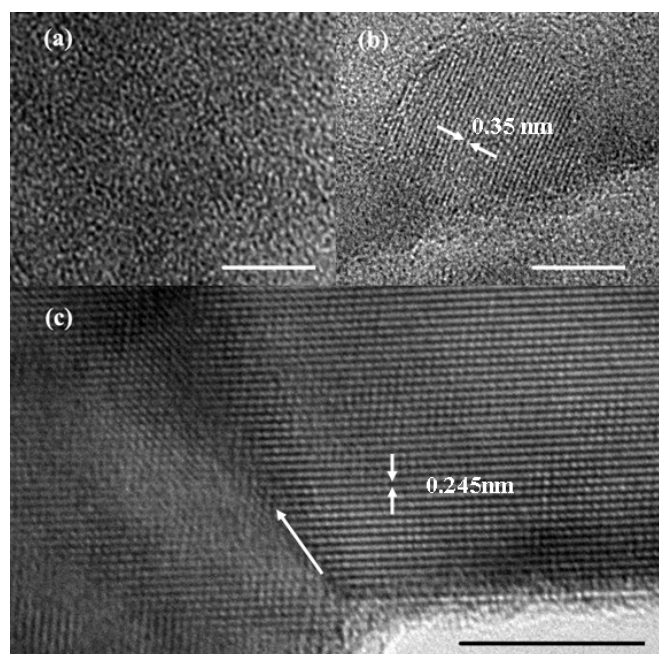


Figure 6.6: HRTEM: ZrO₂-TiO₂ nanotubes calcined at (a) as-prepared,(b) 500, and (c) 1000 °C. (Bar represent 10 nm.)

6.2.4. Raman

To further verify these results, Raman spectra for the bimetallic nanotube samples were measured for several different calcination temperatures, as shown in Figure 6.7. The spectrum for the sample calcined at 500°C (Fig.6.7(a)) shows raman peaks at 142, 395, 517 and 639 cm⁻¹, that can be assigned to the E_g, B_{1g}, B_{1g} /A_{1g}, E_g, modes of the anatase of titania respectively, which agrees with published values.²¹⁹ With increasing calcination

temperature in Fig 6.7(b-d), the intensity of the anatase phase increased, indicating a larger particle size being present with the anatase peak shifting to lower frequencies. Lottici et al ²²⁰ explained this effect as the size-induced pressure effect on the vibrational modes, with the smaller the crystallite size, the higher the pressure and Raman frequencies. After calcining at 900°C (Fig.6.7(e)), three new peaks at 230, 442 and 612 cm^{-1} appeared, which match the literature values for the rutile phase.^{219 220} Upon calcining at 1000°C (Fig 6.7(f)), all anatase related peaks vanished and only the rutile related peaks remain, indicating complete anatase to rutile phase transformation. The Raman results agree with the previous characterization results.

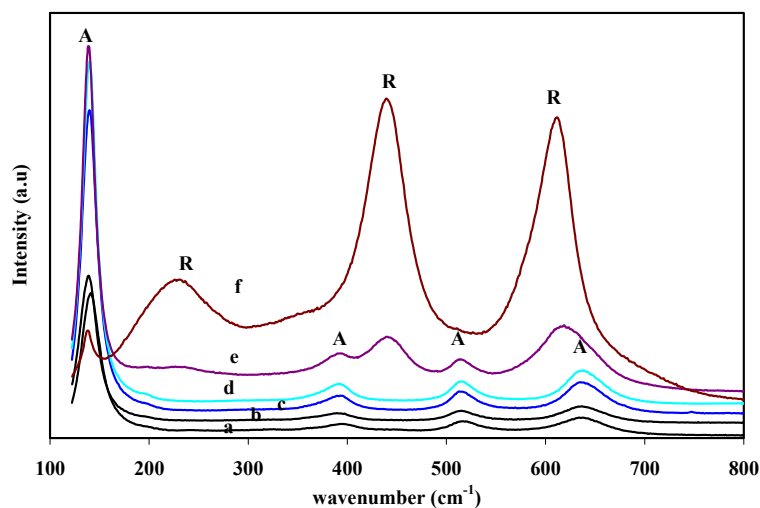


Figure 6.7: Raman spectra of $\text{ZrO}_2\text{-TiO}_2$ nanotubes calcined at: (a) 500, (b) 600, (c) 700, (d) 800, (e) 900, and (f) 1000 °C. (*A-anatase, R-rutile*).

6.2.5. BET Analysis

The textural properties, i.e. the surface area, pore volume, and pore size distributions of the as-prepared and calcined bimetallic nanotubes were characterized by

nitrogen adsorption studies. Figure 6.8 shows the nitrogen adsorption isotherms for both the as-prepared and calcined materials, which exhibit H3 hysteresis loops (to 800 °C), typical for mesoporous materials. The isotherm for the bimetallic metal oxide nanotubes calcined at 1000 °C changes to a type I isotherm, typical for a microporous material.¹⁶⁰ The lower limit of the relative pressure for the hysteresis loop is characteristic of a given adsorbate at a given temperature.¹⁹⁸ It can be seen from Fig. 6.8 for both the as prepared nanotubes, and for those calcined at 300 and 400 °C that the lower pressure limit of the hysteresis loop is at $P/P_0 = 0.4$. Calcinations at higher temperatures increase this value, e.g. at 600 °C, P/P_0 increases to ca. 0.55, while after 800 °C this value increases to 0.6, indicating that the pores are becoming larger as the materials are calcined at higher temperature.

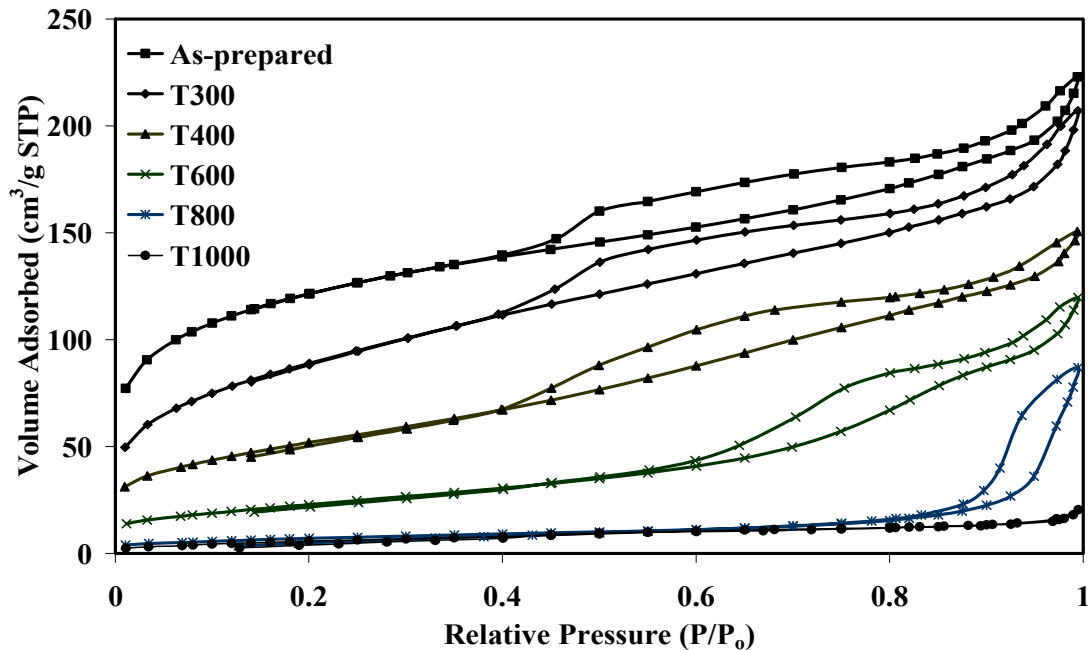


Figure 6.8: N₂ adsorption/desorption isotherms of ZrO₂-TiO₂ nanotubes calcined at different temperatures.

To evaluate the pore size distribution, the as-prepared and calcined materials were plotted as shown in Figure 6.9. The average pore diameter for the as-prepared nanotubes is ca. 3 nm, whereas upon calcination, the pore size became gradually larger and the pore size distribution shifted forming larger pores in expense of the smaller ones. At 600 °C the pore size is ca. 9 nm while when the nanomaterials were calcined at 800 °C, the pore size became more than double ca.19 nm. Calcining the materials at 1000 °C collapsed the small pores, resulting in only larger pores.

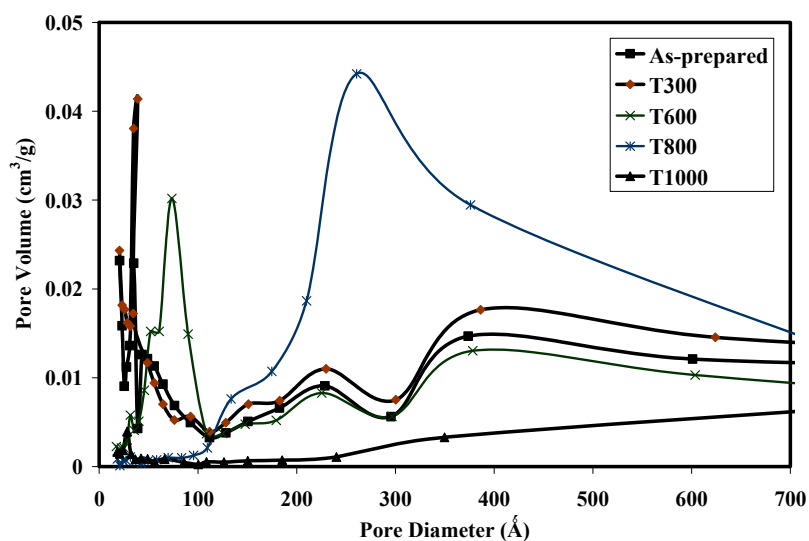


Figure 6.9: BJH pore size distribution of the $\text{ZrO}_2\text{-TiO}_2$ nanotubes calcined at different temperatures.

The surface properties of the $\text{ZrO}_2\text{-TiO}_2$ nanotubes calcined at different temperatures are summarized in Figure 6.10. The as-prepared $\text{ZrO}_2\text{-TiO}_2$ nanotubes having a surface area of $430 \text{ m}^2/\text{g}$, gradually decrease through calcination. Due to the sintering phenomena, the small pores collapse, reducing the pore volume and surface area. The transformations into anatase and rutile crystalline phases will also help to

reduce the surface area. Interestingly, literature values show that pure TiO_2 has almost zero surface area at this high temperature.^{39, 221} Hence, the presence of 10 % zirconia increased the thermal stability, and reduced grain growth rates during the course of heat treatment resulting in moderate ($23 \text{ m}^2/\text{g}$) surface areas at very high temperature.

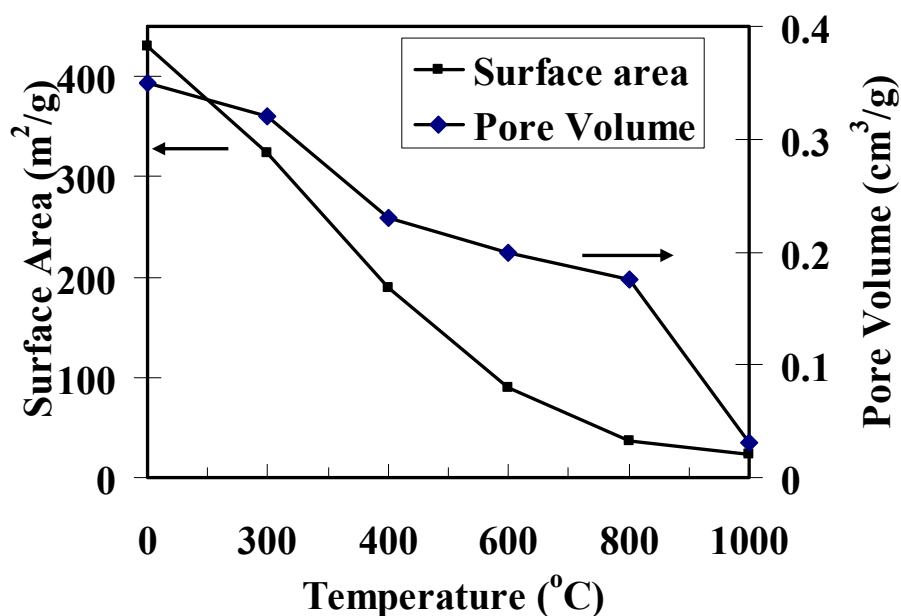


Figure 6.10: Surface area and pore volume of $\text{ZrO}_2\text{-TiO}_2$ nanotubes as a function of calcination temperature.

6.3. Solid State Reaction Kinetics

Kinetic analysis for the thermal decomposition of the as-prepared binary nanotubes was performed according to the models described previously in the introduction section using the TG data. The experimental α -t profiles were examined by fitting the rate equations mentioned previously. For model selection, the calculated value of R^2 was taken as the criterion, and the model with the largest R^2 values selected. The results of the kinetic investigation are shown in Fig. 6.11 and the kinetic parameters are

provided in Table 6.4. It was shown that decomposition generally occurs in two steps: removal of physically absorbed organic residue which occurred up to 200 °C, and then decomposition of chemically bounded organic material continues up to 500 °C. A similar result was reported by He et al.²²² using evolved gas analysis during heat treatment of Ti(OH)₄ hydrogel synthesized by hydrolysis of TiCl₄ with ammonia solution to produce TiO₂ nanocrystal. By observing the different components in the evolved gases, i.e. water at below 230 °C and CO₂ and water between the temperature range 230-900 °C, they proposed the weight loss below 230 °C is due to desorption of adsorbed molecules and in the temperature range of 230-900 °C is due to the combustion of carbonaceous residues. In this project, though evolved gases were not analyzed, the mathematical analysis of the α -t profiles following two different models indicated physically and chemically bounded organic material was decomposed following different mechanisms. The first step ($0 \leq \alpha \leq 0.47$) was best fitted with the second order equation F2 and the calculated activation energy is 25.77 ± 1.4 kJ/ mol and the pre-exponential coefficient equals 3.1×10^{-3} . The second step ($0.47 \leq \alpha \leq 0.97$) was fitted best with the Avrami–Erofeev model with $n=1$ indicating random nucleation and growth processes. The calculated activation energy for the second stage is provided in Table 6.4 i.e. 68 ± 1 kJ/ mol and the pre-exponential coefficient equals 0.3×10^{-3} . The good agreement of the theoretical and experimental degree of conversion values supports the validity of these models. Usually, the decomposition and transformation are characterized by the processes of nucleation of the new phase and its propagation into the old phase, the acceleratory period being dominated by the nucleation rate of the new phase and the decelerator period by its growth rate.²²³ In this study, the longer acceleratory period indicates that nucleation

processes are dominating. This is understandable because after nucleation, organic residues transfer into easily decomposable compound and are removed quickly under the dynamic air heating. However, the exothermic nature of these reactions will lead to an increase of the actual sample temperature above the programmed one, which will accelerate the combustion reaction. Therefore, at the end of both steps, the experimental conversions show little deviation from the model predicted values.

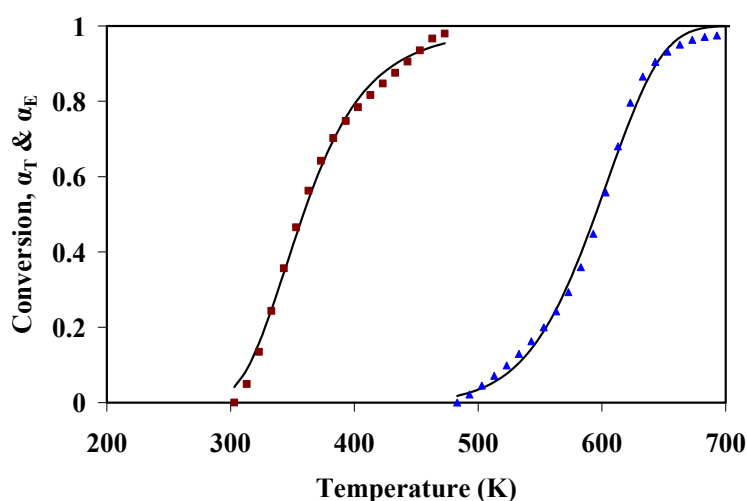


Figure 6.11. Conversion-temperature profiles for different steps of thermal decomposition during heat treatment. [■-Experimental data for step I, ▲- Experimental data for step II, solid line for model predicted value].

Table 6.4: The calculated kinetic parameters for the decomposition of binary nanotubes during heat treatment.

Enviroment	Temp. (K)	Model	n	$k_0 \times 10^3$	E(kJ/mol)	R^2
Air	303-403	Order model	2	3.1	25.77 ± 1.4	0.99
Air	403-773	Avrami-Erofee	1	0.3	68 ± 1.0	0.99

The activation energy for amorphous to anatase and anatase to rutile transformation under non isothermal (NIT) conditions was calculated using the Kissinger equation (Figure 6.12) using the peak temperature in the DSC curves (given in

Appendix). For isothermal (IT) conditions, the phase transformation from anatase to rutile was calculated using Eq. 6.7 as shown by the dashed line in Figure 6.13 for comparison purposes. All calculated activation energies for phase transformation are given in Table 6.5. The activation energy calculated using the NIT method is 131 kJ/mol compared 171 kJ/mol calculated by the IT method. This might be attributed to using different conditions (NIT under dynamic air and IT under static air) and the different experimental techniques. Iida and Ozaki observations support these results²²⁴ as they observed that better crystallinity and phase transformation occurred at lower temperature under flowing air compared to static air, indicating a lower activation energy was required under dynamic air conditions. Therefore, the calculated activation energy from the NIT method is reasonable. In addition, determining the kinetic parameters for crystallization by conventional isothermal heating techniques is tedious and time-consuming. Hence, this NIT method can be used for kinetics analysis of phase transformation.

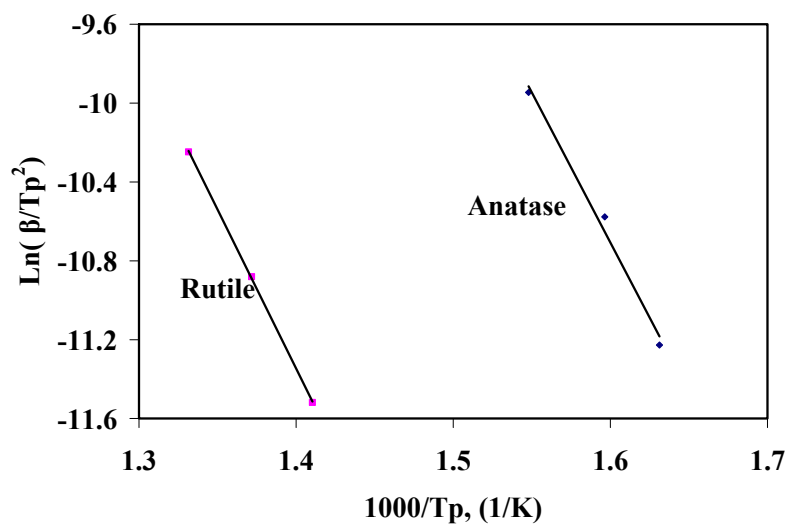


Figure 6.12. Plot of $\ln(\beta/T_p^2)$ vs $1/T_p$ for anatase and rutile phases.

Table 6.5: The calculated activation energy for the phase change of binary nanotubes during heat treatment.

Phase change	Method	E(kJ/mol)	R ²
Amorhous to anatase	NIT	123	0.98
Anatase to rutile	NIT	131	0.99
Anatase to rutile	IT	171	0.93

Figure 6.13 shows the plot of the logarithm of the average crystallite size versus the reciprocal of the calcination temperature (solid lines). A linear relationship is observed and the activation energy for crystal growth of the ZrO₂-TiO₂ nanotubes was calculated as 12.8 kJ/mol and 36.4 kJ/mol for anatase and rutile phases, respectively. These values are higher than those reported for nanocrystalline pure titania,^{216, 225} which is a beneficial effect of Zr doping. In explanation, during the heat treatment, there are two competitive processes: grain growth and A→R phase transformation in the nanocrystalline materials. Both processes are easier for small grain- sized materials because the activation energy for growth and phase transformation is lower.²²⁶

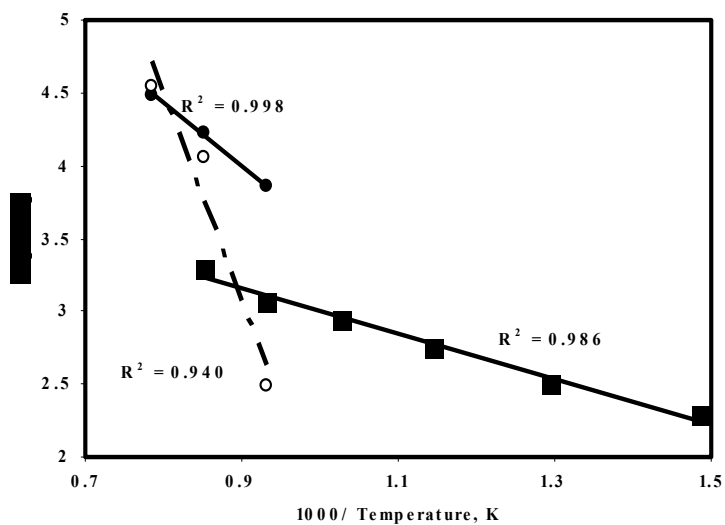


Figure 6.13: Ln of anatase and rutile crystallite size in nm as a function of reciprocal of absolute temperature.(■-Anatase, ●/○rutile).

6.4. Conclusions

The thermal behavior of the $\text{ZrO}_2\text{-TiO}_2$ nanotubes synthesized by an acid modified sol–gel process in scCO_2 has been investigated in detail using SEM, TEM, TG, EDX, FTIR, XRD, HRTEM, Raman and BET analysis. The SEM and TEM analysis confirmed that the morphology of the nanotube structure was preserved at up to 800 °C, whereas further heat treatment deformed the tubes. FTIR and EDX analysis showed that different organic residues were removed depending on the calcination temperature. Along with HRTEM and Raman, XRD results showed anatase nanocrystallites were formed after calcining at 400°C, while no rutile phase appeared until calcining at 700°C, with further heat treatment resulting in a rutile phase transformation and ZrTiO_4 being formed. The activation energy for anatase and rutile crystal growth was calculated and the values were 12.8 and 36.4 kJ/mol, respectively. The activation energy for phase transformation was determined to be 171 kJ/mol, higher than that of the pure TiO_2 nanomaterials. The as-prepared nanotubes had a 430 m^2/g specific surface area (SSA), whereas after calcining at 1000°C, the SSA was reduced to 23 m^2/g . Hence, the ZrO_2 present in the TiO_2 matrix increased thermal stability, reducing grain growth resulting in smaller crystallites, hence preserving the morphology and surface area at high temperatures.

CHAPTER 7

Fe DOPED TiO₂ NANOMATERIALS

7. Introduction

Recently, the sol–gel process is becoming an alternate synthesis route to produce high quality, homogeneous materials with desired nanostructure at low cost.^{96, 196} The sol–gel process involves hydrolysis of a metal precursor to form hydroxide and subsequent polycondensation to form a gel, in an appropriate solvent with/without the presence of a catalyst.¹⁹⁶ At the end of the polycondensation reaction, the excess solvent can be removed by evaporation in an oven at atmospheric pressure (xerogels) or by employing supercritical drying (aerogels). Drying of the gel with supercritical carbon dioxide (scCO₂), forms aerogels, which possess catalytically favourable textural properties resulting in high accessible internal surface areas and consequently the availability of active centers compared to the corresponding xerogels.²⁰³ Therefore, combining the sol–gel technique with supercritical drying is a promising technique to synthesize materials with novel structural and chemical properties that are not easily achieved by other synthesis methods.⁷⁶ Moreover, the strong environmental regulations for reducing VOCs, scCO₂ is becoming an attractive alternative for organic solvents in a wide range of chemical processes due to its nontoxic, nonflammable, inexpensive, naturally abundant, and chemically inert characteristics.^{120, 122, 227} Low viscosity, zero surface tension and high diffusivity of scCO₂ are considered most favorable properties for synthesizing superior ultrafine and uniform nanomaterials. Furthermore, these properties help to increase the reaction rates,^{131, 132} and when the reactions are carried out in scCO₂,

the reaction products can be easily recovered by simply venting the solvent, thus eliminating the drying step, helping to minimize the collapse of the nanostructure. Consequently, the porous structure of the synthesized resultant materials can be maintained. It has been suggested that well ordered mesoporous TiO₂ material may show enhanced catalytic performance due to the large accessible surface area and uniform pore structure. However, several different surfactants have been used as templates to synthesize mesoporous TiO₂, and require high calcination temperatures to remove the template. These problems limit the large scale use of the surfactant assisted synthesis process. Therefore, alternative processes using a green solvent such as scCO₂ is an attractive and promising way to obtain mesoporous materials with enhanced surface area and pore volume.

TiO₂, a widely used photocatalyst, is receiving considerable attention due to TiO₂ having high activity, strong oxidation capability, and chemical stability.^{46, 169, 172, 228-230} However, pure anatase TiO₂ possesses a wide bandgap energy *ca.* 3.2 eV, which is considered a limitation in the practical utilization of this material in solar energy applications. Pure TiO₂ activates at $\lambda < 380$ nm of UV lights, which leaves approximately 95% of the available solar energy unused. In the technical literature, numerous studies have focused on shifting TiO₂'s bandgap to the visible spectral region, that would allow efficient utilization of solar energy and, hence, would greatly expand its application.^{23, 68} Transition metal ion doping is one of the promising approaches to shift the band gap by changing its electronic properties to the visible spectra for absorbing more light. Amongst the various metal ions, due to the unique electronic structure and size that closely matches that of titanium (IV), doping with Fe (III) has been widely used.⁷² However, no

direct correlation between light absorption and photocatalytic activity could be found, and the synthesis process is considered one of the most important factors controlling the reactivity of the Fe-doped TiO₂.^{73, 119} In addition, the literature has shown that the performance of titania nanomaterials also strongly relies on their crystallinity, specific surface area, thermal stability and quantum efficiency.^{17, 50} These properties significantly vary with the synthesis method, type and amount of Fe loading and the subsequent heat treatment.⁷²⁻⁷⁵ Therefore, it is critically important to investigate the effects of Fe doping of TiO₂ which would show superior performance by not only enhancing surface properties but also changing the band gap energy.

This chapter mainly focuses on the effects of Fe doping of TiO₂ nanomaterials by a direct sol-gel process in scCO₂ on the morphology, crystal structure, crystal size, surface area, pore volume, pore size distribution and photo response of the doped nanomaterials.

7.1. Experimental

Fe doped TiO₂ nanomaterials were synthesized at 60 °C and 5000 psig following the standard procedure previously discussed in chapter 3 using the appropriate amount of 1 wt% Fe(NO₃)₃ stock solution and TIP. In a typical experiment, 7.4 mmol TIP, 35 mmol acetic acid and the appropriate amount of stock solution were quickly placed in a 10 mL view cell at 60°C under stirring. CO₂ was added to make the synthesis pressure 5000 psig. After 5 days aging, nanomaterial samples were washed by CO₂. In this category four different samples were synthesized using 0, 1, 1.5, and 2 mL iron stock solution. The starting values of Fe at % in the materials were 0.0, 0.2, 0.36, and 0.49 and named S1, S2,

S3 and S4, respectively. The synthesized materials were calcined at 400, 500 and 600 °C in order to correlate the heat treatment effects on the above mentioned properties of the synthesized nanomaterials. The results of the as-prepared and calcined materials are given below.

7.2. Morphology

The morphology of the synthesized nanomaterials was assessed by SEM and TEM analysis. The SEM images, shown in Fig. 7.1, provide the general morphology and size of the as-prepared undoped and Fe-doped TiO₂ nanomaterials.

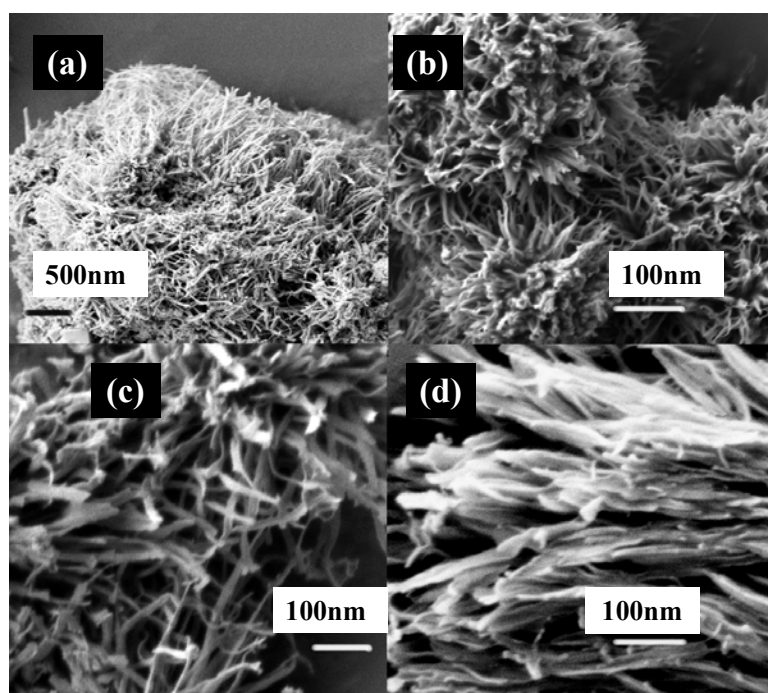
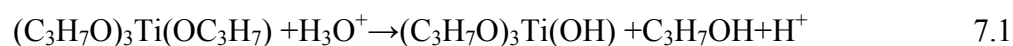


Figure 7.1: SEM: Fe doped TiO₂ nanomaterials: (a) S1-0% (b) S2-0.2%, (c) S3-0.36%, and (d) S4-0.49%. (*Fe in at. %*. All the samples were examined after platinum coating).

From Figure 7.1a, it can be seen that pure TiO₂ nanofibers were formed having 20-50 nm diameters, with lengths up to several microns. Under similar conditions, the Fe doped samples were composed of mainly flake type structures as shown in Figure 7.1b-d. The widths of the flakes become larger with an increased amount of Fe, with dimensions ranging from 20-300 nm. In order to further confirm these results, TEM analysis was conducted for the as-prepared and calcined nanomaterials. The TEM images of the as-prepared pure TiO₂ S1 samples are 50 nm fibers, whereas Fe doped TiO₂ S4 sample are 300 nm sheets (Figure 7.2a and 7.2b). This TEM analysis clearly demonstrates the morphological difference between the unmodified and modified TiO₂ materials. In addition, when calcined at 500 °C, the unmodified TiO₂ (S1) showed larger *ca.*14 nm crystallites (Figure 7.2c) while the Fe doped TiO₂ nanomaterials were porous consisting of smaller *ca.*12 nm crystallites (Figure 7.2d). This analysis shows that the introduction of Fe solution significantly altered the morphology and the properties of the synthesized nanomaterials.

It is believed that the Fe ions impregnate into the TiO₂ matrix, which is mainly responsible for the morphological modification of the doped samples. This hypothesis will be examined further below.

Typically, nanostructure evolution in the modified sol-gel process goes through the following steps: (i) modification, (ii) hydrolysis, (iii) condensation, (iv) nucleation, and (v) growth.¹⁷⁶ After modification, titanium isopropoxide (TIP) undergoes hydrolysis in acidic solution by the following reaction:



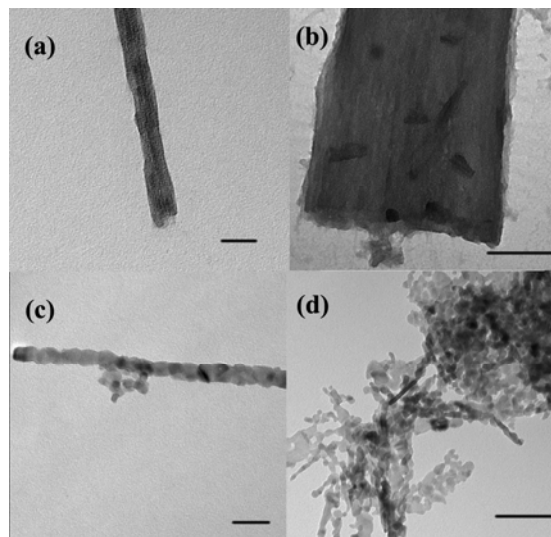


Figure 7.2: TEM: Fe doped TiO₂ nanomaterials: (a) S1-0%, & (b) S4-0.49%, (c) S1, and (d) S4. (*As-prepared (a) & (b), calcined (c)&(d), Bar represent 100 nm.*)

In addition, usually Fe(NO₃)₃ dissociates to produce Fe(OH) in the presence of water according to the following reaction:²³¹



According to the sol-gel principle, the hydrolysis products (Ti-OH and Fe-OH) condense producing metal-oxygen bonds, resulting in the evolution of nanostructure. The reaction rates of the different steps strongly depends on the reactivity of the metal atoms present in the precursors, the working solvents, and the pH of the system. Therefore, the properties of the sol-gel products vary significantly with the above mentioned synthesis variables. The introduction of 1% iron stock solution in isopropanol with pH \approx 0.75, not only changed the pH of the system (pH \approx 2.3) but also increased the solvating ability of the synthesis solvent. The solvating ability of the mixed solvent can be determined using the following equation.^{232, 233}

$$\bar{\delta} = \sum_i \phi_i \delta_i \quad 7.3$$

where, $\bar{\delta}$ is the solubility parameter of the mixed solvent, and ϕ_i and δ_i are the volume fraction and the solubility parameter of solvent i , respectively. The solubility parameters of CO₂ were obtained from Allada's method²³⁴ with the other solvents being calculated using the following equation²³⁵:

$$\delta = \sqrt{\frac{\Delta H_V - RT}{V}} \quad 7.4$$

where, V is the molar volume of the liquid (cm³/mol), ΔH_V is the enthalpy change during vaporization (cal/mol), R is the gas law constant in cal/(mol·K), and T is the temperature in K.

For the unmodified TiO₂ system, considering CO₂ and acetic acid, the solubility parameter was 7.45 (cal/cm³)^{1/2} while for the highest iron containing system (S4) the corresponding value was 8.6 (cal/cm³)^{1/2}. Usually, low solubility promotes supersaturation and inhibits dissolution, reprecipitation, repolymerization, resulting in smaller materials.⁹⁹ The observed morphologies were consistent with this hypothesis. Huang et al. also observed similar effects for N-F-codoped TiO₂ synthesized by the sol-gel-solvothermal method.⁵⁵ However, flakes or a sheet type morphology could not result from the change of the solubility. In order to examine this hypothesis further, TiO₂ was synthesized under the same experimental conditions, i.e. adding the same amount of isopropanol with nitric acid to maintain the pH. It was observed that the morphology of the nanofibers did not change. However, the diameter of the nanofibers became larger, up to 100 nm. Bavykin et al. showed that a sheet-type structure was usually formed using trititanate acid.¹⁰⁶ Yu et al synthesized iron phosphate nanotubes by the solvothermal

process using sodium dodecyl sulfate (SDS) as the template.²³⁶ Rhee et al. synthesized curled nanosheet consisting of a stack of layered ammonium titanate by a simple hydrothermal process using NH_4OH and the titanium precursor.⁵⁸ All the above mentioned works observed that a sheet or flake type nanostructure was formed by addition of Fe into TiO_2 structure. As it is very important to know the composition of the synthesized nanomaterials, XPS analysis was performed. The surface Fe amount was very small, and XPS could not detect Fe. This result is consistent with the published data.⁷³ Interestingly, a very small amount of nitrogen was detected by XPS for the as prepared highest Fe containing system (S4) at the peak position of 399.45 eV. No nitrogen was present in the calcined sample and the literature value for this peak is assigned to N-O.²³⁷ EDX mapping (recorded on a LEO 1530 operated at 20 kV) of the Fe- TiO_2 samples revealed that the Fe and Ti elements are dispersed throughout the samples (Figure 7.3). However, Fe at. % is not uniform. The bulk amount of Fe at % was determined for different samples and given in Table 7.1. The products bulk compositions (0-0.46 \pm 0.1 %) show good agreement with the theoretical values, although it was difficult to detect Fe in S2. From all this analysis, it can be concluded that a flake type morphology from the synthesis in scCO_2 is facilitated from the presence of Fe in the TiO_2 matrix.

Table 7.1: Crystallites size and surface area of undoped and doped nanomaterials calcined at different temperatures.

Sample #	Fe at(%)	crystallites size (nm)			E kJ/mol	Acidity $\mu\text{mol/g}$
		400° C \pm 1	500°C \pm 1	600°C \pm 1		
S1-0.0%	0	9.9	13.7	15.9	11.6	30
S2-0.20%	0.1 \pm 0.1 ^a	9.7	11.9	14.9	10.4	34
S3-0.36%	0.36 \pm 0.1	8.6	11.6	14.6	11.5	40
S4-0.49%	0.46 \pm 0.1	8.8	10.8	13.8	11.2	58

a- Very low concentration difficult to detect.

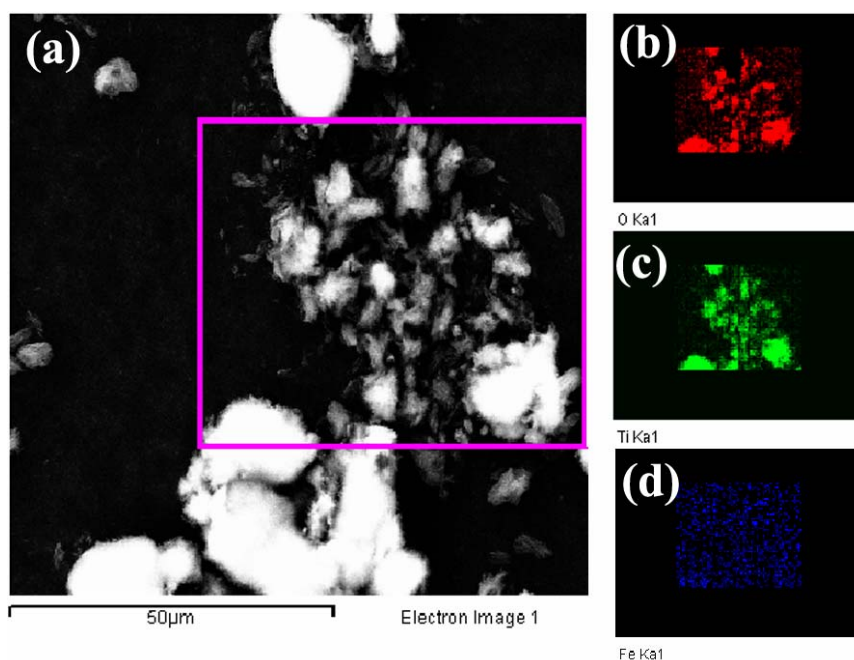


Figure 7.3: O, Ti and Fe mapping for Fe doped TiO₂ (S4) nanomaterials.

7.3. Thermal Analysis

The prepared Fe-TiO₂ samples were further characterized by FTIR analysis to investigate the effect on Fe-doping on the presence of different chemical groups. The powder IR spectra of the as-prepared pure TiO₂ and Fe-TiO₂ nanomaterials are shown in Figure 7.4. As can be seen in this figure, both samples had similar spectra although their peak heights were different at different wavenumbers. The broad peak at 3300 cm⁻¹ is assigned to the -OH group of absorbed water.¹⁵² The peaks at 1548 and 1452 cm⁻¹ are due to symmetric and asymmetric stretching of metal acetate complex, respectively. The frequency difference between the symmetric and asymmetric stretching ($\Delta ca. 100 \text{ cm}^{-1}$) confirms that acetic acid formed bridging complexes with the metal atoms.¹⁵² The small

peaks at 1343 cm^{-1} indicates the presence of the $-\text{CH}_3$ group.¹⁵¹ There were two more small peaks appearing at 1037 and 1024 cm^{-1} , which correspond to the ending and bridging $-\text{OPr}$ groups, respectively. This observation suggests the presence of unhydrolyzed $-\text{OPr}$ groups in the as prepared materials. Sui et al. also reported the presence of $-\text{OPr}$ groups in nanomaterials prepared under similar conditions.^{120, 198} All spectra contain a small peak at 1710 cm^{-1} confirming the residue of unreacted acetic acid. Finally, the bands below 657 cm^{-1} represent the existence of oxo bonds.²³⁸ It is important to emphasize that no peak was detected for the CO_2 , indicating no CO_2 incorporation into the TiO_2 nanomaterials. This powder IR analysis confirms that pure and modified TiO_2 were rather similar in chemical composition.

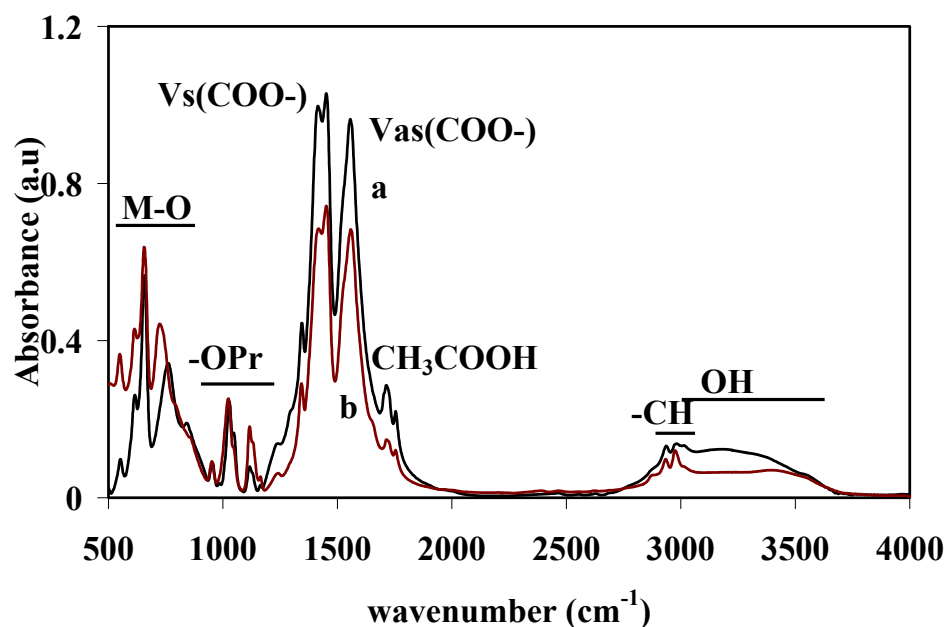


Figure 7.4: Powder ATR-FTIR spectra of as-prepared (a) TiO_2 & (b) Fe doped TiO_2 (S4) nanomaterials.

As mentioned above, although the peak positions were similar, the heights of the peaks were quite different. For instance, if one considers the peaks around 1548 and 1452

cm^{-1} , the amount of metal acetate complex is higher for the unmodified TiO_2 compared to the modified TiO_2 nanomaterials. This indicates that pure TiO_2 contains a greater amount of organic residue compared to that from the Fe doped TiO_2 nanomaterials. In order to obtain more detailed information on the residues present in the as-prepared nanomaterials (which significantly alters the characteristics of calcined products),⁹⁹ TG–DTG analysis was carried out. The results of TG and DTG for the different samples are shown in Figure 7.5. There are three marked stages which are in the ranges (i) 25–125°C, (ii) 125–500°C and more than (iii) 500°C, and the DTG curves in Figure 7.5(b) present two main exothermic peaks corresponding to stages 1 and 2. A small weight loss in the first stage is assigned to the desorption of physically adsorbed water or organic residues. The second exothermic peak is attributed to the burn off of the chemically bonded organic residues. The second exothermic peak is attributed to the burn off of the chemically bonded organic residues.²⁰⁸ The weight loss over 500 °C was extremely small due to only desorption of structural water. Considering the weight loss during stage i, pure TiO_2 lost only 5% wt

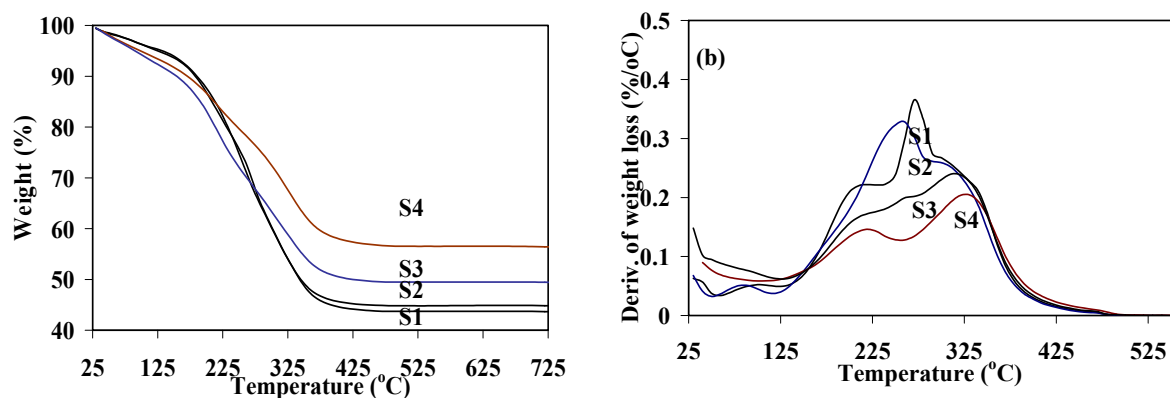


Figure 7.5: (a) TG and (b) DTG curves for Fe doped nanomaterials as a function of temperature.

whereas 9% wt of the modified samples was lost during this stage. Chemically bonded 57% wt of the unmodified TiO₂ nanomaterials was lost during the second stage, whereas only 44% wt lost for the modified nanomaterials during this stage. Comparing this analysis with the FTIR data reveals that Fe doped TiO₂ nanomaterials contain lower amounts of chemically bonded organic residue, and show higher thermal stability. This may be due to the synthesis conditions instead of only the presence of Fe in the TiO₂ matrix. In chapter 6, it was previously shown that in the presence of higher dielectric constant solvents, that more condensed materials were formed, supporting this observation.

7.4. Phase Structure

In order to examine the Fe doping effects on the phase structure and crystallite size, XRD and HRTEM analysis were performed. During heat treatment, the as-prepared materials transform from the amorphous to anatase phases. The as-prepared materials were amorphous, whereas increasing the calcination temperature up to 400 °C, led to the material reorganizing itself, with anatase crystallites beginning to grow, resulting in crystalline material. The XRD patterns (Figure 7.6) of all the calcined samples indicate that the Fe-TiO₂ consists of anatase crystal, with no rutile phase being present. Although all the modified samples consist of anatase crystal, the relative intensity of the peak at *ca.* 25.17° decreased significantly in doped TiO₂ with respect to undoped TiO₂ nanocrystal. There was no distinct Fe peak indicating no phase separation, and demonstrating that the Fe was well integrated into the anatase crystal structure for this composition and calcination temperature. By increasing the calcination temperature from 400 to 600°C,

the peak intensities increased as well as the width of the peaks became narrower, indicating an improvement of the anatase phase, and simultaneous growth of anatase crystallites (Figure 7.4(d-f)).

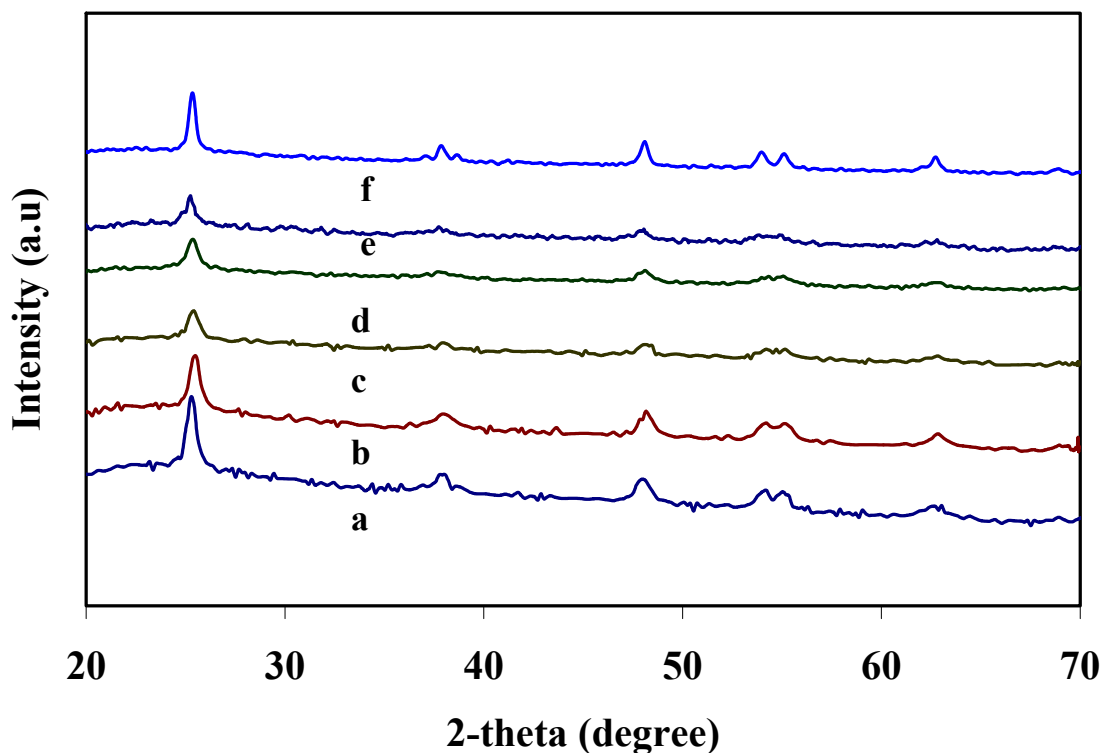


Figure 7.6: Powder XRD spectra of Fe doped TiO_2 nanomaterials: (a) S1- TiO_2 , (b) S2, (c) S3, (a-c) calcined at 500°C (d-f) S4 calcined at $400-600^\circ\text{C}$, respectively.

The crystallite sizes of the calcined samples were estimated from these XRD patterns using Scherrer's equation and are provided in Table 7.1. For the unmodified TiO_2 , the crystallite size was *ca.* 9.9 nm calcined at 400°C , with increasing calcination temperature causing the crystallites to become larger. The sizes were *ca.* 14 nm and 16 nm at 500°C and 600°C respectively. Due to heat treatment, the crystallites also became larger for the doped samples, although the growth rates were lower resulting in smaller crystallite materials at the corresponding calcination temperatures. For example, at 600°C

the doped samples had 14.9, 14.6 and 13.8 nm crystallites for samples S2, S3, and S4 respectively. This analysis along with the literature confirms that a small amount of Fe inhibited the grain growth during heat treatment at moderate calcination temperatures (400-600°C).

In order to quantify the behaviour of the crystal growth, the activation energy required for grain growth of pure and iron doped TiO₂ was estimated using the Arrhenius equation²²⁵:

$$d\ln k/dT = E/RT^2 \quad 7.5$$

where k is the specific reaction rate constant, E is the activation energy, T is the absolute temperature and R is the universal gas constant. It is well established that the value of k is directly related to the grain size. Thus, modification and integration of Equation (7.5) becomes:

$$\ln D = (-E/RT) + A \quad 7.6$$

where D is the grain size and A is the intercept. The plots of lnD versus the reciprocal of absolute temperature 1/T for different samples are linear, as shown in Figure 7.7.

The activation energy for all samples was calculated from the slope of the best fit lines and given in Table 7.1, where the activation energy for anatase crystallites of pure TiO₂ was measured at 11.6 kJ/mol. The activation energy for Fe modified TiO₂ nanomaterials ranged from 10.4-11.5 kJ/mol, and did not show any trend with an increasing amount of iron. However, the values are rather similar to the pure TiO₂ nanomaterial.

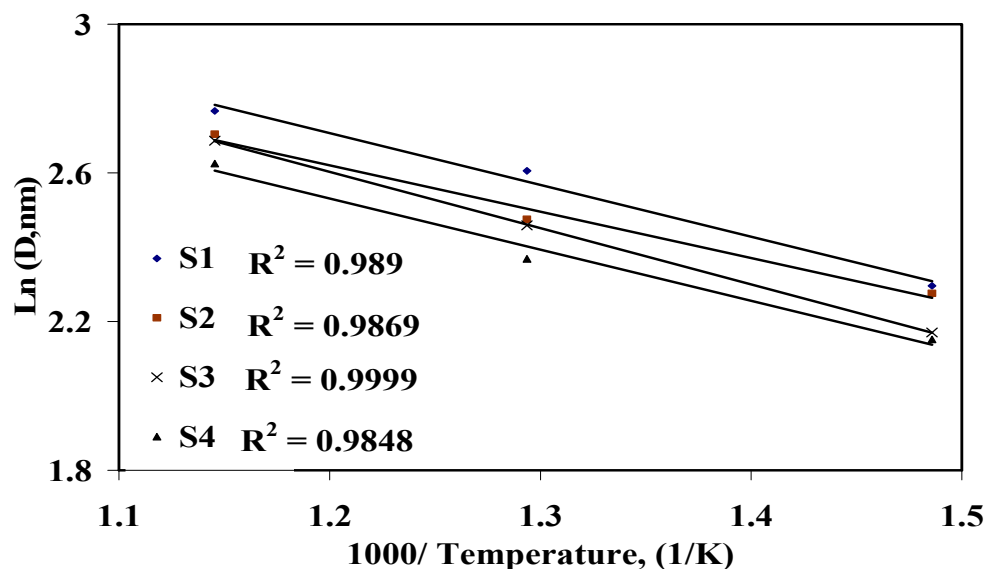


Figure 7.7: Ln size of anatase crystallite in nm as a function of reciprocal of absolute temperature.

In addition to the XRD data, detailed information on the crystal structure, size and defects can be obtained using HRTEM. The HRTEM micrographs of the lattice image of pure titania calcined at 500 °C are given in Figure 7.8(a), showing a grain size of ca.14 nm width with d-spacing 0.35 nm, very close to the lattice spacing of the (101) planes of the anatase phase. The lattice image of doped TiO₂ calcined at 500 °C (Figure 7.8b) shows that these materials are also composed of smaller grain anatase phase. However, all grains were not the same in terms of size and shape. Some were long with significant lattice mismatch and grain boundaries. The HRTEM image also reveals that doped materials are predominately mesoporous.

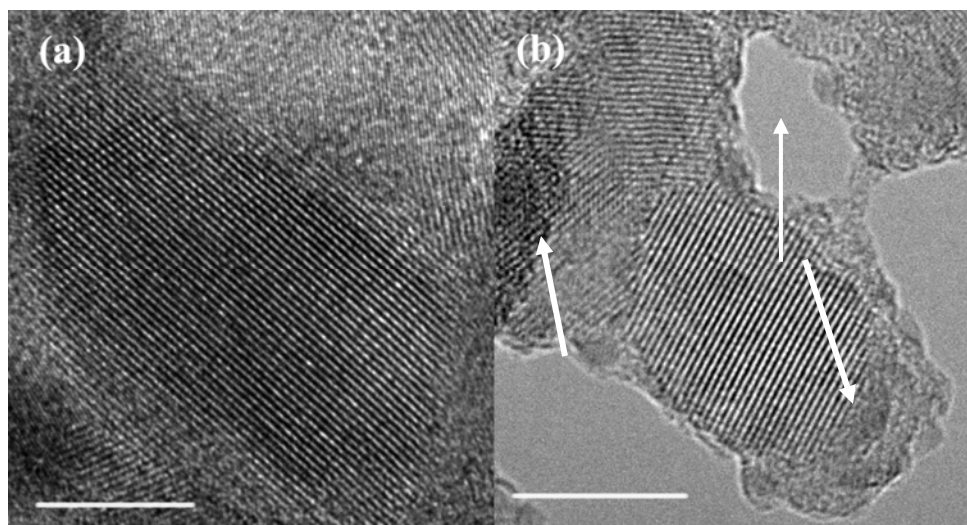


Figure 7.8: HRTEM: (a) S1- TiO_2 , and (b) S4-Fe doped TiO_2 nanomaterials (calcined at 500°C (a) & (b)). (Bar represent 10 nm. Arrows indicate defects and pore).

7.5. Surface Area and Pore Volume

The textural properties, i.e. the surface area, pore volume, and pore size distributions of all samples calcined at 400 , 500 and 600°C were characterized by nitrogen adsorption studies. Figure 7.9a shows the nitrogen adsorption isotherms for the as-prepared materials, which exhibit H3 hysteresis loops for all samples, typical of mesoporous materials.¹⁶⁰ The pore size distributions of the calcined materials are given in Figure 7.9b. The average pore diameter for the pure TiO_2 and materials containing a small amount of Fe i.e. 0.36 at% was *ca.* 11 nm, whereas samples S4 were 20 nm. Upon calcination, the pore size became gradually larger and the pore size distribution shifted to the right, forming larger pores at the expense of smaller ones. At 600°C the pore size was *ca.* 15 nm for all samples except S4, which increased to *ca.* 24 nm. Therefore, Fe doping was favorable for organizing a more ordered mesostructure and maintaining the pore structure at high temperature.

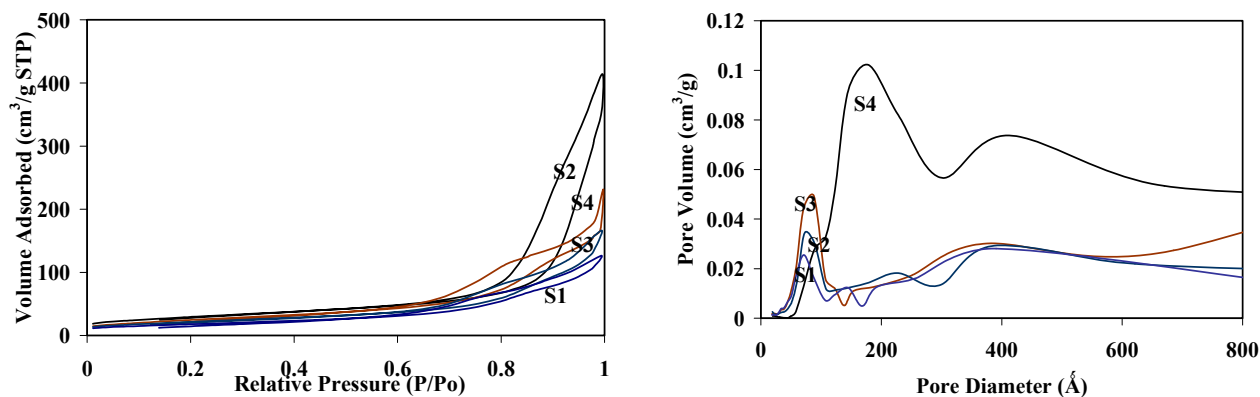


Figure 7.9: (a) N₂ adsorption/desorption isotherms, and (b) BJH pore size distribution of Fe doped TiO₂ nanomaterial calcined at 500 °C.

The surface properties of the Fe-TiO₂ nanomaterials calcined at different temperatures are summarized in Figure 7.10. The 400°C calcined TiO₂ nanomaterials have a surface area of 69 m²/g, and gradually decreased through calcination; becoming 43 m²/g at 600°C. Due to the sintering phenomena, the small pores collapse, reducing the pore volume and surface area. The transformation into anatase crystalline phase is another factor for the reduction in surface area. However, the presence of a small amount of iron inhibits these transformations, resulting in the doped nanomaterials showing higher surface areas compared to the undoped sample. From Figure 7.10, it is very clear that due to heat treatment, the surface area of the doped materials also decreases but the reduction rate was slower. Consequently, the highest iron containing TiO₂ nanomaterials (S4) calcined at 600 °C possess 66.7 m²/g SSA compared to 43 m²/g for pure TiO₂.

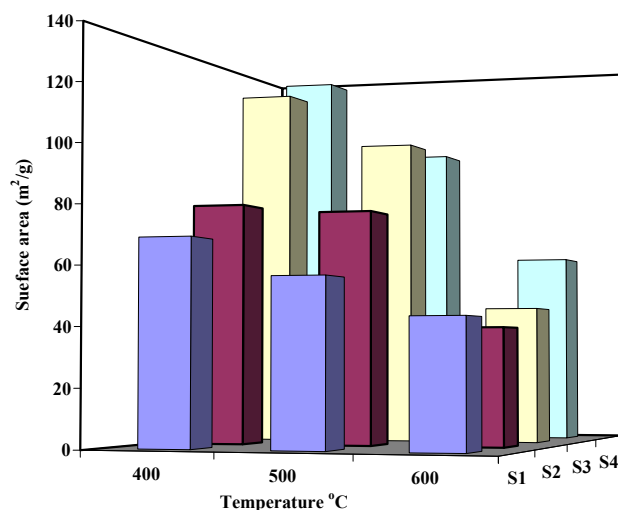


Figure 7.10: BET surface area of Fe doped TiO₂ nanomaterials calcined at different temperatures.

7.6. Surface Acidity

The surface acidity of the catalyst plays an important role in the adsorption of reactants. Moreover, it is well established that adsorption is an important step, which controls the catalytic activity of catalysts. The surface acidity of the synthesized samples was examined by NH₃ chemisorption and is presented in $\mu\text{mol/g}$ of sample in Table 7.1. Pure TiO₂ showed 30 $\mu\text{mol/g}$ surface acidity with this value directly increasing with the Fe content to 34, 40 and 58 $\mu\text{mol/g}$ for samples S2, S3 and S4 respectively. Adan et al. observed similar results for their Fe-doped TiO₂ though they argued that the surface acidity was due to the protons present in the synthesis medium, rather than the presence of iron cations at the sample surface.⁵⁴ However, in a direct sol-gel process no protons were present, confirming that the presence of Fe in the TiO₂ matrix increases surface acidity.

7.7. Photo Response

UV-Vis (diffuse reflectance) spectroscopy is used to analyze the electronic structure of TiO₂ nanomaterials based on the transitions between the valence band and conduction bands (see Section 3.2.7). The diffuse reflectance spectra of the Fe doped TiO₂ nanomaterials calcined at 500 °C are given in Figure 7.11(a). TiO₂ nanomaterials show band-to-band absorption at 380 nm (curve S1). However, all Fe doped TiO₂ nanomaterials exhibit a strong red-shifted band-to-band-type absorption arising from modified nanomaterials (curves S2-S4). A plot of the modified Kubelka-Munk function [$F(R_{\infty})E$]^{0.5} versus the energy of absorbed light E²³⁹ given in Figure 7.11(b) provide band gaps energy *ca.* 3.1 eV for TiO₂ nanomaterials which is the recognized band gap energy of the anatase phase. However, upon introducing Fe into the TiO₂, band gap energy reduced. The value became *ca.* 3 eV for S2 and 2.9 eV for S3 and S4 samples.

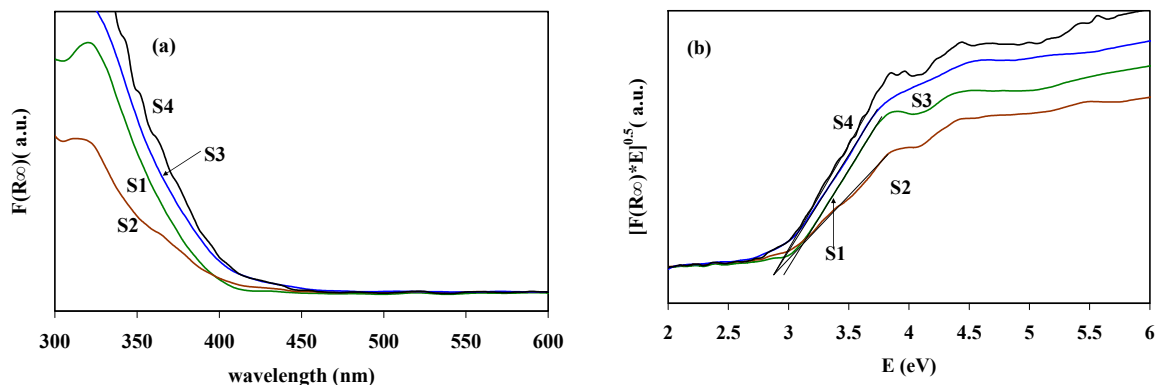


Figure 7.11: The diffuse reflectance spectra of the Fe doped TiO₂ nanomaterials calcined at 500 °C: S1-TiO₂, S2-0.2%, S3-0.36%, and S4-0.49% at. Fe. (a) Kubelka-Munk unit and (b) modified Kubelka-Munk function, respectively.

7.8. Photocatalytic Performance

Photodegradation experiments for all Fe doped samples were performed according to the method described in chapter 3. In addition, a control photodegradation experiment was also performed without catalyst, resulting in a negligible decrease in concentration (below 2%) during the 1-h irradiation period. When the experiment was carried out with catalyst but in the absence of light irradiation, no change in methylene blue concentration was observed. Hence, the decrease of concentration is attributed to the photocatalytic process.

The degradation rate for the different Fe doped TiO₂ photocatalysts was calculated according to eq. 3.13 and is given in Figure 7.12. The degradation rate for pure TiO₂ was 0.086 min⁻¹, with this value was changed with Fe doping. The highest rate was 0.114 min⁻¹ determined for S2 (0.2% Fe) sample with surface area 79 m²/g, 11.9 nm crystallites and 34 μmol/g surface acidity. However, the degradation rates decreased with a further increasing amount of Fe doping. These values were 0.048 and 0.034 min⁻¹ for S3 (0.36 % Fe, surface area 106 m²/g, 11.6 nm crystallites and 40 μmol/g surface acidity) and S4 (0.49 at % Fe, surface area 106 m²/g, 10.8 nm crystallites and 58 μmol/g surface acidity) samples, respectively.

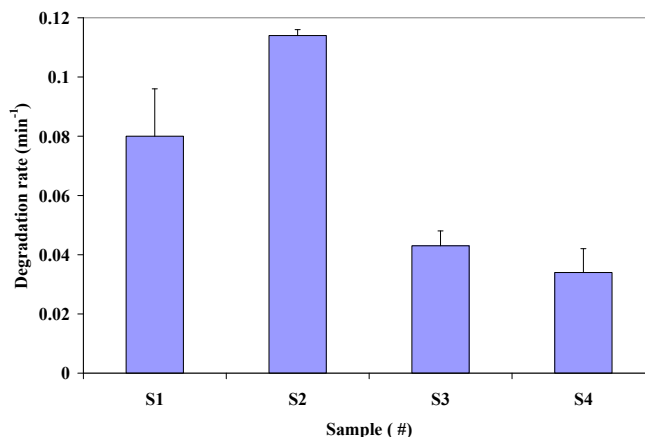


Figure 7.12: The calculated degradation rate of various Fe doped TiO₂ by eq. 3.13.

This observed photocatalytic performance of Fe doped TiO₂ samples can be explained by the higher surface area, mesoporous structure and surface acidity which are favoring the adsorption of reactant molecules and the light absorbance to generate more electron/holes. These factors will enhance the quantum efficiency, leading to higher photocatalytic activity of the S2 sample. In addition, the increase of defects which are observed by HRTEM images could capture electrons and thus reduce their recombination rate. However, a higher amount of Fe (>0.2%) in the TiO₂ matrix could induced too many point defects by Fe in the TiO₂ network, leading to an abrupt decrease in the performance of the photocatalyst.²⁴⁰ This is expected because many investigations have shown that the photocatalytic activity of Fe-doped TiO₂ is strongly dependent on the dopant concentration since the Fe³⁺ ions can serve not only as a mediator of interfacial charge transfer but also as a recombination center.^{241, 242} Hence, with a higher surface area, higher acidity and smaller crystallites compared to S1 and S2, S3 (0.36% Fe) and S4 (0.46% Fe) samples showed lower photocatalytic performance. However, the optimum Fe at % value

depends on the synthesis method, type of precursor and type of intended application. In our case, doping lower than 0.2 at % showed the optimum performance.

7.9. Conclusions

Successful synthesis of Fe doped TiO₂ nanomaterials by the simple sol-gel process in scCO₂ demonstrated that this is a promising technique for synthesizing cation doped TiO₂ nanostructures. Fe doping alters the morphology of the product. Moreover, Fe doping was favorable for organizing a more mesoporous structure and maintaining the pore structure at higher temperatures. It suggests that proper Fe doping to the framework may become an effective way to improve the properties of mesoporous TiO₂ materials. A small amount of Fe doping samples showed better performance; hence, these materials can be used as a photocatalyst for the degradation of organic compounds to prevent environmental pollution.

CHAPTER 8

Zr MODIFIED N DOPED TiO₂ NANOSTRUCTURED MATERIALS

8. Introduction

TiO₂ nanomaterial is a potential candidate for solar applications due to its unique optoelectronic and photochemical properties and being a low cost material, favorable for potential large scale commercial applications. However, pure anatase TiO₂ activates at $\lambda < 380$ nm of UV light, which leaves approximately 95% of the available solar energy unused, which is considered a limitation in the practical utilization of solar energy. In the technical literature, numerous studies have focused on shifting TiO₂'s band gap to the visible spectral region, that would allow efficient utilization of solar energy and, hence, greatly expand its application. Bulk modification by N-doping is one of the well-known methods to enhance the performance of TiO₂ nanomaterials by shifting absorption to the visible range.^{16, 19, 20, 22} However, along with the light absorption, the performance of TiO₂ nanomaterials strongly relies on their crystallinity, crystallite size, crystal structure, specific surface area, and thermal stability. It was previously discussed in chapter 4 that Zr doping increased the surface area, thermal stability and reduced the crystal size of TiO₂ nanomaterials. Moreover, Wang et. al investigated the role of the potential promoter ZrO₂ in enhancing activity of TiO_{2-x}N_x for the oxidation of gaseous organic compounds.⁶² The nitrogen-doped photocatalysts were synthesized by reacting amorphous metal oxide xerogels via a sol-gel process with an ammonia solution, followed by calcining the products. They reported that ZrO₂ helped to preserve the surface area and prevent grain

growth resulting in higher activity. Therefore, simultaneous Zr and N doping would help to enhance the performance of TiO₂ nanomaterials.

Conventionally, large scale multicomponent metal oxides with molecular level homogeneity can be synthesized via a sol-gel process at low cost.⁹⁶ Moreover, the sol-gel process is the most promising method for synthesizing N-doped TiO₂ as discussed in section 2.3.8. However, the conventional sol-gel process requires organic solvents and due to environmental regulations and increased environmental concern, the use of volatile organic compounds (VOCs) is becoming increasingly restricted. Consequently, alternate environmentally friendly solvents and/or processes are a better choice for synthesizing N-doped TiO₂ nanomaterials. Moreover, with low viscosity, “zero” surface tension and high diffusivity, scCO₂ is considered as a favorable solvent for synthesizing superior nanomaterials. Therefore, this chapter focuses on the effects of simultaneous N and Zr doping on the morphology, crystal structure, crystal size, surface area, pore volume and pore size distribution, and the band gap energy of the nanomaterials synthesized by a direct sol-gel process in scCO₂.

8.1. Experimental

Zr modified N doped TiO₂ nanomaterials were synthesized at 60 °C and 5000 psig following the standard procedure previously discussed in chapter 3 using the appropriate amount of TIP, ZPO and TEA. In a typical experiment, 6.6 mmol TIP, 0.4 mmol ZPO, 35 mmol acetic acid and the appropriate amount of TEA were quickly placed in a 10 mL view cell at 60°C under stirring. CO₂ was added to make the synthesis pressure 5000

psig. Initially, a transparent homogeneous phase pale yellow to brown depending on TEA/TIP ratio was observed. After the reaction mixture was stirred about 30 minutes to

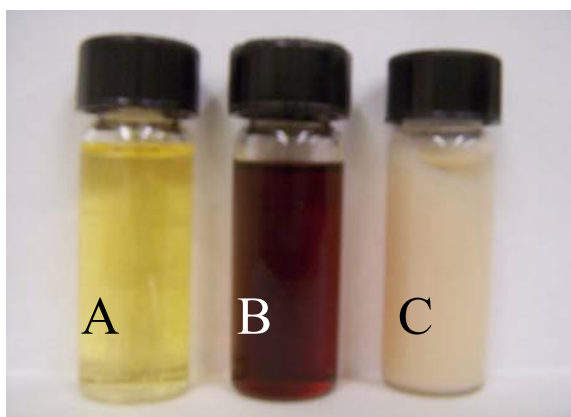


Figure 8.1. Effect of 1:1 Triethylamine/ TIP with Acetic acid at R5, (A) TIP+HOAc formed yellow colour solution , (B) TIP+HOAc+ TEA formed brown solution, (C) TIP+HOAc+TEA+H₂O formed gel.

several hours, the fluids in the view cell became semitransparent then turned white, indicating a phase change and gel formed. However, gel never formed when using TEA/Ti ratios higher than 0.8 shows this Figure 8.1 where (A) TIP+HOAc formed a yellow colored solution. This solution turns into gel within 30 minutes. However, after introducing 1:1 ratio TEA into the system, it formed a brown solution and never formed gel (B). Water was added to break the stability to form gel(C). This observation is consistent with the recent patent filed by Yasutaka et al. for synthesizing stable titanium alkoxide (iso-propoxide) by TEA using a 0.5 to 2 TEA/Ti ratio.²⁴³ After 5 days of aging, a few droplets were vented and placed in a test tube, followed by addition of water. When a higher amount of TEA was used, white precipitate formed indicating incomplete polymerization. However, to maintain consistency, after 5 days of aging, the

nanomaterial samples were washed using CO₂ at a controlled flow rate. The resulting as-prepared nanomaterials were calcined in air at 500 °C using a heating rate of 10 °C/min, holding time of 2 h, and cooling rate to room temperature of 0.5 °C/min. The synthesized calcined materials were characterized using several physiochemical techniques, which were previously described in chapter 3. In this study, two series of N-doped samples (1) pure TiO₂ and (2) Zr modified TiO₂ were prepared and named as TiO₂, TiO₂-N1 and TiO₂-N2 respectively, based on the amount of TEA used in the preparation step. The ratio of TEA/ Ti precursors is 0.4 and 0.6 for sample named N1 and N2, respectively.

8.2. SEM

The morphology and size of the as-prepared materials were characterized by SEM analysis as shown in Figure 8.2. The aerogel powders are composed of particles having 4-6 μm diameter and 5-12 μm length. However, the individual particles consist of structures with different morphologies and different dimensions for pure TiO₂ and the modified systems. The pure TiO₂ nanomaterials (Fig. 8.2(a)) consisted of nanofibers having 20-50 nm dia, while the modified system was composed of mainly small sheet type structure. The N-doped TiO₂ consists of uniform sized sheets with 200 nm width and *ca.* 1 μm length ((Fig. 8.2(b)). However, zirconia and N co-doping altered the morphology. Zr modified N doped TiO₂ exhibited a flower type structure consisting of sheets *ca.* 500 nm width as shown in Fig. 8.2(c). It is an important observation to note here that using a higher amount of triethylamine gave agglomerated nanostructures (Fig. 8.2 (d)).

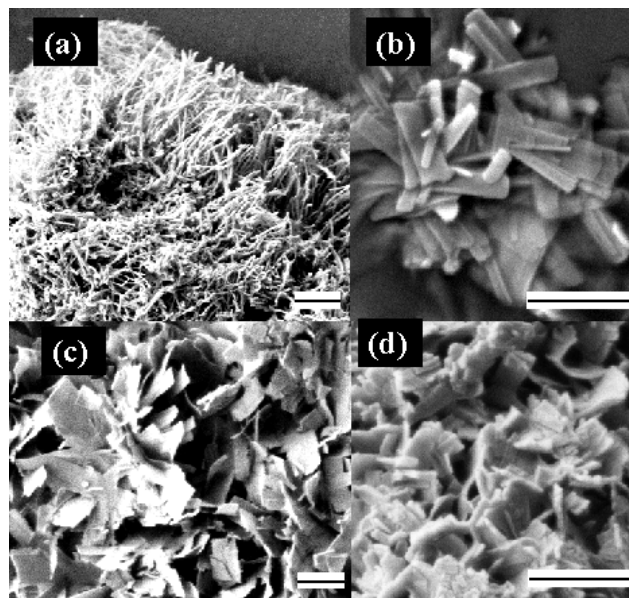


Figure 8.2: SEM: (a) TiO_2 , (b) $\text{TiO}_2\text{-N1}$, (c) $\text{Zr-TiO}_2\text{-N1}$, and (d) $\text{Zr-TiO}_2\text{-N2}$. (Bar represents 500 nm. All the samples were examined after platinum coating).

TEM analysis was performed to obtain more detailed information about the calcined materials, such as crystal size and porosity with the images given in Figure 8.3. It can be seen that calcined pure TiO_2 are fibers with 30 nm diameters whereas all N-doped samples are sheets with 100-300 nm width. The TEM images also confirmed that the doping agent had a significant effect on the crystal size and porosity of the calcined nanomaterials. The measured crystal size for all systems was *ca.* 10-15 nm though the shapes of the crystallites are different. Pure TiO_2 formed nice cubic crystals whereas in the modified system, poor crystallinity was observed. It is known that the Zr and N present in the samples retards the reorganization for forming ordered crystal structures, resulting in poor crystallinity for the modified systems. The TEM images also reveal that the N-doped materials were more porous. Moreover, along with the SEM results, the TEM images also confirm that the materials were very solid (less porous) when a higher

amount of triethylamine was used. This analysis confirmed that zirconium and triethylamine had a significant effect on the morphology and the properties of the products.

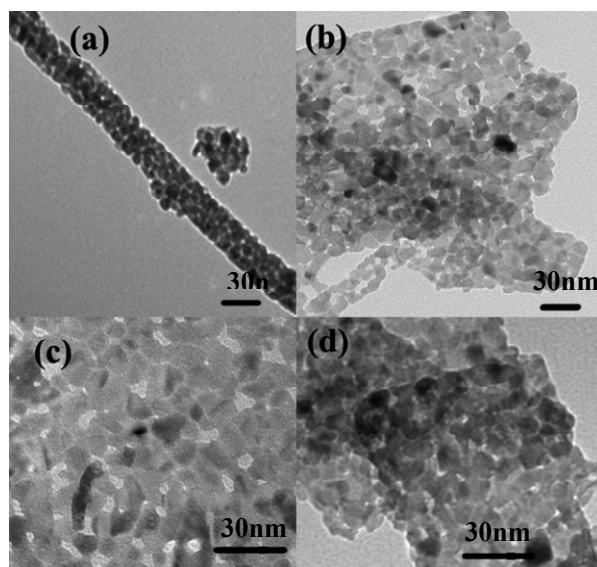


Figure 8.3: TEM: (a) TiO_2 , (b) $\text{TiO}_2\text{-N1}$, (c) $\text{Zr-TiO}_2\text{-N1}$, and (d) $\text{TiO}_2\text{-N2}$. (Bar represents 30 nm).

8.3. Thermal Analysis

TG–DTG analysis was carried out to study the thermal decomposition behavior of the synthesized nanomaterials. The TG curves are given in Figure 8.4(i) along with the DTG curves (Fig. 8.4 (ii)) showing three regions in the range 20–125, 125–500 and above 500 °C. Usually, the first stage is attributed to the removal of physically adsorbed organic residue, while the second range is the burnout of the chemically bounded water and organic material. At the first stage, all samples lost ca. 4-5 % wt although a significant difference was observed in the second stage. The pure TiO_2 sample lost 51 % wt in the second stage, whereas N doped TiO_2 lost 55 % wt. However, upon introducing

6 % Zr into the matrix, the samples became more condensed compared to TiO_2 as previously observed, and only 50 % wt loss was found during this stage.²⁴⁴ Moreover, when triethylamine was introduced into the $\text{ZrO}_2\text{-TiO}_2$ system, the wt loss was less compared to the N doped TiO_2 , i.e. 51%. This analysis showed that the type of dopant had very prominent effects on the decomposition or removal of the organic residue. The DTG curves presented in Fig. 8.4 (ii) clearly show the effects of dopant on the removal of organic residue by heat treatment. The peak position (Fig 8.4(ii) (b) & (d)) shifted to lower values compared to pure TiO_2 (Fig.8.4(ii)(a)) after introducing triethylamine, regardless of Zr modification, indicating easy removal of the residue. However, the opposite phenomenon was observed for zirconia doping, where the Zr cation shifted the peak positions to a higher value (Fig 8.4(ii)(c)) indicating higher thermal stability. This is a well known property of ZrO_2 , which has been observed in many systems.⁸³ The weight loss over 500°C was extremely small for all samples.

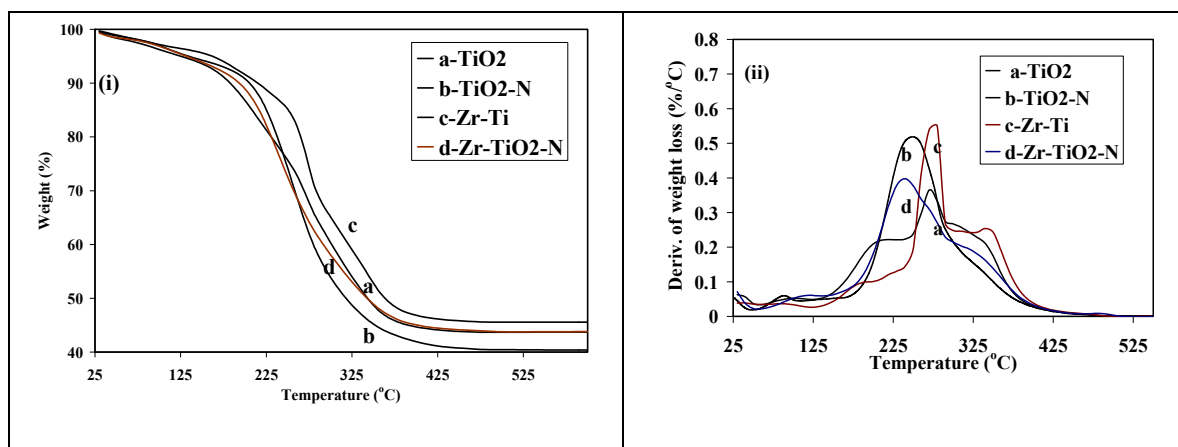


Figure 8.4: TG/DTG curves for N-doped nanomaterials synthesized by sol-gel process as a function of temperature.

Table 8.1: Surface area, pore volume, pore diameter, and crystallites size for calcined undoped and doped nanomaterials.

Sample	Surface area(m ² /g)	Pore V. (cm ³ /g)	Pore dia.(nm)	Crystal size(nm)±1nm	Crystal structure
TiO ₂	56	0.26	18.90	13.75	A
TiO ₂ -N1	78	0.31	13.65	12.86	A
TiO ₂ -N2	65	0.19	11.96	8.72	A
Zr-TiO ₂	81	0.27	13.67	12.31	A
Zr-TiO ₂ -N1	94	0.25	10.26	11.13	A
Zr-TiO ₂ -N2	72	0.33	18.39	6.17	A

8.4. XRD Analysis

The crystal structure and crystallite size of the nanomaterials calcined at 500 °C were examined by XRD, with the spectra given in Figure 8.5. This figure shows that all modified calcined nanomaterials consist of anatase crystal, although the peak intensity as well as the FWHM strongly depends on the type and amount of dopant. The pure TiO₂ showed a very small rutile phase (4% wt) at this temperature, whereas no distinct ZrO₂ or TiN peak is evident, indicating no phase separation, and the dopant was contained in the anatase crystal structure for this composition. However, the crystallite size decreased with the amount of doping introduced into the system. All the crystallite sizes were calculated using Scherer's equation and are given in Table 8.1. It can be seen that the crystal size for pure TiO₂ calcined at 500°C was ca. 13.75 nm, whereas nitrogen doped TiO₂ had 12.86 nm crystallites. A higher amount of triethylamine further reduced the crystallite sizes. The Zr modified nanomaterials had smaller crystallites compared to the unmodified samples, regardless of the amount of triethylamine used. Moreover, triethylamine reduced the crystallinity of the modified samples compared to unmodified

samples. It was previously mentioned that the dopant prevents rearrangement of atoms to form crystal, hence lowering crystallinity and giving smaller size crystallites for the doped samples.

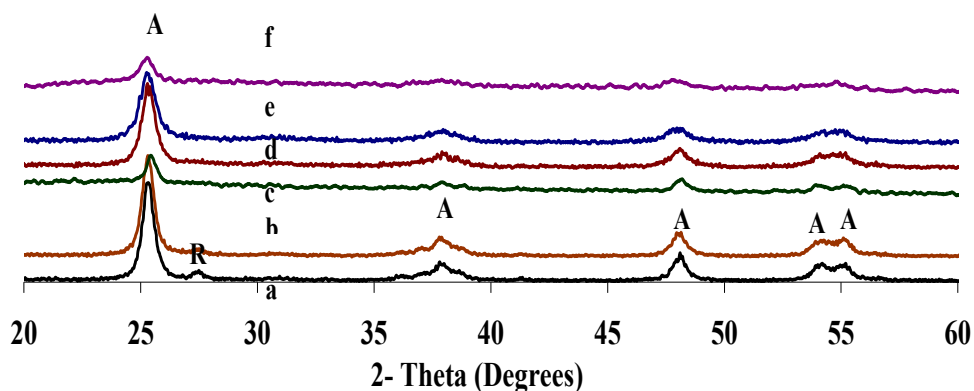


Figure 8.5: Powder XRD spectra of the Zr modified N doped TiO_2 nanomaterials calcined at 500°C : (a) TiO_2 , (b) $\text{TiO}_2\text{-N1}$, (c) $\text{TiO}_2\text{-N2}$, (d) Zr-TiO_2 , (e) $\text{Zr-TiO}_2\text{-N1}$, and (f) $\text{Zr-TiO}_2\text{-N2}$.

8.5. Raman

To further verify these results, Raman analysis was performed on all the N doped samples. The spectra for the samples calcined at 500°C show Raman peaks at 142, 395, 517 and 639 cm^{-1} that can be assigned to the E_g , B_{1g} , B_{1g}/A_{1g} , E_g , modes of the anatase of titania respectively, which agrees with published values.²¹⁹ However, the most intense anatase peak at $\approx 142\text{ cm}^{-1}$ showed significant differences amongst the different samples (Fig. 8.6). The Raman peaks usually display smaller linewidths (FWHM) for larger crystallites due to an increase in the correlation length of the vibrations, with increasing intensity indicating greater concentrations of anatase phase.²²⁰ The FWHM of the anatase peak were *ca.* 11 cm^{-1} for both the Ti and Zr-Ti systems modified with a lower amount of triethylamine. However, this value increased to *ca.* 15 cm^{-1} for samples

prepared using a higher amount of triethylamine. More importantly, the Raman peak intensity reduced to half compared to the previous system, indicating low crystallinity. Moreover, the peaks shifted to higher frequencies, also confirming smaller crystallite sizes were formed.²⁴⁵

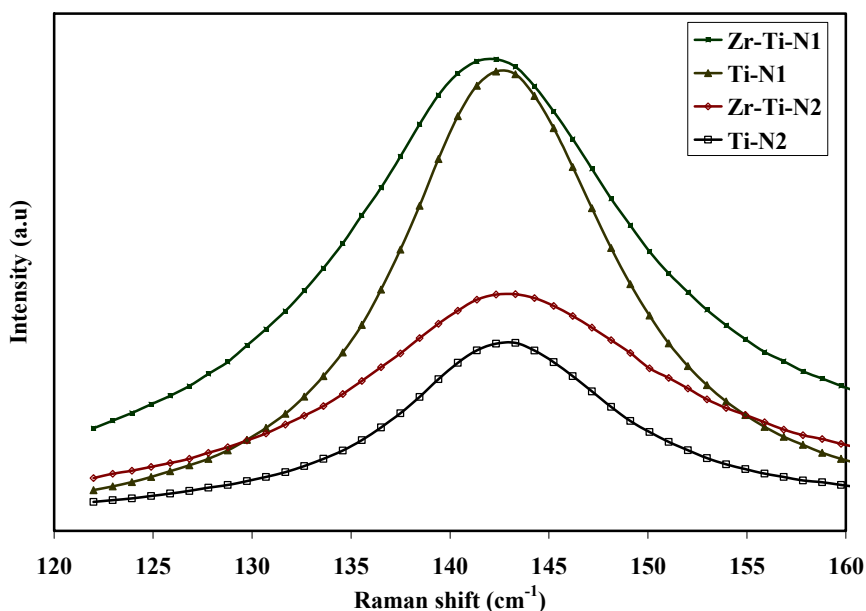


Figure 8.6: Raman spectra around 142 cm^{-1} for Zr modified N doped TiO_2 nanomaterials calcined at $500\text{ }^\circ\text{C}$.

8.6. HRTEM Analysis

To explore the crystal structure in more detail, HRTEM analysis for both the pure TiO_2 and the modified samples calcined at $500\text{ }^\circ\text{C}$ were performed. The HRTEM micrographs for the pure TiO_2 in Fig.8.7 (a) demonstrate long grains having the anatase crystal phase with a d-spacing 0.35 nm . This d-spacing value is assigned to the lattice spacing of the (101) planes of the anatase phase. Upon introducing dopant into the TiO_2 matrix, the crystallites became smaller as was previously observed from the XRD

analysis. However, the HRTEM analysis further reveals that the N doped systems (Fig.8.7 (b-d)) have many defects (grain boundary, lattice mismatch, screw dislocation), which may be due to the presence of alkylamine in the synthesis process. Alkylamines can be selectively adsorbed on certain crystal facets of metal oxides, or form amine complexes with metal alkoxides, thus leading to orientated growth or aggregation of the metal oxide particles.^{27, 246}

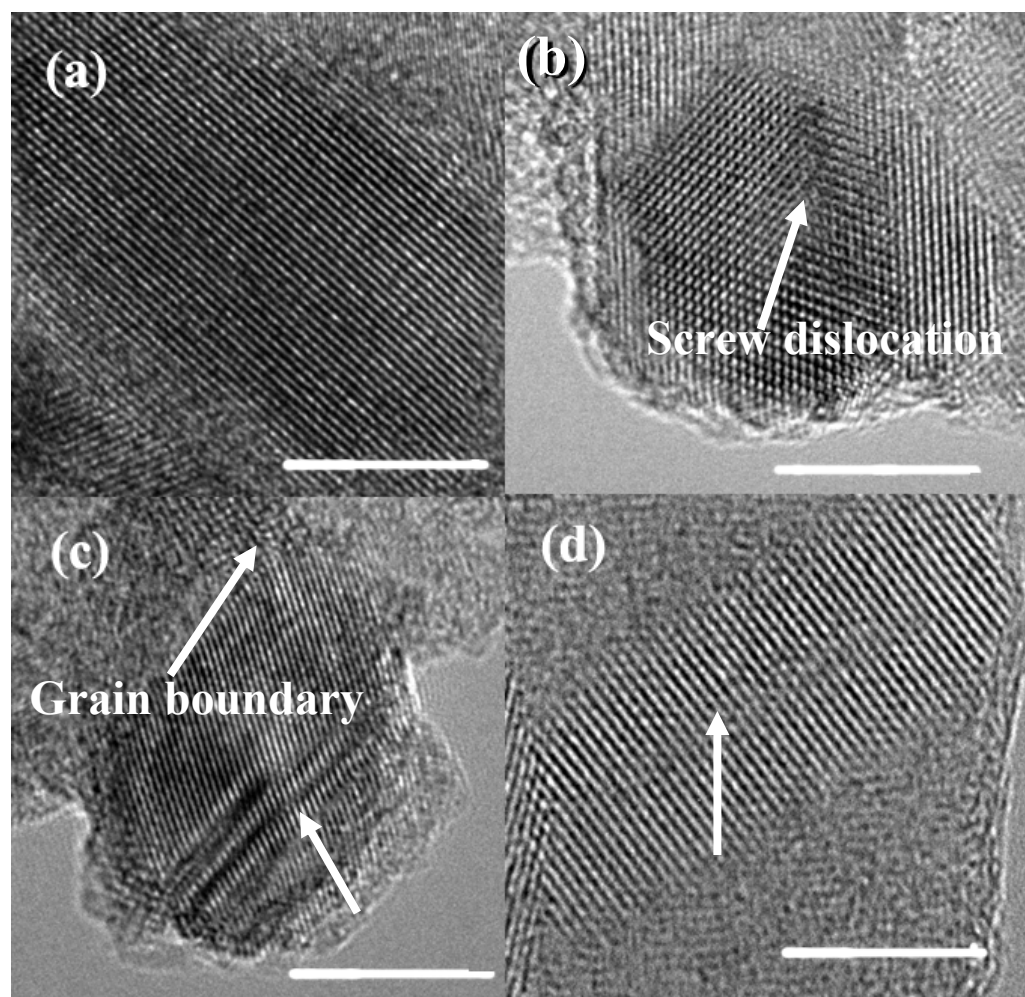


Figure 8.7: HRTEM for N-doped TiO₂ nanomaterials: (a) TiO₂, (b) TiO₂-N1, (c) Zr-TiO₂-N1, and (d) TiO₂-N2. (Bar represent 5 nm. Arrows indicate defects).

8.7. XPS Analysis

Figure 8.8 shows a typical XPS spectrum for the Zr modified N doped TiO₂ nanomaterials synthesized by the sol–gel process in scCO₂. XPS peaks show that the Zr-TiO₂-N powder contains Ti, Zr, O, N, and C elements. The presence of carbon is ascribed to the residual carbon from the precursor solution, and any adventitious hydrocarbon from the XPS instrument itself. This XPS data reveals that the Zr and N elements are incorporated into the TiO₂ crystal lattice, or were adsorbed onto the surface of the crystals. For further analysis of the chemical structure of the investigated TiO₂ samples, five areas of the XPS spectrum: for the Ti 2p around 460 eV, the Zr 3d around 183 eV, the N 1s around 400 eV, the O 1s around 530 eV and the C 1s around 286 eV region were examined. When scanning the Ti 2p and Zr 3d XPS regions, significant differences are observed at the binding energies between the pure TiO₂ and the modified system. According to Gilindo et al., TiO₂ Ti 2p_{3/2} and ZrO₂ Zr 3d_{5/2} showed peaks at the binding energies 458.8 eV and 183 eV, respectively.¹⁸⁶ Previously in chapter 4, it was discussed that introducing a second metal ion into the lattice shifts the binding energy. This XPS analysis revealed that regardless of Zr modification, the binding energy for Ti 2p_{3/2} shifted to lower values compared to pure TiO₂. The small shift of binding energy of the Ti 2p_{3/2} peak is attributed to the change of the valence state of Ti₄⁺. Considering the binding energy of zirconia Zr 3d_{5/2}, which shows a lower value compared to pure zirconia, i.e. 182.70±0.02. The O 1s XPS spectra also shows significant changes upon N incorporation, with the peak shifted to a lower binding energy than the pure oxygen peak in TiO₂. The binding energy for O in TiO₂ is 530 eV, whereas is 529.92 eV for N doped TiO₂. The most interesting changes occur around the C 1s peak, and the resolved C peak

(given in appendix 7) shows that three different types of carbon containing groups are present around 288, 286, and 284 eV, representing the O-C=O, C-N and C-C & C-H groups, respectively. However, only two instead of three carbon groups such as O-C=O and C-C & C-H were present in the pure TiO₂ system. This additional carbon peak indicates that the amine group is directly absorbed onto the surface of the materials, forming metal complexes. It is well known that with two nonbonding electron, nitrogen acts as a Lewis base and forms complexes with electrophilic metal ions.⁹⁹

The analysis of the binding energy of N 1s for the N-doped materials showed that two types of N are present in the as-prepared nanomaterials. An intense peak centered at 401.8 eV and a small peak centered at 399.9 eV, assigned for chemisorbed and interstitial N, respectively.²⁴⁷⁻²⁴⁹ However, the binding energies are greater than the typical binding energy of 397.2 eV in TiN.²⁵⁰ This higher energy shift can be attributed to the 1s electron binding energy of the N atom in the environment of O-Ti-N. When nitrogen substitutes for the oxygen in the initial O-Ti-O structure, the electron density around N is reduced, compared to that in a TiN crystal, because of the O atom bonded to the Ti atom.²⁴⁷ After heat treatment, there is only one peak which is centered at 400 eV. Recently, most of the studies regarding the N doped TiO₂ systems have performed XPS analysis to investigate the chemical state of N. Chen and Burda found that the signal at 401.3 eV in the synthesized nanoparticles is attributed to O-Ti-N, based on the redox chemistry involved.²⁴⁷ In another study, Yang et al. reported a binding energy of 400.1 eV which was assigned to hyponitrite at the surface.²⁴⁸ Thus, the nitrogen state in the doped TiO₂ may vary from case to case. However, very recently Huo et al. reported a peak at 399.6 eV, ascribed to the N species incorporation into the titania matrix.²⁴⁶

Keeping all this in mind, it can be concluded that all N species during calcination were incorporated into the TiO_2 matrix, and the resultant nanomaterials were described as Zr and N codoped TiO_2 .

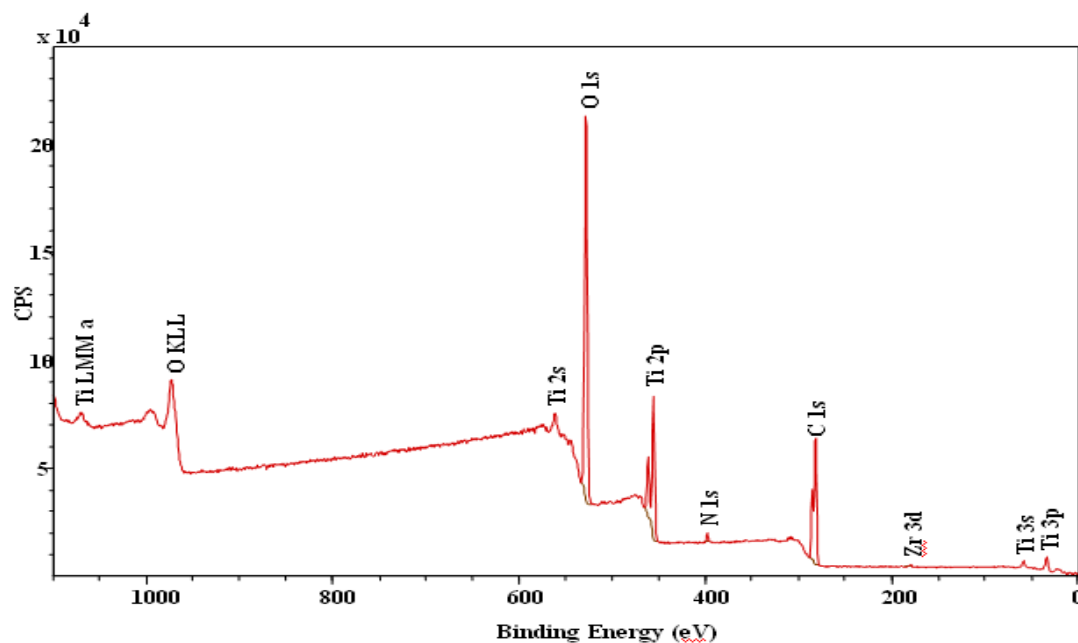


Figure 8.8: Typical XPS spectrum for Zr modified N doped TiO_2 as-prepared nanomaterials.

The calculated surface N to metal ratio of synthesized nanomaterials provided in Table 8.2. shows that surface N to (Ti +Zr) at. ratio depends on the system and heat treatment. When 0.4 at. ratio triethylamine was used, both as-prepared systems possessed the value *ca.* 0.16; after heat treatment, this value became *ca.* 0.012. However, when a higher amount of TEA was used, the surface N concentration was 0.08 ± 0.03 for TiO_2 nanomaterials. This anomalous behavior might be attributed to the isoelectric point of Ti (3.9-8 most of the case *ca.* 5.5).²⁵¹ Due to the low isoelectric surface positive charge of pure TiO_2 , when using higher amounts of TEA,²⁵¹ the TEA absorption is decreased as

shown in Table 8.2. Hence, the % of chemisorbed N (peak position 401 eV) was reduced with an increasing amount of TEA. Moreover, the experimental evidence provided in Figure 8.1 supports this hypothesis.

Table 8.2: Surface N composition of as-prepared and calcined nanomaterials with N peak positions.

Sample	As-prepared						Calcined			
	N/(Ti+Zr) at.	N Pos.	1s Peak area	N Pos.	1s Peak Area	N/(Ti+Zr) at.	N Pos.	1s Peak area		
TiO ₂ -N1	0.16±.01	401.8	97	399.9	7	0.014	398.8	100		
TiO ₂ -N2	0.08±.03	401.9	73	400.0	27	0.004	398.3	100		
Zr-TiO ₂ -N1	0.16	401.8	88	399.7	12	0.012	398.8	100		

8.8. BET Analysis

The surface area and pore volume of the calcined materials were characterized by nitrogen adsorption studies, which were summarized in Table 8.1. Figure 8.8 shows a typical nitrogen adsorption isotherm for calcined TiO₂, which exhibits an H3 hysteresis loop, typical for mesoporous materials.¹⁶⁰ The pore volume for all samples did not follow any clear trend. For example, pure TiO₂ possessed a 0.26 cm³/g pore volume while lower amounts of triethylamine increased the pore volume to 0.31 cm³/g. However, doubling the amount of triethylamine decreased the pore volume significantly. Interestingly, the zirconia modified samples showed the opposite trend. A small amount of nitrogen precursor (0.4 N/Ti) reduced the pore volume to 0.25 cm³/g whereas a higher amount (0.6 N/Ti) increased the pore volume to 0.33 cm³/g. The average pore diameter was *ca.* 10 nm except for the pure TiO₂ and Zr-TiO₂-N2 samples, which showed average pore diameters *ca.* 18 nm. The typical pore size distribution is inset in Fig 8.9 which shows that most pores are bigger than 20 nm, whereas a small number of *ca.* 4 nm dia pores are present in

the samples. The BET surface areas of the calcined materials given in Table 8.1 demonstrate that the modified samples possess higher surface areas compared to the pure TiO_2 . However, the materials synthesized with a higher amount of triethylamine showed a lower surface area. This is expected as the SEM and TEM analysis demonstrated

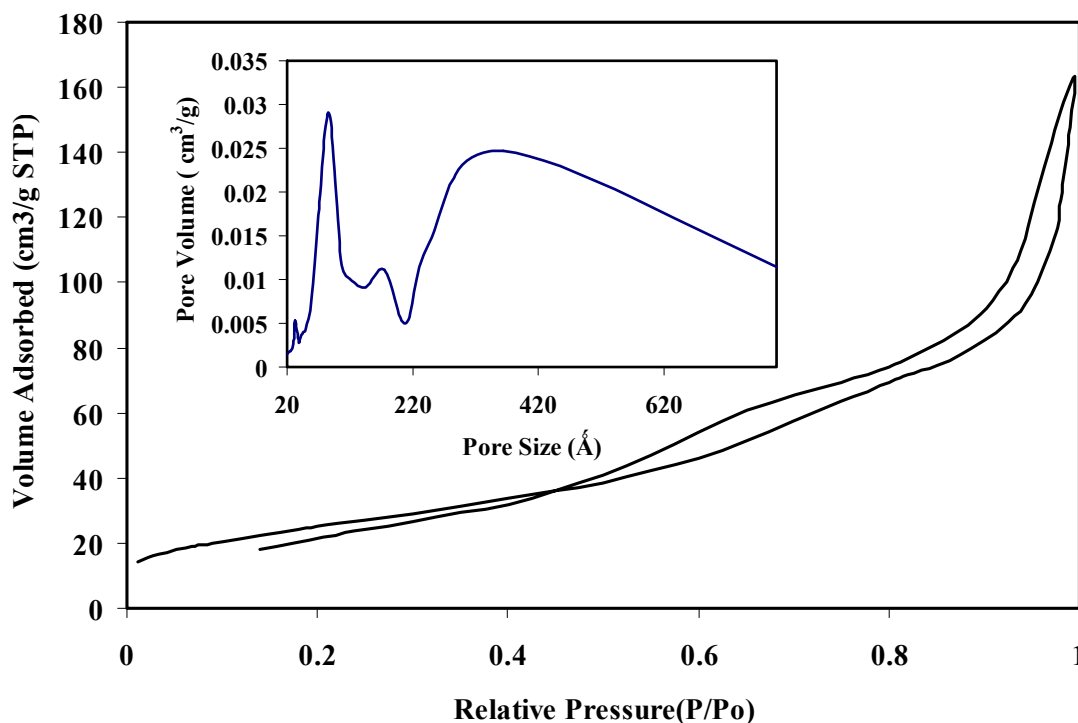


Figure 8.9: N_2 adsorption/desorption isotherm of the Zr modified N doped TiO_2 calcined nanomaterials. Inset shows the pore size distribution.

that denser materials were formed using a higher amount of triethylamine. The origin of this effect likely comes from the hydrolysis and condensation pathways in the sol-gel process. The pure metal alkoxide with the required amount of acetic acid was acidic with a pH of the system *ca.* 2.3. In an acidic medium, the hydrolysis reaction is accelerated. The acid converts negatively charged alkoxide groups into better leaving groups by protonating them. Upon introducing triethylamine into the synthesis process, the pH of

the solution increases. Hence, the hydrolysis rate is decelerated and the condensation kinetics is accelerated upon increasing the pH of the solution. According to Livage et al. the sites A-D in a partially hydrolyzed metal oxo- polymer (Figure 8.10) have different charge distributions. Based on the values of $\delta(M)$ calculated from the partial charge model for sites A-D for a typical partially hydrolyzed polymer (where M= Ti, Zr given in Table 8.2), the reactivity towards nucleophilic attack should decrease as $C \gg B \approx A > D$. The condensation is then directed towards the middle, instead of the ends of the chain. Moreover, triethylamine with a lone pair of electrons acts as a basic catalyst. Hence, in higher pH or higher amounts of triethylamine, more compact materials are produced.

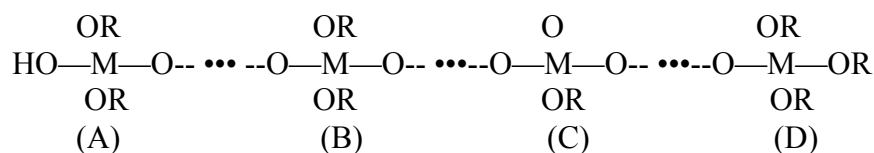


Figure 8.10: A typical partially hydrolyzed metal oxo-polymer.

Table 8.3: Charge distribution according to the partial charge model.

Site	$\delta(\text{Ti})$	$\delta(\text{Zr})$
A	+0.68	+0.71
B	+0.69	+0.72
C	+0.75	+0.77
D	+0.67	+0.69

8.9. Photocatalytic Performance

Photodegradation experiments for Zr modified N doped TiO_2 samples were performed according to the method described in chapter 3. In addition, photodegradation experiments were also performed without catalyst, resulting in a negligible decrease in concentration (below 2%) during the 1-h irradiation period. Complete decolorization was

observed within 1 hour. Therefore, the duration of each experiment was fixed to 1 h and the degradation rate was calculated according to eq. 3.13 and compared with the reference photocatalyst, Degussa P25.

The calculated degradation rate for Zr modified N-doped TiO₂ photocatalyst is given in Figure 8.11. The degradation rate for pure TiO₂ was 0.086 min⁻¹ and this value became 0.186 and 0.203 min⁻¹ for TiO₂-N1 and TiO₂-N2 samples, respectively. In the Zr modified system, without N doping the degradation rate was 0.092 min⁻¹, whereas the value increased to 0.117 and 0.161 min⁻¹ for Zr-TiO₂-N1 and Zr-TiO₂-N2 samples, respectively. The given results indicate that all N-doped samples show better photocatalytic activity compared to the undoped samples. However, the activity enhancement is higher in TiO₂ samples over Zr modified TiO₂ samples. For comparison purposes, the degradation experiment was also performed using commercially available P25 TiO₂ (surface area 50 m²/g), and the calculated value was 0.116 min⁻¹. The degradation rate of N doped TiO₂ was nearly 1.7 times higher than P-25, showing a good potential for practical applications in photocatalysis.

The enhancement in photocatalytic performance of N-doped TiO₂ samples can be explained by the higher surface area with mesoporous structure and defects induced by N doping. The higher surface areas with mesoporous structure favors the adsorption of reactant molecules, as well as light absorbance. Moreover, N-modified samples with smaller crystallites provided higher interfacial and access to active sites. In addition, the increase of defects which were observed by the HRTEM images could capture more photoelectrons and thus reduce their recombination with photoinduced holes. These factors could enhance the quantum efficiency, leading to higher photocatalytic activity.

Therefore, all N doped TiO₂ shows a higher photocatalytic activity compared to undoped TiO₂ nanomaterials.²⁴⁰

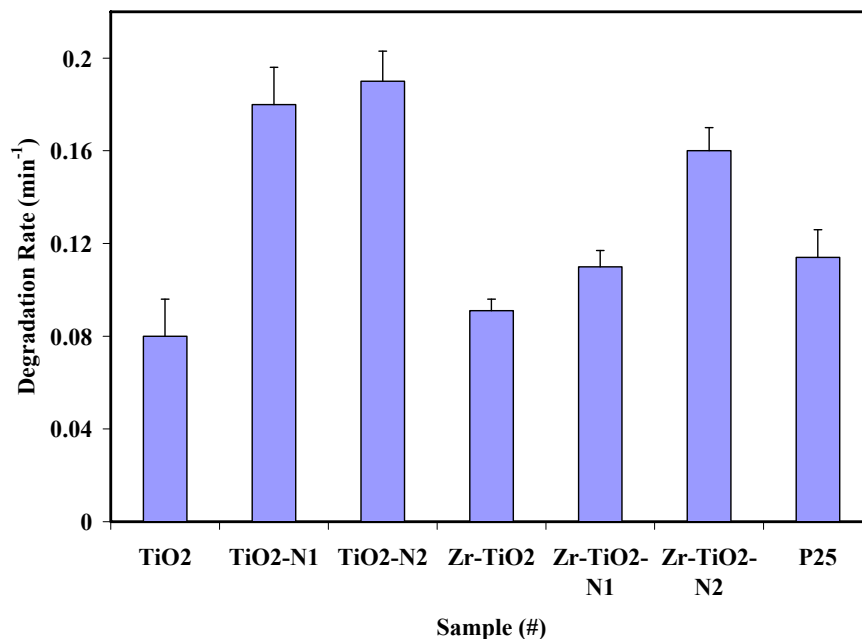


Figure 8.11. The variation of the calculated degradation rate for Zr modified N doped TiO₂ nanomaterials.

8.10. Conclusions

Successful synthesis of ZrO₂ modified N doped TiO₂ nanomaterials by a simple sol-gel process in scCO₂ demonstrated that this is a promising technique for synthesizing anion and cation doped TiO₂ nanostructures. The formed Zr modified TiO₂ nanostructured materials have a high surface area, smaller crystallite size, and greater thermal stability which are highly desirable properties as catalysts, support materials, semiconductors, and electrodes in dye-sensitized solar cells (DSSC). Moreover, all N doped systems showed better performance compared to pure TiO₂ nanomaterials and N-doped TiO₂ showed higher activity compared to commercial P25 TiO₂.

CHAPTER 9

CONCLUSIONS AND RECOMMENDATIONS

9. Introduction

This dissertation presents a simple synthesis route to produce TiO₂-based nanostructured materials by doping with Fe, Zr and N in scCO₂. In order to synthesize the nanomaterials, the direct sol-gel process in CO₂ was carried out in either a 10 or 25 ml view cell. The starting materials were mixed in the view cell and CO₂ was added using a syringe pump. The system was maintained at a constant temperature and pressure until the nanomaterials were formed. After 5 days aging, the formed gel was washed continuously using scCO₂ at a controlled flow rate of 0.5 mL/min, followed by controlled venting. In order to crystallize the amorphous nanomaterials, the synthesized as-prepared materials were calcined at 500 °C. The nanomaterials were characterized by using electron microscopy, FTIR, thermal analysis, XRD, N₂ physisorption, UV-Vis, and TPD. Finally the materials were evaluated as a photocatalyst for degradation of methylene blue. The main conclusions of the present study are given in the following sections.

9.1. Direct Sol-Gel Process in scCO₂

The successful synthesis of TiO₂-based nanostructures by doping with Fe, Zr and N by following the direct sol-gel procedure in CO₂ shows that it is a promising technique for synthesizing multicomponent oxide nanostructured materials. This process has several advantages over conventional sol-gel processes including: (1) producing well-defined nanostructure, e.g nanosheets, nanotubes, and nanorods, (2) very good dispersion, e.g.

10% ZrO₂-TiO₂ nanotubes theoretical composition was matched with the experimental composition $\pm 0.01\%$. (2) high conversions, e.g. about 98 % conversion.; (3) high yield, ca. 6 g of ZrO₂-TiO₂ binary nanotubes were synthesized in a 25 mL view cell; (4) high surface areas; (5) simple operating procedure, e.g. one-pot synthesis; (6) mild operating conditions, e.g. 60 °C and 5000 psig; and (7) environmental benignness.

CO₂ was found to be a superior solvent for the sol-gel process. A low dielectric constant as well as low solubility accelerated the gelation process, reduced the desolution repolymerization resulting in high surface areas, and smaller crystallite materials. In addition, scCO₂ exhibits a low interfacial tension which allows CO₂ to penetrate into the gel network helping to form the well-defined nanostructures. Moreover, pressure had beneficiary effects to produce new materials. Furthermore, extraction and drying in scCO₂ produced ultrafine aerogel having high surface areas.

9.2. The Synthesis Parameters of the Direct Sol-Gel Process in CO₂

The temperature, pressure, concentrations of the reactants, acid to metal alkoxide ratio, doping amount and type of dopant, are very important parameters which significantly alter the morphology, and surface area of the synthesized nanostructure aerogels. For binary nanotubes, very low and high temperatures produced nanorods instead of tubes. Different acid ratios also had significant effects on the morphologies as well as the surface areas, with higher concentrations of starting materials resulting in the formation of nanotubes, whereas low concentrations resulted in the formation of sheets. Regardless of the type of doping, an increasing amount of doping increased the surface

area. Surprisingly, a small amount of N-doping increased the surface area whereas a large amount of triethylamine did not increase the surface area significantly.

9.3. Mechanism of Nanostructure Formation

The mechanism of the TiO₂-based nanostructure especially Ti-Zr nanotube formation in scCO₂ can be explained as a spontaneous growth process. The nanostructure formation is mainly attributed to hexamer formation. Zr introduced into the hexamer structure was quite different from the pure TiO₂ hexamer, and the Zr with different coordination number acts as an impurity in the structure. Due to the presence of Zr or other impurities in the hexamer (or chemisorbed), this helps the preferential condensation in one direction. Hence, it is believed that a long sheet-type structure along the [100] plane was developed in the synthesis process. One can envision that as the sheet structure grows, at a certain stage in order to lower the energy of the system, it either rolls-up or folds along the [010] or [001] plane to form the tubular structure.

9.4. Chemistry of the Direct Sol-gel Process in CO₂

Although the chemistry of the direct sol-gel process for binary TiO₂ and ZrO₂ system or 1% Fe(NO)₃ stock solution or triethylamine introduced system in CO₂ are quite different and might vary the relative reaction rates, the reactions can be summarized as substitution, esterification, hydrolysis and condensation steps. The first step involves a substitution reaction with acetic acid, which resulted in alcohol. In the second step, the alcohol reacts with acetic acid and generates water through an esterification reaction.

Then, the generated water leads to hydrolysis and then subsequent condensation. The reactions can be summarized as:

Substitution:



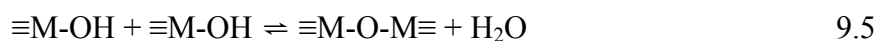
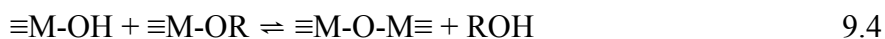
Esterification :



Hydrolysis:



Condensation:



where, M = Ti or Zr or Fe

9.5. Performance of TiO₂-based Nanostructured Materials

Photocatalytic activity of the synthesized pure and modified nanomaterials was evaluated by photodegradation of methylene blue under UV irradiation. All the nitrogen doped systems showed better performance compared to pure TiO₂ nanomaterials. However increasing Fe doping decreased the photodegradation rate. 0.1 % Fe doped TiO₂ and N-doped TiO₂ showed higher activity compared to commercial P25 TiO₂.

9.6. Recommendations

Recommendations for future work include:

1. The successful synthesis of the TiO₂-based nanostructure materials via sol-gel process in scCO₂ is encouraging to extend this method for synthesizing other oxide nanostructures, such as N doped ZnO, Al doped TiO₂, and others.
2. Detailed kinetics study including the effects of temperature, acid to metal alkoxide ratio, and concentration on the sol-gel process for binary ZrO₂-TiO₂ in CO₂ using the in situ ATR-FTIR and Raman techniques will be very helpful to get detailed information about the nanostructure formation.
3. Evaluate these materials as an electrode in solar cells and optimize the synthesis parameters for this application.
4. Modify the surface of TiO₂ by different sensitizing agents such as dye, CdS, CdSe and evaluate as an electrode for solar cell application.
5. Study the direct sol-gel method in CO₂ using a high temperature autoclave to mimic the solvothermal process to produce advanced materials.

References

1. Bent, R. D.; Orr, L.; Baker, R.; Indiana University. Institute for Advanced Study., *Energy : science, policy, and the pursuit of sustainability*. Island Press: Washington, DC ; London, 2002; p xviii, 257 p.
2. Mao, S. S.; Chen, X., Selected nanotechnologies for renewable energy applications. *International Journal of Energy Research* **2007**, 31, (6-7), 619 - 636.
3. Mor, G. K.; Varghese, O. K.; Paulose, M.; Shankar, K.; Grimes, C. A., A review on highly ordered, vertically oriented TiO₂ nanotube arrays: Fabrication, material properties, and solar energy applications. *Solar Energy Materials & Solar Cells* **2006**, 90 2011–2075.
4. Kitano, M.; Matsuoka, M.; Ueshima, M.; Anpo, M., Recent developments in titanium oxide-based photocatalysts. *Applied Catalysis A: General* **2007** 325 1–14.
5. <http://www.canren.gc.ca/>.
6. Oelhafen, P.; Schuler, A., Nanostructured materials for solar energy conversion. *Solar Energy* **2005**, 79, (2), 110-121.
7. Lazarov, M.; Raths, P.; Metzger, H.; Spirkl, W., Optical constants and film density of TiN_xO_y solar selective absorbers. *Journal of Applied Physics* **1995**, 77, (5), 2133.
8. Nalwa, H. S., *Nanostructured materials and nanotechnology*. Concise ed.; Academic Press: San Diego, Calif. London, 2002; p xxiii, 834 p.
9. Goetzberger, A.; Hoffman, U. V., *Photovoltaic Energy Generation Springer* **2005**, Germany.
10. Gratzel, M., Photoelectrochemical cells. *Nature* **2001**, 414, (6861), 338.
11. Fujishima, A.; Honda, K., Electrochemical Photolysis of Water at a Semiconductor Electrode. *Nature* **1972**, 238, (5358), 37-38.
12. Grätzel, M., Photovoltaic and photoelectrochemical conversion of solar energy. *Philosophical Transactions of the Royal Society A: Mathematical, Physical and Engineering Sciences* **2007**, 365, (1853), 993-1005.
13. Wu, J. C. S.; Lin, H.-M.; Lai, C.-L., Photo reduction of CO₂ to methanol using optical-fiber photoreactor. *Applied Catalysis A: General* **2005**, 296, (2), 194-200.
14. Matsuoka, M.; Kitano, M.; Takeuchi, M.; Tsujimaru, K.; Anpo, M.; Thomas, J. M., Photocatalysis for new energy production Recent advances in photocatalytic water splitting reactions for hydrogen production. *Catalysis Today* **2007** 122 51–61.
15. <http://www.titanpe.com/>.
16. Chen, X.; Mao, S. S., Titanium Dioxide Nanomaterials: Synthesis, Properties, Modifications, and Applications. *Chem. Rev.* **2007**, 107, (7), 2891-2959.
17. Ohtani, B.; Ogawa, Y.; Nishimoto, S. i., Photocatalytic Activity of Amorphous-Anatase Mixture of Titanium(IV) Oxide Particles Suspended in Aqueous Solutions. *J. Phys. Chem. B* **1997**, 101, (19), 3746-3752.
18. Qiu, X.; Burda, C., Chemically synthesized nitrogen-doped metal oxide nanoparticles. *Chemical Physics* **2007**, 339, (1-3), 1-10.
19. Asahi, R.; Morikawa, T.; Ohwaki, T.; Aoki, K.; Taga, Y., Visible-Light Photocatalysis in Nitrogen-Doped Titanium Oxides. *Science* **2001**, 293, (5528), 269.

20. Asahi, R.; Morikawa, T., Nitrogen complex species and its chemical nature in TiO₂ for visible-light sensitized photocatalysis. *Chemical Physics* **2007**, 339, (1-3), 57-63.
21. Baiju, K. V.; Shukla, S.; Sandhya, K. S.; James, J.; Warriar, K. G. K., Photocatalytic Activity of Sol-Gel-Derived Nanocrystalline Titania. *J. Phys. Chem. C* **2007**, 111, (21), 7612-7622.
22. Burda, C.; Lou, Y.; Chen, X.; Samia, A. C. S.; Stout, J.; Gole, J. L., Enhanced Nitrogen Doping in TiO₂ Nanoparticles. *Nano Lett.* **2003**, 3, (8), 1049-1051.
23. Chen, C.; Li, X.; Ma, W.; Zhao, J.; Hidaka, H.; Serpone, N., Effect of Transition Metal Ions on the TiO₂-Assisted Photodegradation of Dyes under Visible Irradiation: A Probe for the Interfacial Electron Transfer Process and Reaction Mechanism. *J. Phys. Chem. B* **2002**, 106, (2), 318-324.
24. Durr, M.; Rosselli, S.; Yasuda, A.; Nelles, G., Band-Gap Engineering of Metal Oxides for Dye-Sensitized Solar Cells. *J. Phys. Chem. B* **2006**, 110, (51), 26507-26507.
25. Janus, M.; Morawski, A. W., New method of improving photocatalytic activity of commercial Degussa P25 for azo dyes decomposition. *Applied Catalysis B: Environmental* **2007**, 75 118-123.
26. Iijima, S., Helical microtubules of graphitic carbon. *Nature* **1991**, 354, (6348), 56-58.
27. Zhong, Z.; Lin, M.; Ng, V.; Ng, G. X. B.; Foo, Y.; Gedanken, A., A Versatile Wet-Chemical Method for Synthesis of One-Dimensional Ferric and Other Transition Metal Oxides. *Chem. Mater.* **2006**, 18, (25), 6031-6036.
28. Cao, S.; Yeung, K. L.; Yue, P.-L., An investigation of trichloroethylene photocatalytic oxidation on mesoporous titania-silica aerogel catalysts. *Applied Catalysis B: Environmental* **2007**, 76 64-72.
29. Richter, C.; Wu, Z.; Panaitescu, E.; Willey, R. J.; Menon, L., Ultrahigh-Aspect-Ratio Titania Nanotubes. *Adv. Mater.* **2007**, 19, 946-948.
30. Li, G.; Ciston, S.; Saponjic, Z. V.; Chena, L.; Dimitrijevic, N. M.; Rajh, T.; Graya, K. A., Synthesizing mixed-phase TiO₂ nanocomposites using a hydrothermal method for photo-oxidation and photoreduction applications. *Journal of Catalysis* **2008**, 253, 105-110.
31. Sahel, K.; Perol, N.; Chermette, H.; Bordes, C.; Derriche, Z.; Guillard, C., Photocatalytic decolorization of Remazol Black 5 (RB5) and Procion Red MX-5B— Isotherm of adsorption, kinetic of decolorization and mineralization. *Applied Catalysis B: Environmental* **2007** 77 100-109.
32. Wei, M.; Zhou, H.; Konishi, Y.; Ichihara, M.; Sugiha, H.; Arakawa, H., Synthesis of Tubular Titanate via a Self-Assembly and Self-Removal Process. *Inorg. Chem.* **2006**, 45, (14), 5684-5690.
33. Zhu, B.; Sui, Z.; Wang, S.; Chen, X.; Zhang, S.; Wu, S.; Huang, W., Alternative approaches to fabrication of gold-modified TiO₂ nanotubes. *Materials Research Bulletin* **2006**, 41, 1097-1104.
34. Zhang, S.; Chen, Z.; Li, Y.; Wang, Q.; Wan, L.; You, Y., Preparation of TiO₂ fibers by two-step synthesis method and their photocatalytic activity. *Materials Chemistry and Physics* **2008**, 107 1-5.

35. Dodda, A.; McKinley, A.; Tsuzuki, T.; Saunders, M., Optical and photocatalytic properties of nanocrystalline TiO₂ synthesised by solid-state chemical reaction. *Journal of Physics and Chemistry of Solids* **2007**, 68, 2341–2348.
36. Cristante, V. M.; Prado, A. G. S.; Jorge, S. M. A.; Valente, J. P. S.; Florentino, A. O.; Padilha, P. M., Synthesis and characterization of TiO₂ chemically modified by Pd(II) 2-aminothiazole complex for the photocatalytic degradation of phenol. *Journal of Photochemistry & Photobiology, A: Chemistry* **2008**, 195, (1), 23-29.
37. Herrmann, J. M., Heterogeneous photocatalysis: state of the art and present applications. *Topics in Catalysis* **2005**, 34, (1–4), 49-65.
38. Li, G.; Gray, K. A., The solid–solid interface: Explaining the high and unique photocatalytic reactivity of TiO₂-based nanocomposite materials *Chemical Physics* **2007**, 339, 173–187.
39. Yu, J.; Yu, H.; Chenga, B.; Trapalis, C., Effects of calcination temperature on the microstructures and photocatalytic activity of titanate nanotubes. *Journal of Molecular Catalysis A: Chemical* **2006**, 249, 135-142.
40. Grätzel, M., Conversion of sunlight to electric power by nanocrystalline dye-sensitized solar cells. *Journal of Photochemistry and Photobiology A: Chemistry* **2004**, 164, (1-3), 3-14.
41. Martin, C. R.; Kohli, P., The emerging field of nanotube biotechnology. *Nat Rev Drug Discovery* **2003**, 2, (1), 29-37.
42. Wan, Y.; Ma, J.; Zhou, W.; Zhu, Y.; Song, X.; Li, H., Preparation of titania-zirconia composite aerogel material by sol-gel combined with supercritical fluid drying. *Applied Catalysis A: General* **2004**, 277, 55-59.
43. Pena, J.; Vallet-Regi, M.; San Roman, J., TiO₂-polymer composites for biomedical applications. *J Biomed Mater Res* **1997**, 35, (1), 129-134.
44. Gangopadhyay, R.; De, A., Conducting Polymer Nanocomposites: A Brief Overview *Chem Mater* **2000**, 12, (3), 608-622.
45. Khaled, S. M.; Sui, R.; Charpentier, P. A.; Rizkalla, A. S., Synthesis of TiO₂-PMMA Nanocomposite: Using Methacrylic Acid as a Coupling Agent. *Langmuir* **2007**, 23, (7), 3988-3995.
46. Ramires, P. A.; Giuffrida, A.; Milella, E., Three-dimensional reconstruction of confocal laser microscopy images to study the behaviour of osteoblastic cells grown on biomaterials. *Biomaterials* **2002**, 23, (2), 397-406.
47. Zan, L.; Tian, L.; Liu, Z.; Peng, Z., A new polystyrene–TiO₂ nanocomposite film and its photocatalytic degradation. *Applied Catalysis A: General* **2004**, 264, (2), 237-242.
48. Yuvaraj, H.; Park, E. J.; Gal, Y.-S.; Lima, K. T., Synthesis and characterization of polypyrrole–TiO₂ nanocomposites in supercritical CO₂. *Colloids and Surfaces A: Physicochem. Eng. Aspects* **2008**, (313–314), 300–303.
49. Varghese, O. K.; K., M. G.; Grimes, C. A.; Paulose, M.; Mukherjee, N., A titania nanotube-array room-temperature sensor for selective detection of hydrogen at low concentrations. *Journal of Nanoscience and Nanotechnology* **2004**, 4, (7), 733
50. Pal, M.; GarciaSerrano, J.; Santiago, P.; Pal, U., Size-Controlled Synthesis of Spherical TiO₂ Nanoparticles: Morphology, Crystallization, and Phase Transition. *J. Phys. Chem. C* **2007**, 111, (1), 96-102.

51. Sivakumar, S.; Sibub, C. P.; Mukundan, P.; Pillai, P. K.; Warriar, K. G. K., Nanoporous titania–alumina mixed oxides—an alkoxide free sol–gel synthesis. *Materials Letters* **2004**, *58*, (21), 2664-2669.
52. Aust, U.; Benfer, S.; Dietze, M.; Rost, A.; Tomandl, G., Development of microporous ceramic membranes in the system TiO₂/ZrO₂. *Journal of Membrane Science* **2006**, *281*, (1-2), 463-471.
53. Kitiyanan, A.; Sakulkaemaruethai, S.; Suzuki, Y.; Yoshikawa, S., Structural and photovoltaic properties of binary TiO₂-ZrO₂ oxides system prepared by sol-gel method. *Composites Science and Technology* **2006**, *66*, (10), 1259-1265.
54. Adan, C.; Bahamonde, A.; Fernandez-Garcia, M.; Martinez-Arias, A., Structure and activity of nanosized iron-doped anatase TiO₂ catalysts for phenol photocatalytic degradation. *Applied Catalysis B, Environmental* **2007**, *72*, (1-2), 11-17.
55. Huang, D.-G.; Liao, S.-J.; Liu, J.-M.; Danga, Z.; Petrik, L., Preparation of visible-light responsive N–F-codoped TiO₂ photocatalyst by a sol–gel-solvothermal method. *Journal of Photochemistry and Photobiology A: Chemistry* **2006**, *184*, 282-288.
56. Li, Q.; Xie, R.; Li, Y. W.; Mintz, E. A.; Shang, J. K., Enhanced Visible-Light-Induced Photocatalytic Disinfection of E. coli by Carbon-Sensitized Nitrogen-Doped Titanium Oxide. *Environ. Sci. Technol.* **2007**.
57. Huang, D.-G.; Liao, S.-J.; Liu, J.-M.; Danga, Z.; Petrik, L., Preparation of visible-light responsive N–F-codoped TiO₂ photocatalyst by a sol–gel-solvothermal method *Journal of Photochemistry and Photobiology A: Chemistry* **2006**, *184*, 282-288.
58. Rhee, C. H.; Lee, J. S., Synthesis of nitrogen-doped titanium oxide nanostructures via a surfactant-free hydrothermal route *J. Mater. Res* **2005**, *20*, (11), 3011-3020.
59. Zhang, Q.; Gao, L., One-step preparation of size-defined aggregates of TiO₂ nanocrystals with tuning of their phase and composition. *Journal of the European Ceramic Society* **2006**, *26*, (9), 1535-1545.
60. Yin, S.; Komatsu, M.; Zhang, Q.; Saito, F.; Sato, T., Synthesis of visible-light responsive nitrogen/carbon doped titania photocatalyst by mechanochemical doping *J Mater Sci* **2007**, *42*, 2399–2404.
61. Wu, J. M.; Qi, B., Low-Temperature Growth of a Nitrogen-Doped Titania Nanoflower Film and Its Ability To Assist Photodegradation of Rhodamine B in Water. *J. Phys. Chem. C* **2007**, *111*, (2), 666-673.
62. Wang, X.; Yu, J. C.; Chen, Y.; Wu, L.; Fu, X., ZrO₂-Modified Mesoporous Nanocrystalline TiO_{2-x}N_x as Efficient Visible Light Photocatalysts. *Environ. Sci. Technol.* **2006**, *40*, (7), 2369-2374.
63. Tachikawa, T.; Fujitsuka, M.; Majima, T., Mechanistic Insight into the TiO₂ Photocatalytic Reactions: Design of New Photocatalysts. *J. Phys. Chem. C* **2007**, *111*, (14), 5259-5275.
64. Lin, S.-C.; Lee, Y.-L.; Chang, C.-H.; Shen, Y.-J.; Yang, Y.-M., Quantum-dot-sensitized solar cells: Assembly of CdS-quantum-dots coupling techniques of self-assembled monolayer and chemical bath deposition. *APPLIED PHYSICS LETTERS* **2007**, *90*, 143517.

65. Jia, H.; Xu, H.; Hu, Y.; Tang, Y.; Zhang, L., TiO₂@CdS core-shell nanorods films: Fabrication and dramatically enhanced photoelectrochemical properties. *Electrochemistry Communications* **2007**, *9*, 354–360.
66. Blackburn, J. L.; Selmarten, D. C.; Nozik, A. J., Electron Transfer Dynamics in Quantum Dot/Titanium Dioxide Composites Formed by in Situ Chemical Bath Deposition. *J. Phys. Chem. B* **2003**, *107*, (51), 14154-14157.
67. Robel, I.; Kuno, M.; Kamat, P. V., Size-Dependent Electron Injection from Excited CdSe Quantum Dots into TiO₂ Nanoparticles. *J. Am. Chem. Soc.* **2007**, *129*, (14), 4136-4137.
68. Kumbhar, A.; Chumanov, G., Synthesis of Iron(III)-Doped Titania Nanoparticles and its Application for Photodegradation of Sulforhodamine-B Pollutant. *Journal of Nanoparticle Research* **2005**, *7*, (4-5), 489 - 498.
69. Cong, Y.; Zhang, J.; Chen, F.; Anpo, M.; He, D., Preparation, Photocatalytic Activity, and Mechanism of Nano-TiO₂ Co-Doped with Nitrogen and Iron (III). *J. Phys. Chem. C* **2007**, *111*, (28), 10618-10623.
70. Gracia, F.; Holgado, J. P.; Caballero, A.; Gonzalez-Elipe, A. R., Structural, Optical, and Photoelectrochemical Properties of Mn⁺-TiO₂ Model Thin Film Photocatalysts. *J. Phys. Chem. B* **2004**, *108*, (45), 17466-17476.
71. Han, W. Q.; Wen, W.; Yi, D.; Liu, Z.; Maye, M. M.; Lewis, L.; Hanson, J.; Gang, O., Fe-Doped Trititanate Nanotubes: Formation, Optical and Magnetic Properties, and Catalytic Applications. *J. Phys. Chem. C* **2007**.
72. Ranjit, K. T.; Viswanathan, B., Synthesis, characterization and photocatalytic properties of iron-doped TiO₂ catalysts. *Journal of Photochemistry and Photobiology A: Chemistry* **1997**, *108*, (1), 79-84.
73. Navio, J. A.; Colon, G.; Macias, M.; Real, C.; Litter, M. I., Iron-doped titania semiconductor powders prepared by a sol-gel method. Part I: synthesis and characterization. *Applied Catalysis A: General* **1999**, *177*, 111-120.
74. Yu, J.; Zhou, M.; Yu, H.; Zhang, Q.; Yu, Y., Enhanced photoinduced superhydrophilicity of the sol-gel-derived TiO₂ thin films by Fe-doping. *Materials Chemistry & Physics* **2006**, *95*, (2-3), 193-196.
75. Wang, C.-y.; Böttcher, C.; Bahnemann, D. W.; Dohrmann, J. r. K., A comparative study of nanometer sized Fe(III)-doped TiO₂ photocatalysts: synthesis, characterization and activity. *J. Mater. Chem.* **2003**, *13*, 2322–2329.
76. Aguado-Serrano, J.; Rojas-Cervantes, M. L., Titania aerogels. *Microporous and Mesoporous Materials* **2006**, *88*, (1-3), 205-213.
77. Wang, C. T.; Ro, S. H., Nanocluster iron oxide-silica aerogel catalysts for methanol partial oxidation. *Applied Catalysis A, General* **2005**, *285*, (1-2), 196-204.
78. Kemp, T. J.; McIntyre, R. A., Transition metal-doped titanium(IV) dioxide: Characterisation and influence on photodegradation of poly(vinyl chloride). *Polymer Degradation and Stability* **2006**, *91*, (1), 165-194.
79. Sohn, J. R.; Lee, S. H.; , Effect of TiO₂-ZrO₂ composition on catalytic activity of supported NiSO₄ for ethylene dimerization. *Applied Catalysis A, General* **2007**, *321*, (1), 27-34.
80. Nair, M. P.; Rao, K. V. C.; Nair, C. G. R., Investigation of the mixed oxide materials--TiO₂---SiO₂, TiO₂---SiO₂---Al₂O₃, TiO₂---SiO₂---In₂O₃ and TiO₂---SiO₂--

-RuO₂-In regard to the photoelectrolysis of water. *International Journal of Hydrogen Energy* **1991**, 16, (7), 449-459.

81. Choi, H.; Stathatos, E.; Dionysiou, D. D., Sol-gel preparation of mesoporous photocatalytic TiO₂ films and TiO₂/Al₂O₃ composite membranes for environmental applications

Applied Catalysis B: Environmental **2006**, 63, 60-67.

82. Hernandez-Alonso, M. D.; Tejedor-Tejedor, I.; Coronado, J. M.; Soria, J.; Anderson, M. A., Sol-gel preparation of TiO₂-ZrO₂ thin films supported on glass rings: Influence of phase composition on photocatalytic activity. *Thin Solid Films* **2006**, 502, (1-2), 125-131.

83. Reidy, D. J.; Holmes, J. D.; Morris, M. A., Preparation of a highly thermally stable titania anatase phase by addition of mixed zirconia and silica dopants. *Ceramics International* **2006**, 32, (3), 235-239.

84. Fu, X.; Clark, L. A.; Yang, Q.; Anderson, M. A., Enhanced Photocatalytic Performance of Titania-Based Binary Metal Oxides: TiO₂/SiO₂ and TiO₂/ZrO₂. *Environ. Sci. Technol.* **1996**, 30, (2), 647-653.

85. Neppolian, B.; Wang, Q.; Yamashita, H.; Choi, H., Synthesis and characterization of ZrO₂-TiO₂ binary oxide semiconductor nanoparticles: Application and interparticle electron transfer process. *Applied Catalysis A: General* **2007**, 333, (2), 264-271.

86. Gnatyuk, Y. I.; Yatskiv, V. I.; Smirnova, N. P.; Granchak, V. M.; Eremenko, A. M., Photocatalytic properties of mesoporous TiO₂/ZrO₂ films in gas-phase oxidation of alcohols. *Theoretical and Experimental Chemistry* **2005**, 41, (6), 371-376.

87. Umebayashi, T.; Yamaki, T.; Itoh, H.; Asai, K., Analysis of electronic structures of 3d transition metal doped TiO₂ based on band calculations. *J. Phys. Chem. Solids* **2002**, 63, 1909.

88. Anpo, M.; Kishiguchi, S.; Ichihashi, Y.; Takeuchi, M.; Yamashita, H.; Ikeue, K.; Morin, B.; Davidson, A.; Che, M., The design and development of second-generation titanium oxide photocatalysts able to operate under visible light irradiation by applying a metal ion-implantation method. *Research on Chemical Intermediates* **2001**, 27, (4/5), 459-467.

89. DiValentin, C.; Pacchioni, G.; Selloni, A.; Livraghi, S.; Giamello, E., Characterization of Paramagnetic Species in N-Doped TiO₂ Powders by EPR Spectroscopy and DFT Calculations. *J. Phys. Chem. B* **2005**, 109, (23), 11414-11419.

90. Jung-Yup, L.; Park, J.; Jun-Hyung, C., Electronic properties of N- and C-doped TiO₂. *Applied Physics Letters* **2005**, 87, (1), N.PAG.

91. Nakano, Y.; Morikawa, T.; Ohwaki, T.; Taga, Y., Electrical characterization of band gap states in C-doped TiO₂ films. *Applied Physics Letters* **2005**, 87, (5), N.PAG.

92. Okato, T.; Sakano, T.; Obara, M., Suppression of photocatalytic efficiency in highly N-doped anatase films. *Physical Review B (Condensed Matter and Materials Physics)* **2005**, 72, (11), 115124-6.

93. Li, D.; Haneda, H.; Hishita, S.; Ohashi, N., Visible-Light-Driven N-F-Codoped TiO₂ Photocatalysts. 2. Optical Characterization, Photocatalysis, and Potential Application to Air Purification. *Chem. Mater.* **2005**, 17, (10), 2596-2602.

94. Livraghi, S.; Paganini, M. C.; Giamello, E.; Selloni, A.; Valentin, C. D.; Pacchioni, G., Origin of Photoactivity of Nitrogen-Doped Titanium Dioxide under Visible Light. *J. Am. Chem. Soc.* **2006**, 128, (49), 15666-15671.
95. Serpone, N., Is the Band Gap of Pristine TiO₂ Narrowed by Anion- and Cation-Doping of Titanium Dioxide in Second-Generation Photocatalysts? *J. Phys. Chem. B* **2006**, 110, (48), 24287-24293.
96. Fernandez-Garcia, M.; Martinez-Arias, A.; Hanson, J. C.; Rodriguez, J. A., Nanostructured Oxides in Chemistry: Characterization and Properties. *Chem. Rev.* **2004**, 104, (9), 4063-4104.
97. Kolen'ko, Y. V.; Kovnir, K. A.; Gavrilov, A. I.; Garshev, A. V.; Meskin, P. E.; Churagulov, B. R.; Bouchard, M.; Colbeau-Justin, C.; Lebedev, O. I.; VanTendeloo, G.; Yoshimura, M., Structural, Textural, and Electronic Properties of a Nanosized Mesoporous Zn_xTi_{1-x}O_{2-x} Solid Solution Prepared by a Supercritical Drying Route. *J. Phys. Chem. B* **2005**, 109, (43), 20303-20309.
98. Pierre, A. C., *Introduction to sol-gel processing*. Kluwer Academic Publishers: Boston, 1998; p x, 394 p.
99. Brinker, C. J.; Scherer, G. W., *Sol-Gel Science: The physics and Chemistry of Sol-Gel Processing* Academic press: New York, 1990.
100. Gesser, H. D.; Goswami, P. C., Aerogels and related porous materials. *Chem Rev* **1989**, 89, (4), 765-788.
101. Oh, C. W.; Seong, G.-D. L.; Park, S.; Ju, C.-S.; Hong, S.-S., Synthesis of nanosized TiO₂ particles via ultrasonic irradiation and their photocatalytic activity. *Reaction Kinetics and Catalysis Letters* **2005**, 85, (2), 261.
102. Legrand-Buscema, C.; C. Malibert, S. B., Elaboration and characterization of thin films of TiO₂ prepared by sol-gel process. *Thin Solid Films* **2002**, 418, 79-84.
103. Li, F. B.; Li, X. Z.; Hou, M. F., Photocatalytic degradation of 2-mercaptobenzothiazole in aqueous La³⁺-TiO₂ suspension for odor control. *Applied Catalysis B: Environmental* **2004**, 48, (3), 185-194.
104. Weissman, J. G.; Ko, E. I.; Kaytal, S., Titania-zirconia mixed oxide aerogels as supports for hydrotreating catalysts. *Applied Catalysis A: General* **1993** 94, 45-59.
105. Chang, S. m.; Doong, R. a., Characterization of Zr-Doped TiO₂ Nanocrystals Prepared by a Nonhydrolytic Sol-Gel Method at High Temperatures. *J. Phys. Chem. B* **2006**, 110, (42), 20808-20814.
106. Bavykin, D. V.; Friedrich, J. M.; Walsh, F. C., Protonated Titanates and TiO₂ Nanostructured Materials: Synthesis, Properties, and Applications. *Advanced Materials* **2006**, 18, (21), 2807-2824.
107. Du, G. H.; Chen, Q.; Che, R. C.; Yuan, Z. Y.; Peng, L. M., Preparation and structure analysis of titanium oxide nanotubes. *Applied Physics Letters* **2001**, 79, (22), 3702-3704.
108. Wang, Y. Q.; Hu, G. Q.; Duan, X. F.; Sun, H. L.; Xue, Q. K., Microstructure and formation mechanism of titanium dioxide nanotubes. *Chemical Physics Letters* **2002**, 365, (5-6), 427-431
109. Wang, Y.; Cheng, H.; Hao, Y.; Ma, J.; Li, W.; Cai, S., Photoelectrochemical properties of metal-ion-doped TiO₂ nanocrystalline electrodes. *Thin Solid Films* **1999**, 349, (1-2), 120-125

110. Kim, C. S.; Okuyama, K.; Nakaso, K.; Shimada, M., Direct measurement of nucleation and growth modes in titania nanoparticles generation by a CVD method. *J Chem Eng Jpn* **2004**, 37, (11), 1379.
111. Kim, C.; Nakaso, K.; Xia, B.; Okuyama, K.; Shimada, M., A New Observation on the Phase Transformation of TiO₂ Nanoparticles Produced by a CVD Method. *Aerosol Science & Technology* **2005**, 39, (2), 104-112.
112. Cao, Y.; Yang, W.; Zhang, W.; Liub, G.; Yue, P., Improved photocatalytic activity of Sn⁴⁺ doped TiO₂ nanoparticulate films prepared by plasma-enhanced chemical vapor deposition. *New J. Chem* **2004**, 28218-222.
113. Sudarshan, T. S. In *Coated powders - new horizons and applications*, Advances in Surface Treatment: Research & Applications (ASTRA), Proceedings of the International Conference, Hyderabad, India, 2003; Hyderabad, India, 2003; pp 412-422.
114. Liang, C.; Shimizu, Y.; Sasaki, T.; Koshizaki, N., Synthesis, characterization, and phase stability of ultrafine TiO₂ nanoparticles by pulsed laser ablation in liquid media. *J Mater Res* **2004**, 19, (5), 1551-1557.
115. Nagaveni, K.; Hegde, M. S.; Madras, G., Structure and Photocatalytic Activity of Ti_{1-x} M_xO₂ ; (M = W, V, Ce, Zr, Fe, and Cu) Synthesized by Solution Combustion Method. *J. Phys. Chem. B* **2004**, 108, (52), 20204-20212.
116. Jinsoo, K.; Jae Won, L.; Tai Gyu, L.; Suk Woo, N.; Jonghee, H., Nanostructured titania membranes with improved thermal stability. *Journal of Materials Science* **2005**, 40, (7), 1797-1799.
117. Iwasaki, M.; Davis, S. A.; Mann, S., Spongelike Macroporous TiO₂ Monoliths Prepared from Starch Gel Template. *J Sol-Gel Sci Techn* **2004**, 32, 99-105.
118. Kisch, H.; Sakthivel, S.; Janczarek, M.; Mitoraj, D., A Low-Band Gap, Nitrogen-Modified Titania Visible-Light Photocatalyst. *J. Phys. Chem. C* **2007**, 111, (30), 11445-11449.
119. Maeda, M.; Yamada, T., Photocatalytic activity of metal-doped titanium oxide films prepared by sol-gel process. *Journal of Physics: Conference Series* **2007**, 61, 755-759.
120. Lucky, R. A.; Charpentier, P. A., A one-step approach to the synthesis of ZrO₂ modified TiO₂ nanotubes in supercritical carbon dioxide. *Advanced Materials*. **2008**, 20, (9), 1755-1759.
121. Rayner, C. M., The Potential of Carbon Dioxide in Synthetic Organic Chemistry. *Organic Process Research & Development* **2007**, 11, (), 121-132.
122. Clark, J. H.; Tavener, S. J., Alternative Solvents: Shades of Green. *Org. Process Res. Dev.* **2007**, 11, (1), 149-155.
123. Sui, R., Synthesis and Characterization of Oxide Nanostructures Via a Sol-Gel Route in Supercritical CO₂. *PhD thesis* **2007**.
124. Jia, M., Particle formation in supercritical carbon dioxide by the RESS process. *M.E.Sc. thesis* **2003**.
125. Dobbs, J. M.; Wong, J. M.; Lahiere, R. J.; Johnston, K. P., Modification of Supercritical Fluid Phase Behavior Using Polar Cosolvents. *Ind. Eng. Chem. Res.* **1987**, 26, 56-65.

126. Salmas, C. E.; Androustopoulos, G. P., Rigid Sphere Molecular Model Enables an Assessment of the Pore Curvature Effect upon Realistic Evaluations of Surface Areas of Mesoporous and Microporous Materials. *Langmuir* **2005**, 21, (24), 11146-11160.
127. Woods, H. M.; Silva, M. M. C. G.; Nouvel, C.; Shakesheff, K. M.; Howdle, S. M., Material Processing in Supercritical Carbon Dioxide: Surfactants, Polymers and Biomaterials. *J Mater Chem* **2004**, 14, 1663-1678.
128. O'Neil, A.; Watkins, J. J., Reactive Deposition of Conformal Metal Oxide Films from Supercritical Carbon Dioxide. *Chem. Mater.* **2007**, 19, (23), 5460-5466.
129. King, J. W.; Williams, L. L., Utilization of critical fluids in processing semiconductors and their related materials. *Curr Opin Solid ST M* **2003**, 7, (4-5), 413-424.
130. Charpentier, P. A.; DeSimone, J. M.; Roberts, G. W., Continuous polymerizations in supercritical carbon dioxide. *ACS Symposium Series* **2002**, 819, 113-135.
131. Smirnova, I.; Arlt, W., Synthesis of Silica Aerogels; Influence of the Supercritical CO₂ on the Sol-Gel Process. *Journal of Sol-Gel Science and Technology* **2003**, 28, (2), 175-184.
132. Lee, M.-H.; Lin, H.-Y.; Thomas, J. L., A Novel Supercritical CO₂ Synthesis of Amorphous Hydrous Zirconia Nanoparticles, and Their Calcination to Zirconia. *Journal of the American Ceramic Society* **2006**, 89, (12), 3624-3630.
133. McHugh, M. A.; Krukonis, V. J., *Supercritical fluid extraction : principles and practice*. Butterworths: Boston ; Toronto, 1986; p ix, 507.
134. Darr, J. A.; Poliakoff, M., New Directions in Inorganic and Metal-Organic Coordination Chemistry in Supercritical Fluids. *Chem Rev* **1999**, 99, (2), 495-541.
135. Dixon, D. J.; Johnston, K. P., *Supercritical Fluids. Encyclopedia of Chemical Technology* **1997**, 4th, (23), 452-478.
136. Johnston, K. P., *Supercritical Fluid Science and Technology. American Chemical society, washington, Dc* **1989**.
137. Taylor, L. T., *Supercritical fluid extraction*. Wiley: New York, 1996; p xiv, 181 p.
138. Tadros, M. E. A., Carol L. J.; Russick, Edward M.; Youngman, Michael P., Synthesis of titanium dioxide particle in supercritical CO₂. *J Supercrit Fluids* **1996**, 9, (3), 172-176.
139. Stallings, W. E.; Lamb, H. H., Synthesis of Nanostructured Titania Powders via Hydrolysis of Titanium Isopropoxide in Supercritical Carbon Dioxide. *Langmuir* **2003**, 19, (7), 2989-2994.
140. Hong, S.-S.; Lee, M. S.; Lee, G.-D.; Lim, K. T.; Ha, B.-J., Synthesis of titanium dioxides in water-in-carbon dioxide microemulsion and their photocatalytic activity. *Mater Lett* **2003**, 57, (19), 2975.
141. Guo, G.; Whitesell, J. K.; Fox, M. A., Synthesis of TiO₂ Photocatalysts in Supercritical CO₂ via a Non-hydrolytic Route. *J. Phys. Chem. B* **2005**, 109, (40), 18781-18785.
142. Reverchon, E.; Caputo, G.; Correr, S.; Cesti, P., Synthesis of titanium hydroxide nanoparticles in supercritical carbon dioxide on the pilot scale. *J. Supercrit. Fluids* **2003**, 26, 253.
143. Reverchon, E.; Adami, R., Nanomaterials and supercritical fluids. *The Journal of Supercritical Fluids* **2006**, 37 (1), 1-22.

144. Sun, D.; Liu, Z.; He, J.; Han, B.; Zhang, J.; Huang, Y., Surface sol-gel modification of mesoporous silica molecular sieve SBA-15 with TiO₂ in supercritical CO₂. *Microporous and Mesoporous Materials* **2005**, 80, 165.
145. Tatsuda, N.; Itahara, H.; Setoyama, N.; Fukushima, Y., Preparation of titanium dioxide/activated carbon composites using supercritical carbon dioxide. *Carbon* **2005**, 43, (11), 2358-2365
146. Sun, D.; Huang, Y.; Han, B.; Yang, G., Ti-Si Mixed Oxides Prepared by Polymer in Situ Sol-Gel Chemistry with the Aid of CO₂. *Langmuir* **2006**, 22, (10), 4793-4798.
147. Jensen, H.; Bremholm, M.; Nielsen, R. e. P.; Joensen, K.; Pedersen, J.; Birkedal, H.; Chen, Y.-S.; Almer, J.; Søgaaard, E.; Iversen, S.; Iversen, B., In Situ High-Energy Synchrotron Radiation Study of Sol-Gel Nanoparticle Formation in Supercritical Fluids. *Angewandte Chemie International Edition* **2007**, 46, (7), 1113 - 1116.
148. Loy, D. A.; Russick, E. M.; Yamanaka, S. A.; Baugher, B. M.; Shea, K. J., Direct Formation of Aerogels by Sol-Gel Polymerizations of Alkoxysilanes in Supercritical Carbon Dioxide. *Chem. Mater.* **1997**, 9, (11), 2264-2268.
149. Sui, R.; Rizkalla, A. S.; Charpentier, P. A., Formation of Titania Nanofibers: A Direct Sol-Gel Route in Supercritical CO₂. *Langmuir* **2005**, 21, (14), 6150-6153.
150. Sui, R.; Rizkalla, A. S.; Charpentier, P. A., Synthesis and Formation of Silica Aerogel Particles By a Novel Sol-Gel Route in Supercritical Carbon Dioxide. *J. Phys. Chem. B* **2004**, 108, (32), 11886-11892.
151. Sui, R.; Rizkalla, A. S.; Charpentier, P. A., FTIR Study on the Formation of TiO₂ Nanostructures in Supercritical CO₂. *J. Phys. Chem. B* **2006**, 110, (33), 16212-16218.
152. Nakamoto, K., *Infrared and Raman spectra of inorganic and coordination compounds*. 4th ed.; Wiley: New York ; Toronto, 1986; p xi, 484 p.
153. Venter, M. J.; Willems, P.; Kareth, S.; Weidner, E.; Kuipers, N. J. M.; de Haan, A. B., Phase equilibria and physical properties of CO₂-saturated cocoa butter mixtures at elevated pressures. *The Journal of Supercritical Fluids* **2007**, 41, (2), 195-203.
154. vanSchilt, M. A.; Wering, R. M.; vanMeerendonk, W. J.; Kemmere, M. F.; Keurentjes, J. T. F.; Kleiner, M.; Sadowski, G.; deLoos, T. W., High-Pressure Phase Behavior of the System PCHC-CHO-CO₂ for the Development of a Solvent-Free Alternative toward Polycarbonate Production. *Ind. Eng. Chem. Res.* **2005**, 44, (9), 3363-3366.
155. Schneider, M. S.; Grunwaldt, J. D.; BÅ¹/₄rgi, T.; Baiker, A., High pressure view-cell for simultaneous in situ infrared spectroscopy and phase behavior monitoring of multiphase chemical reactions. *Review of Scientific Instruments* **2003**, 74, (9), 4121.
156. Lazzaroni, M. J.; Bush, D.; Jones, R.; Hallett, J. P.; Liotta, C. L.; Eckert, C. A., High-pressure phase equilibria of some carbon dioxide-organic-water systems. *Fluid Phase Equilibria* **2004**, 224, (1), 143-154.
157. http://en.wikipedia.org/wiki/Differential_scanning_calorimetry.
158. Arai, Y.; Akers, R. J.; Treasure, C. R. G., *Chemistry of powder production*. 1st English language ed.; Chapman & Hall: London, 1996; p ix, 281 p.
159. Spurr, R. A.; Myers, H., Quantitative Analysis of Anatase-Rutile Mixtures with an X-Ray Diffractometer. *Anal. Chem.* **1957**, 29, (5), 760-762.
160. Gregg, S. J.; Sing, K. S. W., *Adsorption, surface area, and porosity*. 2nd ed.; Academic Press: London ; Toronto, 1982; p xi, 303 p.

161. Brunauer, S.; Emmett, P. H.; Teller, E., Adsorption of Gases in Multimolecular Layers. *J Am Chem Soc* **1938**, 60, (2), 309-319.
162. Barrett, E. P.; Joyner, L. G.; Halenda, P. P., The Determination of Pore Volume and Area Distributions in Porous Substances. I. Computations from Nitrogen Isotherms. *J Am Chem Soc* **1951**, 73, (1), 373-380.
163. Lukens, W. W.; Schmidt-Winkel, P.; Zhao, D.; Feng, J.; Stucky, G. D., Evaluating Pore Sizes in Mesoporous Materials: A Simplified Standard Adsorption Method and a Simplified Broekhoff-de Boer Method. *Langmuir* **1999**, 15, (16), 5403-5409.
164. Perkampus, H.-H., *UV-VIS spectroscopy and its applications*. Springer-Verlag: Berlin ; New York, 1992; p ix, 244 p.
165. Feng, L.; Berglund, K. A., ATR FTIR for determination optimal cooling curves for batch crystallization of succinic acid. *J. of Crystal Growth* **2002**, 2, (5), 449-452.
166. Lewiner, F.; F'evotte, G.; Klein, J. P.; Puel, F., Improving Batch Cooling Seeded Crystallization of an Organic Weed-Killer Using On-Line ATR FTIR Measurement of Supersaturation. *J. of Crystal Growth* **2001**, 226, 348-362.
167. Cheng, B.; Qu, S.; Zhou, H.; Wang, Z., Al₂O₃:Cr⁺ Nanotubes Synthesized via Homogenization Precipitation Followed by Heat Treatment. *J. Phys. Chem. B* **2006**, 110, (32), 15749-15754.
168. Cai, Q.; Yang, L.; Yu, Y., Investigations on the self-organized growth of TiO₂ nanotube arrays by anodic oxidization. *Thin Solid Films* **2006**, 515, 1802-1806.
169. Sander, M. S.; Côté, M. J.; Gu, W.; Kile, B. M.; Tripp, C. P., Template-Assisted Fabrication of Dense, Aligned Arrays of Titania Nanotubes with Well-Controlled Dimensions on Substrates. *Advanced Materials* **2004**, 16, 2052-2057.
170. Qiu, J.; Jin, Z.; Liu, Z.; Liu, X.; Liu, G.; Wu, W.; Zhang, X.; Gao, X., Fabrication of TiO₂ nanotube film by well-aligned ZnO nanorod array film and sol-gel process. *Thin Solid Films* **2007**, 515, 2897-2902.
171. Weng, L. Q.; Song, S. H.; Hodgson, S.; Baker, A.; Yu, J., Synthesis and characterisation of nanotubular titanates and titania. *Journal of the European Ceramic Society* **2006**, 26, 1405-1409.
172. Zhang, H.; Li, G. R.; An, L. P.; Yan, T. Y.; Gao, X. P.; Zhu, H. Y., Electrochemical Lithium Storage of Titanate and Titania Nanotubes and Nanorods. *J. Phys. Chem. C* **2007**, 111, (16), 6143-6148.
173. Giddings, J. C.; Myers, M. N.; McLaren, L.; Keller, R. A., High pressure gas chromatography of nonvolatile species. Compressed gas is used to cause migration of intractable solutes. *Science* **1968**, 162, 67-73.
174. Silva, R. F.; Vasconcelos, W. L., Influence of Processing Variables on the Pore Structure of Silica Gels Obtained with Tetraethylorthosilicate. *Materials Research* **1999**, 2 (3), 197-200.
175. Birnie, I., Dunbar P., Esterification kinetics in titanium isopropoxide-acetic acid solutions. *Journal of Materials Science* **2000**, 35, (2), 367-374.
176. Cao, G., *Nanostructures & nanomaterials : synthesis, properties & applications*. Imperial College Press: London, 2004; p xiv, 433 p.
177. Yasue, T.; Tsuchida, Y.; Arai, Y., Crystal shape and preprecipitation conditions of Ca(OH)₂. *Gypsum Lime* **1984**, 189, 17.

178. Kim, K. D.; Kim, H. T., Comparison of the effect of reaction parameters on particle size in the formation of SiO₂, TiO₂, and ZrO₂ nanoparticles. *Materials Letters* **2003**, 57 3211–3216.
179. Doeuff, S.; Henry, M.; Sanchez, C.; Livage, J., Hydrolysis of titanium alkoxides: Modification of the molecular precursor by acetic acid. *Journal of Non-Crystalline Solids* **1987**, 89, (1-2), 206-216.
180. Birnie III, D. P.; Bendzko, N. J., ¹H and ¹³C NMR observation of the reaction of acetic acid with titanium isopropoxide. *Materials Chemistry and Physics* **1999**, 59, (1), 26-35.
181. Bradley, D. C.; Gaze, R.; Wardlaw, W., *J. Chem. Soc.*, **1957**, 469.
182. Sanchez, C.; Livage, J.; Henry, M.; Babonneau, F., Chemical Modification of alkoxide precursors. *Journal of Non-Crystalline Solids* **1988**, 100, 65-76.
183. Jupa, M.; Kickelbick, G.; Schubert, U., Methacrylate-Substituted Titanium-Yttrium Mixed-Metal Oxo Clusters. *European Journal of Inorganic Chemistry* **2004**, 1835 - 1839, 9.
184. Zhu, J.; Zhang, J.; Chen, F.; Iino, K.; Anpo, M., High activity TiO₂ Photocatalysts Prepared by a Modified Sol-gel Method: Characterization and their Photocatalytic Activity for the Degradation of XRG and X-GL. *Topics in Catalysis* **2005**, 35, (3-4), 261-268.
185. Lucky, R. A.; Sui, R.; Charpentier, P. A.; Jennings, M. C., Decakis(μ₂-acetato-κ²O:O')bis(μ₂-isopropoxy- κ²O:O) tetraisopropoxytetra- μ₃-oxo-tetratitaniumdizirconium. *Acta Cryst., E* **2007**, 63, m2429–m2430.
186. Galindo, I. R.; Viveros, T.; Chadwick, D., Synthesis and Characterization of Titania-Based Ternary and Binary Mixed Oxides Prepared by the Sol-Gel Method and Their Activity in 2-Propanol Dehydration. *Ind. Eng. Chem. Res.* **2007**, 46, (4), 1138-1147.
187. Reddy, B. M.; Chowdhury, B.; Smirniotis, P. G., An XPS study of the dispersion of MoO₃ on TiO₂-ZrO₂, TiO₂-SiO₂, TiO₂-Al₂O₃, SiO₂-ZrO₂, and SiO₂-TiO₂-ZrO₂ mixed oxides. *Applied Catalysis A: General* **2001**, 211, (1), 19-30.
188. Chen, Q.; Zhou, W.; Du, G. H.; Peng, L.-M., Trititanate Nanotubes Made via a Single Alkali Treatment. *Advanced Materials* **2002**, 14, (17), 1208-1211.
189. Sui, R.; Rizkalla, A. S.; Charpentier, P. A., Direct Synthesis of Zirconia Aerogel Nanoarchitecture in Supercritical CO₂. *Langmuir* **2006**, 22, (9), 4390-4396.
190. Doeuff, S.; Dromzee, Y.; Taulelle, F.; Sanchez, C., Synthesis and Solid- and Liquid-State Characterization of a Hexameric Cluster of Titanium (IV): Ti₆(O)₂ (p₃-o)₂ (p₂-OC₄H₉)₂(OC₄H₉)₆(O COCH₃)₈. *Inorg. Chem.* **1989**, 28, 4439-4445.
191. Zhong, Z.; Ang, T. P.; Luo, J.; Gan, H. C.; Gedanken, A., Synthesis of One-Dimensional and Porous TiO₂ Nanostructures by Controlled Hydrolysis of Titanium Alkoxide via Coupling with an Esterification Reaction. *Chem. Mater.* **2005**, 17, (26), 6814-6818.
192. Kickelbick, G.; Feth, M. P.; Bertagnolli, H.; Puchberger, M.; Holzinger, D.; Gross, S., Formation of organically surface-modified metal oxo clusters from carboxylic acids and metal alkoxides: a mechanistic study *J. Chem. Soc., Dalton Trans.* **2002**, 3892-3898.

193. Kickelbick, G.; Schubert, U., Oxozirconium methacrylate clusters. $Zr_6(OH)_4O_4(OMc)_{12}$ and $Zr_4O_2(OMc)_{12}$ (OMc = methacrylate). *Chem Ber/Recl* **1997**, 130, (4), 473-477.
194. Kickelbick, G.; Wiede, P.; Schubert, U., Variations in capping the $Zr_6O_4(OH)_4$ cluster core: X-ray structure analyses of $[Zr_6(OH)_4O_4(OOC-CH=CH_2)_{10}]_2(\mu-OOC-CH=CH_2)_4$ and $Zr_6(OH)_4O_4(OOCR)_{12}(PrOH)$ (R = Ph, CMe = CH₂). *Inorganica Chimica Acta* **1999**, 284, (1), 1-7.
195. Kickelbick, G.; Feth, M. P.; Bertagnolli, H.; Puchberger, M.; Holzinger, D.; Gross, S., Formation of organically surface-modified metal oxo clusters from carboxylic acids and metal alkoxides: a mechanistic study. *J. Chem. Soc., Dalton Trans.* **2002**, 3892-3898.
196. Mackenzie, J. D.; Bescher, E. P., Chemical Routes in the Synthesis of Nanomaterials Using the Sol-Gel Process. *Acc. Chem. Res.* **2007**, 40, (9), 810-818.
197. Kayan, A., Solvent Effect on Complexation of Titanium Tetraethoxide with Allylacetate. *Journal of Inorganic and Organometallic Polymers and Materials* **2005**, 158, (3), 361-365.
198. Ranjit, K. T.; Klabunde, K. J., Solvent Effects in the Hydrolysis of Magnesium Methoxide, and the Production of Nanocrystalline Magnesium Hydroxide. An Aid in Understanding the Formation of Porous Inorganic Materials. *Chem. Mater.* **2005**, 17, (1), 65-73.
199. Boiadjieva, T.; Cappelletti, G.; Ardizzone, S.; Rondinini, S.; Vertova, A., Nanocrystalline titanium oxide by sol-gel method. The role of the solvent removal step. *Phys. Chem. Chem. Phys.* **2003**, 5, 1689-1694.
200. Melada, S.; Signoreto, M.; Ardizzone, S. A.; Bianchi, C. L., Physico-chemical features and catalytic activity of sulfated zirconia prepared by sol-gel method. The role of the solvent evaporation step. *Catalysis Letters* **2001**, 75, (3-4), 199-204.
201. Kauffman, G. W.; Jurs, P. C., Prediction of Surface Tension, Viscosity, and Thermal Conductivity for Common Organic Solvents Using Quantitative Structure-Property Relationships. *J. Chem. Inf. Model.* **2001**, 41, (2), 408-418.
202. Gash, A. E.; Tillotson, T. M.; Satcher Jr., J. H.; Hrubesh, L. W.; Simpson, R. L., New sol-gel synthetic route to transition and main-group metal oxide aerogels using inorganic salt precursors. *Journal of Non-Crystalline Solids* **2001**, 285, (1-3), 22-28.
203. Gao, Y. P.; Sisk, C. N.; Hope-Weeks, L. J., A Sol-Gel Route To Synthesize Monolithic Zinc Oxide Aerogels. *Chem. Mater.* **2007**.
204. Ranjit, K. T.; Martyanov, I.; Demydov, D.; Uma, S.; Rodrigues, S.; Klabunde, K. J., A review of the chemical manipulation of nanomaterials using solvents: Gelation dependent structures. *Journal of Sol-Gel Science and Technology* **2006**, 40, (2-3), 335-339.
205. Bradley, D. C.; Mehrotra, R. C.; Gaur, D. P., *Metal alkoxides*. Academic Press: London ; New York, 1978; p viii, 411 p.
206. Rao, C. N. R.; Raveau, B., *Transition metal oxides : structure, properties, and synthesis of ceramic oxides*. 2nd ed.; Wiley-VCH: New York, 1998; p xi, 373 p.
207. Kazarian, S. G.; Vincent, M. F.; Bright, F. V.; Liotta, C. L.; Eckert, C. A., Specific Intermolecular Interaction of Carbon Dioxide with Polymers. *J Am Chem Soc* **1996**, 118, (7), 1729-1736.

208. Spijksma, G. I.; Huiskes, C.; Benes, N. E.; Kruidhof, H.; Blank, D. H. A.; Kessler, V. G.; Bouwmeester, H. J. M., Microporous Zirconia–Titania Composite Membranes Derived from Diethanolamine-Modified Precursors. *Advanced Materials* **2006**, 18, 2165–2168.
209. Zou, H.; Lin, Y. S., Structural and surface chemical properties of sol-gel derived TiO₂-ZrO₂ oxides. *Applied Catalysis A: General* **2004**, 265, (1), 35-42.
210. Avrami, M., Granulation, Phase Change, and Microstructure Kinetics of Phase Change. III. *The Journal of Chemical Physics* **1941**, 9, (2), 177-184.
211. Avrami, M., Kinetics of Phase Change. II Transformation-Time Relations for Random Distribution of Nuclei. *The Journal of Chemical Physics* **1940**, 8, (2), 212-224.
212. Avrami, M., Kinetics of Phase Change. I General Theory. *The Journal of Chemical Physics* **1939**, 7, (12), 1103-1112.
213. Hossain, M. M.; de Lasa, H. I., Reactivity and stability of Co-Ni/Al₂O₃ oxygen carrier in multicycle CLC. *J AIChE Journal* **2007**, 53, (7), 1817 - 1829.
214. Brown, M. E., *Introduction to thermal analysis : techniques and applications*. 2nd ed.; Kluwer Academic Publishers: Dordrecht ; Boston, 2001; p xi, 264 p.
215. Kissinger, H. E., *J. Res. Natl. Bur: Stand. (US)* **1956**, 57, 217.
216. Burns, A.; Hayes, G.; Li, W.; Hirvonen, J.; Demaree, J. D.; Shah, S. I., Neodymium ion dopant effects on the phase transformation in sol-gel derived titania nanostructures. *Materials Science and Engineering B* **2004**, 111, (2-3), 150-155.
217. Hu, Y.; Tsai, H. L.; Huang, C. L., Phase transformation of precipitated TiO₂ nanoparticles. *Materials Science and Engineering A* **2003**, 344, (1-2), 209-214.
218. Zhang, H.; Banfield, J. F., Phase transformation of nanocrystalline anatase-to-rutile via combined interface and surface nucleation. *Journal of Materials Research Bulletin* **2000**, 15, 437-448.
219. Zhang, Y.-H.; Chan, C. K.; Porter, J. F.; Guo, W., Micro-Raman spectroscopic characterization of nanosized TiO₂ powders prepared by vapor hydrolysis. *Journal of Materials Research Bulletin* **1998**, 13, (9), 2602-2609.
220. Lottici, P. P.; D. Bersani; M. Braghini; Montenero, A., Raman scattering characterization of gel-derived titania glass. *Journal of Materials Science* **1993**, 28, 177-183.
221. Sahni, S.; Reddy, S. B.; Murty, B. S., Influence of process parameters on the synthesis of nano-titania by sol-gel route. *Materials Science & Engineering A* **2007**, 758-762.
222. He, D.; Lin, F., Preparation and photocatalytic activity of anatase TiO₂ nanocrystallites with high thermal stability. *Materials Letters* **2007**, 61, (16), 3385-3387.
223. Shannon, R. D.; Pask, J. A., Kinetics of the Anatase-Rutile Transformation. *Journal of American ceramic society* **1965**, 48, (8), 391-398.
224. Iida, Y.; Ozaki, S., Growth and Phase Transformation of Titanium Oxide During Calcination. *J. Am. Ceram. Soc.* **1961**, 44 (3), 120-127.
225. Jang, J. S.; Kim, H. G.; Ji, S. M.; Bae, S. W.; Jung, J. H.; Shon, B. H.; Lee, J. S., Formation of crystalline TiO₂-xNx and its photocatalytic activity. *Journal of Solid State Chemistry* **2006**, 179, (4), 1067-1075.
226. Ding, X.-z.; Liu, X.-h., Correlation between anatase-to-rutile transformation and grain growth in nanocrystalline titania powders. *Journal of Materials Research* **1998**, 13, (9), 2556-2559.

227. Johnston, K. P.; Shah, P. S., Making Nanoscale Materials with Supercritical Fluids. *Science* **2004**, 303, (5657), 482-483.
228. Zhu, K.; Neale, N. R.; Miedaner, A.; Frank, A. J., Enhanced Charge-Collection Efficiencies and Light Scattering in Dye-Sensitized Solar Cells Using Oriented TiO₂ Nanotubes Arrays. *Nano Lett.* **2007**, 7, (1), 69-74.
229. Chi, B.; Victorio, E. S.; Jin, T., Synthesis of Eu-doped photoluminescent titania nanotubes via a two-step hydrothermal treatment. *nanotechnology* **2006**, 17, 2234-2241.
230. Kocher, M.; Daubler, T. K.; Harth, E.; Scherf, U.; Gugel, A.; Neher, D., Photoconductivity of an inorganic/organic composite containing dye-sensitized nanocrystalline titanium dioxide. *Applied Physics Letters* **1998**, 72, (6), 650-652.
231. Dong, W.; Wu, S.; Chen, D.; Jiang, X.; Zhu, C., Preparation of α -Fe₂O₃ Nanoparticles by Sol-Gel Process with Inorganic Iron Salt. *Chemistry Letters* **2000**, 496-497.
232. Gordon, L. J.; Scott, R. L., Enhanced Solubility in Solvent Mixtures. I. The System Phenanthrene-Cyclohexane-Methylene Iodide. *J Am Chem Soc* **1952**, 74, (16), 4138-4140.
233. Barton, A. F. M., *CRC handbook of solubility parameters and other cohesion parameters*. CRC Press: Boca Raton, Fla., 1983; p 594 p.
234. Allada, S. R., Solubility Parameters of Supercritical Fluids. *Ind. Eng. Chem. Process Des. Dev.* **1984**, 23, 344-348.
235. Fried, J. R., *Polymer science and technology*. 2nd ed.; Prentice Hall Professional Technical Reference: Upper Saddle River, NJ, 2003; p xvii, 582 p.
236. Yu, D.; Qian, J.; Xue, N.; Zhang, D.; Wang, C.; Guo, X.; Ding, W.; Chen, Y., Mesoporous Nanotubes of Iron Phosphate: Synthesis, Characterization, and Catalytic Property. *Langmuir* **2007**, 23, (2), 382-386.
237. Milosev, I.; H.H, S.; B, N., Oxidation of Ternary TiZrN Hard Coatings Studied by XPS. *Surface and Interface analysis* **1998**, 26, 242-248.
238. Jitianu, A.; Raileanu, M.; Crisan, M.; Predoi, D.; Jitianu, M.; Stanciu, L.; Zaharescu, M., Fe₃O₄-SiO₂ nanocomposites obtained via alkoxide and colloidal route. *Journal of Sol-Gel Science and Technology* **2006**, 40, (2-3), 317 - 323.
239. Kisch, H.; Sakthivel, S.; Janczarek, M.; Mitoraj, D., A low-band gap, Nitrogen-modified Titania Visible-Light Photocatalyst. *J. phys. Chem. C* **2007**, 111, 11445-11449.
240. Zhu, J.; Ren, J.; Huo, Y.; Bian, Z.; Li, H., Nanocrystalline Fe/TiO₂ Visible Photocatalyst with a Mesoporous Structure Prepared via a Nonhydrolytic Sol-Gel Route. *J. Phys. Chem. C* **2007**, 111, (51), 18965-18969.
241. Zhang, Z.; Wang, C. C.; Zakaria, R.; Ying, J. Y., Role of Particle Size in Nanocrystalline TiO₂-Based Photocatalysts. *J. Phys. Chem. B* **1998**, 102, (52), 10871-10878.
242. Zhoua, M.; Yu, J.; Chenga, B., Effects of Fe-doping on the photocatalytic activity of mesoporous TiO₂ powders prepared by an ultrasonic method. *Journal of Hazardous Materials* **2006**, B137 1838-1847.
243. YASUTAKA, T.; YUTAKA, O., Manufacture of storage stable and uniform aqueous solutions containing titanium. *Jpn. Kokai Tokkyo Koho* **2001**, 6.
244. Lucky, R. A.; Charpentier, P. A., Synthesis of Zr-Ti Binary metal oxide nanostructure via acid modified sol-gel route in scCO₂.

245. Lucky, R. A.; Charpentier, P. A., Thermal Behavior of ZrO₂ modified TiO₂ Nanotubes Synthesized in scCO₂. **submitted**.
246. Huo, Y.; Bian, Z.; Zhang, X.; Jin, Y.; Zhu, J.; Li, H., Highly Active TiO₂-xN_x Visible Photocatalyst Prepared by N-Doping in Et₃N/EtOH Fluid under Supercritical Conditions. *J. Phys. Chem. C* **2008**.
247. Chen, X.; Burda, C., Photoelectron Spectroscopic Investigation of Nitrogen-Doped Titania Nanoparticles. *J. Phys. Chem. B* **2004**, 108 15446-15449.
248. Yang, J.; Bai, H.; Tan, X.; Lian, J., IR and XPS investigation of visible-light photocatalysis-Nitrogen-carbon-doped TiO₂ film. *Applied Surface Science* **2006**, 253, 1988-1994.
249. Diwald, O.; Thompson, T. L.; Goralski, E. G.; Walck, S. D.; Yates, J. T., The Effect of Nitrogen Ion Implantation on the Photoactivity of TiO₂ Rutile Single Crystals. *J. Phys. Chem. B* **2004**, 108, (1), 52-57.
250. Saha, N. C.; Tompkins, H. G., Titanium nitride oxidation chemistry: An x-ray photoelectron spectroscopy study. *Journal of Applied Physics* **1992**, 72, (7), 3072.
251. Brunelle, J. P., Preparation of Catalysts by Metallic Complex Adsorption on Mineral Oxides'. *Pure and Applied Chemistry* **1978**, 50, 1211-1229.

Appendices

Appendix 1. Copyright Permissions of Advanced Materials

We hereby grant permission for the requested use expected that due credit is given to the original source. For material published before 2006 additionally: Please note that the author's permission is also required. If material appears within our work with credit to another source, authorisation from that source must be obtained. Credit must include the following components: - Books: Author(s)/ Editor(s) Name(s): Title of the Book. Page(s) Publication year. Copyright Wiley-VCH Verlag GmbH & Co. KGaA. Reproduced with permission.- Journals: Author(s) Name(s): Title of the Article. Name of the Journal. Publication year. Volume. Page(s). Copyright Wiley-VCH Verlag GmbH & Co. KGaA. Reproduced with permission.

Appendix 2. Copyright Permissions of Acta Crystallographica Journals

If you wish to include material from your own article in a publication, prior permission is not required, subject to the following conditions:

- Reproduction is intended in a primary journal, secondary journal, CD-ROM, book or thesis.
- The original article in which the material appeared is cited.
- IUCr's copyright permission is indicated next to the Figure/Table in print. In electronic form, this acknowledgement must be visible at the same time as the Figure/Table, and must be hyperlinked to Crystallography Journals Online (<http://journals.iucr.org/>).

Crystallography Journals Online [partners](#) and [site credits](#).

Copyright © International Union of Crystallography

Appendix 3. Physical Properties of the Raw Materials Used in this dissertation.

Name	Formula	Molecular weight (g/mol)	Density (g/cm ³)	Purity (%)	Boiling point (°C)	Melting point (°C)
Titanium isopropoxide	C ₁₂ H ₂₈ Ti	284.26	0.97	97	240	18-20
Zirconium propoxide	C ₁₂ H ₂₈ Zr	327.58	1.058	70	-	-
Acetic acid	C ₂ H ₄ O ₂	60.05	1.06	99.7	117.9	16.6
Ethanol	C ₂ H ₆ O	46.07	0.789	99.95	78.3	-114.1
2-Propanol	C ₃ H ₈ O	60.10	0.785	99.5	82.4	-88.5
Hexene	C ₆ H ₁₄	86.18	0.659	99	69	-95
Xylenes	C ₆ H ₄ (CH ₃) ₂	106.17	0.86	reagent	-----	137-140
Ferric nitride nonahydrated	Fe(NO ₃) ₃ .9H ₂ O	404	-----	98	47	-----
Triethylamine	(C ₂ H ₅) ₃ N	101.19	0.726	99	88	-115
Methylene blue	C ₁₆ H ₁₈ ClN ₃ S	319.85	0.98	0.05 wt	---	-----

Appendix 4. Powder XRD Analysis Conditions.

Experimental parameters for Bruker D8 Discover diffractometer

Type of radiation	CuK α 1+K α 2 = 1.54184 Å
Power	40 kV x 40 mA
Type of scan	Coupled
Number of frames	3 (merged)
Beam Diameter	500 μ m
2 θ range	4.9° - 93.95°

Experimental parameters for Rigaku (Rigaku - Geigerflex CN2029) diffractometer

Type of radiation	CuK α 1+K α 2 = 1.54184 Å
Power	40 kV x 35 mA
Type of scan	Coupled
Step Size	0.05
Step Time	2sec
2 θ range	2.0° - 115.0°

Appendix 5. Typical EDX spectrum for binary Zr-Ti nanomaterials

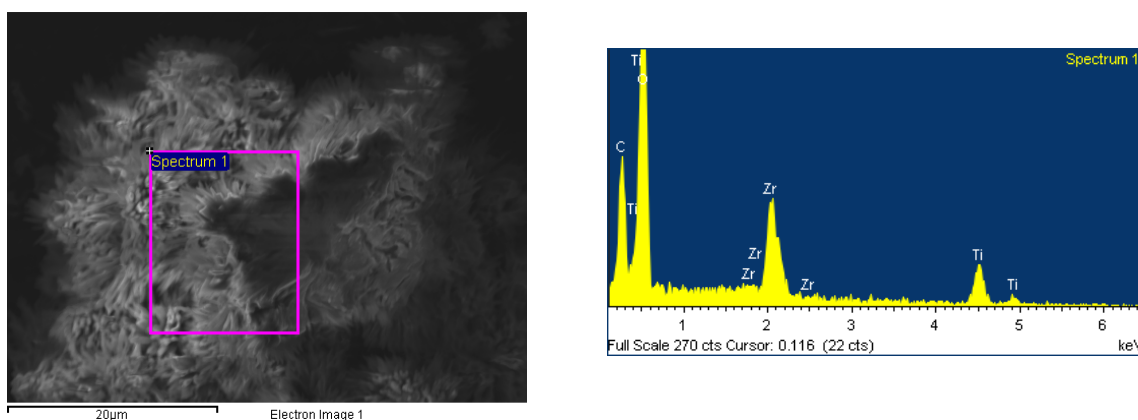


Figure A.1. A typical EDX spectrum for 20% Zr composition samples.

Appendix 6. Typical DSC curves for binary Zr-Ti nanomaterials at different heating rate.

DSC curves for binary Zr-Ti nanomaterials at different heating rates provided in Figure A.2 show two exothermic peaks representing phase transformations. According to the technical literature, the first and second peaks represent amorphous to anatase and anatase to rutile transformations, respectively. Although the phase transformation

temperature strongly depends on the synthesis method, the amount of impurities present and the heat treatment method, most of the reported values ranged ca. 300-450 °C for anatase and 450-800 °C for the rutile transformation. The positions of the phase transformation in this dissertation are within these ranges.

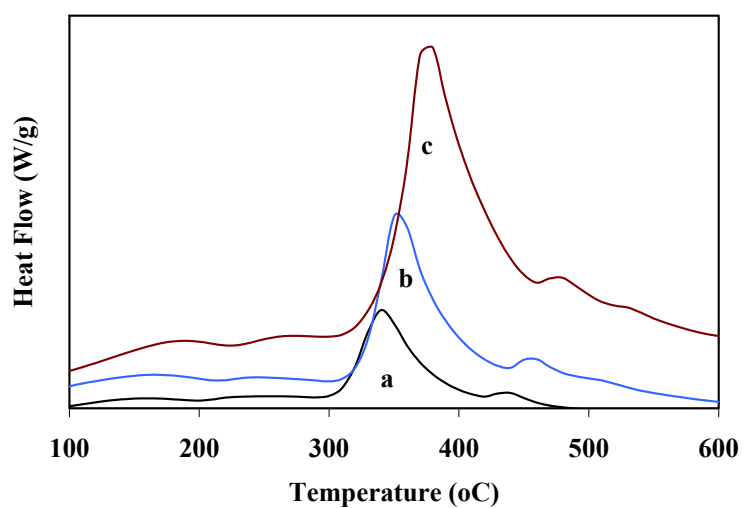


Figure A.2: DSC curves for 10% ZrO₂-TiO₂ in air using heating rate (a) 5 °C/min, (b) 10 °C/min, and (c) 20 °C/min.

Appendix 7. Typical XPS deconvoluted spectra for N doped TiO₂ nanomaterials.

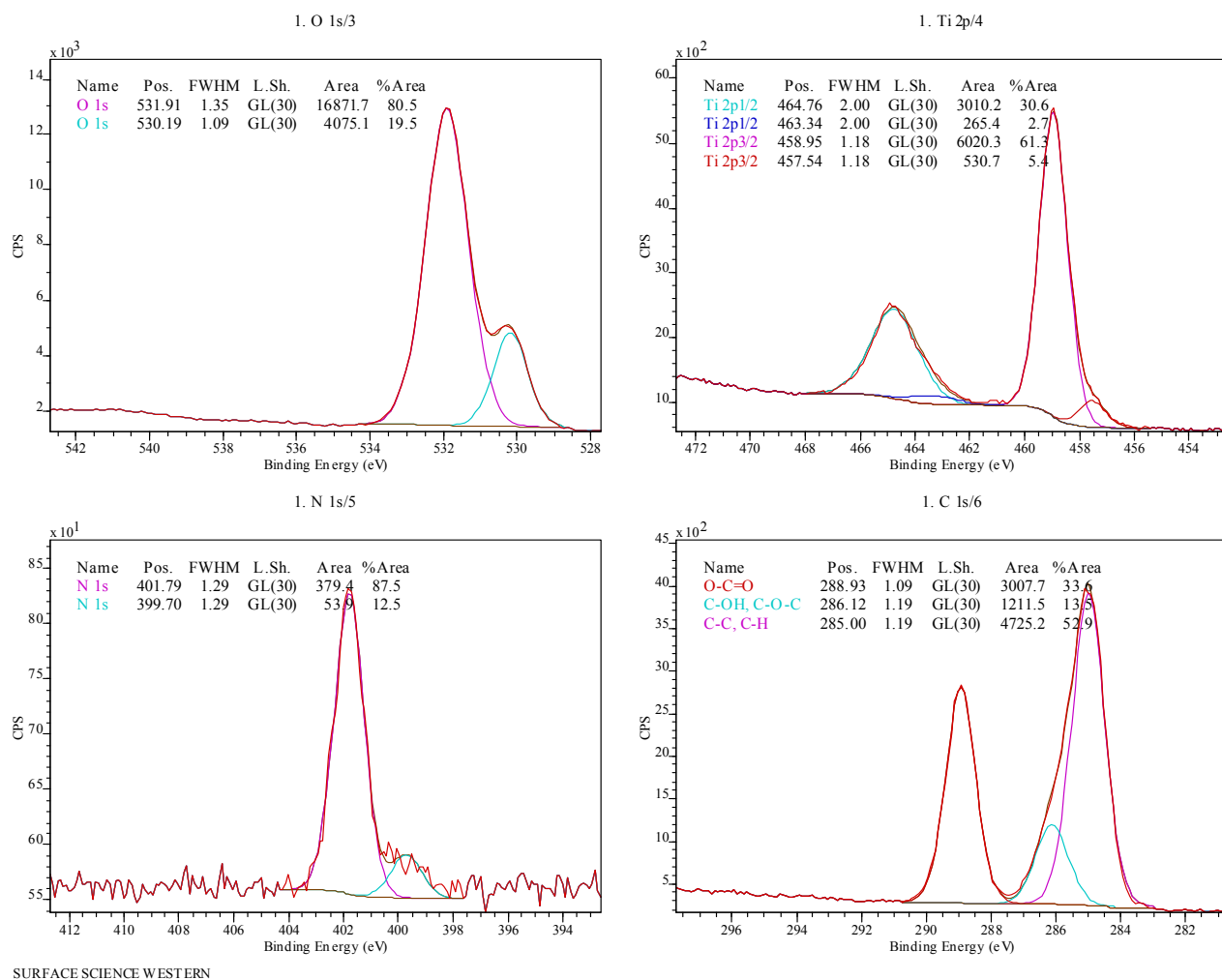


Figure A.3: Typical deconvoluted xps spectra of different component present in the N-doped TiO₂ nanomaterials.

Appendix 8. Evaluation of the modified nanomaterials as a photocatalyst.

a) Photocatalytic decomposition mechanism

The mechanism of the photocatalytic decomposition of the MB dye using the nanoTiO₂ is briefly reviewed here. The chemical structure of the MB dye is schematically shown in Figure A.4. The MB dye has a cationic configuration in an aqueous solution, which results in its adsorption through the Coulombic interaction with the OH⁻ ions

present on the surface of TiO₂ nanocrystallites. As described schematically in section 2.11 in Figure 2.1, when the MB dye and TiO₂ catalyst suspension is irradiated with the UV radiation, the e⁻/h⁺ pair is created within the TiO₂ nanocrystallites due to ejection of an electron from the valence band into the conduction band, leaving behind a hole in the valence band (charge-carrier generation). The generated holes may react with the surface-adsorbed OH⁻ ions forming the ·OH radicals. The ·OH radicals may also be formed by the reaction of dissolved oxygen (O₂) with the generated electrons and the protons forming the hydrogen peroxide (H₂O₂) as an intermediate product, which subsequently gets decomposed to the OH radical by releasing the OH ion into the aqueous solution. The overall reaction may be summarized as the interfacial charge transfer radicals thus formed are mainly responsible for the degradation of the MB dye through its successive attacks via formation of several intermediate products.

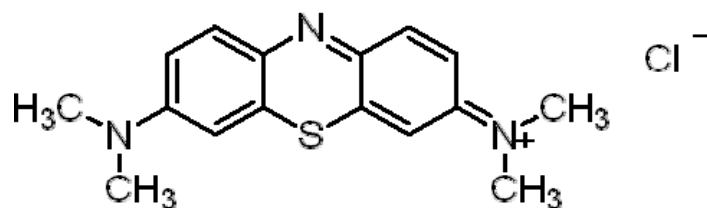


Figure A.4: Chemical structure of methylene blue.²¹

The overall reaction, which results in the decomposition of the MB dye into carbon dioxide (CO₂), nitrate (NO₃⁻) ions, sulfate (SO₄⁻) ions, protons, and water. The efficacy of the above mechanism in decomposing the MB dye depends on the effectiveness of the photocatalytic process in transferring the photoinduced e⁻/h⁺ pair from the particle volume to the particle surface, and subsequently to the surface-adsorbed

species. The generated e-/h+ pair, hence, must migrate to the particle surface as a separate entity; however, if the TiO₂ nanocrystallite size is relatively larger, which increases the travel distance for the e-/h+ pair, then they may recombine within the particle volume before reaching the particle surface (volume charge-carrier recombination).

b) Photodegradation Kinetics

When a semiconductor catalyst is illuminated with photons whose energy is equal to or greater than the band-gap energy, the semiconductor absorbs these photons, resulting in creation of electron-hole pairs, which dissociate into free electrons in the conduction band and holes in the valence band. Simultaneously, in the presence of a fluid phase (gas or liquid), spontaneous adsorption occurs and according to the redox potential of each adsorbate, an electron transfer proceeds towards acceptor molecules, whereas a positive hole is transferred to a donor molecule.

Each ion formed subsequently reacts to form the intermediates and final products. As a consequence of reactions, the photonic excitation of the catalyst appears as the initial step of the activation of the whole catalytic system. The photon energy is adapted to the absorption by the catalyst, not to that of the reactants. The activation of the process goes through the excitation of the solid but not through that of the reactants. Hence, there is no photochemical process in the adsorbed phase but only a true heterogeneous photocatalytic regime as demonstrated further. As for classical heterogeneous catalysis, the overall process can be decomposed into five independent steps:

- I. Transfer of the reactants in the fluid phase to the surface.

- II. Adsorption of at least one of the reactants.
- III. Reaction in the adsorbed phase.
- IV. Desorption of the product(s).
- V. Removal of the products from the interface region.

The only difference with conventional catalysis is the mode of activation of the catalyst in which the thermal activation is replaced by a photonic activation. However, the activation mode is not concerned with steps I, II, IV and V, although photoadsorption and photodesorption of some reactants, mainly oxygen, do exist. Step III contains all the photoelectronic processes and there is no photochemistry in the adsorbed phase. The Langmuir-Hinshelwood kinetic model is widely used to describe the kinetics of photodegradation of many organic compounds, and is described as:

$$r = -\frac{dc}{dt} = \frac{kKc}{1 + Kc} \quad A.1$$

where r is the rate of reaction (mol/L.min), c is the equilibrium concentration of reagent (mol/ L), t is the time (min), k is the rate constant (1/min), and K is the Langmuir constant (L/mol). This equation is simplified to a pseudo-first-order expression, when the concentration of reagent being reacted is too low, as

$$r = -\frac{dc}{dt} = kc \quad A.2$$

Equation (A.2) can be integrated, resulting in

$$\ln \frac{c_o}{c} = kt \quad A.3$$

where c is the dye concentration at instant t (mol/L), c_0 is the dye concentration at $t = 0$ (mol/L), k is the pseudo-first-order rate constant (1/min), and t is the irradiation time (min).

c) Evaluation

After performing the degradation experiment, the concentration of the residual dye was determined according to the procedure described in section 3.2 using the following calibration curve.

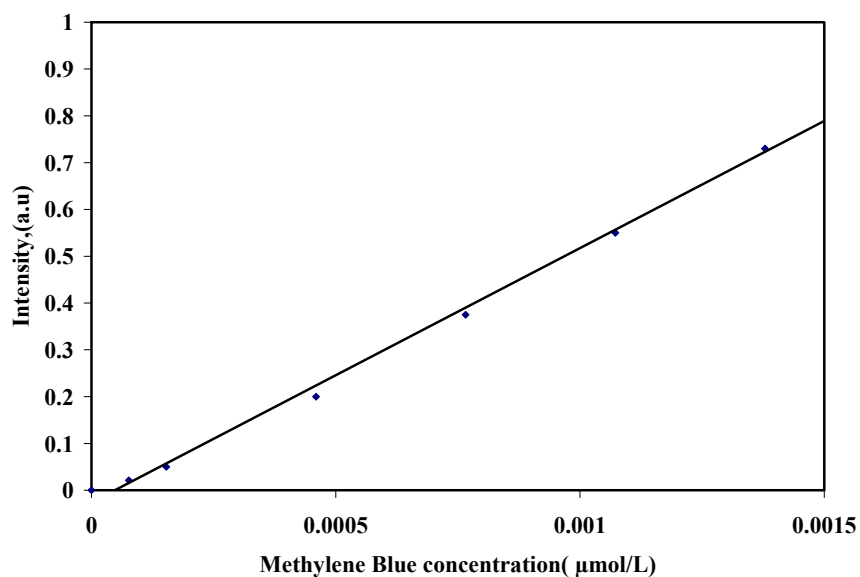


Figure A.5: Calibration curve to determine methylene blue concentration.

Using the residual dye concentration and equation 3.13, the following plots were constructed. The slope of the straight line provides the degradation rate for the particular sample for this specific run.

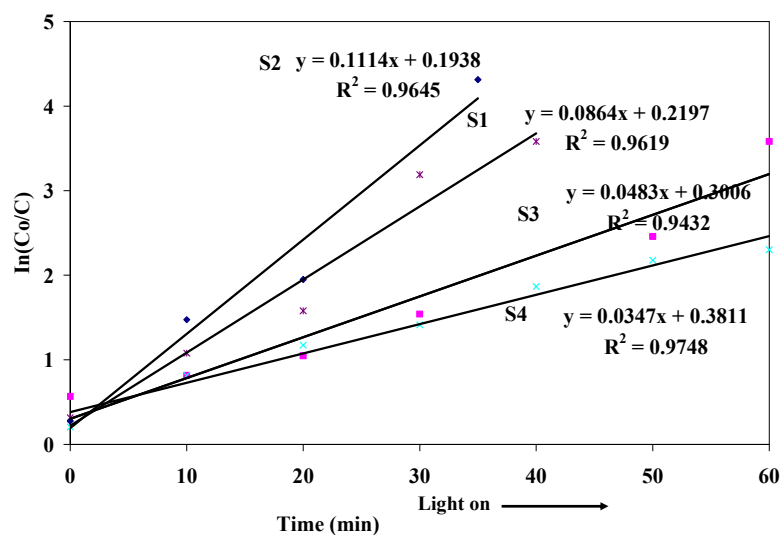


Figure A.6: Variation in the residual MB dye concentration (obtained using eq 3.13) as a function of UV radiation exposure time.

Appendix 9. ZrO₂/TiO₂ Binary Nanotubes as Fillers

The ZrO₂-TiO₂ nanotubes -PMMA nanocomposite samples with 0 to 6 wt % functionalized nanofillers were prepared by bulk polymerization technique following Khaled et al. reported procedure.⁴⁵ The procedure is briefly described here. First, as prepared nanotubes were calcined at 600 °C to obtain crystallinity and thermodynamic stability. Then the surface of the bimetallic nanotubes was functionalized as 1.25 g of calcined ZrO₂-TiO₂ nanotubes powder dispersed in 200 mL iso-propanol with the aid of ultrasonic agitation, followed by reacting with 20 mL of methacrylic acid at 80 °C with stirring for 48 h. The reaction product was then filtered and washed using ultrapure distilled water and dried at 80 °C for 8 h under vacuum. The nanocomposite was synthesized at room temperature using a known amount of PMMA powder and MMA liquid (weight of powder/weight of liquid 2.2) following bulk polymerization technique.

The powder portion contained 99.2 wt % PMMA beads (57.7 nm) and 0.8 wt % BPO. The liquid portion contained MMA (95.9 wt %), a dimethacrylate cross-linker (4 wt %), and an activator (0.1 wt %) for room-temperature initiator decomposition. After that, the dynamic Young's moduli and shear moduli for each specimen was evaluated by means of an ultrasonic technique using a pulse/function generator (811A 20MHzHewlett-Packard), a storage oscilloscope (60 MHz V-665 Hitachi), and lithium niobate piezoelectric crystals at 20-MHz resonant frequency for transmitting and receiving the ultrasonic signals.

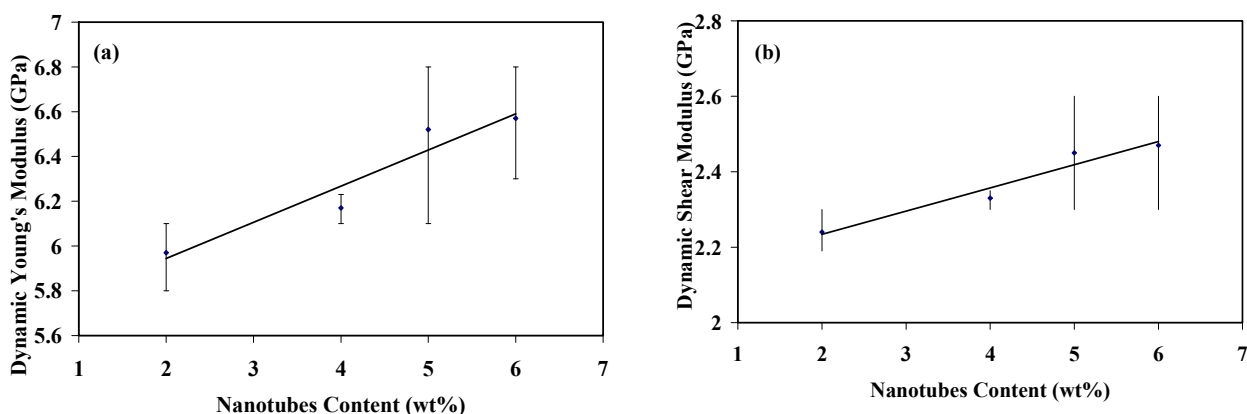


Figure A.7: Mechanical properties of (a) dynamic Young's modulus and (b) dynamic Shear modulus versus weight percentage of the ZrO_2-TiO_2 Nanotubes.

The dynamic Young's and Shear moduli for the prepared nanocomposite with various wt% nanofillers is provided in Figure A.7. It can be seen that both moduli increase with nanofiller's wt%. The dynamic Young's modulus ranged from 5.97 to 6.57 GPa and shear modulus varies from 2.24 to 2.47 GPa with changing the wt% of nanofillers from 2 to 6%. The mechanical properties of the nanocomposites strongly depend on the ability to transfer the external load between the reinforcing nanofiller

phase and the matrix. It is already reported that functionalization resulting the chemical bonding between the nanofiller and the PMMA matrix produced significantly higher values of elastic moduli. In addition, high interfacial surface area has positive effects on increasing the mechanical properties by enhancing adhesion between the nanofiller and polymer matrix. Hence, in this study functionalized binary nanotubes with high surface area ($80 \text{ m}^2/\text{g}$) show high elastic moduli, which is promising for potential bone cement application. In addition, it is anticipated that $\text{ZrO}_2\text{-TiO}_2$ binary nanotubes will provide better radioopacity compared to TiO_2 nanomaterials. As ZrO_2 is better radioopacifier and is used in commercial bone cement. Future investigations will focus further developing this area.

CURRICULAM VITA

Name: Rahima Akter Lucky

Place of Birth Farid pur, Bangladesh

Post-Secondary Education and Degrees: Bangladesh University of Engineering and Technology (BUET)
Dhaka, Bangladesh
1991-1996 B.Sc. in Chemical Engineering

Bangladesh University of Engineering and Technology (BUET)
Dhaka, Bangladesh
1997-1999 M.Sc. in Chemical Engineering

The University of Western Ontario
London, Ontario, Canada
2004-2008 Ph.D. in Chemical Engineering

Related Work Experience: Dec. 1996 to Dec. 1999
Lecturer

Jan. 2000 to Oct. 2001
Assistant Professor
Department of Chemical Engineering
Bangladesh University of Engineering and Technology (BUET)

Teaching Assistant
The University of Western Ontario
2004-2008

List of Publications:

PUBLICATIONS:

Lucky, R. A.; Charpentier, P. A., A one-step approach to the synthesis of ZrO₂ modified TiO₂ nanotubes in supercritical carbon dioxide. *Advanced Materials*. 2008, 20(9), 1755-1759.

Lucky, R. A.; Sui, R.; Charpentier, P. A.; Jennings, M. C., Decakis(μ_2 -acetato- κ_2 O:O')bis(μ_2 -isopropoxy- κ_2 O:O) tetraisopropoxytetra- μ_3 -oxo-tetratitaniumdizirconium *Acta Cryst.*, E 2007, 63, m2429–m2430.

Lucky, R. A.; Charpentier, P. A., Thermal Behavior of ZrO₂ modified TiO₂ Nanotubes Synthesized in scCO₂. (In preparation)

Lucky, R. A.; Charpentier, P. A., Effects of solvent in one-pot synthesis of ZrO₂-TiO₂ nanomaterials via acid modified sol-gel process. (In preparation)

Lucky, R. A.; Charpentier, P. A., Synthesis of Zr-Ti Binary metal oxide nanostructure via acid modified sol-gel route in scCO₂. (In preparation)

Lucky, R. A.; Charpentier, P. A., Zr Modified N doped TiO₂ nanostructured materials by a surfactant free Sol-Gel process in supercritical CO₂ for solar energy applications. (In preparation)

Lucky, R. A.; Charpentier, P. A., Effects of the Process Variables on the 10% ZrO₂ modified TiO₂ nanotubes synthesis in supercritical CO₂. (In preparation)

CONFERENCE PROCEEDINGS:

Lucky, R. A.; Paul A. Charpentier, N-doped TiO₂ Nanostructure via Sol-gel Route in Supercritical CO₂. 20th Canadian Symposium on Catalysis, Kingston, Canada. 2008

Lucky, R. A.; Paul A. Charpentier, Synthesis and Characterization of Fe doped TiO₂ nanomaterials in scCO₂. ACSAICHE Joint spring meeting, New Orleans, LA, 2008

Lucky, R. A.; Paul A. Charpentier, ZrO₂ modified N-doped TiO₂ nanomaterials from scCO₂. AICHE annual meeting, salt lake city, Utha, 2007

Lucky, R. A.; Charpentier, P. A., Ti-Zr binary metal oxide nanomaterials in scCO₂.- Nanoforum, Waterloo, Canada, 2007